Excitons in Lead Halide Perovskite Nanocrystal systems : In Depth Investigation of the Fine Structure, Phonon Interactions and Energy transfers

Victor Guilloux



Thèse de doctorat de Sorbonne Université

Réalisée à l'Institut des Nanosciences de Paris

École doctorale n°564 : Physique en Île-de-France

Spécialité : Physique

Excitons in Lead Halide Perovskite Nanocrystal systems: In Depth Investigation of the Fine Structure, Phonon Interactions and Energy transfers

---

Par Victor GUILLOUX

Dirigée par Laurent LEGRAND

Et Thierry BARISIEN

Présentée et soutenue publiquement le 12/11/2024

Devant un jury composé de :

Mme Stéphanie BUIL	Rapportrice
M. Louis BIADALA	Rapporteur
M. Thierry GUILLET	Examinateur
M. Alberto BRAMATI	Président du jury
M. Laurent LEGRAND	Directeur de thèse
M. Thierry BARISIEN	Co-encadrant de thèse

Remerciements

En premier lieu, je souhaite remercier les membres du jury pour le temps qu'ils ont consacré à l'évaluation de ce travail de thèse. Merci à Stéphanie Buil et Louis Biadala d'avoir rapporté sur ce manuscrit, à Thierry Guillet pour son rôle dans l'examen de ce travail, et enfin à Alberto Bramati pour avoir accepté de présider le jury de soutenance.

J'aimerais ensuite adresser mes plus sincères remerciements à mes deux encadrants de thèse, Laurent Legrand et Thierry Barisien. Laurent, merci d'avoir accepté de diriger cette thèse et de m'avoir accompagné tout au long de cette aventure doctorale. Que ce soit sur les enjeux scientifiques, dans mes débuts en tant qu'enseignant, ou même pour naviguer dans les méandres administratifs d'avant soutenance, ton soutien a été essentiel à chaque étape. Thierry, merci également de m'avoir pris sous ton aile. Ton expertise en aspects expérimentaux et numériques m'a permis d'acquérir une rigueur scientifique précieuse, qui m'accompagnera tout au long de ma carrière. La disponibilité constante dont vous avez tous deux fait preuve, votre soutien face à mes nombreuses questions et doutes, ainsi que le partage généreux de vos connaissances scientifiques ont fait de cette période une expérience d'une grande richesse intellectuelle. Cerise sur le gâteau, depuis la préparation au concours de l'école doctorale jusqu'à celle de la soutenance, vous avez su instaurer une ambiance de travail agréable et bienveillante, que je tiens à souligner ici.

Les laboratoires de physique fonctionneraient au ralenti sans leurs ingénieurs de recherche. Un immense merci à Florent Margaillan, pour son expertise technique indispensable sur les chaînes laser utilisées dans ce travail et pour son enthousiasme constant à partager ses connaissances. Merci également à Mathieu Bernard, pour son aide précieuse et son grand savoir-faire en cryogénie et en vide, et aussi pour les innombrables réparations de pompes turbomoléculaires ! Enfin, merci à Silbé Majrab, pour sa contribution dans l'interfaçage électronique des diverses plateformes expérimentales utilisées au cours de cette thèse.

Je tiens également à remercier chaleureusement les membres permanents de l'équipe Photonique et Cohérence de Spin de l'INSP : Maria Chamarro, Christophe Testelin, Frédérick Bernardot et Alex Chin, pour leur disponibilité, leurs réponses toujours pertinentes à mes questions, et leurs diverses contributions au travail présenté dans ce manuscrit.

Ce travail de thèse, centré sur les nanocristaux, n'aurait jamais pu voir le jour sans les nombreux *batchs* de solutions colloïdales fournis par Emmanuel Lhuillier. Je tiens donc à le remercier pour sa réactivité constante dans la production de nanocristaux de grande qualité tout au long de ce projet et, surtout, pour m'avoir transmis l'envie d'étudier ces objets fascinants lorsque j'étais encore étudiant en Master. Un autre aspect crucial de ce travail repose sur la contribution théorique de Kaïs Boujdaria et Amal Grihbi, de l'Université de Carthage. Leur expertise essentielle, tant dans la modélisation k.p que dans les calculs de structure fine excitonique, a fourni les bases solides pour interpréter nos résultats expérimentaux. Enfin, je souhaite remercier Hernán Míguez et toute son équipe de l'Institut des Sciences des Matériaux de Séville pour la réalisation des échantillons de nanocristaux de pérovskite en matrice mésoporeuse. Cette collaboration a donné des résultats prometteurs qui mèneront, je l'espère, à une belle publication.

L'INSP est un laboratoire dynamique, en partie grâce à la forte implication de ses doctorants, avec qui j'ai eu le plaisir de partager de nombreux moments de convivialité. Merci en particulier à Anatole, Brieuc, Lucille, Ashwin, Benoît et Guillaume B., ainsi qu'à la relève : Antoine, Guillaume L., Hugo et Robin, pour ces bons moments passés à parler physique, politique et parfois de sujets plus légers (surtout ces derniers !). Vous avez rendu les repas du CROUS meilleurs et la traditionnelle bière du vendredi soir encore plus rafraîchissante.

Merci également au soutien de mes amis en dehors du laboratoire : le *Milly gang* (Tom, Dylan, Guillaume, les Bastiens, Charline, Célie, Clara, Max, Julie, Cédric) et les copains de Paris (Benjamin, Rachid, Julia, Zak, Clément, Pauline, Léo, Valérie). Je n'ai pas pu vous voir autant que je l'aurais souhaité cette année, mais ça va changer, c'est promis.

Enfin, je tiens à adresser mes remerciements les plus sincères à mes proches. À vous, Papa et Maman, merci pour votre soutien indéfectible à chaque étape de mes projets. Ce long voyage étudiant arrive enfin à son terme et si je peux aujourd'hui en récolter les fruits, c'est en grande partie grâce à votre présence et à votre encouragement constant. Juliette, Clémentine, Olivier (et Charlotte !), un immense merci à vous aussi. Vous m'avez offert de précieux moments d'évasion, loin de la physique et m'avez rappelé qu'il y a aussi plein d'autres belles choses dans la vie. J'ai hâte de pouvoir enfin consacrer plus de temps à ces instants partagés avec vous !

Abstract

Over the past decade, a new generation of colloidal nanocrystals (NCs) has emerged in the field of semiconductor quantum dots: the lead halide perovskite (LHP) NCs. Their remarkable emission properties, combined with a simple and cost-effective synthesis, have generated significant interest in these materials and their optoelectronic applications. Indeed, perovskite NCs exhibit very high photoluminescence (PL) yields, largely due to their unique band structure and the position of defect states within it. Additionally, LHP NCs offer highly tunable emission across the entire visible spectrum by adjusting their chemical composition and morphology. The exciton, a bound state between the electron and the hole, lies at the heart of the optical properties of these NCs and is a crucial element in their study. In particular, the fine structure of this state, which results from the exchange interaction between the electron and the hole, has been the subject of significant research, motivated by the use of these systems in quantum technologies, notably as single-photon sources.

This work is set within this context and focuses on the exciton fine structure (EFS) of the band edge exciton and the parameters influencing its properties. Time-resolved and steady-state optical spectroscopy techniques are applied to two LHP materials: the chloride compound $CsPbCl_3$ and the hybrid $FAPbBr_3$. The study of $CsPbCl_3$ NCs forms the core of this manuscript. Through cryogenic temperature PL spectroscopy experiments on single objects, the bright states of the EFS are revealed for the first time in this compound and compared to a theoretical model. The observed variation in the energy gaps between the bright levels of the EFS is explained by the crystal symmetry, its dielectric environment, and the NC shape. Moreover, the spectral response of exciton species such as biexcitons and trions, as well as exciton-phonon composites, are presented. The influence of phonons on the emission and exciton coherence properties in single NCs is studied in detail with temperature. Finally, time-resolved spectroscopy enables the observation of PL decays. The behavior of these decays with temperature is then explained by a thermal mixing model between dark and bright states, involving the lattice optical phonons. This model thus reveals the position of the dark state within the EFS, thereby completing its description.

The last part of the manuscript focuses on the study of $FAPbBr_3$ NCs encapsulated in a porous matrix. The NCs are synthesized directly within the pores of the host matrix, without ligands. This system is first studied at low NC density to determine whether the spectral response of single objects can be observed and, more generally, whether the host-matrix strategy could be a valuable access to phases of spatially dispersed single NCs. Finally, spectroscopy on samples of high NCs density is performed. The excitation by a femtosecond laser reveals an amplified spontaneous emission effect. Furthermore, the emission dynamics in this system suggests the existence of energy transfers between the NCs. The associated results are compared to numerical simulations of the PL dynamics based on Förster energy transfer between nearest neighbors that allow to obtain a first estimation of the transfer rate between ideally coupled NCs.

This Thesis contributes to the expansion of knowledge on excitons within LHP NCs. The chloride compound $CsPbCl_3$ holds a special place within this class of materials, and the experiments conducted on it further reinforce the theoretical model of the EFS. Finally, the investigations related to $FAPbBr_3$ NCs in a porous matrix illustrate how new processing approaches might be used to change the emission properties at the individual scale or within interacting NC ensembles.

Résumé de la thèse

Au cours des dix dernières années, une nouvelle génération de nanocristaux (NCx) colloïdaux a émergé dans le paysage des boîtes quantiques semi-conductrices : les NCx pérovskite (PVK) d'halogénure de plomb. Des propriétés d'émission remarquables, combinées à une synthèse simple et économique, suscitent un engouement autour de ces matériaux et de leurs applications optoélectroniques. En effet, les NCx PVK montrent des rendements de photoluminescence (PL) très élevés, en grande partie grâce à leur structure de bande particulière et à la position des états de défauts au sein de celle-ci. De plus, les NCx PVK offrent une grande modulabilité d'émission sur l'ensemble du spectre visible, *via* l'ajustement de leur composition chimique et de leur morphologie. L'exciton, état lié entre l'électron et le trou, est au cœur des propriétés optiques de ces NCx et constitue un élément essentiel dans leur étude. En particulier, la description de la structure fine de cet état, produit de l'interaction d'échange entre l'électron et le trou, fait l'objet d'importants travaux de recherche, motivés par l'utilisation de ces systèmes dans des technologies quantiques, notamment comme sources de photons uniques.

Ce travail s'inscrit dans ce contexte et se focalise sur la structure fine excitonique (SFE) des excitons dits "de bas de bande" et les paramètres influençant ses propriétés. Des techniques de spectroscopie optique, résolues en temps ou non, y sont appliquées à deux matériaux PVK : le composé chloré $CsPbCl_3$ et l'hybride $FAPbBr_3$. L'étude des NCx de $CsPbCl_3$ constitue le cœur de ce manuscrit. Par des expériences de spectroscopie de PL menées à température cryogénique

sur objets uniques, les états brillants de la SFE sont révélés pour la première fois dans ce composé et confrontés à un modèle théorique. La variation observée dans les écarts énergétiques entre niveaux brillants de la SFE est expliquée par la symétrie cristalline, l'environnement diélectrique et la forme des NCx. Par ailleurs, les réponses spectrales d'espèces comme le biexciton ou le trion, ainsi que celle des "espèces composites" exciton-phonon, sont présentées. L'influence des phonons sur les propriétés d'émission et de cohérence de l'exciton fait l'objet d'une étude approfondie en température sur des NCx individuels. Enfin, un montage de spectroscopie résolue en temps permet l'observation des déclins de PL. Le comportement de ces déclins avec la température est alors expliqué par un modèle de mélange thermique entre état noir et brillant, impliquant les phonons optiques du réseau. Ce modèle révèle ainsi la position de l'état noir au sein de la SFE, complétant sa description.

La dernière partie du manuscrit porte sur l'étude des NCx de $FAPbBr_3$ encapsulés en matrice poreuse. Les NCx sont synthétisés directement dans les pores de la matrice hôte, sans ligands. Ce système est d'abord étudié à faible densité de NCx afin de déterminer si l'observation de la réponse spectrale d'objets uniques y est possible. Enfin, la spectroscopie d'échantillons contenant une forte densité de NCx est réalisée. L'excitation par une source laser femtoseconde met en évidence un effet d'émission spontanée amplifiée. Par ailleurs, la dynamique d'émission dans ce système suggère l'existence de transferts d'énergie entre NCx. Ces résultats sont alors confrontés à des simulations numériques basées sur un modèle de transfert d'énergie Förster entre plus proches voisins. Une première estimation du taux de transfert entre NCx voisins et "idéalement couplés" est ainsi obtenue.

Ce travail de thèse contribue à l'élargissement des connaissances sur l'exciton au sein des NCx PVK. Le composé chloré $CsPbCl_3$ occupe une place particulière dans cette classe de matériaux et les expériences menées sur celui-ci viennent renforcer le modèle théorique de la SFE dans les PVKs aux halogénures de plomb. Enfin, les résultats relatifs aux NCx $FAPbBr_3$ en matrice poreuse contribuent à une meilleure compréhension des propriétés d'émission de ces objets dans un environnement peu exploré, à l'échelle individuelle ou au sein d'ensembles de NCx en interaction.

Contents

INTRODUCTION

Last year, the Nobel Prize in Chemistry was awarded to Mungi G. Bawendi, Louis E. Brus, and Alexey Ekimov for their groundbreaking work on the discovery and synthesis of colloidal quantum dots. These quantum dots are nanoscale materials, whose dimensions have been reduced in all three spatial directions to the nanometer range, typically comprising from hundreds to hundreds of thousands of atoms. Their scientific exploration began in the late 1970s Soviet Union, when Ekimov investigated the optical properties of glass doped with copper chloride (CuCl) particles. The absorption spectrum of this material exhibited exciton-like resonances that were shifted in energy compared to bulk CuCl material [1]. Since quantum confinement effects had already been described in epitaxial quantum wells, Ekimov deduced that these CuCl particles were, in fact, 3D-confined nanocrystals embedded within the glass matrix [2]. He later collaborated with A. Efros to develop a theory describing the optical properties of quantum dots, which is still in use today [3, 4]

Working at the same time at Bell Laboratories in New Jersey, Louis Brus took a different approach by generating colloidal nanocrystals of cadmium sulfide (CdS) in aqueous media. As the colloidal solutions aged, Brus observed a redshift in the optical transitions of the particles, which he attributed to a size effect caused by Ostwald ripening [5, 6]. Over the following years, his group refined the colloidal synthesis of various II-VI semiconductors, including CdS, CdSe, and ZnS, in aqueous media [7], and made significant contributions to the theoretical understanding of these nanomaterials.

In the early 1990s, Mungi Bawendi, a former postdoctoral fellow from Brus's group, perfected the colloidal synthesis of II-VI nanocrystals in collaboration with his PhD students, J. Norris and C. Murray. Their method introduced the use of organic solvents, rapid injection of precursors at elevated temperatures, and the addition of capping ligands to stabilize the quantum dots in solution [8]. This innovative approach, known as the Hot-Injection synthesis method, allowed for precise control over the nucleation and growth of the quantum dots, enabling fine modulation of their size and, by extension, their optical properties. Today, hot-injection synthesis remains the method of choice for producing colloidal quantum dots of semiconductors.

Semiconductor quantum dots are still an emerging technology but have already found applications in several domains. In biology, their broad absorption spectrum, narrow emission lines, photochemical stability, and the ability to functionnalize the surfaces of these objects have led to their use as fluorescent biological markers in living cells [9, 10] (although their toxicity, due to the presence of heavy metals, still represents a considerable issue). The ability of quantum dots to efficiently convert light into electrical energy across a broad spectral range has also led to their use as absorbing layers in solar cells [11] or for the fabrication of photodetectors [12]. Regarding light emission, the most widespread application is undoubtedly the quantum dot-based LED, which has enabled the production of a new generation of LED displays [13, 14]. Additionally, quantum dots have been used as optical gain media in quantum dot lasers [15], and in quantum optics, their ability to emit single, ungrouped photons makes them promising candidates for single-photon sources [16].

In 2015, a new class of colloidal quantum dots emerged: the Metal Halide Perovskite (MHP) nanocrystals (NCs). The first successful synthesis was achieved by the group of M. Kovalenko at ETH Zürich using the hot injection method [17]. Since then, research on MHP NCs has surged worldwide, driven by their exceptional properties compared to the traditional II-VI quantum dots. These properties include significantly larger absorption coefficients, allowing them to capture more light over a broader spectral range, and higher photoluminescence quantum yields, leading to a brighter emission [18]. Perovskite NCs also exhibit narrower emission lines, producing purer or more saturated colors [17, 19]. Another key advantage of these NCs is their intrinsic tolerance to defects, eliminating the need for the additional passivation layers that are commonly required for II-VI quantum dots. Finally, the synthesis of perovskite nanocrystals is simpler, performed at lower temperatures and is time and cost effective, all of this making their production easily scalable [20]. These advantages have made perovskite NCs highly attractive for the previously mentioned applications but their photophysics is less known and further research input is needed to fully understand these exceptionnal optical properties.

As with other quantum dots, the optical properties of perovskite NCs are governed by band-edge electronic excitations, which form electron-hole pairs bound by the Coulomb interaction, known as excitons. While perovskite NCs share some similarities with II-VI semiconductor quantum dots, their distinctive crystal lattice symmetry and electronic band structure require a new theoretical framework to describe the exciton and its fine structure. A significant breakthrough was achieved in 2018 by the group of A. Efros, which adapted the existing exciton fine structure theory for II-VI quantum dots to MHP NCs [21]. Since then, several research groups have contributed to refining this model [22, 23, 24], and while the description of the exciton in MHP NCs has made a lot of progress it still remains an active topic of investigations.

In this context, the experimental work presented in this manuscript aims at expanding the general knowledge of the optical properties of MHP NCs by investigating the impact of key parameters that are known to contribute to the exciton fine structure (EFS) through the electron-hole exchange interaction. Specifically, the following parameters are considered: the crystal phase symmetry, dielectric confinement, and the anisotropy in the general shape of the NCs. This work benefits from the advances made over the last three decades in the optical spectroscopy of single emitters at cryogenic temperatures to explore an MHP material that has been left aside due to its poorer emission properties: the chloride perovskite compound $CsPbCl_3$. This material is of significant interest for general models of the perovskite family due to its largest exciton binding and optical transition energy, representing an extremum in what MHP materials can be. Additionally, the latter part of this manuscript investigates a hybrid organic-inorganic perovskite compound, the formamidinium lead bromide ($FAPbBr_3$), in the form of NCs embedded in a mesoporous silica matrix. The primary focus will be on understanding how the optical properties of these NCs adapt to their new environment. By examining these specific materials, valuable insights will be provided into the optical properties of MHP NCs and the results will contribute to the ongoing development of theoretical models describing their excitonic behavior.

The manuscript is structured into five chapters. In Chapter 1, the structural, electronic, and optical properties of MHP NCs are introduced. The exciton fine structure in these materials is described using a model based on electron-hole exchange interaction. Interactions between the exciton and its environment are also discussed, and a few notable applications are reviewed. This chapter serves as the theoretical foundation for the rest of the manuscript.

In Chapter 2, after introducing the Hot-Injection synthesis method used to produce the MHP NCs, various experimental setups for studying the optical responses of perovskite NCs—both in assemblies and at the individual object level—are presented. Specifically, the absorption and micro-photoluminescence (micro-PL) spectroscopy setups, used between liquid helium and room temperature, are described. The confocal microscopy configuration is also discussed, and the equipment necessary for performing time-resolved PL studies is outlined.

Chapter 3 presents the first set of results on the chloride perovskite compound $CsPbCl_3$. Micro-PL optical spectroscopy at liquid helium temperature allows to resolve the spectral signature of the exciton fine structure in this material. The repetition of these experiments enables the creation of a statistical ensemble of measurements, which helps to unveil the impact of NC shape anisotropy on the fine structure splittings, based on the theoretical framework established in Chapter 1. This chapter will also reveal the spectral signature of charged exciton species like the biexciton and the trion.

Chapter 4 continues the investigation of $CsPbCl_3$, focusing on the coupling of the exciton to

lattice vibrations. After revealing the energetic landscape of optical phonons through Raman spectroscopy, their interactions with the exciton are studied using direct and time-resolved spectroscopic measurements. In particular, exciton-phonon coupling is employed to reveal the EFS dark state, using a thermal mixing model between the bright and dark states. At the end of this chapter, the exciton fine structure of $CsPbCl_3$ NCs is fully characterized.

In the final chapter, Chapter 5, a different perovskite system, the $FAPbBr_3$ NCs, is studied within a new environment, consisting of a matrix of silica beads. This system is first examined at a low NC density, as an attempt to improve the isolation and chemical stability of the NCs. Subsequently, samples with higher NC densities are used to investigate collective behaviors. A non-linear effect in the emission of these samples is reported at high excitation power. Finally, the emission dynamics of high-density NC samples demonstrates a reduction in radiative lifetime with increasing energy, interpreted as Förster Resonance Energy Transfer (FRET) between neighboring NCs. Using a grid model of FRET between adjacent NCs, simulations provide access to the transfer rate between ideally coupled NCs in this system.

CHAPTER

EXCITONS IN METAL HALIDE PEROVSKITE NANOCRYSTALS 1

This Chapter provides a detailed description of metal halide perovskite (MHP) nanocrystals (NCs), with a focus on their electronic and optical properties. It begins by establishing the theoretical foundations necessary for understanding the experiments and results presented later in this manuscript. The first section will introduce the materials under study: the MHP NCs and their structural characteristics. The following section will investigate the electronic properties of MHP NCs. The $\boldsymbol{k} \cdot \boldsymbol{p}$ theory will be briefly introduced and applied to the modelization of the electronic band structure of MHPs. The effects of the reduction of the dimensionality towards the NC will also be discussed. The third section will be interested in the optical properties of MHP NCs that are intrisincally linked to the exciton. The energy fine structure of the exciton will be modelized by taking into account the electron-hole exchange interaction and the different structural parameters of the NC that impact its magnitude. In the fourth section, a focus will be made on the different mechanisms that are linked to the loss of exciton coherence. Finally the last section will briefly introduce the reader to some of the most interesting uses of MHP NCs either for optoelectronic devices or more advanced applications in quantum technologies.

1.1 Metal Halide Perovskites

Metal halide perovskites (MHPs), and more specifically $CsPbX_3$, were first synthesized at the end of the 19^{th} century by H.L. Wells *et al.* at Yale university [25]. The description as perovskite

structures came much later in 1958 when the Danish scientist C.K.Møller used powder and single crystal X-ray diffraction to determine their crystal symmetry [26] while providing the first description of the absorption spectral range in these materials. In 1978, hybrid organic-inorganic perovskites (HOIP) were synthesized for the first time by D.Weber in Stuttgart, replacing the Cesium cations (Cs^+) by the organic Methylammonium ($CH_3NH_3^+$) cation [27]. At this point a large interest started to grow around these materials due to their enhanced optoelectronic properties.

The first commercial light emitting devices based on luminescent HOIP were developped in the 1990s by a team of researchers at the T.J Watson Research center in New York, and by the end of the 20^{th} century M.Chikao *et al.* developed an optical absorption layer for solar cells using a rare-earth based perovskite compound in Japan. This spurred enthusiasm towards the fabrication of perovskite based solar cells and the first major success came in 2009 when Kojima *et al.* reported the development of a photovoltaic cell based on a methylammonium HOIP absorption layer achieving a solar energy conversion efficiency of 3.8% [28]. Since then, conversion yields of up to 25.7% [29] have been reached with perovskites solar cells. Thanks to their tunable band gap, they are expected to catch up with single crystal silicon devices and even reach the Shockley-Queisser limit of 31%.

Another significant breakthrough - of utmost interest to this work - came in 2015 when the group of M.V.Kovalenko achieved the first colloidal synthesis of MHP nanocrystals at ETH Zurich [17]. The study of these nanocrystals emerged as one of the most dynamic area in materials research primarily due to their unique set of properties: a fine spectral tunability, a high tolerance to defects, high photoluminescene quantum yields (PLQY), fast radiative decay rates and narrow-band photoluminescence. These characteristics, investigated throughout this manuscript, make MHP nanocrystals ideal materials for a wide range of optoelectronic applications.

1.1.1 Crystal structure and polymorphs

MHPs are semiconductor materials adopting the well-known structure of perovskite ABX_3 where X represents a halide anion (Cl^-, Br^-, I^- or a combination of these) B a divalent metallic cation (Pb^{2+}, Sn^{2+}, Ge^{2+}) and A is a monovalent cation, which can be either inorganic (Cs^+) or organic (Formamidinium FA^+; Methylammonium MA^+) [26]. The archetypal perovskite lattice has a cubic symmetry (O_h point group) and consists of a network of corner sharing octahedra $[BX_6]^{4-}$ with the A cations occupying the 12 coordinated cuboctahedral interstitial spaces in between, as depicted on Fig. 1.1 [30].

The structural stability of perovskite materials is usually estimated with two primary factors: the tolerance factor t and the octahedral factor μ [31, 32]. Introduced in 1926, Goldschmidt's

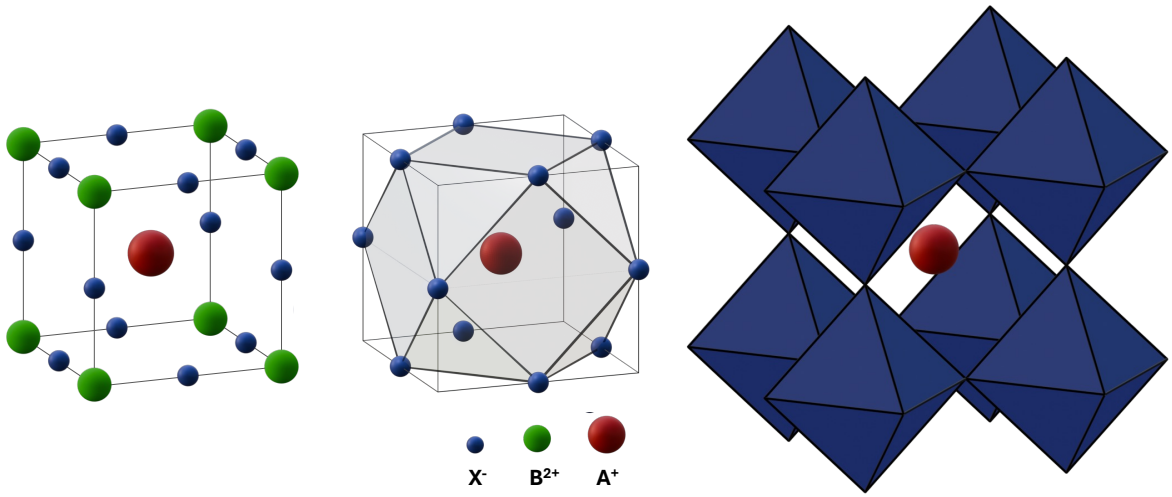

Figure 1.1: The cubic perovskite lattice structure (O_h point group). A unit cell is represented on the left. The central illustration highlights (grey shaded area) the cuboctahedral cavity created by the halide X^- anions. The figure on the right side illlustrates the sub-lattice of corner sharing octahedra formed by B^{2+} cations surrounded by six halide X^- anions.

tolerance factor t predicts empirically whether or not the A cation can fit in the cuboctahedral cavity (See the central illustration of Fig. 1.1) formed by the surrounding octahedra. It is defined as [33]: $t = (r_A + r_X)/\sqrt{2}(r_B + r_X)$ where r_A, r_B, r_X are the radii of the ions involved in the structure. This factor shows that the available choice for the A cation is rather limited in MHPs: either large inorganic cations such as Cs^+ and Rb^+ or small organic ions like MA^+ and FA^+ are suitable [34]. The octahedral factor μ is defined as $\mu = r_B/r_X$ and controls the stability of the $[BX_6]^{4-}$ octahedra [31, 35]. Again the integration of the B-site cation is constrained by ionic size restrictions imposed by the octahedron formed by the X^- anions. As a rule of thumb, the perovskite structure can be formed with a reasonable degree of stability when t lies between 0.8 and 1, and μ from 0.44 to 0.90 [35].

Lower symmetry crystal phases:

In ideal cubic structures, such as the oxide perovskite $SrTiO_3$, the t-factor converges to 1. However, for most perovskite structures, the A cation radius is slightly too short which leads to structural distortions that change the angle formed by the $B - X - B$ bonds along one or two directions. This process, depicted on Fig. 1.2 enhances the overall stability of the structure by reducing the size of the cuboctahedral cavity but lowers its symmetry which results in the emergence of a tetragonal (D_{4h} point group) and an orthorhombic (D_{2h}) crystal phase [30, 36, 37]. Thus, compared to the cubic crystal phase, the volume of the unit cell is doubled in the tetragonal case and quadrupled for the orthorhombic one.

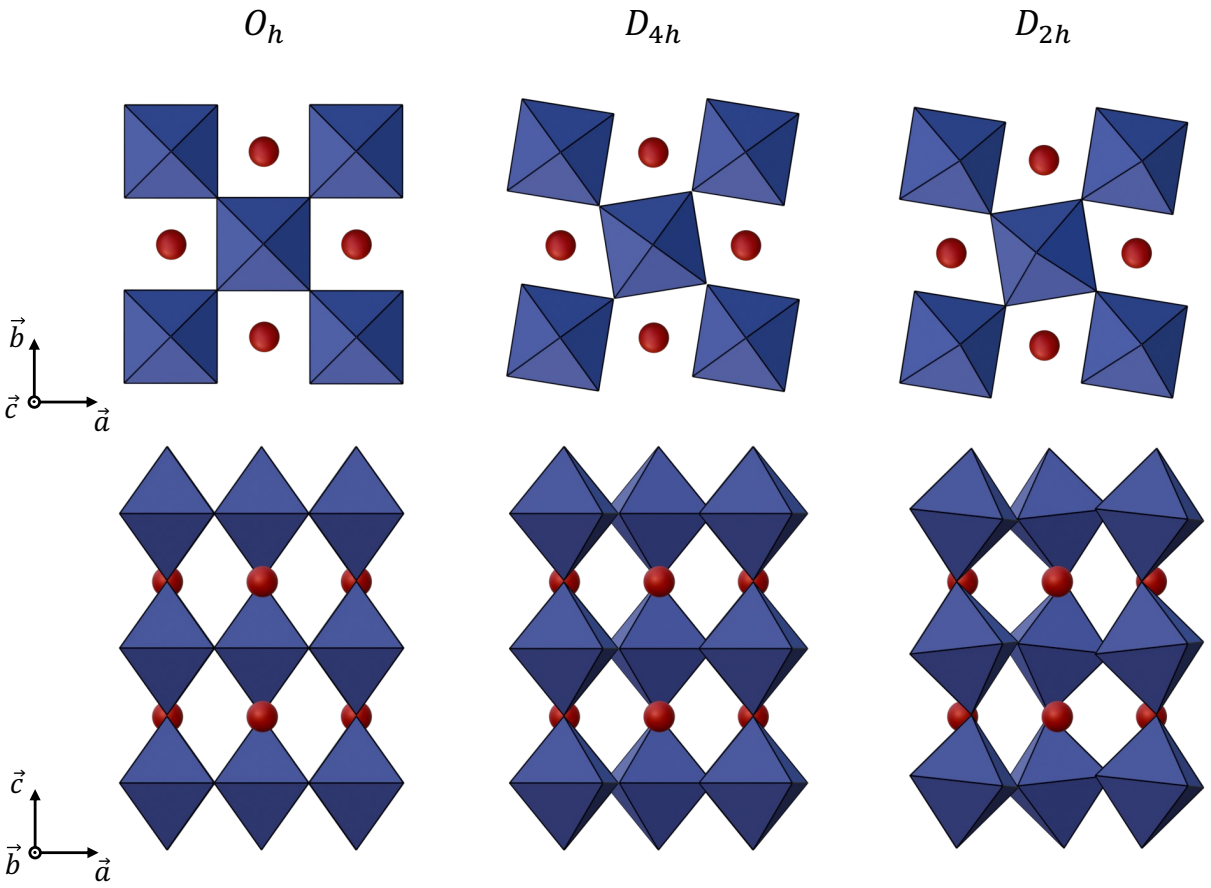

Figure 1.2: Illustration of the octahedral tilts for the three distinct crystal phases, cubic O_h, tetragonal D_{4h} and orthorhombic D_{2h} of MHPs. In the O_h phase no octahedral tilt is observed. The tetragonal phase shows octahedra rotations $\pm\alpha$ around the **c** axis. In the orthorhombic phase, a rotation $\pm\alpha$ of the octahedra around the **c** axis and $\pm\beta$ around the **b** axis are represented.

Under atmospheric pressure this phenomenon is well documented in MHPs and the three crystal phases, represented along two different crystallographic directions in Fig. 1.2, have been widely observed for each compound. The highest-symmetry cubic phase (O_h) exists predominantly at high temperature, the orthorhombic phase (D_{2h}) at the lowest temperatures and the tetragonal phase (D_{4h}) is generally found in between [36, 38]. Finally, it is already worth noting that when the dimensionality of MHPs is lowered (as with the nanocrystals studied in this work), the tetragonal phase is still regularly observed, even below the phase transition temperature measured on bulk [39, 40, 41, 42]. The phenomenon is not yet clearly understood but could originate from a thermally activated dynamic disorder in these structures that creates $D_{4h} \leftrightarrow D_{2h}$ fluctuations of the crystal structure on different time scales at high or low temperature [43, 44].

1.1.2 MHP nanocrystals

Inorganic nanoparticles have become one of the main pillars of nanosciences, allowing researchers to understand fundamental nanoscale effects and exploit them to engineer advanced materials. This brief review will focus on the bottom-up approaches for fabricating nanoparticles, which are constructive techniques involving the growth and self-assembly of atoms and molecules.

One of the most prominent bottom-up methods, widely used in both research and industry, includes epitaxial techniques such as MOCVD (Metal Organic Chemical Vapor Deposition) and MBE (Molecular Beam Epitaxy). These methods involve the deposition of material —whether in gas, liquid, or solid phase— layer by layer onto a substrate, typically within a reactor [45]. Epitaxy offers excellent control over the shape and size of the resulting nanostructures. The ability to grow materials directly on a substrate makes epitaxial techniques highly suitable for creating nanomaterials that can be integrated into "on-chip" devices [46, 47]. However, epitaxy is a resource-intensive process, both in terms of cost and time. For example, Molecular Beam Epitaxy (MBE), the most precise epitaxial technique for producing thin films, requires ultra-high vacuum reactors where elements are slowly sublimed and condensed onto the substrate at a growth rate of around one micron per hour, while the equipment cost can reach millions of euros [45].

Another widely used bottom-up approach is colloidal synthesis, a chemical technique first introduced by Bawendi, Murray, and Norris in 1993 to produce CdE (E = S, Se, Te) nanocrystals [8]. Colloidal synthesis involves dissolving chemical precursors in a solvent and applying specific treatments to initiate the crystal growth [48, 49]. The result is the formation of nanoparticles as a colloidal suspension directly in the solution.

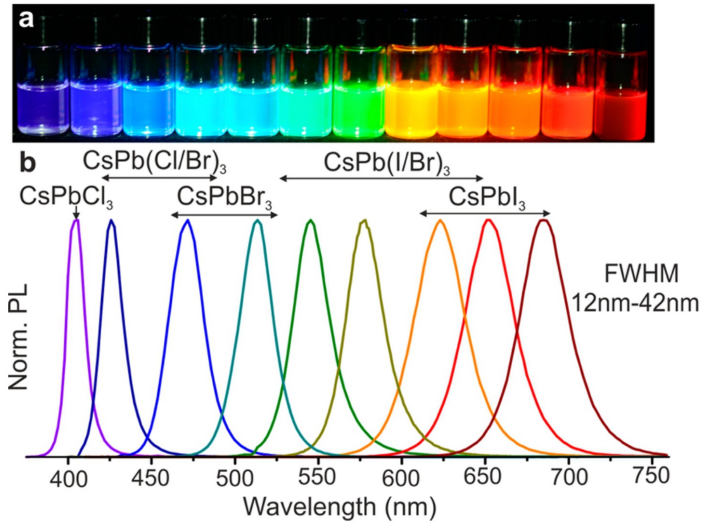

Figure 1.3: a. Solutions containing colloidal suspensions of inorganic perovskite nanocrystals under UV light illumination. **b.** Typical emission spectra of the colloidal solutions presented above. Figure adapted from Protesescu *et al.* [17]

This method offers several advantages. First, it is cost-effective: the precursors and ligands used are typically inexpensive, and the necessary laboratory equipment is often already available in chemistry labs. Colloidal syntheses can also be easily scalable and fast; for instance, the synthesis of metal halide perovskite nanocrystals (NCs) *via* hot injection method, requires only about 2 hours of preparation and around 10 seconds of actual crystal growth [17]. Furthermore, reaction parameters, such as temperature and ligand choice, can be adjusted to precisely influence the shape and size distribution of the resulting nanoparticles, with highly uniform sizes achievable within a few monolayers [18]. However, despite these advantages, colloidal NCs are hardly addressable as individual components and can be challenging to integrate or couple to optoelectronic devices. Furthermore, they often suffer from stability issues, particularly over exposure to various environmental agents or after re-dispersion in solution. The MHP NCs studied in this work were synthesized using the colloidal synthesis approach first described for perovskite NCs by L. Protesecu and coauthors in 2015 [17]. This method will be further discussed in Chapter 2.

1.2 Electronic structure of Metal Halide Perovskites

A complete description of the optical properties of MHPs, relies primarily on the calculation of the electronic band structure around their band-gap. Indeed, the electronic band structure of semiconductors dictates the width of their electronic band gap which in turn drives the optical wavelength of the emitted light. Furthermore, the exciton, discussed later in this Chapter, is constructed from the conduction and valence band states. Thus, the symmetry and energy of these states are needed. In this section the electronic band structure of MHPs will be presented around their band gap after a brief introduction of the $\mathbf{k}\cdot\mathbf{p}$ theory. The effect of the dimensionality reduction towards quantum confined NCs will also be discussed.

1.2.1 Electronic structure of Semiconductors

Under the Born-Oppenheimer and mean field approximations, electrons in semiconductors are characterized by wavefunctions which are eigenstates of the following stationary one-electron Schrödinger equation:

$$H\psi(\mathbf{r}) = \left[\frac{p^2}{2m_0} + V(\mathbf{r})\right]\psi(\mathbf{r}) = E\psi(\mathbf{r}) \tag{1.1}$$

where p is the momentum operator, $\psi(\mathbf{r})$, E and m_0 are respectively the wavefunction, energy and mass of an electron and $V(\mathbf{r})$ is the electrostatic potential created by the crystal lattice. Deriving the band structure of a material, consists in solving Eq. 1.1. Given the periodicity of $V(\mathbf{r})$, the Bloch theorem allows one to write the wavefunctions solution of Eq. 1.1 as Bloch waves

such that:

$$\psi_{n\mathbf{k}}(\mathbf{r},\mathbf{k}) = u_{n\mathbf{k}}(\mathbf{r})e^{i\mathbf{k}.\mathbf{r}} \tag{1.2}$$

Where n is a band index, $\mathbf{k}$ is the wavevector taken in the first Brillouin zone and $u_{n\mathbf{k}}(\mathbf{r})$ is a function that has the same periodicity as the lattice:

$$u_{n\mathbf{k}}(\mathbf{r}+\mathbf{R}) = u_{n\mathbf{k}}(\mathbf{r}) \tag{1.3}$$

with $\mathbf{R}$ being a lattice vector. For every band of index n there is a relationship between the energy $E_{n\mathbf{k}}$ and the wavevector $\mathbf{k}$. The combination of all of these dispersion relations forms the so called band structure of the material.

A possible approach to calculate this band structure consists in the application of the $\mathbf{k}\cdot\mathbf{p}$ theory. The use of this empirical method yields analytical expressions for band dispersion relations and the effective masses of charge carriers around the semiconductor energy band gap [50]. By injecting the Bloch wave of Eq. 1.2 into the one-electron Schrödinger Eq. 1.1, and applying the momentum operator on the Bloch waves, the so-called $\mathbf{k}\cdot\mathbf{p}$ equation is finally obtained:

$$\left(\frac{p^2}{2m_0} + \frac{\hbar\mathbf{k}\cdot\mathbf{p}}{m_0} + \frac{\hbar^2k^2}{2m_0} + V\right)u_{n\mathbf{k}} = E_{n\mathbf{k}}u_{n\mathbf{k}} \tag{1.4}$$

Thus, for $k = k_0 = 0$ Eq. 1.4 can be written as:

$$\left(\frac{p^2}{2m_0} + V\right)u_{n0} = E_{n0}u_{n0} \quad \text{with } n \in \mathbb{N}^* \tag{1.5}$$

Assuming that E_{n0} represents an extremum within the energy dispersion, we can then investigate different small wavevectors $\mathbf{k}$ close to the band extremum by treating the $\mathbf{k}\cdot\mathbf{p}$ and k^2 terms as perturbations of the $k_0 = 0$ solutions using either degenerate or non-degenerate perturbation theory. In the situation of a non-degenerate band, the $u_{n\mathbf{k}}$ functions at the first order in perturbation take the following form:

$$u_{n\mathbf{k}} = u_{n0} + \frac{\hbar}{m_0}\sum_{n'\neq n}\frac{\langle u_{n0}|\,\mathbf{k}\cdot\mathbf{p}\,|u_{n'0}\rangle}{E_{n0}-E_{n'0}}u_{n'0} \tag{1.6}$$

Since E_{n0} is an extremum, $E_{n\mathbf{k}}$ must have a quadratic behavior in $\mathbf{k}$ in the vicinity of $k = 0$. Consequently, the linear first order term vanishes and one needs to go to the second order in perturbation:

$$E_{n\mathbf{k}} = E_{n0} + \frac{\hbar^2k^2}{2m_0} + \frac{\hbar^2}{m_0^2}\sum_{n'\neq n}\frac{|\langle u_{n0}|\,\mathbf{k}\cdot\mathbf{p}\,|u_{n'0}\rangle|^2}{E_{n0}-E_{n'0}} \tag{1.7}$$

Thus, still considering small values of k one has:

$$E_{n\mathbf{k}} = E_{n0} + \frac{\hbar^2 k^2}{2m^*} \tag{1.8}$$

where m^* is defined as the effective mass of the band. Comparing Eq. 1.7 and 1.8 one finally obtains an expression for the effective mass:

$$\frac{1}{m^*} = \frac{1}{m_0} + \frac{2}{k^2 m_0^2} \sum_{n' \neq n} \frac{|\langle u_{n0}| \, \mathbf{k} \cdot \mathbf{p} \, |u_{n'0}\rangle|^2}{E_{n0} - E_{n'0}} \tag{1.9}$$

These relations express that, while considering small values of k, charge carriers have a dispersion relation given by Eq. 1.8 and resembling that of a free electron with an effective mass determined by Eq. 1.9. The great power of $\mathbf{k} \cdot \mathbf{p}$ theory lies in its minimal requirements, only necessitating the knowledge of the energy gaps and optical matrix elements (that are quantities measurable experimentally) around high symmetry points within the first Brillouin zone. This feature makes it highly convenient for the interpretation of optical spectra and therefore relevant to this work. With the incorporation of additional perturbative terms, one can even have access to the band structure of a material inside entire first Brillouin zone [50].

Of course, the simple $\mathbf{k} \cdot \mathbf{p}$ expression presented in Eq. 1.5 only treats the rather simplistic problem of a unique non-degenerate band. A more sophisticated expression will be introduced in the next section for MHP materials considering degenerate bands and spin-orbit interaction.

1.2.2 Electronic band structure of bulk MHPs

Throughout this manuscript, the optical properties of MHPs will be extensively discussed, requiring a precise understanding of the behavior of charge carriers in bulk MHPs. Since optical transitions primarily occur near the band gap of the material, a local description of the band structure will be used through multi-band $\mathbf{k} \cdot \mathbf{p}$ models (considering, at least, a conduction and a valence band), similar to those commonly used for other semiconductor materials [51]. Much like the one band $\mathbf{k} \cdot \mathbf{p}$ model discussed in the previous section, these models allow one to build an effective mass Hamiltonian that describes the energy of the charge carriers near the band gap while considering the contribution from multiple electronic bands, whether degenerate or non-degenerate to obtain a more accurate description.

The general idea is to consider the atomic orbitals of the elements of the material that con-

tribute to the electronic properties around the band gap[1]. Using symmetry considerations in the point group under investigation (Oh, D_{4h} or D_{2h} for the different crystal phases of perovskites), the irreducible representations of these orbitals can be determined in the point group of interest. Once this has been established, the basis functions associated with the appropriate irreducible representations are employed to construct the electronic Bloch functions, forming the orthogonal basis in which the $\boldsymbol{k} \cdot \boldsymbol{p}$ Hamiltonian will be expressed.

In MHPs, the presence of heavy metal cations like lead (Pb) in the crystal lattice generates a strong spin-orbit coupling that lifts the degeneracy of electronic states of angular momentum L≠0 [52] near the band gap. To include this interaction, the $\mathbf{k} \cdot \mathbf{p}$ Hamiltonian introduced in Eq. 1.4 is modified as:

$$H = \frac{p^2}{2m_0} + \frac{\hbar^2 k^2}{2m_0} + V(r) + \frac{\hbar \mathbf{k} \cdot \mathbf{p}}{m_0} + \frac{\hbar}{4m_0^2 c^2} (\nabla V \times \mathbf{p}) \cdot \sigma \tag{1.10}$$

where the last term represents the spin-orbit Hamiltonian with σ the Pauli operator. Each element of the Hamiltonian Eq. 1.10 is evaluated in the Bloch states basis using symmetry considerations. The number of elements in the basis depends on the number of atomic orbitals that were initially considered for conduction and valence. For example, with MHPs, considering electronic states that transform like the atomic orbitals s ($L = 0$), p_x, p_y, p_z ($L = 1$) in the O_h point group, one gets 8 Bloch states for conduction and 8 for valence (counting the spin degeneracy).

A full 40 bands $\mathbf{k} \cdot \mathbf{p}$ model involving valence and conduction bands of s, p and d ($L = 2$) symmetry was developed by Steinmetz *et al.* in connection to this work for inorganic MHPs and detailed in the supplementary material of [53]. The left side of Fig. 1.4 presents their results and the calculated band structure for $CsPbCl_3$ in the O_h crystal phase. One can see that MHPs (other compounds are presented in the paper and show similar results) have a direct bandgap, located at the R point of the first Brillouin zone. Interestingly, these calculations generally demonstrate that the choice of the cation (Cs^+, FA^+, MA^+) has a poor influence on the electronic properties of MHPs as compared to the "sub-lattice" formed by the PbX_6 octahedra. Compared to more conventionnal II-VI semiconductors, the band structure also appears inverted with a conduction band of p symmetry whose degeneracy is lifted by the spin-orbit interaction by an amount $\Delta_{SO} =$ 1.6 eV.

Regarding optical transitions, due to the large spin-orbit coupling, a good approximation consists in only considering the elements related to the valence and the "split-off" conduction band (associated to the R_6^+ and R_6^- irreducible representations respectively) in the $\mathbf{k} \cdot \mathbf{p}$ Hamiltonian. Doing so, one is left with a 4×4 Hamiltonian in the $\{|V_1\rangle, |C_1\rangle, |V_2\rangle, |C_2\rangle\}$ basis defined by:

[1]The 'weight' of these atomic orbitals near the band gap is typically provided by first-principles calculations.

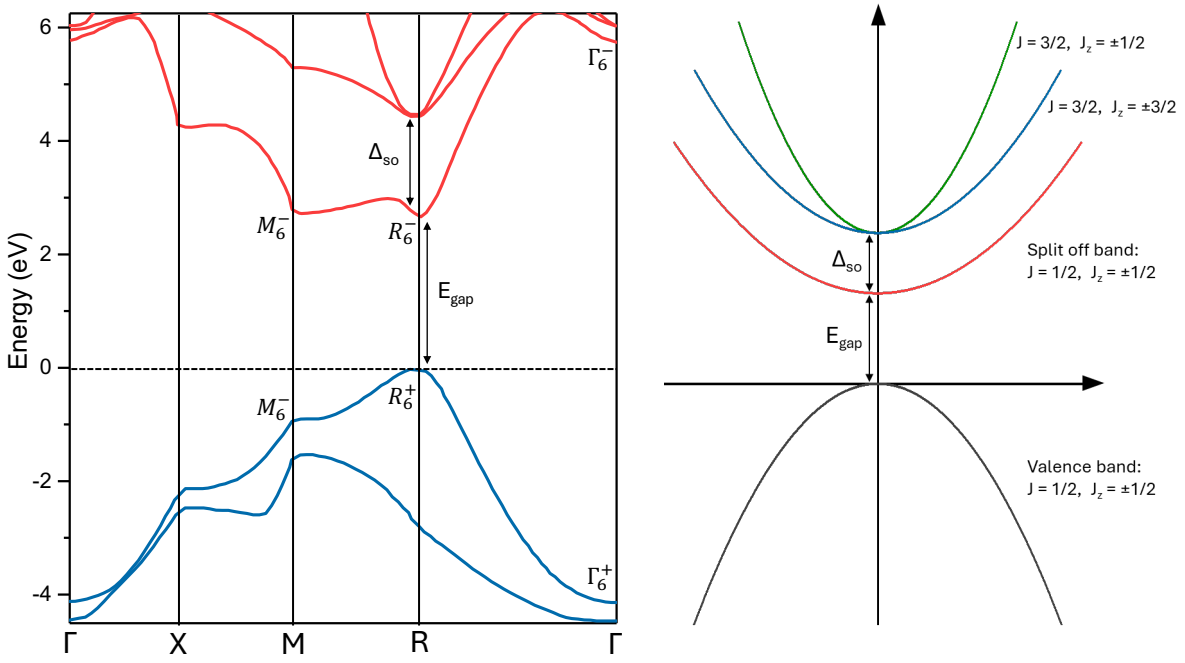

Figure 1.4: Left: Energy band structure of bulk $CsPbCl_3$ obtained from a 40-band $\mathbf{k} \cdot \mathbf{p}$ model, adapted from Steinmetz *et al.* [53]. The authors found here a bulk band gap energy of $E_g = 2.7$ eV and a spin orbit coupling parameter value of $\Delta_{SO} = 1.6$ eV. Right: illustration of the simplified band structure around the R point of the first Brillouin zone.

$$\begin{cases} |V_1\rangle = |j_v = 1/2,\, j_z^v = \ \ 1/2\rangle = |S\uparrow\rangle \\ |V_2\rangle = |j_v = 1/2,\, j_z^v = -1/2\rangle = |S\downarrow\rangle \\ |C_1\rangle = |j_c = 1/2,\, j_z^c = \ \ 1/2\rangle = \dfrac{i}{\sqrt{3}}\left[|X\downarrow\rangle + i\,|Y\downarrow\rangle - |Z\uparrow\rangle\right] \\ |C_2\rangle = |j_c = 1/2,\, j_z^c = -1/2\rangle = \dfrac{i}{\sqrt{3}}\left[|X\uparrow\rangle - i\,|Y\uparrow\rangle - |Z\downarrow\rangle\right] \end{cases} \tag{1.11}$$

The corresponding Hamiltonian and its diagonalisation procedure will not be detailed here but is fully discussed in [54, 53, 55]. After diagonalisation of the 4×4 Hamiltonian one can find the energy of the conduction band (valence set at 0 eV), the effective masses of the carriers near the band edges. The right part of Fig. 1.4 presents the simplified band structure of MHPs near the band gap.

1.2.3 From bulk to low dimension Semiconductors

The excitement around the field of Nanosciences comes essentially from the fact that materials acquire very different properties when they are scaled down to nanometer sizes. As demonstrated in the previous section, within the effective mass approximation, charge carriers in bulk semi-

conductors (such as electrons and holes) exhibit a free particle behavior within their respective energy bands, provided that their masses are replaced by an "effective" mass. This is no longer the case when a semiconductor is reduced in size along one or more dimensions.

Indeed, when the material size approaches the same order of magnitude as the De Broglie wavelength of a carrier wavefunction (about 10 nm at 300 K), the motion of the carriers becomes restricted, and a phenomenon known as quantum confinement emerges. This effect significantly influences the carriers energy levels and density of states, leading to new electronic and optical properties within the material. Three primary types of confined nano-structures are usually identified and illustrated on Fig. 1.5:

- The two-dimensional (2D) systems, also referred to as quantum wells, where carriers are confined in only one dimension.
- One-dimensional (1D) systems, or quantum wires, characterized by confinement in two dimensions.
- Zero-dimensional (0D) systems, known as quantum dots or nanocrystals, where carriers are confined in all three spatial directions.

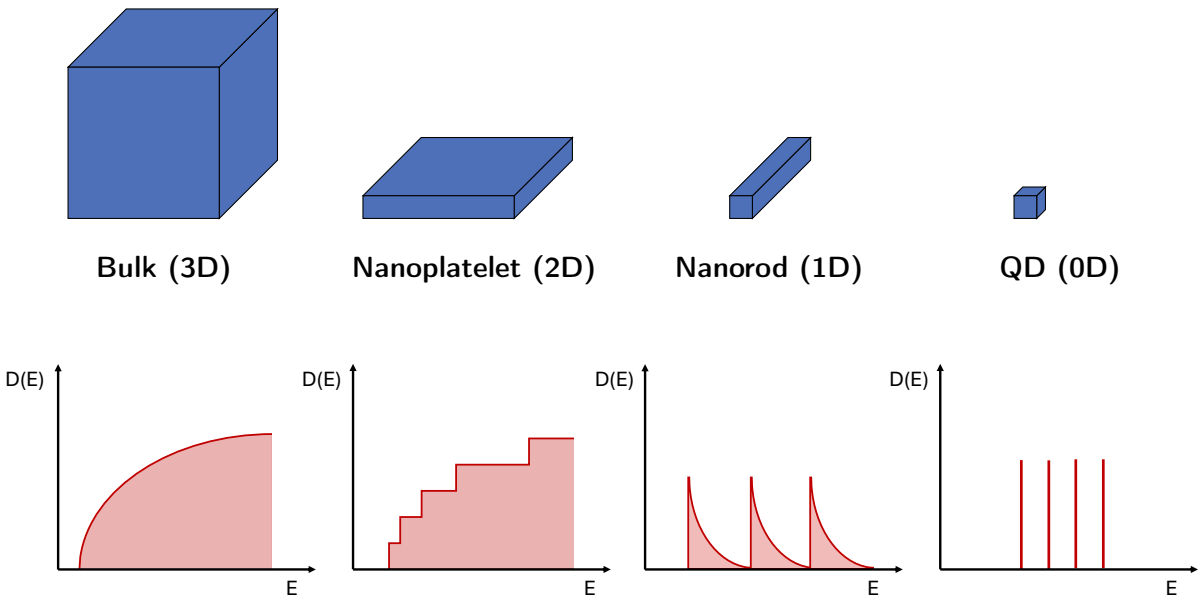

Figure 1.5: Top row: Illustration of the diversity of confined objects, from the Bulk (3D) to the quantum dot (0D). Bottom row: The density of states expected for each nanostructure.

In the case of a NC, and following the model of a particle in an 3D box of infinite potential barriers, the energy levels and carriers wavefunctions can be expressed as followed:

$$\psi_{n_x,n_y,n_z} = \sqrt{\frac{2^3}{L_x L_y L_z}} \sin\left(\frac{n_x \pi x}{L_x}\right) \sin\left(\frac{n_y \pi y}{L_y}\right) \sin\left(\frac{n_z \pi z}{L_z}\right) \tag{1.12}$$

$$E_{n_x,n_y,n_z} = \frac{\hbar^2 \pi^2}{2m} \left[\left(\frac{n_x}{L_x}\right)^2 + \left(\frac{n_x}{L_x}\right)^2 + \left(\frac{n_x}{L_x}\right)^2\right] \tag{1.13}$$

where $n_i\,(i = x, y, z)$ are quantum numbers arising from the boundary conditions and L_i is the length of the box in direction i. Fig. 1.5 illustrates this quantum confinement effect, and how the bulk energy bands turn into distinct energy levels in strongly confined NCs.
The expression given in Eq. 1.13 is valid for a strong confinement applied to the NC. In reality, different regimes of quantum confinement exist over a particular dimension between the bulk material and the quantum dot. This will be discussed further in the following section.

1.3 Optical properties of MHP nanocrystals

One of the most interesting properties of semiconductors is their ability to promote electrons from a valence band to a conduction band under the absorption of light (or *e.g* the application of an electric field) providing that the excitation brings an amount of energy greater than or equal to the band gap. This process leaves a positively charged hole in the valance band that can interact attractively by Coulomb force with the conduction band electron to form a bound electron-hole state called the exciton, a neutrally charged quasi-particle.

Two types of excitons are usually distinguished. The first one, the Frenkel exciton, is generally encountered in materials with a low dielectric constant like inorganic semiconductors for example. The low dielectric constant reduces the screening of the Coulomb interaction between the electron and the hole which leads to a large binding energy and a spatial extent approximately limited to a single unit cell. Thus Frenkel excitons are usually bound to a specific atom, molecule or defect of the material structure [56, 57, 58]. The second type of exciton is called the Wannier-Mott exciton. It is usually encountered in inorganic semiconductors and will therefore be the focus of this work. In this case, due to the high dielectric constant and the light effective masses of the charge carriers in these materials, the electron and hole are separated over multiple unit cells, resulting in a highly delocalized exciton wave function [58, 59]. Since the exciton can move freely within the crystal lattice this type of excitation is also referred to as a free exciton.

The objective of this section is to familiarize the reader with the theoretical framework used throughout this manuscript to describe the exciton in MHP NCs, its fine structure and its optical properties.

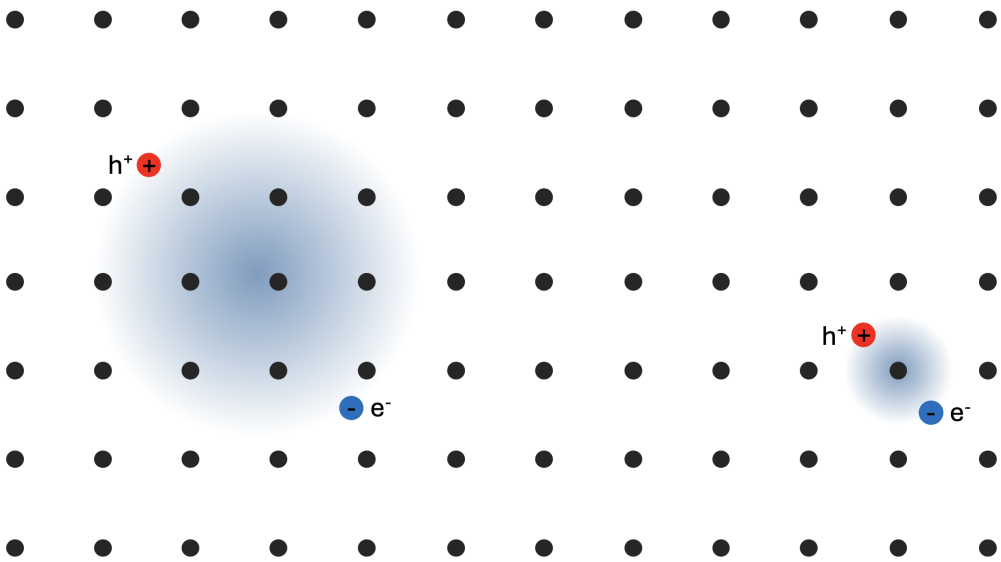

Figure 1.6: Illustration of the Wannier-Mott exciton (left) and the Frenkel exciton (right).

1.3.1 Exciton in bulk semiconductors

Before modelizing excitons inside quantum confined nanostructures let us first provide a description in bulk MHPs. For bulk semiconductors, in the framework of the effective mass approximation, the total wave function of an exciton can be written as:

$$\Psi(\mathbf{r}_e, \mathbf{r}_h) = \Phi(\mathbf{r}_e, \mathbf{r}_h) f(\mathbf{r}_e, \mathbf{r}_h) \tag{1.14}$$

$\Phi(\mathbf{r}_e, \mathbf{r}_h) = e^{i\mathbf{k}_0(\mathbf{r}_e - \mathbf{r}_h)} u_c(\mathbf{r}_e) u_v(\mathbf{r}_h)$ is the Bloch part where $u_c(\mathbf{r}_e)$, $u_v(\mathbf{r}_h)$ are the periodic functions associated to the band edge conduction and valence band states obtained *via* the $\mathbf{k} \cdot \mathbf{p}$ analysis for example. The $f(\mathbf{r}_e, \mathbf{r}_h)$ factor represents the envelope function for the exciton and describes its orbital and center of mass motion, it is found solving the Schrödinger equation:

$$\left[\frac{\hat{\boldsymbol{p}}_e^2}{2m_e} + \frac{\hat{\boldsymbol{p}}_h^2}{2m_h} + \frac{e^2}{4\pi\epsilon_0\epsilon_1 |\mathbf{r}_e - \mathbf{r}_h|} \right] f(\mathbf{r}_e, \mathbf{r}_h) = E f(\mathbf{r}_e, \mathbf{r}_h) \tag{1.15}$$

where the third term on the left side of Eq. 1.15 represents the Coulomb potential between the two carriers in a medium of dielectric constant ϵ_1. Since Eq. 1.15 describes a two-body problem, the center of mass frame will be used and Eq. 1.15 is changed to:

$$\left[\frac{\hat{\boldsymbol{P}}^2}{2M} + \frac{\hat{\boldsymbol{p}}^2}{2\mu} + \frac{e^2}{4\pi\epsilon_0\epsilon_1 |\mathbf{r}|} \right] f(\mathbf{R}, \mathbf{r}) = E f(\mathbf{R}, \mathbf{r}) \tag{1.16}$$

where $\hat{\boldsymbol{P}}$ and $\hat{\boldsymbol{p}}$ are the momentum operators associated to the center of mass motion and electron-hole relative motion respectively. $M = m_e + m_h$ is the total effective mass, $\mu = m_e m_h/(m_e + m_h)$ the reduced mass of the system and m_e, m_h are the electron and hole effective mass respectively. The solutions of Eq. 1.16 are well established and can be expressed simply as the product of a plane wave associated to the center of mass motion $\mathbf{R} = (m_e\mathbf{r}_e + m_h\mathbf{r}_h)/(m_e + m_h)$ and a hydrogenoïd wave function $\phi_{nlm}(\mathbf{r}) = R_{nl}(r)Y_{lm}(\theta, \phi)$ where $R_{nl}(r)$ is the radial part in the relative electron-hole coordinates ($\mathbf{r} = \mathbf{r}_e - \mathbf{r}_h$) and $Y_{lm}(\theta, \phi)$ is a spherical harmonic function. For instance, the envelope function of the exciton ground state $1s$ is given by:

$$f(\mathbf{R}, \mathbf{r}) = \frac{1}{\sqrt{V}} e^{i\mathbf{K}\cdot\mathbf{R}} \phi_{1s}(\mathbf{r}) \quad \text{with:} \quad \phi_{1s}(\mathbf{r}) = \frac{1}{\sqrt{\pi a_X^3}} e^{-\frac{r}{a_X}} \tag{1.17}$$

$a_X = m_0 a_0/\mu\epsilon_1$ is called the exciton Bohr radius with a_0 the hydrogen Bohr radius and ϵ_1 the relative permittivity. Since the center of mass moves freely around the lattice, its energy is given by $E_K = \hbar^2 K^2/2M$. Regarding the relative motion, the energy is quantized and given by $E_n = R_X/n^2$ where R_X is the exciton Rydberg defined below. Taking all of this together, the energy of the exciton is finally given by:

$$E_n = E_g + \frac{\hbar^2 K^2}{2M} - \frac{R_X}{n^2} \text{ with: } R_X = \frac{\mu}{m_0 \epsilon_1^2} R_y \tag{1.18}$$

Where $R_y = 13.6$ eV is the Rydberg constant of hydrogen.

1.3.2 Exciton in confined MHP nanocrystals

The objective of this paragraph is to derive the model that will give us the energy and wavefunction of an exciton in MHP NCs[2]. This work particularly emphasizes the effects of the crystal phase, the dielectric environment and the NCs general shape on the exciton properties. The model presented in this section takes these aspects into account and is constructed in a rather general way. Thus, in the following, the NCs crystal phase will be undertermined between cubic O_h, tetragonal D_{4h} or orthorhombic D_{2h}. The NCs are also considered as cuboids with dimensions that are generally different, *i.e* $L_x \neq L_y \neq L_z$. In the framework of the effective mass approximation an exciton in such NC can be described by the following Hamiltonian:

$$H_X = \sum_{i=e,h} \left[\frac{p_i^2}{2m_i} + V_i^{conf} \right] + V_C(\mathbf{r}_e, \mathbf{r}_h) + E_g \tag{1.19}$$

[2]The term 'exciton' in strongly confined nanostructures is misleading since the Coulomb potential energy becomes much weaker than the confinement energy. The electron and hole WFs are separable and one should speak of 'electron-hole pair' instead of exciton. However, the MHP NCs studied in this work will always stay in a limit of intemediate to weak confinement, thus the exciton denomination will be used.

where the first term is the kinetic energy of the electron (hole), V_C a Coulomb potential between the two charges (described further in the next section), V_i^{conf} is a confinement potential taken null inside the nanocrystal and infinite outside in a first approximation and E_g represents the bulk band gap energy.

The exciton total wave function is given by Eq. 1.14 where the periodic Bloch functions $u_c(\mathbf{r}_e)$, $u_v(\mathbf{r}_h)$ contained in $\Phi(\mathbf{r}_e, \mathbf{r}_h)$ are determined by the band edge conduction and valence states $\left|j_i, j_z^i\right\rangle$ (with $i = v, c$ for valence or conduction respectively) developed for MHPs with the $\mathbf{k} \cdot \mathbf{p}$ model described in Sec. 1.2.2:

$$\begin{cases} |V_1\rangle = |j_v = 1/2,\, j_z^v = \ \ 1/2\rangle = |S\uparrow\rangle \\ |V_2\rangle = |j_v = 1/2,\, j_z^v = -1/2\rangle = |S\downarrow\rangle \\ |C_1\rangle = |j_c = 1/2,\, j_z^c = \ \ 1/2\rangle = i\left[-\alpha\,|X\downarrow\rangle - i\beta\,|Y\downarrow\rangle + \gamma\,|Z\uparrow\rangle\right] \\ |C_2\rangle = |j_c = 1/2,\, j_z^c = -1/2\rangle = i\left[-\alpha\,|X\uparrow\rangle + i\beta\,|Y\uparrow\rangle + \gamma\,|Z\downarrow\rangle\right] \end{cases} \tag{1.20}$$

In these expressions, $\alpha^2+\beta^2+\gamma^2 = 1$. The expression of the parameters α, β and γ depend on the symmetry of the crystal lattice. Indeed, Eq. 1.11 were given for MHPs of cubic O_h symmetry but another term due to the crystal field has to be taken into account when the symmetry of the lattice is lowered from cubic to tetragonal [39, 60, 61]. In the orthorhombic case, since the symmetry is lowered along two directions, the crystal field has two contributions. Therefore, depending on the crystal phase, and using the results of [40], the expressions of these parameters are given in the following Tab. 1.1:

	$\mathbf{O_h}$	$\mathbf{D_{4h}}$	$\mathbf{D_{2h}}$
$\boldsymbol{\alpha^2}$	$1/3$	$\cos^2\theta/2$	$\frac{\cos^2\theta}{2}\left(1+\frac{\xi}{E_C-E_{C'}}\right)^2$
$\boldsymbol{\beta^2}$	$1/3$	$\cos^2\theta/2$	$\frac{\cos^2\theta}{2}\left(1-\frac{\xi}{E_C-E_{C'}}\right)^2$
$\boldsymbol{\gamma^2}$	$1/3$	$\sin^2\theta$	$\sin^2\theta$

Table 1.1: Expression of the α, β, and γ parameters for the three crystal phases of MHPs.

In the expressions provided in Tab. 1.1 the angle θ is defined by $\tan 2\theta = 2\sqrt{2}\Delta_c/(\Delta_c - 3T)$, where Δ_c and T represent the spin orbit and crystal field parameters respectively. E_C and $E_{C'}$ are the energies of the $|j_c = 1/2,\, j_z^c = \ \pm 1/2\rangle$ and $|j_c = 3/2,\, j_z^c = \ \pm 3/2\rangle$ conduction bands respectively provided in [40]. Finally, ξ is an additional crystal field contribution due to the $D_{4h} \rightarrow D_{2h}$ symmetry reduction. One can see that in the limit $\xi \rightarrow 0$ the D_{4h} expressions are retrieved.

The envelope function that intervenes in the expression of the total exciton WF (Eq. 1.14) needs to be adapted here to take into account the effect of the quantum confinement on the exciton. In this context, the bulk exciton Bohr radius a_X is a valuable length scale to estimate the influence of this confinement on the exciton properties of a semiconductor. The exciton wave function starts to be affected by quantum confinement when a dimension of the NC L_i $(i = x, y, z)$ approaches a_X. Three different regimes of quantum confinement are usually distinguished:

- **Weak confinement:** If the size of the nanoparticle remains larger than the exciton Bohr radius, such that $L_i \gg a_X$, the exciton center of mass motion becomes restricted while relative motion of the electron-hole pair stays unaffected. In this case, the associated wave functions remain separable and one can write:

$$f_{WC}(\mathbf{R}, \mathbf{r}) = \psi(\mathbf{R})\phi_{1s}(\mathbf{r}) \tag{1.21}$$

  where $\psi(\mathbf{R})$ is the particle in a box wave function given in Eq. 1.12 which, adapted to the ground state exciton center of mass motion, writes:

$$\psi(\mathbf{R}) = \sqrt{\frac{8}{L_x L_y L_z}} \cos\left(\frac{\pi X}{L_x}\right) \cos\left(\frac{\pi Y}{L_y}\right) \cos\left(\frac{\pi Z}{L_z}\right) \tag{1.22}$$

- **Strong confinement:** When the size of the nanoparticle gets smaller than the exciton Bohr radius *i.e* $L_i \ll a_X$ the energy term due to quantum confinement becomes much larger than the energy associated to the electron-hole Coulomb interaction which can then be treated as a first order perturbation. Hence, excitons are not formed and the electron and hole motions are treated separately. Thus, one can write the envelope function in this limit as:

$$f_{SC}(\mathbf{r}_e, \mathbf{r}_h) = \psi_e(\mathbf{r}_e)\psi_h(\mathbf{r}_h) \tag{1.23}$$

  Where $\psi_i(\mathbf{r}_i)$ is given by:

$$\psi_i(\mathbf{r}_i) = \sqrt{\frac{8}{L_x L_y L_z}} \cos\left(\frac{\pi x_i}{L_x}\right) \cos\left(\frac{\pi y_i}{L_y}\right) \cos\left(\frac{\pi z_i}{L_z}\right) \quad i = e, h \tag{1.24}$$

- **Intermediate confinement:** In this regime the NC size is comparable to the exciton Bohr radius such as $L_i \approx a_x$. The confinement energy is large enough to affect the charge carriers but the electron and hole motion can no longer be treated separately as they are correlated. The envelope function has no simple analytical expression but a variational approach with

a one parameter trial function can be used here:

$$f_{IC}(\mathbf{r}_e, \mathbf{r}_h) = \mathcal{N}(a) e^{-|\mathbf{r}_e - \mathbf{r}_h|/a} \psi_e(\mathbf{r}_e) \psi_h(\mathbf{r}_h) \tag{1.25}$$

where a is the variational parameter, $\mathcal{N}(a)$ a normalization factor and $\psi_i(\mathbf{r}_i)$ $i = e, h$ are given by Eq. 1.24. The best trial WF is obtained through the minimization of $E_X = \langle \Psi | \mathcal{H}_X | \Psi \rangle$ with respect to the parameter a.

1.3.3 Dielectric confinement

Inorganic semiconductors generally possess a much higher dielectric constant than their surrounding medium (*i.e* vacuum, air or ligands for NCs). According to the principles of electrostatics, a charge inside the semiconductor (medium 1) tends to maximize the polarization of its surrounding environment. Therefore, near an interface where the dielectric constant drops from a higher value ϵ_1 inside the SC to a lower value, ϵ_2, outside, the charge tends to be repelled from the interface. The effect on the charge electric field and potential can be modeled quite easily by placing an imaginary charge in medium 2 [62]. In bulk materials this behavior is generally neglected because the charge carriers or the exciton can simply move away from the interfaces and Coulomb interactions will take the well known form written in Eq. 1.15.

In NCs however, as the size is reduced the charge carriers have an increased sensitivity to their surrounding environment and can no longer move away from the interfaces. Let us first consider for simplicity a semiconductor quantum well surrounded by two interfaces with a medium of lower dielectric constant. This situation was first elegantly described by M. Kumagai and T. Takagahara in 1989 [63]. The effect on a charge placed inside the well can once again be modelized by imaginary charges placed behind the interfaces on the outside. Since the thickness of quantum wells is only a few nanometers, an imaginary charge on one side will affect the charge on the inside which in turns affect the other imaginary charge on the other side of the well. To include this "chain reaction" effect, one can therefore add more charges behind each 1^{st} imaginary charge, then the 2^{nd} ones, and so on, until a full "lattice" of imaginary charges is created Fig. 1.7 provides a visual description of this situation.

Thus one can write the potential felt by the charge inside the well and due to all the imaginary charges as:

$$V_l^{self} = \frac{e^2}{4\pi\epsilon_0\epsilon_1} \sum_{\substack{n\neq 0 \\ n=-\infty}}^{+\infty} \frac{1}{2(x_l - x_{ln})} \left(\frac{\epsilon_1 - \epsilon_2}{\epsilon_1 + \epsilon_2} \right)^{|n|} \tag{1.26}$$

Where $l = e, h$ and $x_{ln} = (-1)^n x_l + nL_x$. This potential is called "self potential" because it

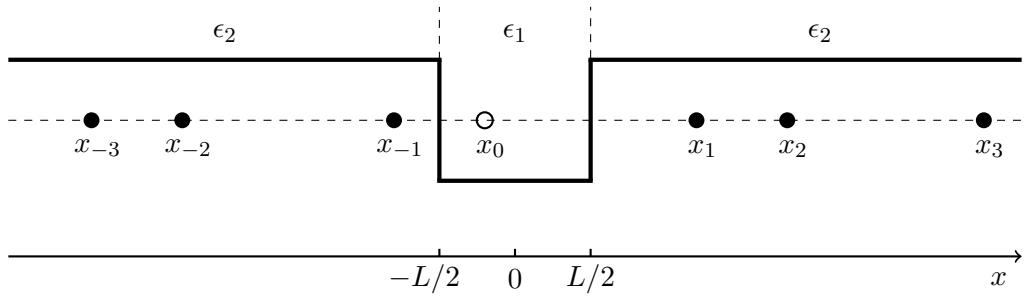

Figure 1.7: Illustration of a quantum well of permittivity ϵ_1 containing a single real charge x_0. To model the effect of the in-homogeneous dielectric environment (due to the external medium of permittivity ϵ_2) on this charge, imaginary charges x_n are placed along axis x on each side of the well. Adapted from [63].

takes into account the Coulomb interaction between the real charge and its own image charges. It tends to increase the energy of the charge carrier. Since this work is focused on electron-hole pairs or excitons this potential has to be considered both for the electron and the hole.
This is of course not the only Coulomb interaction that comes into play here: in this image charges description the Coulomb interaction between the real hole and the real electron and all of the interactions between these real carriers and their opposite imaginary charges also need to be included. In the spirit of Eq. 1.26 this is done writing:

$$V_{e-h} = -\frac{e^2}{4\pi\epsilon_0\epsilon_1}\sum_{n=-\infty}^{+\infty}\frac{1}{(x_e - x_{hn})}\left(\frac{\epsilon_1-\epsilon_2}{\epsilon_1+\epsilon_2}\right)^{|n|} \tag{1.27}$$

This Coulomb potential is attractive and tends to lower the energy of the carriers and increase the exciton binding energy.

As mentioned earlier in this section, this work focuses mostly on anisotropic nanocubes and so the confinement will be present in all three directions of space. Both expressions given above can rather easily be extended to this situation and thus the following expressions are obtained:

$$V_l^{self}(\boldsymbol{r}_l) = \frac{e^2}{4\pi\epsilon_0\epsilon_1}\sum_{\substack{m=-\infty\\ m\neq 0}}^{+\infty}\sum_{\substack{n=-\infty\\ n\neq 0}}^{+\infty}\sum_{\substack{p=-\infty\\ p\neq 0}}^{+\infty}\frac{1}{2}\frac{\eta^{|m|+|n|+|p|}}{\sqrt{(x_l-x_{lm})^2+(y_l-y_{ln})^2+(z_l-z_{lp})^2}} \tag{1.28}$$

$$V_{e-h}(\boldsymbol{r}_e,\boldsymbol{r}_h) = -\frac{e^2}{4\pi\epsilon_0\epsilon_1}\sum_{m=-\infty}^{+\infty}\sum_{n=-\infty}^{+\infty}\sum_{p=-\infty}^{+\infty}\frac{\eta^{|m|+|n|+|p|}}{\sqrt{(x_e-x_{hm})^2+(y_e-y_{hn})^2+(z_e-z_{hp})^2}} \tag{1.29}$$

where $\eta = (\epsilon_1-\epsilon_2)/(\epsilon_1+\epsilon_2)$ was used. Considering Eq. 1.28 and 1.29 the total Coulomb

potential is written as $V_C = V_e^{self} + V_h^{self} + V_{e-h}$. Finally, it is worth noting that if $\epsilon_1 = \epsilon_2$, $V_l^{self} = 0$ and V_{e-h} takes the usual electron-hole Coulomb expression provided in Eq. 1.15.

1.3.4 Exciton fine structure in MHP nanocrystals

In semiconductor NCs, the optical band edge is characterized by a variety of optical transitions. The exciton state, which is initially degenerate, is split into multiple sub-levels by the electron-hole exchange interaction creating the so-called exciton fine structure. Let us start this discussion by constructing the Bloch states of a bound electron-hole pair in an MHP NC. The electron states are just the conduction band edge states of Eq. 1.20 *i.e* $|j_e, j_z^e\rangle = |j_c, j_z^c\rangle = |1/2, \pm 1/2\rangle$ and the hole states are derived by applying the time reversal operator to the valence band edge states which gives $\left|j_h, j_z^h\right\rangle = \mathcal{I}\,|j_v, j_z^v\rangle = |1/2, \mp 1/2\rangle$. Thus, using the conventional combination rules of angular momenta, four exciton states can be created and comprise a triplet associated to the total angular momentum $J = 1$, and a singlet for $J = 0$:

$$\begin{cases} |1\rangle = |J = 1, J_z = 1\rangle = |{}^1\!/_2, {}^1\!/_2\rangle \\ |0_B\rangle = |1, 0\rangle = \dfrac{1}{\sqrt{2}}\left[|{}^{-1}\!/_2, {}^1\!/_2\rangle + |{}^1\!/_2, {}^{-1}\!/_2\rangle\right] \\ |{-1}\rangle = |1, -1\rangle = |{}^{-1}\!/_2, {}^{-1}\!/_2\rangle \\ |0_D\rangle = |0, 0\rangle = \dfrac{1}{\sqrt{2}}\left[|{}^{-1}\!/_2, {}^1\!/_2\rangle - |{}^1\!/_2, {}^{-1}\!/_2\rangle\right] \end{cases} \tag{1.30}$$

where $|1\rangle, |0_B\rangle, |{-1}\rangle$ are the exciton states associated to the triplet with total angular momentum $J = 1$ and projection along the z axis $J_z = 1, 0, -1$ and $|0_D\rangle$ is the state associated to the total angular momentum $J = 0$ with projection $J_z = 0$ along z. So far, the exciton states presented in Eq. 1.30 are degenerate and their energy can be found by applying the Hamiltonian provided by Eq. 1.19 to the corresponding total exciton wave-function.

However, this picture of the exciton in MHP NCs still lacks the consideration of an essential quantum mechanical effect: the electron-hole exchange interaction. Indeed, considering an exciton described by the state $\Psi(\boldsymbol{r_e}, \boldsymbol{r_h})$ the indistinguishability of fermions and the Pauli exclusion principle imply that any matrix element $\langle\Psi|\, V_{e-h}\,|\Psi\rangle$ where V_{e-h} is the e-h Coulomb interaction potential, has two components:

$$J = \frac{-e^2}{4\pi\epsilon}\int\int d\boldsymbol{r_1} d\boldsymbol{r_2} \frac{|\Psi(\boldsymbol{r_e} = \boldsymbol{r_1}, \boldsymbol{r_h} = \boldsymbol{r_2})|^2}{|\boldsymbol{r_1} - \boldsymbol{r_2}|} \tag{1.31}$$

$$K = \frac{-e^2}{4\pi\epsilon}\int\int d\boldsymbol{r_1} d\boldsymbol{r_2} \frac{\Psi^*(\boldsymbol{r_e} = \boldsymbol{r_1}, \boldsymbol{r_h} = \boldsymbol{r_2})\Psi(\boldsymbol{r_e} = \boldsymbol{r_2}, \boldsymbol{r_h} = \boldsymbol{r_1})}{|\boldsymbol{r_1} - \boldsymbol{r_2}|} \tag{1.32}$$

The first term J is called "direct Coulomb" since it describes the classical electrostatic interaction between two charges of opposite signs. The second term K represents an interaction that

has no classical equivalent and called the exchange integral (also named "indirect Coulomb"). This term mixes the electron and hole spin momentum and lifts the degeneracy of the exciton fine structure states.

Although this brief description of the EI can help to comprehend the origins of the e-h EI, it is misleading because in reality the electron and the hole that compose the exciton are only quasiparticle perturbations of a many-electron system composing the semiconductor. The theory of the e-h EI in semiconductors was developped in the 1960-1970s by the groups of Bir and Pikus [64, 65] and Denisov and Makarov [66]. The developments presented in these papers are quite complex and hardly attainable. As a consequence, the following will briefly describe how the EI is commonly handled and how it was considered in the present work through a collaboration with the group of K.Boujdaria at the University of Carthage.

In semiconductor NCs the general idea is to separate the exchange interaction into two components: (i) an analytical part that describes the exchange at the scale of the lattice unit cell, called short range EI (ii) a non analytical part that expresses the symmetry reduction due to the confinement potential in the NC and that is therefore called the long range EI. Taking both terms into account, the total Hamiltonian describing the exciton can be written as:

$$\mathcal{H} = \mathcal{H}_X + \mathcal{H}_{SR} + \mathcal{H}_{LR} \tag{1.33}$$

where $\mathcal{H}_X$ is the exciton Hamiltonian containing the direct Coulomb e-h interaction and given by Eq. 1.19. $\mathcal{H}_{SR}$, $\mathcal{H}_{LR}$ are respectively the short and long range contribution of the e-h EI. The objective of the following paragraphs is to express these two EI terms in the exciton basis provided by Eq. 1.30.

Short range Hamiltonian in the exciton basis:

In 1980, Rössler and Trebin [67] demonstrated that the analytical component of the exchange interaction (EI) could be expressed in real space as a spin-dependent contact interaction, thus referred to as the short-range (SR) EI. This interaction takes the following form:

$$\mathcal{H}_{SR} = \frac{1}{2} C(\mathcal{J} - \boldsymbol{\sigma_e} \cdot \boldsymbol{\sigma_h}) \delta(\mathbf{r_e} - \mathbf{r_h}) \tag{1.34}$$

where $\mathcal{J}$ represents the 4×4 unitary matrix, $\boldsymbol{\sigma_e}$, $\boldsymbol{\sigma_h}$ are vector operators with components corresponding to the Pauli matrices for the electron and hole respectively and $\delta(\boldsymbol{r_e} - \boldsymbol{r_h})$ is the delta function. In this expression C is the so-called SR exchange constant whose calculation can be made from experimental measurements [54, 55, 67, 68]. The short range Hamiltonian $\mathcal{H}_{SR}$

takes the following form in the exciton basis $\{|1\rangle, |-1\rangle, |0_B\rangle, |0_D\rangle\}$:

$$\mathcal{H}_{SR} = \frac{3}{2}\Delta_{SR}\pi a_X^3 \mathcal{K} \begin{pmatrix} \alpha^2+\beta^2 & -\alpha^2+\beta^2 & 0 & 0 \\ -\alpha^2+\beta^2 & \alpha^2+\beta^2 & 0 & 0 \\ 0 & 0 & 2\gamma^2 & 0 \\ 0 & 0 & 0 & 0 \end{pmatrix} \tag{1.35}$$

In this Hamiltonian, $\Delta_{SR} = (2/3)C/\pi a_X^3$ contains the SR constant C and a_X, the exciton Bohr radius. The parameters α, β and γ depend on the amplitude of the spin-orbit coupling and the crystal field. Their expressions were provided for each MHP crystal phase in Tab. 1.1. The factor $\mathcal{K}$ is an overlap integral of the exciton envelope function and expresses the probability for the electron and the hole to be in the same unit cell *i.e*:

$$\mathcal{K} = \int_V |f(\mathbf{r},\mathbf{r})|^2 \, d\mathbf{r} = \frac{27}{8}\frac{|\mathcal{N}(a)|^2}{L_x L_y L_z} \tag{1.36}$$

where $f(\mathbf{r},\mathbf{r})$ is given by Eq. 1.25, L_x, L_y, L_z are the edge lengths of the NC and $\mathcal{N}(a)$ is a normalization factor from Eq. 1.25.

Long range Hamiltonian in the exciton basis:

Although the long range can often be neglected in EFS calculations for semiconductor NCs of isotropic shapes, it is essential for this work since it encompasses the effects of the NC shape anisotropy that will be investigated in Chap. 3. To describe the long range (LR) EI in NCs, the following expression is generally used [55, 69, 23]:

$$\mathcal{H}_{LR}\begin{pmatrix} \mathbf{r}'_e & \mathbf{r}'_h \\ \mathbf{r}_e & \mathbf{r}_h \end{pmatrix} = \sum_{i,j} \mathfrak{Q}^{ij}_{\substack{c'\mathcal{I}v \\ \mathcal{I}v'c}} \frac{\partial^2}{\partial r_e^i \partial r_h^j} \mathcal{W}(\mathbf{r}_e,\mathbf{r}'_h)\, \delta(\mathbf{r}_e-\mathbf{r}_h)\, \delta(\mathbf{r}'_e-\mathbf{r}'_h) \tag{1.37}$$

In this expression, $\mathcal{W}$ is obtained from Eq. 1.29 by taking $-V_{e-h}$ and replacing ϵ_1 by ϵ_X, the dielectric constant at the exciton resonance. The Bloch states in the conduction band (the hole in the valence band) are denoted by the symbols c, c' (v , v'), while the coordinates of the electrons and holes are denoted by the symbols $(\mathbf{r}_e,\mathbf{r}'_e)$ and $(\mathbf{r}_h,\mathbf{r}'_h)$, respectively. The time-reversal operator, $\mathcal{I}$, alters the linear momentum $\mathbf{p}$ and the angular momentum by their opposite while leaving $\mathbf{r}$ unchanged. The $\mathfrak{Q}$ matrix involves the products of the momentum operators [64,

70], its matrix elements are provided by:

$$\Omega^{ij}_{\substack{c'\mathcal{I}v \\ \mathcal{I}v'\,c}} = \frac{\hbar^2}{m_0^2} \frac{\langle c'|\, p_i\, |\mathcal{I}v'\rangle \langle \mathcal{I}v|\, p_j\, |c\rangle}{\left(E_c^0 - E_v^0\right)\left(E_{c'}^0 - E_{v'}^0\right)} \tag{1.38}$$

where m_0 is the free electron mass and p_i (p_j) is the i (j) component of the $\mathbf{p}$ momentum; E_ν^0 ($\nu = c, c', v, v'$) is the ν^{th} band energy.

To obtain the LR Hamiltonian in the exciton basis the first step is to take the Fourier transform of the Coulomb potential $\mathcal{W}$ to facilitate the calculations (as with many problems in electrostatics). Then this potential is derived partially with respect to the electron and hole coordinates for every position of the image charges. After this, the matrix elements of the LR Hamiltonian, $\langle\Psi|\, \mathcal{H}_{LR}\, |\Psi\rangle$, ($\Psi(r,r)$ being the total exciton WF), are obtained after the calculation of the matrix elements of equation Eq. 1.38. For clarity reasons, the derivation of the long range Hamiltonian will not be performed in this paragraph but further details can be found in Appendix A or equivalently in the work published by the author and his collaborators (see the Supplementary Material of [71]).

In the exciton basis $\{|1\rangle, |-1\rangle, |0_B\rangle, |0_D\rangle\}$ the LR exchange Hamiltonian finally takes the following form:

$$\mathcal{H}_{LR} = \begin{pmatrix} \Sigma_d & \Sigma_{od} & 0 & 0 \\ \Sigma_{od} & \Sigma_d & 0 & 0 \\ 0 & 0 & \Sigma_z & 0 \\ 0 & 0 & 0 & 0 \end{pmatrix} \tag{1.39}$$

Note that the $\mathcal{H}^{LR}$ matrix and $\mathcal{H}^{SR}$ matrix have the same structure. In Eq. 1.39, Σ_d, Σ_{od} and Σ_z are given by:

$$\begin{cases} \Sigma_d = \left[\alpha^2 E_{P_{S,x}} I_x + \beta^2 E_{P_{S,y}} I_y\right] \Lambda\pi^9 \left(\dfrac{\pi a_X^3}{L_x^3}\right)\left(\dfrac{3\,|\mathcal{N}(a)|^2}{rs}\right) \\ \Sigma_{od} = \left[-\alpha^2 E_{P_{S,x}} I_x + \beta^2 E_{P_{S,y}} I_y\right] \Lambda\pi^9 \left(\dfrac{\pi a_X^3}{L_x^3}\right)\left(\dfrac{3\,|\mathcal{N}(a)|^2}{rs}\right) \\ \Sigma_z = 2\gamma^2 E_{P_{S,z}} I_z \Lambda\pi^9 \left(\dfrac{\pi a_X^3}{L_x^3}\right)\left(\dfrac{3\,|\mathcal{N}(a)|^2}{rs}\right) \end{cases} \tag{1.40}$$

where, $E_{P_{S,j}} = \left(2m_0/\hbar^2\right) P_{S,j}^2$ ($j = x, y, z$) are the Kane energies under the D_{2h} point group symmetry (orthorhombic crystal phase), associated to the Kane interband matrix elements involved in Eq. 1.38. Their values can either be deduced from experimental data or by calculation from the multiband $\mathbf{k}\cdot\mathbf{p}$ model. For NCs of cubic crystal symmetry (O_h point group), the parameters $P_{S,j}$ have the same values $P_{S,x} = P_{S,y} = P_{S,z}$ whereas under the tetragonal (D_{4h}) symmetry: $P_{S,x} = P_{S,y} = P_{S,\rho} \neq P_{S,z}$. The parameter Λ can be expressed in terms of the material and

general constants as follow:

$$\Lambda = \frac{1}{3E_g^2}\frac{\hbar^2}{2m_0}\frac{e^2}{\epsilon_0\epsilon_X}\frac{1}{\pi a_X^3} \tag{1.41}$$

The parameters r and s of Eq. 1.40 are defined by $r = L_y/L_x$ and $s = L_z/L_x$ and describe the shape elongation or contraction of the NCs (modeled as a rectangular cuboid). The exchange integrals, denoted I_l ($l = x, y, z$), have very sophisticated expressions that are detailed in Appendix A. These integrals encompass the correction caused by the dielectric effects on the exchange interaction while strongly depending on the parameters r and s. Thus, any modification of the NC shape or dielectric environment will change the amplitude of the LR exchange interaction.

Eigenvalues and eigenstates of the exchange Hamiltonian:

Following the description of both contribution of the exchange interaction in the exciton basis, the total exchange Hamiltonian $\mathcal{H}_{exch} = \left(\mathcal{H}^{SR} + \mathcal{H}^{LR}\right)$ can finally be diagonalized and admits four non degenerate eigenvalues and corresponding eigenstates that comprises three bright exciton states ($|X\rangle$, $|Y\rangle$, $|Z\rangle$) and one dark state ($|D\rangle$):

$$\begin{cases} E_{|X\rangle} = \left[2\Lambda_x E_{P_{S,x}} + 3\Delta_{SR}\right]\mathcal{K}\alpha^2\pi a_X^3 \;\;;\;\; |X\rangle = \dfrac{1}{\sqrt{2}}\left[|{+1}\rangle - |{-1}\rangle\right] \\ E_{|Y\rangle} = \left[2\Lambda_y E_{P_{S,y}} + 3\Delta_{SR}\right]\mathcal{K}\beta^2\pi a_X^3 \;\;;\;\; |Y\rangle = \dfrac{1}{\sqrt{2}}\left[|{+1}\rangle + |{-1}\rangle\right] \\ E_{|Z\rangle} = \left[2\Lambda_z E_{P_{S,z}} + 3\Delta_{SR}\right]\mathcal{K}\gamma^2\pi a_X^3 \;\;;\;\; |Z\rangle = |0_B\rangle \\ E_{|D\rangle} = 0 \;\;;\;\; |D\rangle = |0_D\rangle \end{cases} \tag{1.42}$$

where the parameter Λ_l is defined as $\Lambda_l = \frac{8\pi^9}{9}\Lambda I_l$ ($l = x, y, z$) with Λ previously expressed in Eq. 1.41 and I_l the exchange integral defined in Eq. A.13.

With Eq. 1.42 the exciton fine structure is fully characterized. The great advantage of these expressions is their general character. Indeed, they allow a full calculation of the energetic landscape of the exciton fine structure in any MHP material providing that the involved constants for this material are known. The crystal phase of the given material can also be adjusted by changing the value of the Kane energy parameters $E_{P_{S,i}}$ and the parameters α, β and γ (defined in Tab. 1.1). Additionally, and of upmost importance for the work presented in this manuscript, the adjustment of the parameters r, s, η that come into play in the exchange integrals I_l (equation Eq. A.13) allow for a change of the NC shape and dielectric discontinuity at the interface.

The exciton fine structure (EFS) of MHP materials is summarized on the level diagram pre-

sented in Fig. 1.8. On the top row, the EFS expected for each crystal phase is presented for NCs of perfect cubic shape, *i.e* $L_x = L_y = L_z$ ($r = s = 1$). The second row shows the effects of a change of the parameter r and s values on the EFS with a special focus on the tetragonal crystal phase (that will be central in the following chapters). One can see that depending on the direction of the NC distortion, the degeneracy of the states $|X\rangle$ and $|Y\rangle$ is lifted or not.

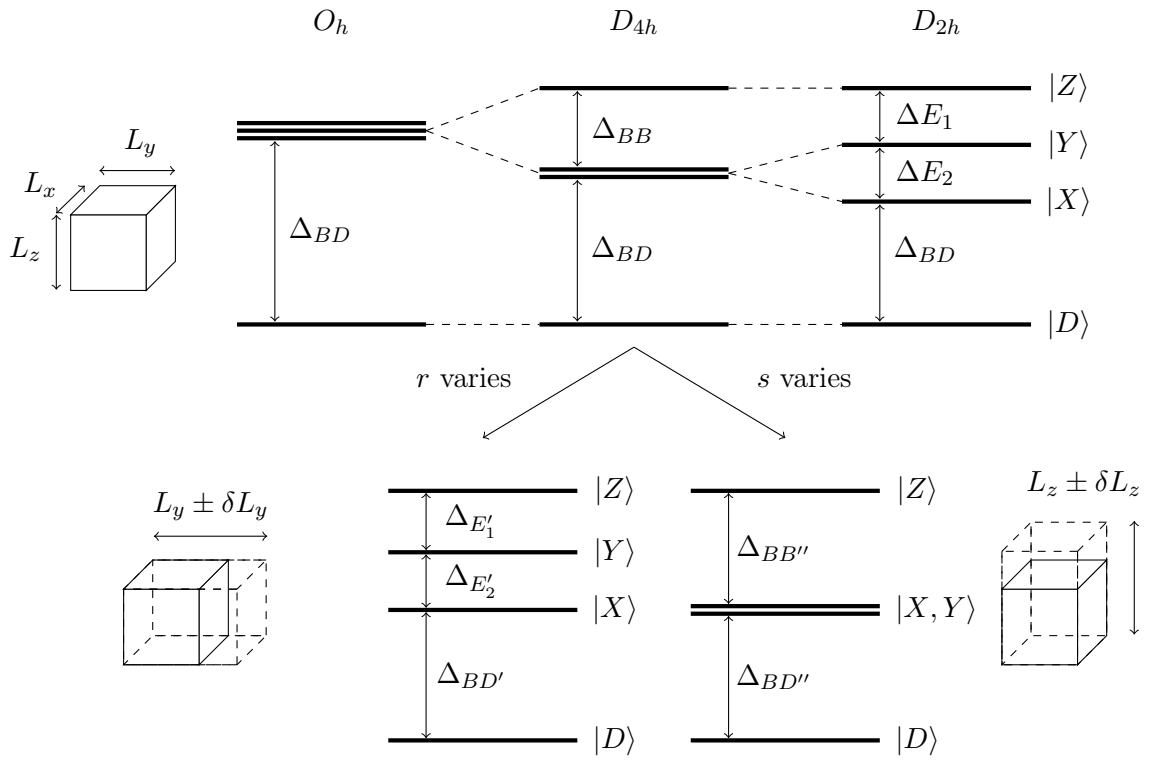

Figure 1.8: EFS energy levels diagram in MHPs. The top part of the Figure illustrates how the fine structure levels split when the crystal phase varies from cubic (O_h) to orthorhombic (D_{2h}) while the shape of the NC is kept perfectly cubic. On the bottom, the effect of the NC shape anisotropy is taken into account on the tetragonal phase (D_{4h}) specifically by adjustment of the parameter $s = L_z/L_x$ or $r = L_y/L_x$. Note that the highest symmetry axis of the D_{4h} phase is assumed to be parallel to the NC axis z.

As a final comment here, note that the expressions provided in Eq. 1.42 are only "semi-analytical" for the parameters Λ_l (containing the I_l integrals) and $\mathcal{K}$ (that contains the exciton wavefunction normalization factor, $\mathcal{N}(a)$) have to be determined *via* numerical computation.

1.3.5 Oscillator strength of exciton fine structure transitions

The optical properties of MHP NCs arise from the coupling of the EFS states presented in the last section to the electromagnetic field. The objective of this paragraph is to calculate the oscillator strength of some of the different optical transitions associated to the EFS. The interaction

Hamiltonian describing the coupling of light to an electrical dipole is given by:

$$H_{int} = -\frac{q}{m_0}\mathbf{A}(\boldsymbol{r},t)\cdot\hat{\mathbf{p}} + \frac{q^2\mathbf{A}^2(\boldsymbol{r},t)}{2m_0} \tag{1.43}$$

where $\hat{\mathbf{p}}$ is the momentum operator and $\mathbf{A}(\boldsymbol{r},t)$ is the vector potential. In the following only linear processes are considered and so the Coulomb Gauge will be used. In the Coulomb Gauge, the vector potential can be expressed as a plane wave $\mathbf{A}(\boldsymbol{r},t) = A_0 e^{i(\mathbf{k}\cdot\mathbf{r}-\omega t)}\hat{\mathbf{e}}$ and one has $\mathbf{E}(\boldsymbol{r},t) = -\partial\mathbf{A}(\boldsymbol{r},t)/\partial t$. Since optical transitions are considered in this work, their wavelengths are much larger than the NC size *i.e* $\lambda \gg L$ (where L is the edge length of the NC). Thus, the dipole approximation can be used. All in all, the interaction Hamiltonian finally takes the following form:

$$H_{int} \approx -\frac{iqE_0}{m\omega}e^{-i\omega t}\hat{\mathbf{e}}\cdot\hat{\mathbf{p}} \tag{1.44}$$

The transition rate between two electronic states of energy E_i and E_f is given by Fermi's golden rule:

$$\Gamma_{i\to f} = -\frac{2\pi}{\hbar}|\langle f|\, H_{int}\,|i\rangle|^2\delta(E_f - E_i - \hbar\omega) \tag{1.45}$$

Eq. 1.44 and 1.45 tell us that the transition rate $\Gamma_{i\to f}$ is proportional to $|\langle f|\,\hat{\mathbf{e}}\cdot\hat{\mathbf{p}}\,|i\rangle|^2$ where $\langle f|\,\hat{\mathbf{e}}\cdot\hat{\mathbf{p}}\,|i\rangle$ is called the dipole moment of the transition $i \to f$.

Let us now consider the absorption of a photon of energy $\hbar\omega$ polarized along z in a MHP NC. The initial and final states are given by the vacuum $|0\rangle$ and the exciton $|\Psi(r,r)\rangle$ state respectively, one can write:

$$|\langle\Psi(\boldsymbol{r},\boldsymbol{r})|\,\hat{\mathbf{e}}\cdot\hat{\mathbf{p}}\,|0\rangle|^2 = |\langle 0_B|\,\hat{p}_z\,|0\rangle|^2\left|\int d\boldsymbol{r} f(\boldsymbol{r},\boldsymbol{r})\right|^2 \tag{1.46}$$

with $f(\boldsymbol{r},\boldsymbol{r})$ the envelope function and $|0_B\rangle = |Z\rangle$ is the exciton state associated to a linear dipole along the z direction. Thus, the transition dipole moment is given in this case by:

$$\langle 0_B|\,\hat{p_z}\,|0\rangle = \frac{1}{\sqrt{2}}\left[\langle C_1, V_1|\,\hat{p}_z\,|0,0\rangle + \langle C_2, V_2|\,\hat{p}_z\,|0,0\rangle\right] \tag{1.47}$$

$$= \frac{1}{\sqrt{2}}\left[\langle C_1|\,\hat{p}_z\,|V_1\rangle + \langle C_2|\,\hat{p}_z\,|V_2\rangle\right] \tag{1.48}$$

where the electron-hole representation associated to the exciton was switched to the electron-electron representation with Bloch states $|C_{1,2}\rangle$, $|V_{1,2}\rangle$ defined in Eq. 1.20 [68, 72]. Keeping only the non zero terms associated to $|Z\rangle$ in Eq. 1.20 one gets:

$$\langle 0_B|\,\hat{p_z}\,|0\rangle = -i\frac{\gamma}{\sqrt{2}}\left[\langle Z\uparrow|\,\hat{p}_z\,|S\uparrow\rangle + \langle Z\downarrow|\,\hat{p}_z\,|S\downarrow\rangle\right] = -i\sqrt{2}\frac{\gamma m_0}{\hbar}P_{S,z} \tag{1.49}$$

In this expression, $P_{S,z} = (\hbar/m_0)\,\langle Z|\,\hat{p}_z\,|S\rangle$ is the Kane inter-band matrix element. Thus, the square of the optical transition dipole moment associated to the absorption of light linearly po-

larized along the z direction is finally given by:

$$|\langle\Psi(\boldsymbol{r},\boldsymbol{r})|\,\hat{\mathbf{e}}\cdot\hat{\mathbf{p}}\,|0\rangle|^2 = E_{P_{S,z}}\sin^2\theta\left|\int d\boldsymbol{r}\,f(\boldsymbol{r},\boldsymbol{r})\right|^2 \tag{1.50}$$

where $E_{P_{S,z}} = 2m_0^2P_{S,z}^2/\hbar^2$ and the expression of $\sin^2\theta$ was discussed in the paragraph following Tab. 1.1. From there one can calculate the oscillator strength f_Z associated to the exciton state $|Z\rangle$ [72]:

$$f_Z = \frac{2E_{P_{S,z}}K}{E_Z m_0}\sin^2\theta \tag{1.51}$$

where K is the square of the overlap integral from Eq. 1.50 and E_Z is the energy of the transition from state $|Z\rangle$ to the vacuum. The oscillator strength of the other EFS states can be calculated the same way. Doing so with the exciton state $|D\rangle = |0_D\rangle$ the dipole moments $\langle Z|\,\hat{p}_z\,|S\rangle$ cancel each other in Eq. 1.49 which will inevitably lead to $f_D = 0$, an expected result for this dark exciton state.

1.3.6 Additional exciton species

When the excitation power is increased, the density of photo-generated free carriers and excitons will be enhanced in the NC. The Coulomb interaction between these charge carriers can lead to the formation of charged excitons or exciton molecules that are studied in the following section.

Trion:

A trion is a three-particle state composed of an electron-hole pair (or exciton) and an additional charge that is either an electron for the negative trion X^- or a hole for the positive one X^+. Thus, the creation of a trion implies the ionization of the NC, which can happen through the doping of the material [73, 74] or by an Auger recombination process [75]. In the latter case, the energy liberated by an exciton recombination is transferred to one of the charge carriers composing a second exciton. When this energy is high enough, the carrier can be ejected from the material, leaving the NC with a net electric charge. After this ionization process, a single carrier is left in the NC and the photo-generation of an additional exciton leads to the trion formation by Coulomb interaction between the single carrier and the new exciton, seen on Fig. 1.9. The energy of the trion is governed by the attractive Coulomb interaction between the two opposite charge carriers with an additional carrier-carrier repulsion. Therefore the binding energy of a trion is always lower than that of the exciton and one can write $\Delta_{X^\pm} = (E_X + E_i) - E_{X^\pm}$ with $i = h, e$ for a positive or negative trion respectively. Furthermore, the three particle state formed by the trion is not split by the exchange interaction [76]. To see this let us take the example of the

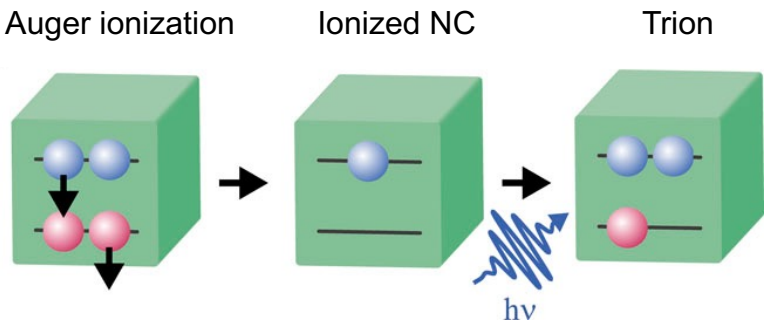

Figure 1.9: Illustration showing the mechanism behind the formation of a negatively charged Trion in a NC by Auger ionization. Adapted from [75].

negative trion X^-. This trion state is spin degenerate and can either be $|\uparrow\downarrow\uparrow\rangle$ or $|\uparrow\downarrow\downarrow\rangle$ (with $\uparrow$,$\downarrow$ designating the hole spin). In either case, two electron-hole exchange terms of the same amplitude but opposite signs are obtained and cancel each other. Experimentally, all of these arguments lead to a trion emission characterized by a single spectral line associated to a circular polarization (due to the spin degeneracy of the trion state).

Biexciton:

Biexcitons are quasi-particles composed of two electrons and two holes that can be viewed, in analogy with the dihydrogen molecule, as exciton molecules. They are formed by the Coulomb interaction between two excitons leading to a biexciton state $|XX\rangle$ of energy E_{XX} that is lower than that of two non interacting excitons ($|X\rangle$ of energy E_X) *i.e* $E_{XX} < 2E_X$. The difference Δ_{XX} between the two is the biexciton binding energy and thus $\Delta_{XX} = 2E_X - E_{XX}$.

Fig. 1.10 illustrates the resulting energy level structure known as the "biexciton cascade". During its recombination, the biexciton can either go through the path represented in red on Fig. 1.10 (and associated to the exciton state named $|Y\rangle$) or *via* the blue path (associated to the state $|X\rangle$). If the two intermediate exciton states have a smaller fine structure splitting Δ_{FSS} than the radiative linewidth, the two recombination paths become indistinguishable and pairs of polarization entangled photons are generated [77]. This is the most important application of the biexciton cascade but it requires a very fine control over the EFS splittings. In the case of MHP NCs the adjustment of Δ_{FSS} can be achieved by controlling the anisotropic growth of the NCs (as seen in Sec. 1.3.4) or by directly readjusting the exciton states energies with an electric field by Stark effect [78].

During optical spectroscopy experiments, the spectral signature of the biexciton will appear as a red shifted multiplet with inverted polarization properties when compared to the EFS lines (*i.e* if the high energy EFS transition has an horizontal linear polarization, the high energy biexciton

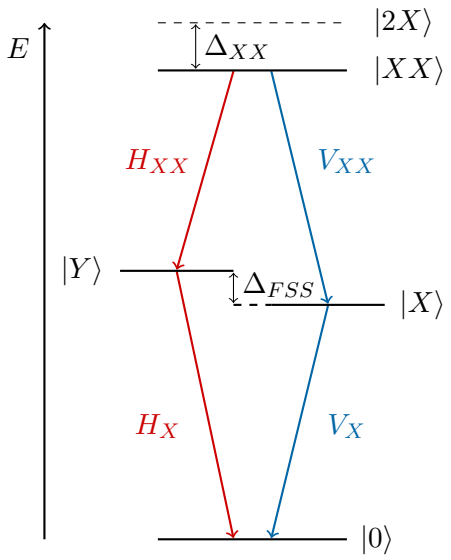

Figure 1.10: Energy level diagram of the neutral exciton and biexciton, commonly known as the Biexciton cascade. The exciton fine structure states are represented by $|X\rangle$ and $|Y\rangle$ with energy $E_X \pm \Delta_{FSS}/2$ where Δ_{FSS} represents the fine structure splitting between two bright states. The biexciton binding energy is given by $\Delta_{XX} = 2E_X - E_{XX}$. One can see that if Δ_{FSS} approaches 0 the two recombination paths (red and blue arrows) of linear polarization H (Horizontal) and V (vertical) become indistinguishable. Note that for clarity, the splittings represented on the diagram are not to scale. In reality, $\Delta_{FSS} \ll \Delta_{XX}$.

transition will have a vertical linear polarization and *vice versa*). This behavior is explained by the fact that much like the trion, the biexciton state is not split by the exchange interaction since all the exchange terms cancel each other [76, 79]. Therefore the energy of the transitions towards the exciton will only depend on the fine structure splitting between the exciton states, as seen on Fig. 1.10.

1.4 Exciton interacting with its environment

The underlying atomic lattice and its environment are expected to interact with the charge carriers confined in the NC. This section presents a brief overview of these interactions with a special focus on the exciton-phonon interactions.

1.4.1 Dephasing

Let us first understand why these interactions are important for this work. Like any other quantum state, an exciton inside a semiconductor lattice has a certain duration over which it remains coherent, meaning that the phase relationship between the different components of this state is well preserved. This particular duration is often called the coherence time (or dephasing time) and

denoted as T_2. When every other coherence damping processes are neglected, the recombination of an exciton is governed by the spontaneous decay of its population towards the ground state, in other word here, by spontaneous emission. Thus, in such ideal system the coherence time of the exciton is given by $T_2 = 2T_1$ where T_1 represents the radiative lifetime of the exciton.

In reality however, the coherence time of an exciton is usually drastically reduced by its interaction with the environment. These interactions do not lead to a change in the exciton population but rather alter its phase. A timescale is generally attributed to the combination of all of these events and called the pure dephasing time denoted as T_2^*.

Considering both of these coherence damping processes, the following relation provides the dephasing rate $(1/T_2)$ for an exciton inside a NC:

$$\frac{1}{T_2} = \frac{1}{2T_1} + \frac{1}{T_2^*} \tag{1.52}$$

The understanding of these timescales is crucial for the design and interpretation of experiments in quantum optics and quantum computing, where the control of quantum states is of fundamental importance. For these applications, the objective is to find systems with the longest coherence time T_2 while suppressing the pure dephasing mechanisms to the maximum to tend towards $T_2 \approx 2T_1$ where the emitted photons become indistinguishable. This limit represents a formidable challenge to reach because quantum systems are never completely isolated from their surrounding environment. Since semiconductor NCs are solid state systems, two major sources of pure dephasing are the fluctuations in the electrical environment (spectral diffusion) and exciton-phonon coupling *i.e.* coupling to the thermally induced lattice vibrations (phonon bath), both presented in the next paragraphs.

1.4.2 Electrical environment

The electrical environment of a NC can have a huge impact on the coherence properties of the exciton. The presence of charges arises from the occupation fluctuations of the available states in the surrounding environment and leads to time-dependent shifts in the local electric field. These fluctuations result in small variations in the energy levels of the exciton through the Stark effect and random phase shifts of the quantum state, contributing to dephasing. Since most of these charge fluctuations are due to the presence of nearby traps or impurities, one way to limit their impact is to passivate the surfaces of the NCs and improve the synthesis conditions to limit the number of defects in the NC lattice.

1.4.3 Exciton-Phonon coupling

The presence of a crystal lattice surrounding the exciton in solid-state systems provides the ideal environment for exciton-phonon coupling. Three main mechanisms of exciton-phonon interaction are usually distinguished: the deformation potential, the piezoelectric coupling and the Fröhlich coupling. The following only presents a brief review of these mechanisms but a rigorous mathematical treatment can be found in [80, 81, 82].

Coupling to deformation potentials:

The electronic band structure of a material is very sensitive to the inter-atomic distances. Thus, the atomic displacement induced by lattice vibrations will slightly change the energy of excited carriers inside the crystal lattice. This form of carrier-phonon coupling is generally described by deformation potentials, *i.e* potentials that depend on the relative volume change $\delta V/V$ of the material due to the deformation. The phonons involved in this type of coupling are usually low energy acoustic phonons. Since the occupation number of these modes is given by the Bose-Einstein distribution, $n(T) = 1/(exp(\hbar\omega/k_B T) - 1)$, their low energy (usually a few 100 μeV in MHPs) allow them to exist even at cryogenic temperatures and to interact with the exciton state.

Piezoelectric Coupling:

Piezoelectric coupling occurs in materials that lack a center of symmetry, meaning that they possess piezoelectric properties. In such materials, mechanical stress can induce an electric polarization, and conversely, an electric field can cause mechanical deformation. When an acoustic phonon propagates through a piezoelectric material, it deforms its atomic lattice and induces an electric field that can interact with the electrons. In this manuscript, phonons are essentially investigated in fully inorganic perovskite materials (like $CsPbCl_3$) which are centrosymetric materials. Thus, piezolectric coupling wil not be considered further.

Fröhlich coupling:

Fröhlich coupling describes the interaction between electrons and optical phonons in polar materials, such as ionic crystals (e.g., $CsPbX_3$, NaCl, GaAs). In these materials, when a longitudinal optical (LO) phonon mode is excited, it generates a local electric field due to the displacement of ions with opposite charges. This electric field can then interact with charge carriers in the material, leading to a modification of the exciton energy. Like the acoustic phonons, the occupa-

tion of the optical phonon modes is governed by the Bose-Einstein statistics. Since their energy is usually much larger (*e.g* $\sim$ 10 meV in $CsPbCl_3$) they do not "perturbate" the exciton at the lowest temperatures. At high temperature however their occupancy is much larger and since MHP materials are highly ionic compounds, the Fröhlich interaction generally dominates all the exciton-phonon scattering mechanisms at temperatures above $\sim$ 50 K typically.

1.5 Short review of MHP NCs applications

Now that MHP NCs and their optical properties have been presented, let us close this introductory chapter by reporting some of the most promising applications of these materials. Note that the short following review will be restricted to the description of light emission devices, which are closely related to this work and will thus not mention photovoltaic applications that represent another important area of research in perovskite materials.

Light emitting devices:

One of the first optoelectronic application that comes to mind when speaking about perovskite NCs are LEDs. These devices emit light *via* the radiative recombination of electrically injected e-h pairs inside their active layer *i.e* the region containing the semiconductor NCs. The high oscillator strength of the optical transitions characterizing MHP NCs, alongside their defect tolerant band structure (for Br^- and I^- based compounds at least) have led to the observation of near-unity Photoluminescence Quantum Yields (PLQY) and translate, application wise, into brighter LEDs. Moreover, these systems show narrow emission peaks of full width at half maximum (FWHM) typically in the range of 20–30 nm at room temperature which leads to a high color purity of LED emission [17, 18].

The relatively easy adjustment of the halide composition and quantum confinement in these systems results in a high tunability of their band gap and, naturally, of their emission wavelength over the entire visible spectrum [17]. Thus, red and green emitting LEDs, based on MHP NCs, have been widely reported in the litterature and already achieve external quantum efficiencies (EQE) between 15 to 30 % (see *e.g* [83, 84, 85] for red LEDs and [86, 87, 88] for green emission). Regarding blue LEDs, MHP NCs suffer from issues that are rather general to all semiconductors: A reduced choice in the available compounds to generate wide band gap structures and a larger proportion of trap states that lead to non-radiative recombination in these large band gaps [89]. The strategies for developing blue MHP NCs based LEDs include the use of mixed Cl^- and Br^- halide materials *i.e* $ABBr_{1-x}Cl_x$ where $0 \leq x \leq 1$ [90], highly quantum confined structures like quasi-2D perovskite structures [91] and passivation to reduce the number of defects on their

surfaces [92]. Fig. 1.11 shows a brief overview of the progress that has been made over the last decade regarding the quantum efficiency of perovskite based LEDs alongside other quantum dots (essentially II-VI semiconductors) and organic LED technologies for comparison.

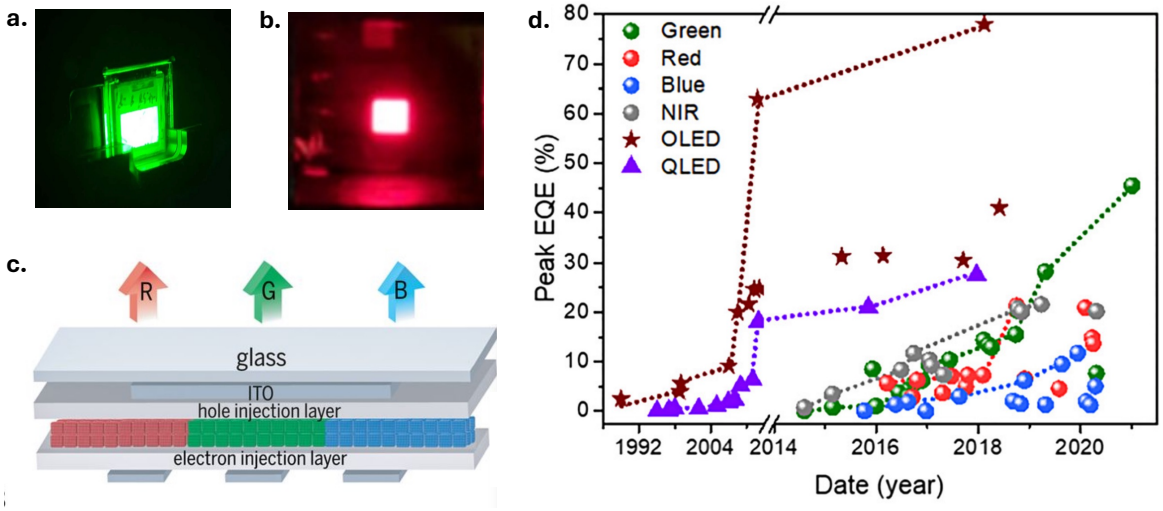

Figure 1.11: MHP based LEDs. **a,b.** Images of green [86] and red [93] LEDs under operation. **c.** Concept of an LED display based on an MHP NCs active layer [94] **d.** Evolution of the external quantum efficiency (EQE) at peak luminance for MHP and other LED technologies. The Brown and purple lines and symbols represent organic and II-VI semiconductor quantum dots LEDs respectively. Reprinted from [95].

Finally, LEDs based on MHP NCs face additional challenges such as photostability (especially due to their moisture and oxygen sensitivity) [96, 97, 98], operational longevity, and environmental safety (the B site cation being lead in many perovskite NCs) [99]. Even though many research groups are actively working on these issues [100, 101], further progress still need to be made for a widespread commercial use of these devices.

Lasers:

For laser emission to happen, a gain medium needs to reach population inversion *i.e* a situation where the number of emitters in an excited state overcomes that of emitters in their ground state. When this situation is reached, stimulated emission can occur and, with the appropriate resonant configuration, leads to light amplification of high coherence. Therefore, in such systems, lasing is triggered as long as the gain surpasses the non-radiative losses in the optical medium.

In this context, perovskite nanostructures are highly promising for laser applications. The unique combination of properties mentioned in the previous paragraph makes them well-suited for efficient, tunable, and low-threshold lasing. Additionally, the emission of MHPs essentially

comes from the radiative recombination of bright exciton states that can show a high binding energy in confined systems such as nanoplatelets and quantum dots, thus favoring a high exciton gain even at room temperature [102]. Finally, non radiative recombination channels are reduced by the defect tolerance of these materials, the inefficient bright-dark exciton state relaxation [22, 71], and the ultrafast stimulated emission processes occuring on a shorter time scale that non-radiative Auger recombination [103, 104, 105]. Although several studies have already reported optical gain or laser emission with hybrid or all inorganic MHPs in the visible spectrum [106, 107, 108, 109] most of these demonstrations used a pulsed laser as excitation pump. Fig. 1.12 shows the example of a lasing MHP device made out of a $\sim$ 10 μm $MAPbI_3$ nanowire (NW) by the group of X-Y.Zhu in 2015 [106]. The lasing here is characterized by a large non linear intensity increase above the pump fluence threshold, a strong reduction of the emission linewidth (down to $\Delta\lambda = 0.2$ nm) and an acceleration of the emission decay dynamics ($\tau \leq 20$ ps).

Perovskite laser gain media operating under continuous wave (CW) excitation have been much less reported in the literature [110, 111, 17]. Under such excitation conditions, and due to the low thermal conductivity of perovskites [112, 113], the lattice can rapidly overheat by Joule heating which then leads to the degradation of these soft-lattice materials and to the accumulation of lattice defects. [114]. Finally, the largest remaining challenge for the realization of MHP based lasers is the design of an electrically excited gain medium (coupled to a resonator) with a lasing threshold sufficiently low for practical uses [115, 116]. In these excitation conditions the overheating is even worse due to a poorer conversion of optical to electrical energy. To this day, no efficient solutions have been found to these issues. New strategies are being explored among which the polaritonic one that could allow to combine an electrical pumping to the low threshold density lasing obtained through polariton condensation. Among the rapidly developing literature in the field the reader can refer to references [117, 118] for a first insight into the possibilities offered by the approach.

Single photon sources:

A single-photon source is a system that emits light in the form of individual photons (*i.e.* one at a time), in contrast to classical light sources, which emit multiple photons simultaneously (in bunches). These sources are crucial for various applications in quantum technologies, particularly in fields like quantum cryptography, computing, and communication [119]. In their ideal form, such light sources are represented by an isolated two level system comprising an excited state $|1\rangle$ and a ground state $|0\rangle$. Through the spontaneous relaxation $|1\rangle \rightarrow |0\rangle$, indistinguishable photons (*i.e.* in the same pure quantum state) are emitted at time intervals characterized by the radiative

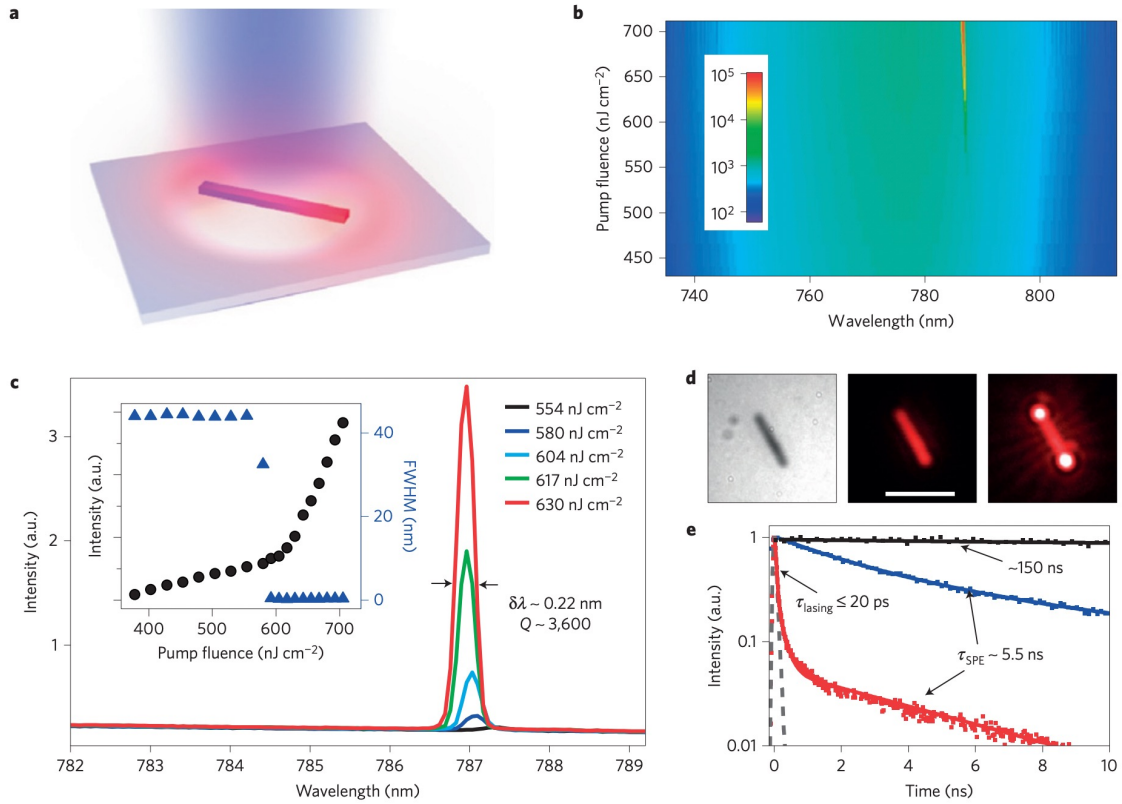

Figure 1.12: Lasing $MAPbI_3$ NW device. **a.** Illustration of the lasing device on its SiO_2 substrate and under pulsed excitation (Δt = 150 fs, Rep. rate 250 kHz, λ = 402 nm). **b.** PL intensity map as a function of the pump fluence and the emission wavelength. **c.** Emission spectra captured at different pump fluences. The black dots in the inset show the evolution of the emission intensity with the pump fluence (note the non linear regime above the fluence threshold of $\sim$ 600 nJ/cm^2). The blue triangles give the emission linewidth evolution with pump fluence with a clear drop around $\sim$ 600 nJ/cm^2. **d.** Optical image (left) of a single NW. The middle and right images show the NW emission below and above the lasing threshold. **e.** Emission decay measurements for below (blue curve) and above (red curve) the lasing threshold (black curve is a measurement at very low fluence). A strong reduction of lifetime is clearly observed in the stimulated emission regime (with a residual background of spontaneous emission). Figure reprinted with permission from [106]

lifetime τ_1 of the transition.

For practical systems however (*e.g.*, semiconductor NCs), this ideal picture is degraded by the interaction of the "two level" system of interest with its environment. Indeed, Sec. 1.4.1 explained that several mechanisms can lead to the decoherence of the exciton state: coupling to lattice vibrations [120] fluctuating electrostatic charge distribution in the environment [121] or even hyperfine interaction with nuclear spins [122]. In these conditions, the emitted photons loose their indistinguishability and single nature. Therefore, key quantities to measure for the evaluation of practical single-photon sources are: the single photon purity (how reliably the single-photon source emits one photon at a time, without multi-photon events), the indistinguishability (how

identical the emitted photons are in terms frequency, polarization etc.) and brightness (driven by the rate at which single photons are emitted by the source).

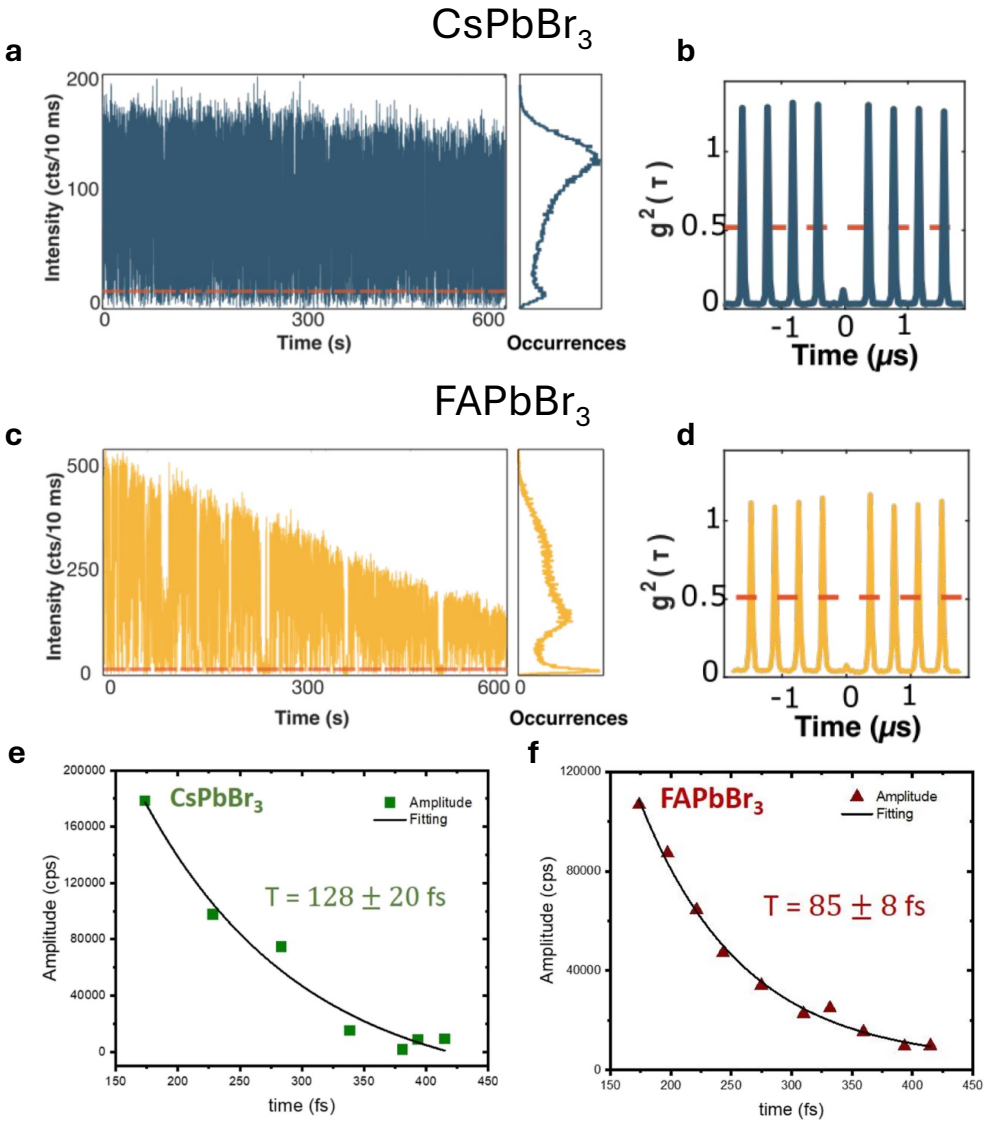

Figure 1.13: Comparison of the single photon emission properties for two materials: $CsPbBr_3$ and $FAPbBr_3$. **a,c.** PL blinking measurements for each material. $CsPbBr_3$ shows a better photostability under illumination over time with less frequent blinking. The histogram on the side shows the number of occurences on the same intensity range. Two "on" and "off" states are observed with higher "off" state occurences in the case of $FAPbBr_3$ **b,d.** Second order correlation function obtained through HBT two-photon coincidence measurements on a single emitter for each compound. Over multiple measurements, the authors found a $g^{(2)}(\tau = 0) < 0.1$ for 56% of $CsPbBr_3$ and 75 % of $FAPbBr_3$ NCs. **e,f.** Coherence time measurements for each compound obtained by two-Photon time-resolved near-field scanning optical microscopy experiments. Both materials have $T_2 \approx 100$ fs with a slightly longer coherence time for $CsPbBr_3$. **a,b,c,d.** are adapted from [123] and **e,f** from [124]

Using a Hanbury Brown and Twiss (HBT) interferometer, F. Hu *et al.* demonstrated in 2015 the room temperature single photon emission from MHP NCs with a 0.06 probability of pho-

ton coincidence at zero time delay and per excitation pulse [125] [3]. Since then, MHP NCs and their bright EFS transitions have been highly investigated for their potential use as single photon sources [126, 127, 123, 128]. The high PLQY measured in MHPs alongside the ease of tunability of their emission wavelength (particularly towards long wavelengths) makes them excellent candidates for bright single-photon sources. Additionally, unlike many single-photon sources that require cryogenic temperatures to operate (*e.g.,* self assembled quantum dots or trapped atoms) the large exciton binding energy of MHP NCs allow the emission of single photons at room temperature [129]. Fig. 1.13 reports typical measurements characterizing the single photon emission of MHP NCs.

As of today, many issues still need to be addressed for the use of MHP NCs as efficient single photon sources. First, their quick degradation when exposed to light and moisture reduces their long-term photostability (see Fig. 1.13). Another limitation comes from the blinking of their emission that randomly switches between "on" and "off" states over time [126, 123]. Addressing these issues, D'Amato and coauthors have demonstrated the higher photostability of $CsPbBr_3$ and later used Zn^{2+} doped $CsPbBr_3$ NCs to observe a clear diminution of the PL blinking [127]. Perovskite NCs generally exhibit lower photon indistinguishability compared to other quantum emitters, such as quantum dots or color centers. This is due to the already mentioned spectral diffusion and phonon interactions at room temperature, which affect the homogeneity of emitted photons in terms of phase, polarization, and frequency. A common method to deal with this issue and ensure a large photon extraction is to couple the quantum emitter to a cavity [130] or a photonic circuit [131]. These structures have been shown to enhance the radiative recombination rate (by Purcell effect), which in turn, reduces the influence of the dephasing processes and improves the brightness of the emitter. However, this remains less developed for NCs when compared to self assembled quantum dots since the later have, by nature, a better "on-chip" integration potential. Notably, recent work by S. Jun *et al.* successfully coupled a single $CsPbBr_3$ NC, capped with zwitterionic ligands, to a circular Bragg grating (CBG). This configuration demonstrated an enhanced photon extraction, attributed to improved emission directionality, and achieved a two-fold increase in the radiative recombination rate [132]. While the improvement in recombination rate was moderate, these results offer promising prospects for the integration of metal halide perovskite NCs into photonic devices.

[3] The second order correlation function will not be introduced here, but to be more precise, they measured its value at a zero time delay (τ) between the two detectors (avalanche photodiodes) of their set-up *i.e* $g^{(2)}(\tau = 0)$

Conclusion

This introductory chapter presented the theoretical background that will be applied throughout this manuscript to study the optical properties of MHP NCs. It began with a brief overview of the perovskite structure and the various crystal phases accessible to MHPs, followed by an introduction to their electronic band structure and the $\mathbf{k} \cdot \mathbf{p}$ method typically used for its calculation. The chapter then explored the optical properties of MHP NCs, focusing on the theoretical construction of excitons in both bulk and quantum-confined materials. The description of excitons was further refined by incorporating the electron-hole exchange interaction, which resulted in the breaking of exciton state degeneracy and the emergence of bright and dark exciton fine-structure states. Additionally, the concept of multicharged exciton species, such as biexcitons and trions, was introduced, followed by the various dephasing mechanisms that typically lead to exciton decoherence in these materials. Finally, the chapter provided a brief review of optoelectronic and quantum applications, highlighting the broad application potential of this work

CHAPTER

2 EXPERIMENTAL METHODS

Centered around nanocrystals, this work encompasses an extensive range of experimental platforms that bridge chemistry and physics at Paris Institute for Nanosciences (INSP). The primary objective of this chapter is to provide the reader with a comprehensive understanding of the diverse methods and equipment involved in the production of the results presented throughout this manuscript. Sec. 2.1 will discuss the hot injection method used to produce the lead halide perovskite (LHP) nanocrystals at the center of this work: the cuboid $CsPbCl_3$ NCs. Sec. 2.2 discusses the preparation of diluted colloidal solutions of nanocrystals and their deposition on substrates. Lastly, the primary focus of this PhD work has been on optical spectroscopy techniques, and Sec. 2.3 will introduce the absorption and micro-photoluminescence spectroscopy setups along with their associated equipment.

2.1 Nanocrystals synthesis

The past three decades have seen the discovery of a wide variety of nanocrystals which was naturally accompanied by significant progress in the development of colloidal synthesis methods. In their 1993 groundbreaking paper, Murray, Norris, and Bawendi [8] demonstrated the first colloidal synthesis of II-VI semiconductor nanocrystals using the Hot-Injection (HI) method. Today, it remains the method of choice for synthesizing colloidal nanocrystals with a narrow size distribution. The objective of this section is to detail this method and apply it in the context of lead halide

perovskite (LHP) nanocrystals production. It will become apparent that the change of reaction parameters like the temperature, concentration or type of ligands along with the reaction time have dramatic effects on the sizes, morphologies and optoelectronic properties of these nanomaterials. These parameters were extensively manipulated to produce the nanocrystals discussed in this work.

2.1.1 Hot Injection

The hot injection method is based on the pioneering work of La Mer and Dinegar who explained in a 1950 study [133] how the synthesis of monodisperse colloids relies on a swift nucleation process followed by a controlled growth of the nuclei. Nucleation is triggered by the quick injection of a pre-synthesized monovalent cation precursor (caesium-oleate for instance for inorganic LHPs) into a high temperature solution (typically from 100°C to 200°C) containing the other precursors (PbX_2), a solvent and some surfactant molecules called ligands (Oleic Acid, Oleylamine) that passivate the surfaces, control the size and shape of the nanocrystals and prevent their aggregation. This injection triggers the thermal decomposition of the precursors, leading to a critical concentration of the resulting metallic ions and anions in the solution. The formation of new nuclei then lowers the excess ion concentration. The growth of these particles continues as ions from the solution are added to the nuclei of the newly formed nanocrystals. Since the concentration of ions is now below the critical concentration for nucleation, these species only contribute to the growth of existing particles, rather than forming new nuclei resulting in a higher size homogeneity. Finally, once the concentration of ion precursors has been sufficiently reduced, the particles growth persists through a process known as Ostwald ripening. During this process, the larger nanocrystals (NCs) continue to expand, while the smaller ones dissolve due to their higher chemical potential.

In the context of this work, the LHP NCs were synthesized directly at INSP by E. Lhuillier and followed, with slight adjustments, the protocol initially introduced by Protesescu *et al.* in 2015 [17]. To be more specific, the HI synthesis of colloidal NCs typically adopts the following procedure:

- **Cs-Oleate solution preparation**: In a three-neck balloon, cesium carbonate (Cs_2CO_3) is dissolved in a mixture of oleic acid (OA) and octadecene (ODE). The balloon is then degassed under vacuum for 30 minutes at 110°C. After this, the atmosphere is replaced with argon, and the temperature is raised to 200°C for 10 minutes. Once the cesium salt has completely dissolved, the temperature is lowered below 110°C, and the flask is further degassed for 10 minutes. The resulting solution is used as the Cs-precursor in the next steps

of the synthesis.

- **Other precursors solution preparation**: In a three-neck balloon, a lead halide salt PbX_2 (X = Cl, Br, I) is introduced with octadecene (ODE). The balloon is first degassed at room temperature until the bubbling of the solution slows down, and degassed at 110°C for the next 30 minutes. Oleic acid is injected into the flask, and once the vacuum has been recovered, oleylamine (OLA) is also added. The degassing process is continued at 10°C for 30 minutes. The atmosphere is then switched to nitrogen, and the temperature set to 180°C.

- **Hot injection**: Cs-oleate solution is injected into the lead halide one still at 180°C. The reaction is conducted for a few seconds and a color change is observed (color will depend on the selected halogen). The heating mantle is removed, and the flask is cooled using an ice bath or some fresh air.

- **Centrifugation and cleaning**: The obtained solution is centrifuged at 6000 rpm during 5 min. The supernatant containing the excess of ligands and unreacted byproducts is discarded and the obtained pellet redispersed in a solvent of low polarity like hexane or toluene.

In the last step the need for an apolar "storage" solvent highlights the fact that due to their ionic nature and the dynamic bonding of the ligands [134] perovskite NCs are highly reactive with polar solvents such as water and ethanol. Thus, to prevent their degradation, the solutions are usually stored in sealed chemistry vials protected from light. Despite these efforts coalescence of the nanocrystals along with a redshift of their emission is inevitably observed after a few days to a few months (depending on the type and shape of the LHP NCs).

2.1.2 Size and shape control

The hot-injection method offers a high level of control to modify the particles sizes and shapes by varying the reaction time, temperature and the concentration and combination of ligands. As a consequence of the strong ionic nature of their bonds, LHP NCs grow in a matter of a few seconds and so the adjustment of the reaction time is generally not convenient for controlling their absolute sizes or shapes. Instead, this can be managed by changing other parameters like the reaction temperature, the concentration of ligands or precursors, and the size of the capping ligands. Besides the isotropic nanocube geometry, the fabrication of NCs with anisotropic shapes is performed inducing growth preferences along certain directions by altering the synthesis conditions.

For example, in its original 2015 paper, the group of M.V.Kovalenko varied the temperature from 140°C to 200°C to generate $CsPbX_3$ nanocubes (X = Cl, Br, I) of sizes ranging from 4 to 15 nm [17] and this has been reproduced several times since then (see [135, 136] for examples). On

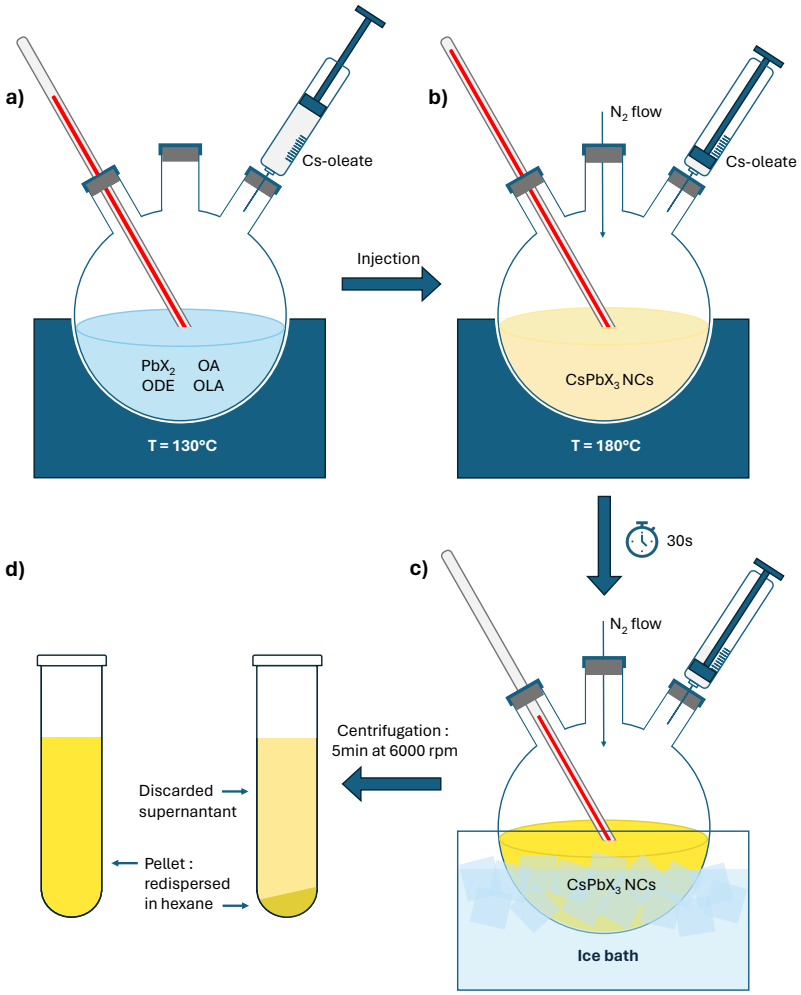

Figure 2.1: Scheme of the hot injection method. a) PbX_2 is disolved into ODE with the ligands. b) The temperature is raised to 180°C, the atmosphere switched to N_2 and the Cs-Oleate solution is injected. c) The reaction is quenched with an ice bath after 30s. d) After centrifugation the pellet is redispersed in a non polar solvent.

the other hand several groups demonstrated that under 130°C objects start to grow anisotropically producing 2D objects such as nanoplatelets (NPLs) that get thinner and thinner the lower the temperature gets [135, 137, 138, 139].

Regarding ligands, another study conducted with $CsPbBr_3$ demonstrated that increasing the length of the caboxilic acid capping ligand (Oleic acid, OA) while keeping the reaction temperature at 170°C decreased the edge length of the nanocubes from 13 to 9.5 nm on average [140]. On the other hand, by reducing the length of the OLA ligand, they showed -alongside with other groups- that 2D geometries with thicknesses down to only few unit cells even at high temperature could be achieved [140, 141, 142].

Several studies also changed the concentration ratio of ligands and precursors and reported effects of size and shape modifications [137, 139]. In 2018 Almeida *et al.* [139] proposed that

key parameters here are the oleic acid and oleylamine concentrations. During the synthesis, oleic acid and oleylamine can interact and form an hydrogen bonded ionic salt called ammonium carboxylate. This process is exothermic and implies that at high temperature the two ligands coexist separately while lower temperatures favors the ammonium carboxylate salt form. It is now well accepted [143, 144] that oleylammonium ($OLAH^+$) can compete with surface Cs^+ cations during the growth of the nanocrystals. Keeping this in mind, varying the temperature or changing the acid/base equilibrium directly in solution by adding more oleic acid or other acids such as HBr will increase the concentration of $OLAH^+$ and trigger this competition effect.

Although these mechanisms explain how the growth could slow down on all the nanocrystals surfaces it is still not entirely clear as to why it happens only on specific facets of the nanocrystals leading to anisotropic forms. A possible reason could come from the preferential binding of oleylammonium on certain facets (as observed by Zhang *et al.* on LHP nanowires [145]) leading to a surface energy reduction that would slow the growth on these facets [146].

2.1.3 Structural characterization: Electron microscopy

Electron microscopy offers detailed insights into the size and shape of the nanocrystals (NCs) synthesized through hot injection. The quality and uniformity of the synthesized material can be directly verified on the images and statistics of these parameters can be compared to the sizes inferred from the optical response of the NCs, which are subject to quantum confinement. For this work, a JEOL 2010 transmission electron microscope operating at 200 keV was used. The TEM samples were prepared by placing a drop of rather high concentration of NCs from the solutions (typically a dilution factor of 10) on a copper grid coated with carbon. Fig. 2.2 presents an example of the images that can be captured with this equipment.

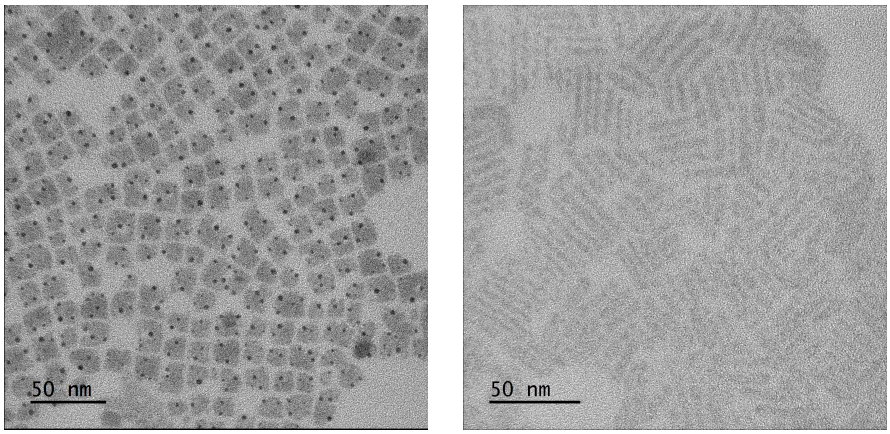

Figure 2.2: TEM images of LHP NCs. Image on the left side shows nanocubes of $CsPbBr_3$ while nanosticks (1D objects) of the same material are presented on the right side. The dark spots on the left side image are attributed to the reduction of Pb^{2+} ions to Pb^0 by the electron beam.

2.2 Sample processing

After the synthesis of the NCs, a few processing steps, described in the following paragraph, have to be performed in order to fabricate the final samples that are used in single object spectroscopy experiments.

2.2.1 Dilution

The colloidal solutions described in Sec. 2.1 contains a large concentration of nanocrystals (NCs). While these solutions would be suitable for TEM and spectroscopic ensemble measurements or integration into certain optoelectronic devices, they cannot be used as such in this work where intrinsic individual responses are desired. To make the observation of the optical response of individual nanocrystals possible, it is thus necessary to heavily dilute the solutions. This dilution process was done using the same solvent as the one used for the colloidal solutions storage, namely hexane or toluene. Additionally, about 3% in mass of either polystryrene (PS) or Poly(methyl methacrylate) (PMMA) was frequently added to these diluted solutions in order to later create a protective film embedding the NCs upon deposition onto their substrate.

The dilution factor depends on the initial concentration of precursors during the HI synthesis and on the chosen deposition technique as elaborated in the next paragraph but would usually range from a few hundreds to 10^4 times.

2.2.2 Deposition

The diluted colloidal solutions of NCs are not really handy as such. To perform the spectroscopic characterization of their content they need to be deposited on a substrate. Usually the substrate is a square 5 mm $\times$ 5 mm glass cover-slip of 120 μm thickness that allows a good cryogenic thermalization of the NCs when working at low temperature. It was also empirically observed that the nanocrystals have a tendency to stick to the surface irregularities. When dealing with strongly diluted solutions small grooves can be made with a diamond tip on the surface of the glass cover-slips to attract the NCs during their deposition. This has mainly two benefits: during single object micro photoluminescence measurements the experimentalist just has to follow these grooves to find NCs and secondly the surface "landscape" generated that way would provide a wider range of available orientations of the nanocrystals on the surface. The glass cover-slips were cleaned prior to NCs deposition using soap water and a sonication bath for 10 minutes and again with acetone for another 15 minutes. Two distinct methods are used to deposit the NCs: the spin coating and the drop casting both detailed below.

Spin coating

The glass cover-slip is clamped on a spinning platform. A drop from the colloidal solution is deposited with a micro-pipette on the cover-slip and the rotation is launched. After this process and the evaporation of the solvent, the thickness of the deposited layer will first depend on the properties of the colloidal solution like its viscosity and the nanoparticles concentration and secondly on the programmable spin coater settings: the acceleration and its duration, the maximum constant angular velocity reached and its duration as well.

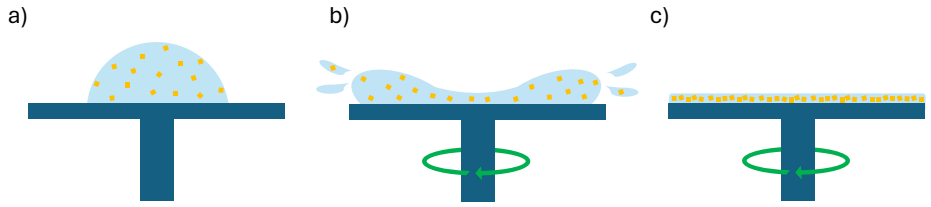

Figure 2.3: Illustration of the spin coating method: **a)** A drop of the colloidal solution is deposited on a glass substrate. **b)** The sample holder starts rotating ejecting most of the solution out of the substrate. **c)**

Drop casting

Here a droplet of the diluted NCs solution is deposited directly on the glass cover-slip with a micro-pipette. The solvent then evaporates leaving either the NCs or a thin film on the surface depending on whether or not the solution contained PS or PMMA.

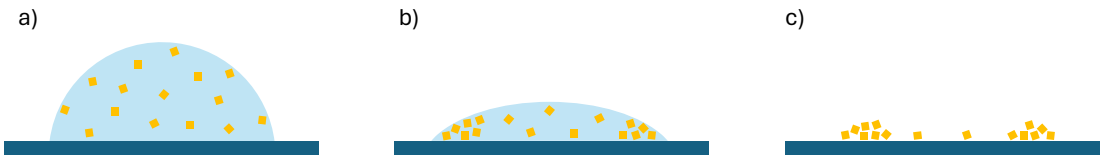

Figure 2.4: Illustration of the drop casting method: **a)** A drop of the colloidal solution is deposited on a glass substrate. **b)** As the solvent starts to evaporate most of the NCs are pushed towards the edges. **c)** When the solvent has completely evaporated a "coffee ring" mark of NCs is left on the substrate.

As depicted on Fig. 2.4 this method has the tendency to leave a circle of higher density of objects on the substrate after the solvent evaporation. This phenomenon called the "coffee ring effect" is due to a capillary flow inside the deposited droplet that pushes the NCs in the center towards the solvent/air interface when the solvent evaporates. Although it can be inconvenient when a homogeneous layer of nanocrystals is desired, for single object spectroscopy, the density gradient of NCs around the ring can actually be useful for progressively reaching single objects left around it. However, if a homogeneous distribution of single NCs is wanted on the surface of

the sample, it was found that the use of a octane/hexane solvent combination (in a 1:20 ratio) could prevent the appearance of the coffee ring effect.

2.3 Optical spectroscopy techniques

Ever since Newton built the first spectroscope by decomposing light through a prism, spectroscopy has played a crucial role in countless discoveries in the fields of physics and chemistry. It is an essential instrument for the comprehension of atomic and molecular mechanisms, chemical structures and, of course, for the understanding of optoelectronic phenomena inside semiconductor materials. In the context of this work one can divide the spectroscopic tools into two classes: the absorption and photoluminescence (PL) techniques. These two methods are often complementary and this section details the experimental setups that were used for both.

2.3.1 Absorption spectroscopy

Absorption spectroscopy consists in measuring the intensity I of light passing through a sample of chromophores, comparing it to the intensity before the sample, I_0, and providing an output of the ratio I/I_0 (called the transmittance) at every wavelength of interest. The absorbance can then be deduced $A = -log(I/I_0)$ and depends, as stated by Beer-Lambert law, on the thickness of the active material, the concentration of chromophores, and the molar extinction coefficient. The technique plays a central role in this work, as it provides basic information about the allowed optical transitions in the material under study, their energies and absolute (or relative) oscillator strength. Contrary to photo-luminescence (PL), absorption measurements inform about the transitions in a system that is not subject to geometrical relaxation and can thus - in general - be directly compared to theoretical predictions as far as excited states are concerned.

These experiments were realized using a UV-Vis-NIR Cary 5000 spectrophotometer from Varian. The device comprises two light sources (Tungsten filament and deuterium arc UV lamps) associated to two detectors (Hammamatsu R928 photomultiplier tube for the 175 to 900 nm range and a - not documented - cooled PbS photocell for the near infrared spectral range) offering, in total, a 175 - 3300 nm wavelength range. Note that, for the work presented in this manuscript, only a limited interval (350 - 700 nm typically) was covered. In this context, great attention was also paid to the detection of any possible contributions from the glass or quartz substrate response below 400 nm. This work thus took advantage of a high performance spectrophotometer with a limiting resolution of less than 0.05 nm in the UV-visible range as well as a wavelength reproducibility of less than 0.025 nm. These specifications were well beyond the challenges raised by the materials, even at low temperature.

Two types of experiments could be performed using this instrument. The first kind were absorbance measurements on cuvettes of colloidal NCs solutions at room temperature. The second kind of experiments could be done from room to cryogenic temperature *i.e.* 300 K to 10 K. Here a Helium gas cryostat was installed inside the Cary 5000 measurement chamber. The cold finger (placed in line 1) had two samples holders: one for the NCs sample itself and the other for the bare substrate. An uncoated piece of substrate was then placed in the sample holder of the second measurement line to cancel its contribution to the measured signal (sample *vs* bare substrate configuration). The substrate - substrate configuration provides a correction curve that additionally allows to compensate - in part - for the instrument response and that is therefore subtracted to the absorption curve (obtained from the sample - substrate configuration).

2.3.2 Photoluminescence spectroscopy

Upon photoexcitation of electrons within a semiconductor material, relaxation can occur through radiative or nonradiative mechanisms. Photoluminescence (PL) spectroscopy is an experimental technique designed to collect and analyze the emitted light after its decomposition through a dispersive element such as a diffraction grating. While this technique primarily measures the light emitted after radiative relaxation, insights into non-radiative processes can be gathered by looking at the dynamics of the emitted light, as discussed in the following.

The experimental set up used in this work is illustrated in Fig. 2.5 and can be segmented into three principal sectors: the excitation laser sources, the confocal microscope, and the detection equipment.

Excitation

For any radiative recombination to actually happen the energy of the laser sources must exceed that of the different optical transitions of NCs that are investigated. While no resonance experiments were carried out in this work, it is still generally desirable to be as close as possible to the targeted optical transitions in order to prevent the photo-excitation to undesired higher energy levels and minimize the focal shift potentially induced by axial chromatic aberrations in the confocal optics. Hence, three different laser sources were used in this work.

The first was a Thorlabs DJ532 solid-state laser emitting a 532 nm continuous wave. This laser is mounted on a Thorlabs TCLDM9 connected to a temperature (for stabilization) and output power controller. Due to its continuous operation the risk of high peak power pulses that could damage the NCs is reduced. The emission wavelength centered at 532 nm makes it also highly visible to the human eye enabling safe and easier pre-alignment of the optical setup at a relatively low power before moving on to the other higher energy and power laser sources.

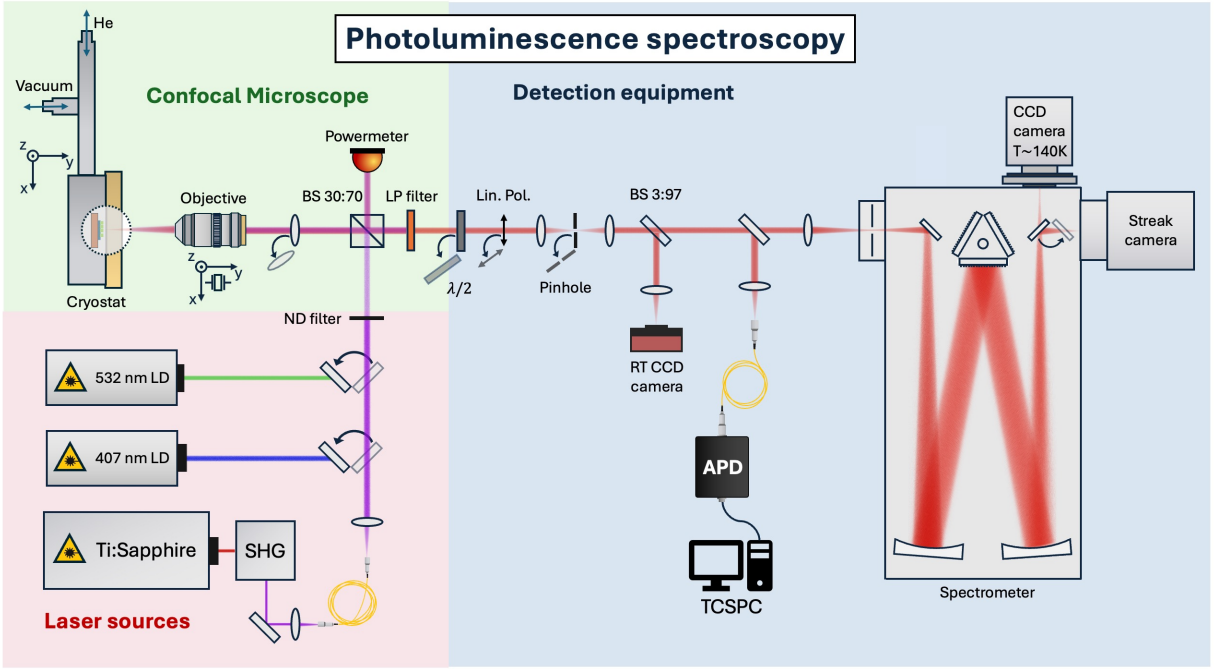

Figure 2.5: Illustration of the PL spectroscopy set up used in this work. Three distinct regions are represented: The excitation area (red background) comprising the different laser sources used in this work. The confocal microscope (green background area) with the beam splitter, the microscope objective and the cryostat. The detection set up (blue background) with the CCD camera, the TCSPC and APD module, the spectrometer and the streak camera. Note that the curved arrows illustrate the possible movement of their associated optical elements.

Time-resolved PL measurements require a pulsed laser source capable of producing short bursts of laser emission to excite the studied materials followed by an off period long enough to let the material relax radiatively. For such applications, a Ti:Sapphire laser (Tsunami, Spectra Physics) is well suited. This laser generates picosecond light pulses at an 82 MHz repetition rate through active mode locking achieved with an acousto-optic modulator placed within its cavity. The emission wavelength can be tuned from 700 nm to 1000 nm using a birefringent filter, and second harmonic generation can be achieved with a BBO crystal giving access to the 350 to 500 nm wavelength span. The Ti:Sapphire laser beam is then coupled to a single mode optical fiber redirected to the experiment table.

The high repetition rate of the Ti:Sapphire laser results in 12 ns intervals between pulses, which may be limiting when studying emitter dynamics of longer timescales. Consequently, a pulsed PICOPOWER 405 nm laser diode from Alphalas was also used. The pulse duration is set around 70 ps and the repetition rate is tunable from 1 Hz to 40 MHz.

Finally, for all three laser sources, different systems of converging lenses and pinholes (or the optic fiber extremity acting as a point source for the Ti:Sapphire) allow the recovery of spatially filtered and collimated laser beams with diameters equivalent to that of the entrance pupil of the

microscope objective. Some neutral density filters are also regularly inserted along the optical paths to adjust the laser power reaching the samples.

Confocal microscope

The second part of the set up (green area of Fig. 2.5) can be thought of as a confocal optical microscope working in the reflection configuration *i.e.* a microscope that has the ability to provide images with a weak depth of field or equivalently that allows to collect selectively light coming from a thin "slice" (section) of the sample. Its first element is a 70:30 beam splitter cube from Thorlabs that allows light to pass in one direction and reflects it towards the detection systems in the other direction while preserving the polarization properties of the light passing through. Right after the beam splitter a microscope objective is used to focus the excitation beam on the sample and collect the PL emission. A modified PAL-100-NIR-LC15 from Optosigma specifically designed to work through the 1.5 mm of the cryostat glass window is used. It has a focal length $f = 2$ mm (N.A $= 0.53$) and a spot size diameter (assuming an incident 550 nm Gaussian laser beam) of 1 μm. This objective also features a rather good transmission in the UV and is infinity corrected, a prerequisite for its use in an afocal microscopy configuration. The objective is mounted on a stack of three piezo-electric actuators (P-611.3 NanoCube from PI) enabling 120 μm range of movement along the three spatial directions with a sub-micrometer resolution.

The collimated PL light is focused on the spectrometer entrance slit using an achromatic lens whose focal length is adapted to the spectrometer aperture ($f/9.7$) in order to guarantee an optimal spectral resolution in the experiments. In this configuration the sample plane and the spectrometer slit plane are conjugated planes. The slit itself acts as an efficient spatial filter avoiding to resort to an additional pinhole - lenses combination along the beam path (see Fig. 2.6)

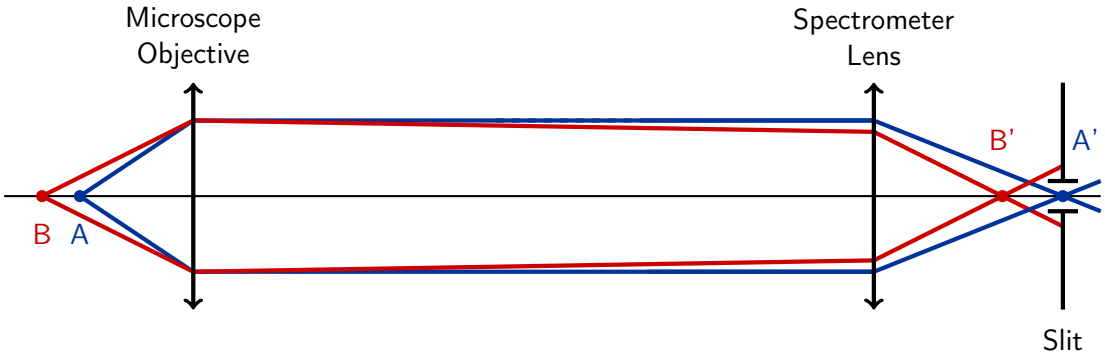

Figure 2.6: Illustration of the focal configuration used in the single object experiments. The spectrometer slit acts as an efficient spatial filter that rejects light that does not come from the emitting NC plane (point A). Here, A', the image of A forms between the slits of the spectrometer while the light from B is imaged in B' and only a small fraction of it passes through the slits.

Most of the photoluminescence (PL) measurements are conducted at cryogenic temperatures

to avoid the thermal broadening of the emission linewidths. To help with this, a MicrostatHiRes cryostat manufactured by Oxford Instruments is positioned so that the samples are located at the focal distance of the objective. This sophisticated instrument comprises a copper cold finger onto which the glass coverslips coated with nanocrystals (NCs) are fixed using a silver lacquer, ensuring optimal thermalization of the samples. The back of the cold finger is in thermal contact with a liquid helium circulation system, enabling the samples to reach a temperature as low as 7 K. Furthermore, temperature adjustments spanning from 7 K to 300 K are done thanks to a heating resistor connected to a control unit, providing precise temperature control throughout the experiments. The cold finger is also designed so that in-plane deformations are minimized when temperature is varied, allowing to keep the object of interest under focus throughout the experiments. In general, corrections in the objective position are required along the optical axis direction and are well known and controlled so that efficient light collection and collimation are achieved at any temperature.

Detection

The detection instruments within the micro-PL spectroscopy setup (blue region of Fig. 2.5) offer flexibility for conducting both time-resolved and classical spectral analyses. They allow studies on samples of varying concentrations, from NCs ensembles to individual objects.

At the core of this setup is the ACTON SP2750 spectrometer from Roper Scientific-Princeton Instruments, that ensures the spectral decomposition of the incoming PL. It features a turret containing three gratings (300, 600, and 1200 gr/mm) and has a focal length of 750 mm. This instrument images the dispersed light either on the sensor of a SPEC10 CCD camera cooled to 140 K with liquid nitrogen or on the entrance slit of a streak camera for time-resolved experiments. The pixel sizes of the CCD detector, the opening of the spectrometer entrance slits and the selected grating give an overall 100 μeV spectral resolution around 450 nm (working with the 1200 gr/mm grating). This resolution proves sufficient for the observation of exciton fine structure lines whose separations are found lower than 1 meV as discussed in the subsequent Chapters.

Regarding spectroscopy measurements on samples of low NCs density a Thorlabs CMOS camera (LP126MU - Kiralux) is used to capture images of the photoluminescence and track the areas susceptible to contain single objects. When used alongside the spectrometer, a glass slab is placed in the detection path to reflect 3 % of the incident power towards the CMOS camera. A system of lenses encompassing a 100 μm pinhole mounted on a flipping holder additionally allows - if necessary - the selection of the emission from a single object as illustrated in Fig. 2.7. Note that in most of our experiments the confocal effect due to the spectrometer slit was found enough

to be able to isolate the PL emission of a single NC.

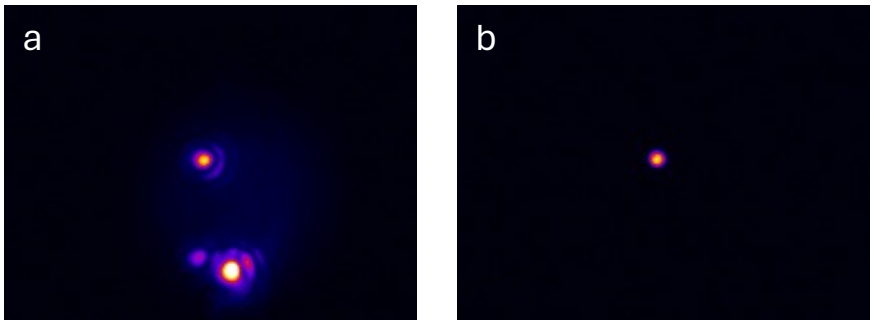

Figure 2.7: Images of the PL from single NCs. Image **b.** shows the PL of the central object of image **a.** after its selection through the pinhole.

Another system extensively used during single object spectroscopy is a motorized half wave plate combined to a linear polarizer whose transmission axis is aligned with the grating of the spectrometer. It is interesting to check whether or not the emitted PL from NCs has a linear polarization. For example, as mentioned in Chapter 1 the exciton fine structure of single LHP NCs is composed of bright states expected to emit linearly polarized light after recombination. To verify this experimentally the angle θ between the half wave plate and the polarizer is varied by a step by step rotation of the motorized waveplate ($\lambda/2$). At each position the incoming linearly polarized PL makes an angle β with the passing axis of the polarizer. Thus the intensity after projection on this axis is written $I = E_0^2 cos^2(\beta - 2\theta)$ and the intensity maxima will be reached for $\theta = \beta/2 + n\pi$. Taking a spectrum for each value of θ we can then verify if the PL intensity follows the relation given above for a linear polarization by plotting the PL intensity variation with 2θ as shown on Fig. 2.8.

Time-resolved PL (TRPL) spectroscopy was also used throughout this work as an important tool to characterize the photogenerated states. The emission dynamics of fluorescent species over time provides an insight into processes such as carrier recombination and energy transfer within nanocrystals. The processes under focus typically occur on the tens of picosecond to tens of nanoseconds timescale, sometimes with an extremely low number of emitted photons. Therefore, detectors with excellent sensitivity and very fast processing electronics are necessary.

A streak camera (C5680 from Hamamatsu) enables the study of emission dynamics in systems with relaxation time scales ranging from a few tens of picoseconds to ~1 ns. It receives the dispersed light from the spectrometer as an input and produces three-dimensional output images in which the luminescence intensity is observed as a function of wavelength and time (see Fig. 2.9). Its operating principle is based on the conversion of incident photons into photo-electrons using a photocathode. The photo-electrons undergo acceleration by an electric field, followed by deflection through the application of a high voltage (*i.e.* another field) perpendicular

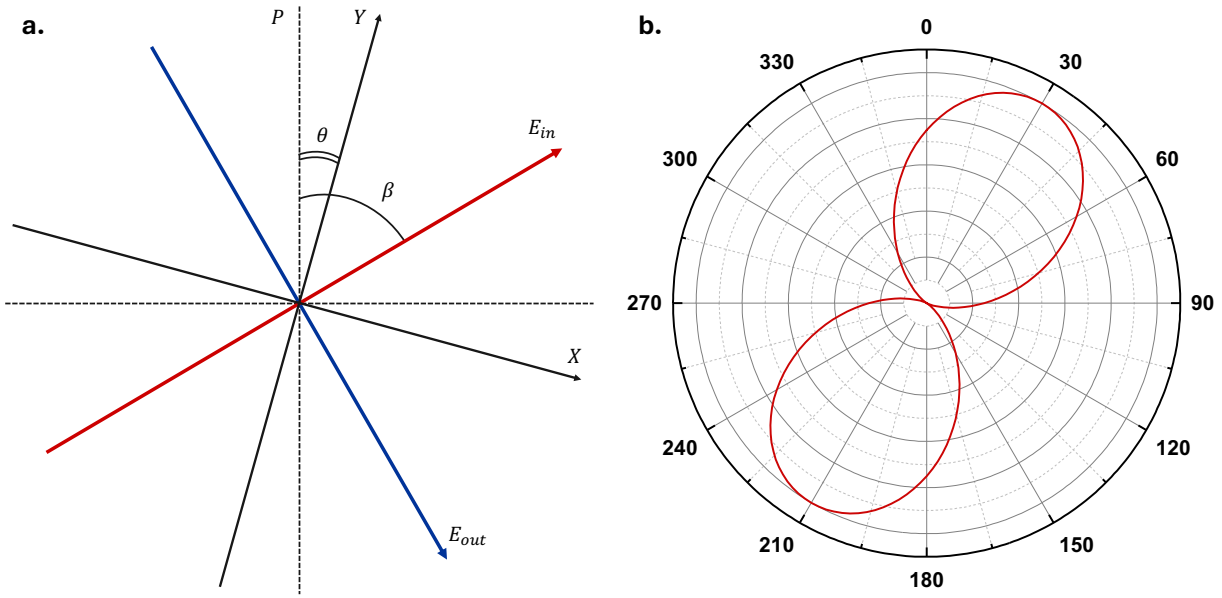

Figure 2.8: a. Angles involved in the polarisation analysis of NCs emission. For an initial PL emission E_{in} linearly polarized and making an angle β with the polarizer P the angle with the polarizer after the half-wave plate is $(\beta - 2\theta)$ with θ being the angle between the polarizer and the plate axis Y. **b.** Polar diagram showing the theoretical intensity behavior of linearly polarized PL passing through the half-wave plate and polarizer system as a function of 2θ. Note that for this simple case the emitting dipole lies in the plan perpendicular to the optical axis.

to the accelerating field. The deflection voltage is synchronized with the incoming light pulses (the synchronization signal being provided by a fast photodiode receiving a fraction of the pulsed laser beam). Depending on their arrival time in the chamber, the electrons are thus more or less deflected by the amplitude of the high voltage, which allows to convert their time of arrival into spatial information. After the chamber a micro-channel plate (MCP) essentially acts as a gain amplifier for the photo-electrons which are then projected onto a phosphorescent screen that will emit photons at each point of impact. The vertical axis of this screen then represents the time of arrival (after proper instrument calibration) and the horizontal axis the wavelength of the incident photons. The emitted photons from the screen are then captured by a CCD camera, which finally transmits the data to a computer. With the 2 ns caliber, the temporal resolution of the instrument is approximately 15 ps, but can be significantly degraded by laser instabilities that result in a dispersion of trigger times for each acquisition (referred to as "jitter"). Therefore, resolutions of 20-25 ps are more realistic under operating conditions (in particular for acquisitions requiring averaging over a large number of frames).

For PL decays longer than the 2 ns time window of the streak camera, another type of in-

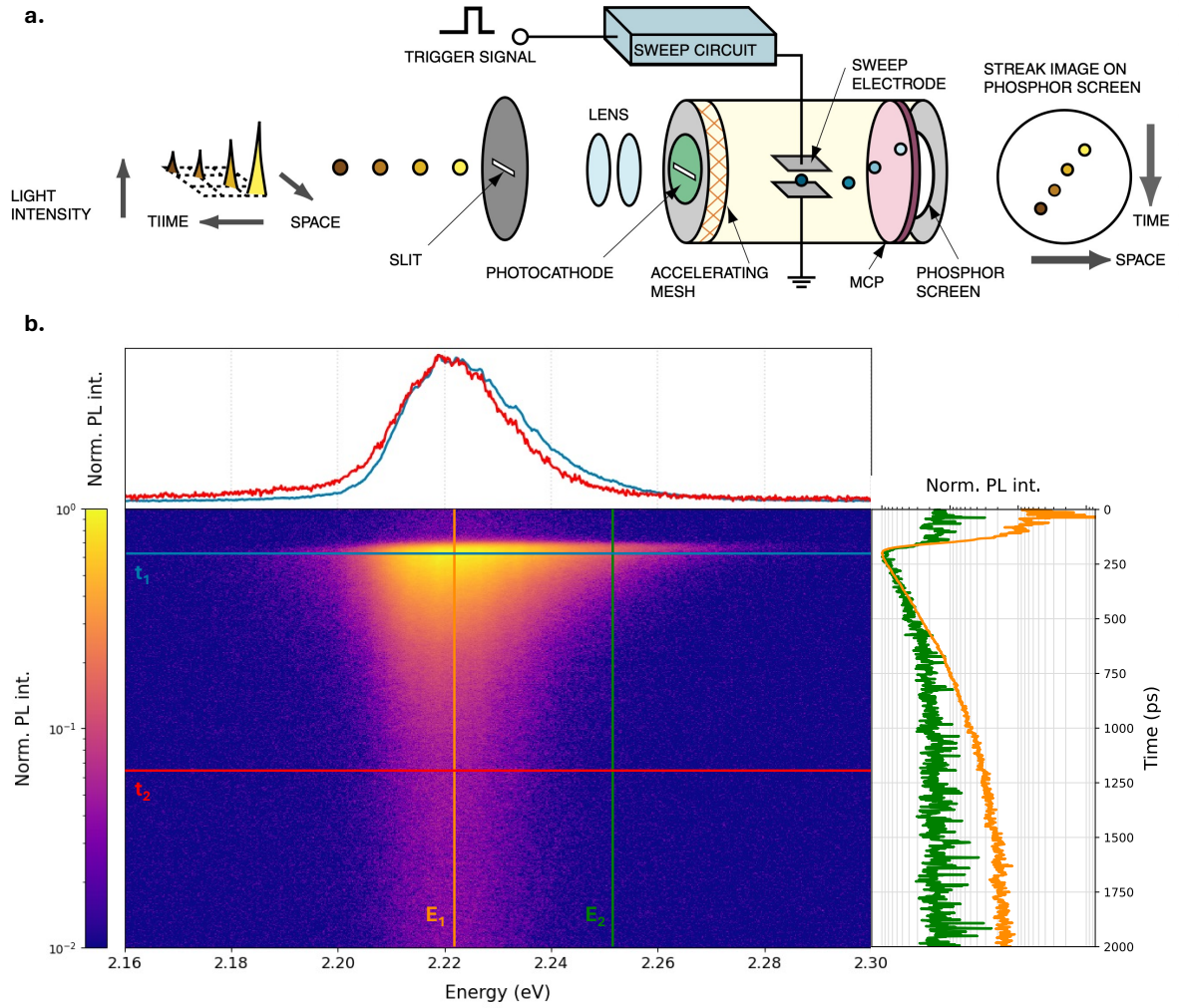

Figure 2.9: a. Illustration depicting the working principle of the streak camera. Adapted from [147]. **b.** Example of an image captured with the streak camera displaying the normalized PL intensity variations with time and emission wavelength for a sample of $FAPbI_3$. The PL spectra presented on top represent the normalized sum of the PL intensity over 50 ps around the time t_1 and t_2 while the PL decays, presented on the right side, are summed over 10 meV around the energies E_1 and E_2.

strument has to be used. A good solution can be found using a time correlated single photon counter (TCSPC), like the Time-harp 260 from PicoQuant, coupled to an avalanche photodiode (APD) (from MPD). During these counting experiments, the Time-harp module first needs a "clock" to tell it when to start and stop counting. This start/stop triggering is done using the pulses of the laser source by connecting it either to the 405 nm laser diode controller or if we use the Ti:Sapphire pulsed laser to the periodic signal generated by the aforementioned photodiode. Once a counting experiment has started the APD detects the single photons from PL emission and sends a signal to the TCSPC module that will measure the time difference between the start of the experiment and the arrival of the photon. By repeating the experiment numerous times, this setup enables the construction of an histogram of photon arrival times (see Fig. 2.10). This

provides access to the profile of the temporal decay of photoluminescent emission. Rigorous analysis of these decays requires a thorough understanding of the response function (*i.e.* the impulse response) of the counter used. Thus, during our decay measurements, the actual recorded signal is the convolution product between the response function (referred to as IRF hereafter) and the absolute optical response of the emitter system. When the relaxation constant of the emission is of the same order as the constant characterizing the IRF, the consideration of the IRF becomes particularly critical.

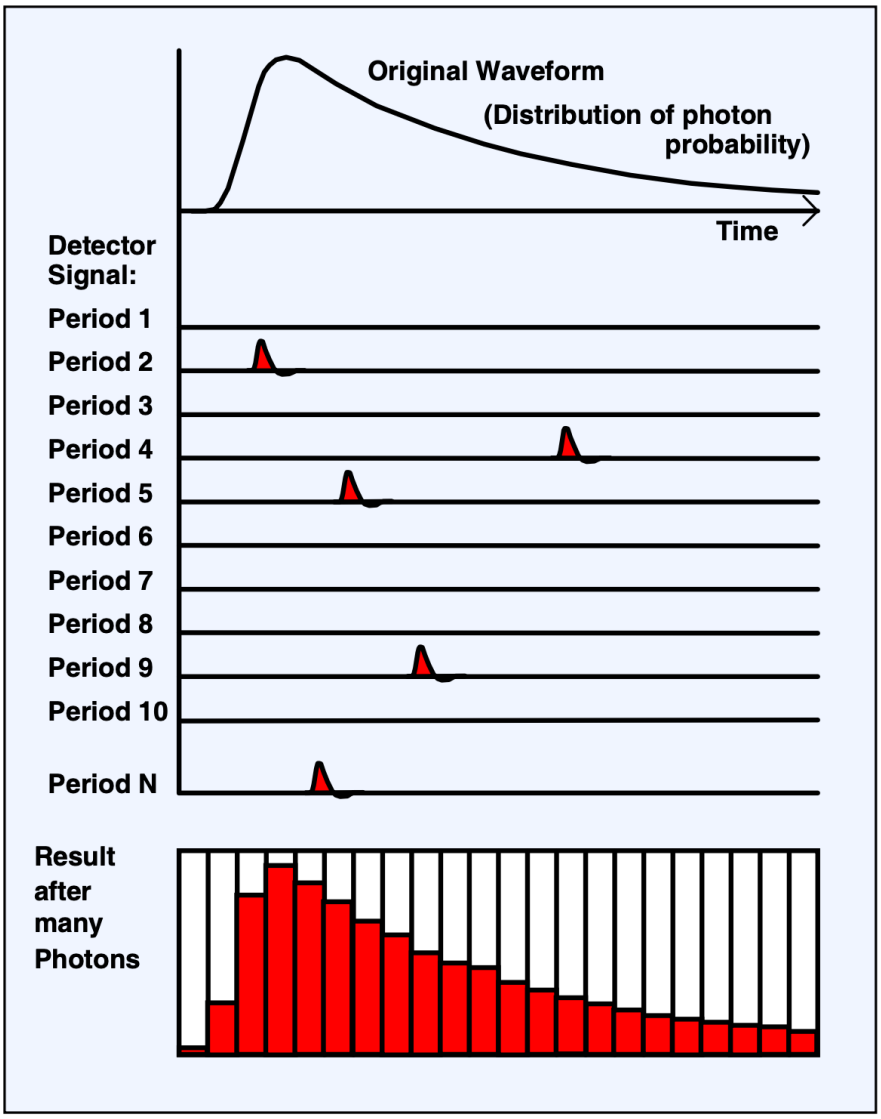

Figure 2.10: Illustration depicting the working principle of the TCSPC experiments, adapted from [148]. Photons arrival times are measured over N periods (*i.e.* after N laser pulses) and an histogram is built by summing all of the photon arrival times.

Finally, in order to maintain single photon statistics (and "correct" building of the arrival time histograms) only one in 20 to 100 excitation pulses should generate a count at the detector [148]

otherwise distortions of the dynamics occur, an effect known as "pile up". It was thus carefully verified that the average rate (at the detector) did not exceed 1 % to 5 % of the excitation rate and most of the experiments were performed with a ratio close to 1 % or slightly less.

Conclusion

In this chapter, the colloidal synthesis of LHP NCs and the experimental tools and spectroscopic techniques used for the study of their optical properties were described. The absorption spectrocopy, ensemble PL and TEM equipment allow one to unveil some structural properties of the NCs. The confocal microscopy system, which can operate at a temperature of 7 K, allows for the investigation of the photoluminescence properties of the band-edge exciton fine structure. In particular, correlations between the structural aspects and the optical properties of single objects can be achieved. Finally, the combination of a Streak camera and a time correlated single-photon counter offers the opportunity to perform in-depth time resolved studies of the PL emission by revealing the dynamics of the excited-state populations. The study of the PL intensity decays as a function of temperature was found essential to track the energy position of non-emitting states, as detailed in the next chapters.

CHAPTER

OPTICAL PROPERTIES OF $CsPbCl_3$ NANOCRYSTALS 3

Within the metal halide perovskite (MHP) family, the chloride compound $CsPbCl_3$ stands out and possesses the widest energy band gap, resulting in light absorption and emission on the UV edge of the visible spectrum for the most confined nanocrystals [149, 150]. The band-edge exciton, which is central to the material optoelectronic properties, is characterized by the strongest electron-hole Coulomb interaction, resulting in a small Bohr radius and the largest binding energy among all MHPs [149, 151, 152]. While quantum confinement and halide selection have proven to be an efficient way to tune the emission response of MHPs [17] numerous studies have demonstrated further control over the optical and magnetic properties of $CsPbCl_3$ through doping of transition metal ions [153]. Indeed, the substitution of Pb^{2+} ions by Mn^{2+} ions results in an additional emission band in the red spectral region and alters the magnetic properties of $CsPbCl_3$ [154]. Moreover, it plays an important role in improving the efficiency and the stability of photovoltaic devices by converting absorbed UV light into visible red light. [155]. It has also been demonstrated that rare earth ion doping of NCs could further expand the emission capabilities: implementation of electroluminescent white light emitting devices could be achieved thanks to Sm^{3+} doping [156], whereas near-infrared emission was obtained by incorporation of Yb^{3+} ions [154, 157].

Undoped $CsPbCl_3$ nanocrystals (NCs) still suffer from rather low 5-10% photoluminescence quantum yields (PLQY), generally attributed to surface vacancies of Chloride ions that generate trap states deep into their band gap [89, 158, 159, 160]. However, recent studies have shown that this intrinsic 'flaw' is avoidable and that the PLQY can be enhanced through simple adjustments

during or after the colloidal syntheses [161, 162, 19, 163].

Thus the remarkable properties of $CsPbCl_3$ have a great potential for the development of optoelectronic devices such as UV or white LEDs, photodetectors and scintillators [164, 165, 166]. Yet, more sophisticated applications towards photonics and quantum technologies either based on the fine control of the excited states energy tranfers or the coupling to resonators and nanoguides [167] will require a full understanding of the emission properties of this material and, in particular, a complete description of the band edge exciton and its fine structure which is still lacking for this LHP compound.

This Chapter aims at responding to this issue and presents a comprehensive study of the optical properties associated with undoped $CsPbCl_3$ nanocubes, both as dense ensembles and individual emitters. The micro-PL spectroscopy measurements performed clearly identify single NC emission patterns and indicate that the exciton fine structure (EFS) bright-state splitting amplitudes are - as expected due to enhanced Coulombic effects - among the largest within MHP-NCs of comparable average size. The experimental results are thoroughly correlated to EFS calculations based on the e-h EI and crystal field model in crystals of tetragonal symmetry (D_{4h} point group) and takes explicitly into account the large dielectric mismatch between the object and its environment as well as the actual NC cuboid shape. Considering shape anisotropy as an independent significant parameter, the model is refined by applying NC deformations in the simulations and provides an explanation for the large dispersity of bright states splitting energies observed in this compound.

3.1 Characterisation of $CsPbCl_3$ nanocrystals

As highlighted in Chap. 1, quantum confinement has profound effects on the optoelectronic properties of MHPs while NCs distortions or any departures from isotropic symmetries will impact the band edge exciton and the energy separation of its fine structure levels. Therefore, providing a good interpretation of single object optical spectroscopy measurements will rely on the precise knowledge of the crystal structure, the general morphology, the level of shape anisotropy and the ensemble optoelectronic properties of these perovskite NCs.

3.1.1 Crystal structure

Following the synthesis of NCs, transmission electron microscopy (TEM) images can be extremely effective to confirm the presence of the expected material in the colloidal solution and potentially determine its crystal phase. The left side of Fig. 3.1 shows an example of such an image, obtained after deposition of a solution containing a high concentration of the synthesized material on a TEM copper grid.

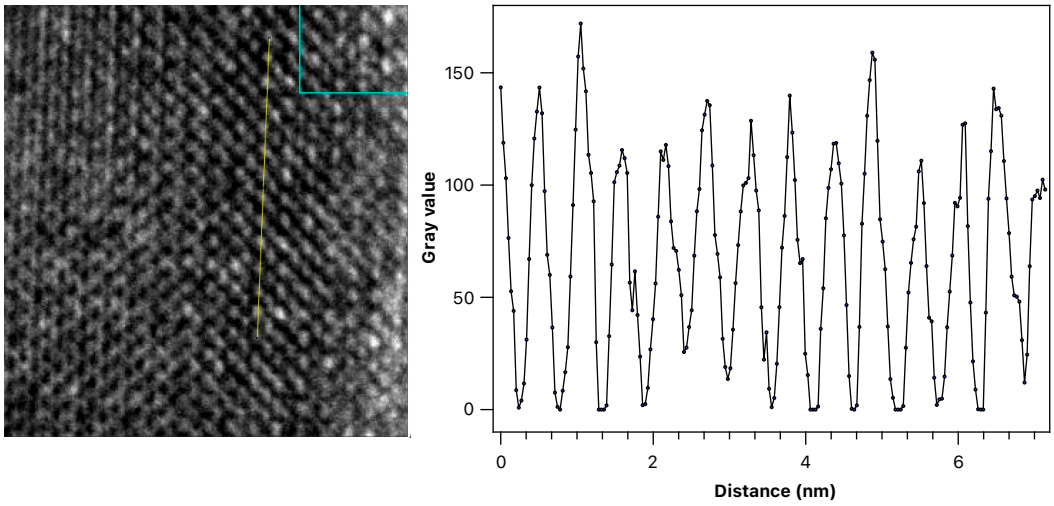

Figure 3.1: Left: Bright field TEM image of a $CsPbCl_3$ nanocube. Right: Intensity profile of the yellow line drawn on the left hand side image.

In this image, one can observe raws of individual atoms on the surface of a single NC. The yellow line traced across the image corresponds to the intensity profile depicted on the right side of Fig. 3.1. Regular maxima of intensity are seen and by measuring the spacing over 13 maxima, an average distance of 0.55 ± 0.02 nm is obtained, consistent with lattice parameter measurements in the cubic crystal phase of $CsPbCl_3$ NCs reported by [26, 168, 169] at ~ 0.56 nm. Chap. 1 discussed the existence of three different crystal phases in LHP NCs depending on the temperature: Cubic O_h, Tetragonal D_{4h} and Orthorhombic D_{2h}, observed respectively at $T > 47°C$; $37°C < T < 47°C$ and $T < 37°C$ in bulk $CsPbCl_3$ [170, 171]. Unfortunately the TEM resolution does not allow to distinguish between these phases and, more importantly, the images were captured at room temperature while most of the spectroscopic measurements detailed in the following sections of this Chapter were performed at cryogenic temperatures.

Another approach commonly used to determine the crystal symmetry of a compound is X-ray diffraction (XRD). Although a lot of such experiments were done at room temperature, for $CsPbCl_3$ very few studies have been performed at low temperature and only bring partial information. The issue of identifying the crystal structure and correlating it to the optical response will be more extensively discussed when inspecting the micro-PL spectra measured on single NCs.

3.1.2 Morphology of $CsPbCl_3$ NCs

To facilitate our understanding of the optical spectroscopy measurements conducted on lead chloride perovskite NCs, a comprehensive analysis of their sizes and shapes was performed using transmission electron microscopy (TEM). Examples of the resulting images are depicted on Fig. 3.2.

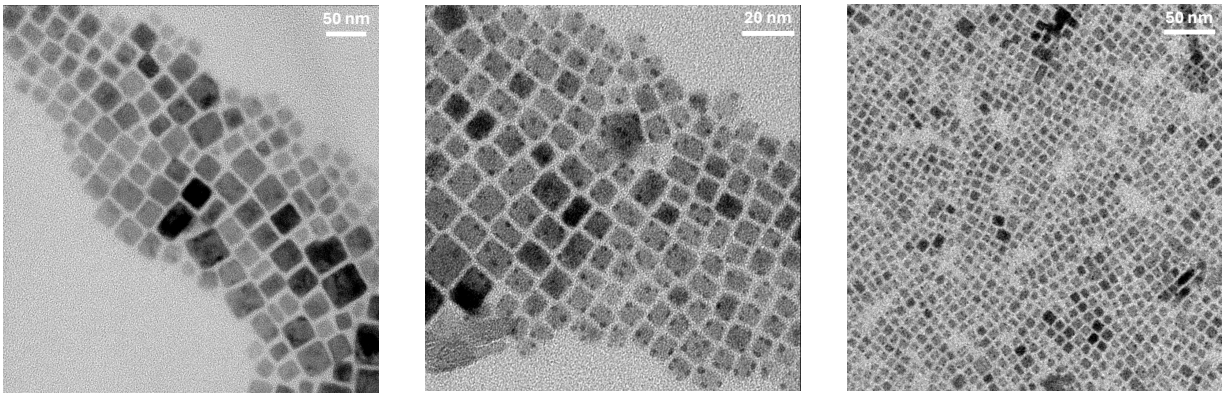

Figure 3.2: Bright field TEM images of $CsPbCl_3$ nanocubes taken at three different locations and magnifications. Dark dots can be seen on the central image and are attributed to the reduction of Pb^{2+} ions to Pb^0 by the electron beam. This reduction is followed by the diffusion of Pb atoms, resulting in the formation of metallic aggregates that appear darker in TEM images [172].

The resolution achieved in these images allows for the differentiation and measurement of the two dimensions lying parallel to the surface. On the left side of Fig. 3.3, a 2D size distribution histogram was constructed based on the lateral dimensions of approximately 500 NCs, with the longer dimension denoted as L_1 and the shorter one as L_2. This histogram reveals that the most prevalent classes of sizes correspond to lateral dimensions L_1 and L_2 being approximately of the same magnitude, with an average value of $L_i \approx 8.0 \pm 0.5$ nm.

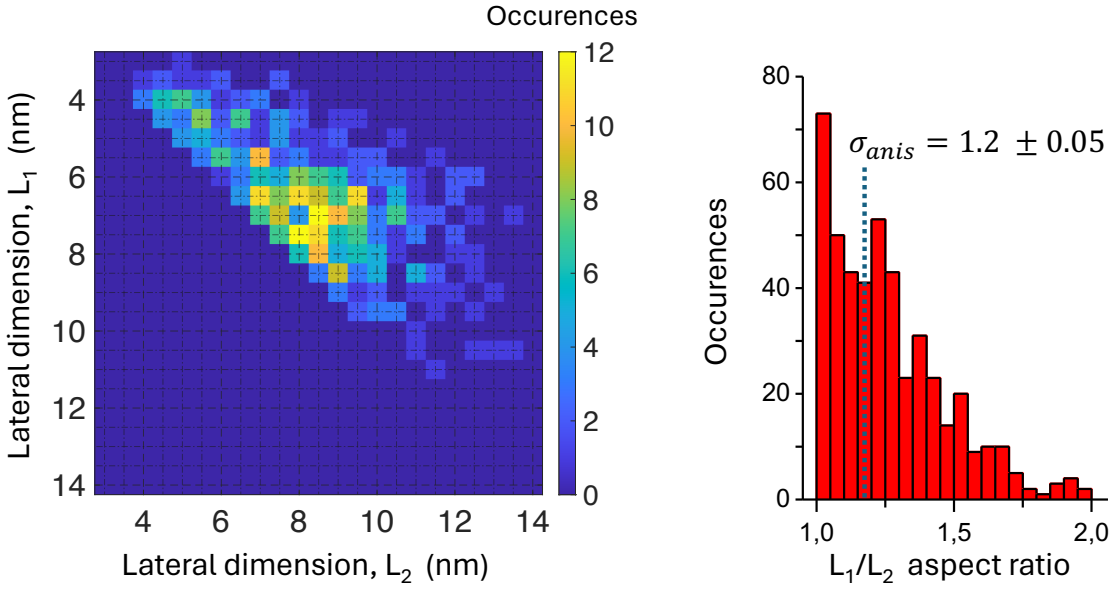

Figure 3.3: Lateral lengths distribution of $CsPbCl_3$ nanocubes. Left: 2D histogram of the lateral sizes distribution (L_1 and L_2, $L_1 \geq L_2$) of the observed NCs. Right: Histogram of the L_1/L_2 ratio distribution, with standard deviation σ_{anis}.

Although the TEM images do not provide a direct insight into the third dimension of the NCs, it can reasonably be assumed that it aligns with the average length of the other two dimensions. This assumption stems from the fact that the hot injection synthesis method employed was not adjusted to produce highly anisotropic forms such as nanoplatelets (see Sec. 2.1.2). Consequently, the majority of the NCs can be categorized as possessing either a cubic morphology or a closely resembling one. Beyond that, one can see that a large proportion of the NC population belongs to classes out of the $L_1 = L_2$ line, highlighting a significant degree of shape anisotropy. The right side of Fig. 3.3 presents a histogram of the length ratio L_1/L_2, and offers a preliminary but relevant estimation of the shape anisotropy magnitude of the NCs. Here, the standard deviation, denoted as σ_{anis}, is found to be approximately 1.2 ± 0.05 and constitutes a characteristic anisotropy parameter that will be taken into account to some extent during the analysis of the micro-PL results discussed in the subsequent sections. In fact, since L_1 and L_2 are not associated to any particular lateral dimensions of the nanocrystals (*i.e.* for each object $L_{1,2} = L_x$, L_y, L_z) the anisotropy factor range that should be considered lies between $\sigma_{anis}^{-1} - \sigma_{anis}$ *i.e.* within the [0.8 , 1.2] interval.

3.1.3 Optical properties of nanocrystal ensembles

Now that the morphology of the $CsPbCl_3$ nanocubes has been established, consistency with the ensemble optical responses can be verified. Optical absorption measurements were carried out for different temperatures ranging from 300 K to 10 K, and the resulting spectra are presented on the left side of Fig. 3.4. These spectra are representative of lightly diluted $CsPbCl_3$ NCs phases, prepared on thin glass substrates using the drop-casting method described in Chap. 2. Several absorption peaks are evidenced, and their energy position as a function of temperature is plotted on the graph located on the right side. In perovskite materials and NCs the bandgap energy is governed by the Pb s to the halide p covalent antibonding interaction, which translates into a blue shift of the transitions with increasing temperature [173].

Here all the resonances obey the usual Varshni relation $E_X(T) = E_0 - (\alpha T^2)/(\beta + T)$ [174] where E_0 is the exciton transition energy at $T = 0$ K, and α, β are empirical constants of the model. Initially the model was built to reproduce the usual shift observed on band to band transitions in semiconductors. Writing $\Delta E_g(T) = E_X(T) - E_0$, this energy gap change is believed to arise from two different temperature dependent mechanisms:

- A dilatation of the lattice that was shown to lead to a linear variation of ΔE_g with T at high temperature.
- An electron-lattice interaction for which theoretical treatments show that ΔE_g scales differently whether T is lower or higher than the Debye temperature T_θ with $\Delta E_g \propto T$ if $T \gg T_\theta$

and $\Delta E_g \propto T^2$ if $T \ll T_\theta$.

Hence the Varshni formula manages to operate a phenomenological unification of the main influences governing the behavior of band to band transitions in temperature. For $CsPbCl_3$ a linear behavior is observed, due to a low β temperature ($\approx$ 10 K). The parameter α is found around 300 μeV/K. The monotonous behavior of all the transition energies is indicative of the absence of phase transition over the considered temperature range. Furthermore, both parameter values are characteristic of perovskite materials [120]. All of this indicates that the electronic transitions are intrinsic to the semiconductor lattice and do not originate from impurities or synthesis by-products.

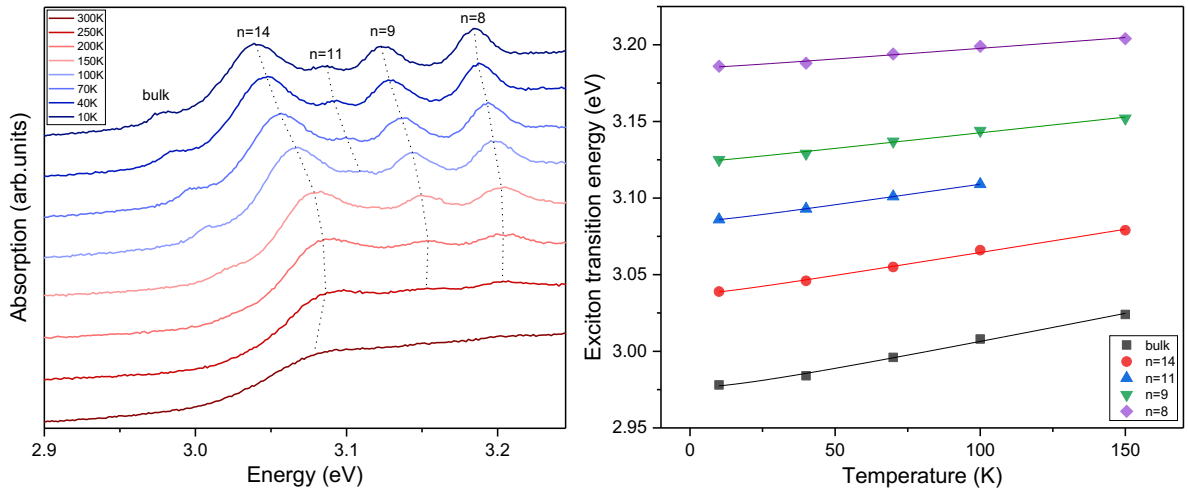

Figure 3.4: Left side: Absorption spectra of a $CsPbCl_3$ nanocubes ensembles taken at temperatures ranging from 300 to 10 K. The closest number of monolayer matching their energy at 10 K is provided according to the simulations presented in Fig. 3.5. Right side: The energy of each absorption transition is followed with temperature. The experimental points are fitted with a Varshni law presented in the text.

These absorption peaks most likely correspond to different population sizes of NCs. To confirm this hypothesis, numerical simulations were conducted and their results are reported on Fig. 3.5. These simulations predict the exciton transition energy as a function of the NC size under various regimes of quantum confinement and dielectric confinement applied to cubic shaped NCs. In this figure, the red curve was derived using Eq. 1.23 for a strong confinement regime, while the green curve gives the results for a weak quantum confinement applied to the exciton, as determined by Eq. 1.21. As already mentioned in Chap. 1 the case of the intermediate quantum confinement regime is more challenging due to the absence of analytical solution. Therefore, a variational calculation was performed to determine the exciton energy in this regime as represented by the set of blue curves. Given the average size of the $CsPbCl_3$ NCs studied in this work - $\langle L \rangle \approx 8$ nm - the ratio $\langle L \rangle / a_X = 4.7$ justifies the use of the intermediate confinement regime in the following.

This regime was also preferred by other authors for NCs of similar sizes [55].

Additionally, three distinct dielectric environments were tested by changing the value of the dielectric contrast parameter defined as $\eta = (\epsilon_1 - \epsilon_2)/(\epsilon_1 + \epsilon_2)$ where ϵ_1, ϵ_2 are the dielectric permittivity inside and outside the nanocrystal respectively. In $CsPbCl_3$ Ghribi *et al.* [175] found $\epsilon_1 = 6.56$ while $\epsilon_2 = 6.6$, 2 and 1 were considered to simulate dielectric environments made of other $CsPbCl_3$ NCs, organic ligands and air respectively.

The transition energies measured from the absorption spectrum at $T = 10$ K were also included in this graph, along with the corresponding number of monolayers (taking a lattice parameter $a = 0.56$ nm [176]) that best matches the observed transitions. At this point, there is clearly an overall agreement between the spectral range expected to be of importance given the spectroscopic data (around 3 eV) and the energy range associated to transitions of NCs of sizes revealed by the histogram of Fig. 3.3.

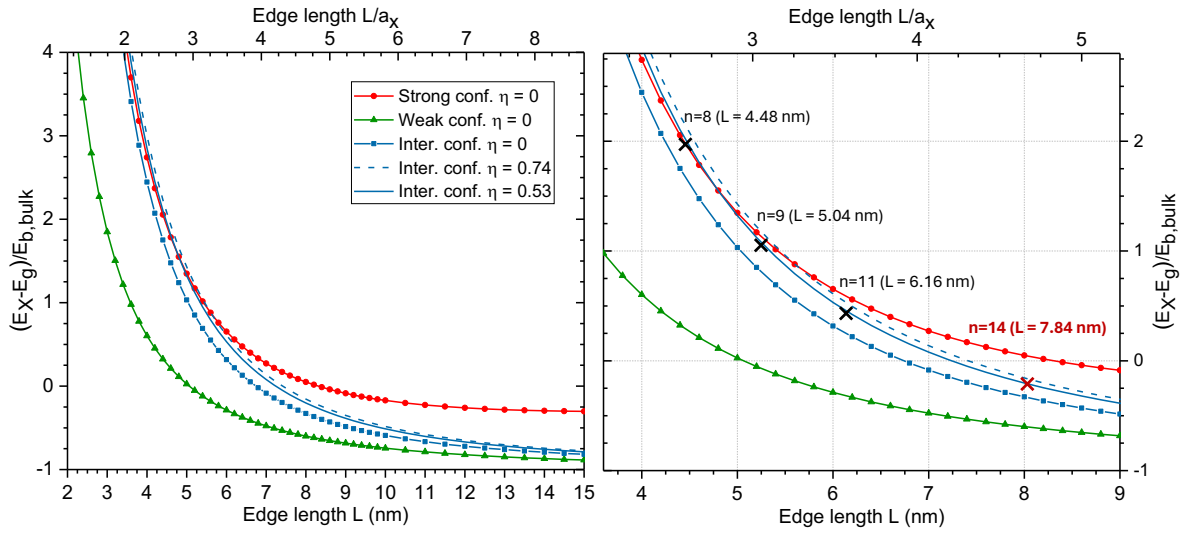

Figure 3.5: Simulated exciton transition energy, $E_X - E_g$ (in units of the bulk exciton binding energy, $E_{b,bulk}$), as a function of the absolute edge length, L (and L/a_X parameter), in cubic-shaped $CsPbCl_3$ NCs. Red and green lines are simulations in the strong and weak confinement limits respectively while the blue lines are the variational calculations results for an intermediate quantum confinement with three different dielectric environments. Note that the resonances observed on Figure 3.4 are represented by the black and red "X" markers and that the associated closest number of elementary cells, n, alongside the corresponding absolute NC size L are also displayed.

Focusing now on the band edge, Fig. 3.6 presents a comparison between the absorption (blue line) and photoluminescence (red line) spectra, both measured on $CsPbCl_3$ NCs ensembles at $T = 10$ K. The band edge absorption is dominated by a strong peak, X_0, centered at 3.041 eV, while a weaker intensity peak, X_1, is detected at higher energy ($X_1 \approx 3.086$ eV) and a satellite, X_b, is identified at lower energy ($X_b \approx 2.98$ eV). Considering objects with an average edge length $\langle L \rangle = 8.0$ nm and $\epsilon_2 = 2$ (*i.e.* $\eta = 0.53$, which is consistent with NCs covered with organic lig-

ands) the simulation curve of Fig. 3.5 predicts $E_X \approx 3.043$ eV. This is in close agreement with the experimental value found here, $X_0 = 3.041$ eV. However, the proximity of the calculated exciton resonance to the experimental value should be approached with caution, as fluctuations in the dielectric environment (see Fig. 3.5) or variations in NC shape anisotropy can cause the transition energy to change within a few meV typically. Nonetheless, the good agreement allows for the identification of X_0 as the zero-phonon excitonic transition. This also leads to a reasonably good interpretation of the overall steady-state optical response, as discussed further. At higher energy, X_1 can be explained by the optical response of $6-6.5$ nm nanocubes. Larger size NCs form the tail of the size distribution and most likely contribute to the low-energy structure, X_b, noticing that free exciton transitions were clearly identified in bulk-like crystalline films (2.992 eV at 2 K)[149]. Finally, slight variations (a few meV) are obtained as the dielectric contrast is varied (becoming larger for higher energy transitions) and they may add to the energy fluctuations associated with the size dispersion to explain the broadening of the absorption peak.

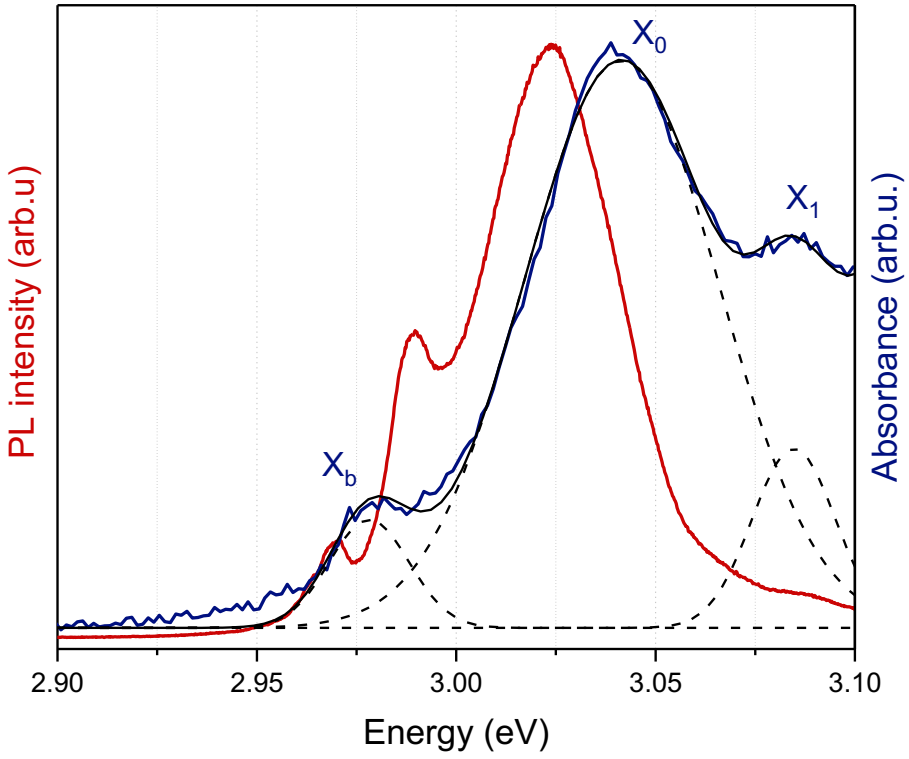

Figure 3.6: Absorption (blue line) and photoluminescence (red line) spectra of a lightly diluted phase of $CsPbCl_3$ nanocubes dispersed on a glass coverslip (T = 10 K). The solid black line is an adjustement made out of three Gaussian contributions (dashed black lines).

Regarding the ensemble photoluminescence (PL), the spectrum is clearly Stokes-shifted relative to the absorption. The origin of the Stokes-shift in perovskite NCs is a debated topic.

Performing PL, PL excitation (PLE) and transient differential absorption (TDA) spectroscopy measurements on single and ensembles of NCs, Brennan and coauthors ruled out any extrinsic cause of this Stokes-shift due to the size distribution of the NCs, the reabsorption by other NCs or the formation of polarons [177]. Moreover, their measurements on NCs of different average sizes revealed a general increase of the Stokes-shift with the confinement in inorganic LHPs [178]. Since all of their experimental results point towards an origin that is intrinsic to the electronic structure, the same group modelled the joint electronic density of states of $CsPbX_3$ compounds with atomistic *ab initio* method. They finally proposed that the Stokes-shifted PL in inorganic LHPs results from the presence of a confined hole state located tens of meV above the valence band edge depending on the level of confinement applied to the NCs.

Back to Fig. 3.6, the main PL structure is attributed to the emission of the X_0 absorption transition with a red shift $\Delta_{SS} \approx 16$ meV a value that matches the one reported by Brennan and coauthors [177] for $CsPbCl_3$ NCs with $\langle L \rangle \approx 8.0$ nm. The central sharper structure peaks at 2.99 eV, an energy that corresponds to a 25 meV shift from the main exciton peak X_0. This difference matches the LO_2 phonon energy evidenced in several studies [170, 41, 179], meaning that a phonon replica line is most likely observed. Following the absorption analysis, the lower energy PL peak can be seen as the emission line associated with X_b. The lower Stokes shift with respect to X_b (≈ 8 meV) is an indication of the poor level of confinement that subsists in the objects responsible for this emission, in agreement with the work of Brennan and co-authors [177].

Before introducing the reader to the spectroscopy of single objects, a brief summary of the results presented so far on the chloride compound needs to be done. The NCs studied in this work have a cuboid geometry with an average edge length $\langle L \rangle \approx 8$ nm. A statistically significant proportion of these objects present a shape anisotropy that corresponds to an increase or decrease of $\langle L \rangle \approx$ between 0 to 20% in one or more dimensions. The first round of optical spectroscopy measurements performed on NCs ensembles gives an exciton transition at 3.041 eV in absorption and 3.025 eV in emission for NCs of 8 nm edge length, with a stokes shift of $\Delta_{SS} = 16$ meV between the two, that should be observed on single objects and grows with the confinement. Optical phonons are expected to play an important role on the emission properties since their replicas are already observed on the emission spectra.

3.2 Exciton fine structure in $CsPbCl_3$ NCs

Following the characterisation of the $CsPbCl_3$ NCs morphology and their ensemble optical properties, the spectroscopic investigation of single objects will be conducted. This will provide insights into the fine structure of the band edge exciton state and the symmetries of its constitutive sub-

levels. In LHP NCs, the exciton fine structure (EFS) has been extensively studied over the last ten years in numerous studies by A. Efros [21, 180], and P. Tamarat [39, 22, 181] groups, while our group also made significant contributions [40, 53, 23]. Despite the prediction of the largest energy splittings in the $CsPbCl_3$ system, no studies had been conducted on this compound prior to this work, probably due to the poor PL quantum yield (PLQY) of this material that renders light collection more challenging and the necessity to adapt optical spectroscopy set ups to lower wavelengths (typically 390 to 420 nm). Experimentally, optical micro-PL spectroscopy on single objects has proven multiple times to be the appropriate tool for the EFS observation, as it allows for the elimination of the inhomogeneous spectral broadening due to size dispersivity and enables the measurement of emission lines as thin as a few hundreds of μeV in width, provided that the system is studied at temperatures close to liquid Helium.

3.2.1 Single object micro-PL spectroscopy

The experimental set-up that is one of the basis of the study was presented in Chap. 2 in details and will not be further described throughout this section that focuses on single NCs spectroscopy. The spectral response of four individual $CsPbCl_3$ NCs is presented in Fig. 3.7, along with a polar diagram that analyzes the polarization of each spectral line of the structure. The spectra are composed of two Lorentzian-shaped components of linewidths measured between 0.6 and 1 meV and splittings from 0.5 and 3 meV, well above the experimental energy resolution of 100 μeV. These components exhibit orthogonal '8 shaped' intensity profiles on the polar diagrams, which are characteristic of crossed linear polarisations in this type of experiment.

In approximately 15 % of all cases, a different type of spectrum was observed experimentally and is presented on Fig. 3.8. This time the emission pattern is composed of three Lorentzian-shaped spectral lines with linewidths and splittings similar to the 'two-peak' spectra. Again, the inserted polar diagrams demonstrate that these transitions all have linear polarizations.

As described in Chap. 1 the exciton fine structure of LHP NCs, and specifically here of $CsPbCl_3$, arises from the electron-hole exchange interaction. This leads to a lift of the exciton state degeneracy and results in two energetically separated sublevels in the high symmetry case: a 3-fold degenerate state with total angular momentum $J = 1$, known as the bright state, and a lower energy singlet state with $J = 0$, whose transition is dipole forbidden and therefore called a dark state. Further symmetry reduction of the system (either through changes in the *crystal phase* or the *NC shape*), results in a splitting of the $J = 1$ state and leads to a fine structure composed - in the lowest symmetry cases - of three well separated bright states and a dark state.

Although the linewidths and polar diagrams of both sets of spectra presented on Fig. 3.7 and 3.8 are typical of the emission response of individual objects, they do not provide sufficient proof

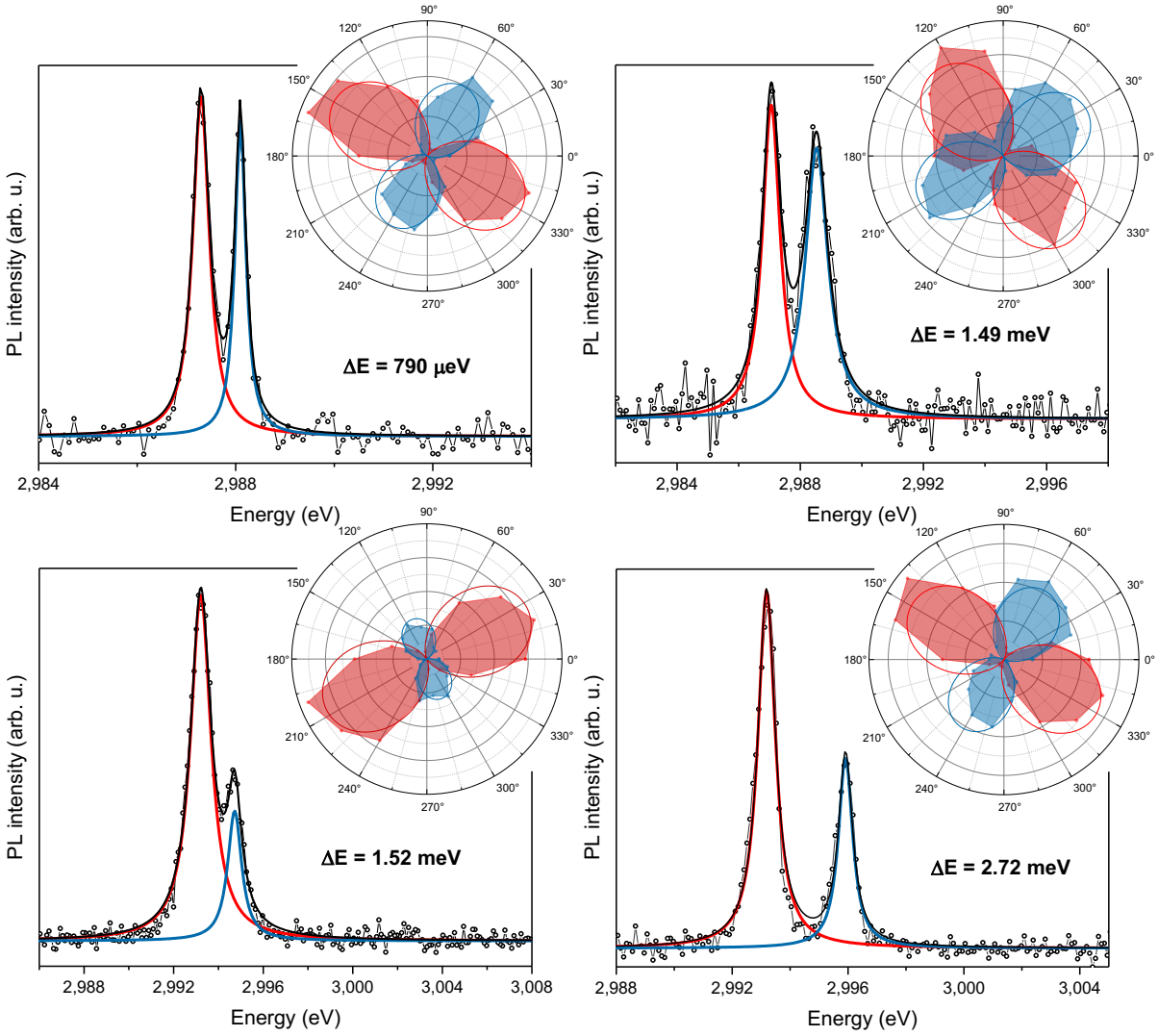

Figure 3.7: Spectra of exciton fine structure doublets observed with $CsPbCl_3$ nanocubes at T = 7 K (highest proportion of patterns - 85 % - observed throughout the experiments). Red and blue lines are the Lorentzian fits, black line is the cumulative fit. The insets are polarisation analysis of both spectral lines with their respective fits.

of the individual nature of the observed spectral responses. After all, different combinations of individual object emissions could match the ones reported by the experiments. To confirm the observation of single objects PL, a commonly used experiment consists in acquiring spectra at regular time intervals to create PL maps in the energy-time domain.

Fig. 3.9 shows the results of such experiment for an EFS doublet and triplet. Under the influence of local electric fields created by trapped charges on the NC surface or in its direct environment, concerted spectral shifts of the EFS peaks are clearly observed. These shifts are manifestations of the Stark effect affecting the exciton, and their same amplitudes clearly demonstrate that the measured optical responses originate from the same particle in both cases. This

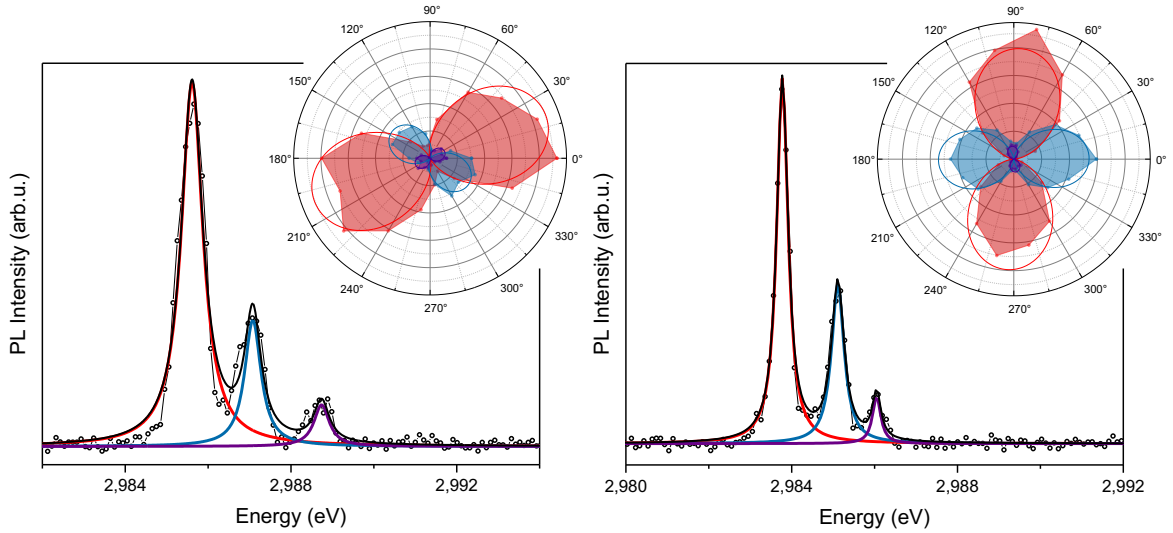

Figure 3.8: Spectra of exciton fine structure triplets observed with $CsPbCl_3$ nanocubes at T = 7K. Red and blue lines are the Lorentzian fits, black line is the cumulative fit. The insets are polarisation analysis of all spectral lines with their respective fits.

figure also provides insight into the level of spectral stability characteristic of excitonic transitions. With shift amplitudes of 300-500 μeV, the spectral diffusion seems to have a greater impact here than in bromide and iodide systems, also likely explaining that significantly larger EFS peak linewidths (comparatively ~ 2 times larger) are measured for $CsPbCl_3$ NCs at 7 K [39, 40, 182].

Interpreting the spectra and associated polar diagrams in Fig. 3.7 and 3.8 is a challenging task. Moreover, there is a striking feature that has to be explained regarding the statistics of the energy splittings. Fig. 3.10 reports the inter-bright states splitting energies Δ_{BB} observed across a set of 75 two-peak spectra, plotted against their PL transition energies (taken at the lower peak energy). The graph also includes the theoretical projection associated to Δ_{BB} and made while varying the edge length L of cubic-shaped NCs subject to an intermediate quantum confinement regime within an environment characterized by a dielectric constant $\epsilon_2 = 2$ (depicted by the dark red curve). This theoretical curve was derived from numerical calculations in the EFS model discussed in Sec. 1.3.4, while intentionally neglecting the anisotropy for the moment. On the graph, the Δ_{BB} curve is translated towards lower energies to compensate for the Stokes shift so that it intersects with the average splitting line at the average PL transition energy of individual objects, $\langle E_X \rangle = 2.993$ eV.

One can see that the bright-states energy splittings measured experimentally do not align along the theoretical Δ_{BB} curve. Instead, a wide dispersion of the Δ_{BB} values is evidenced over the 2.98 – 3.00 eV interval. Indeed the splitting energies span from 0.51 meV to 3.11 meV with a $\langle \Delta_{BB} \rangle = 1.48$ meV average and ~ 0.54 meV standard deviation. Despite a reasonable agreement regarding a subpart of the experimental sample, the striking point is the overall weak correlation

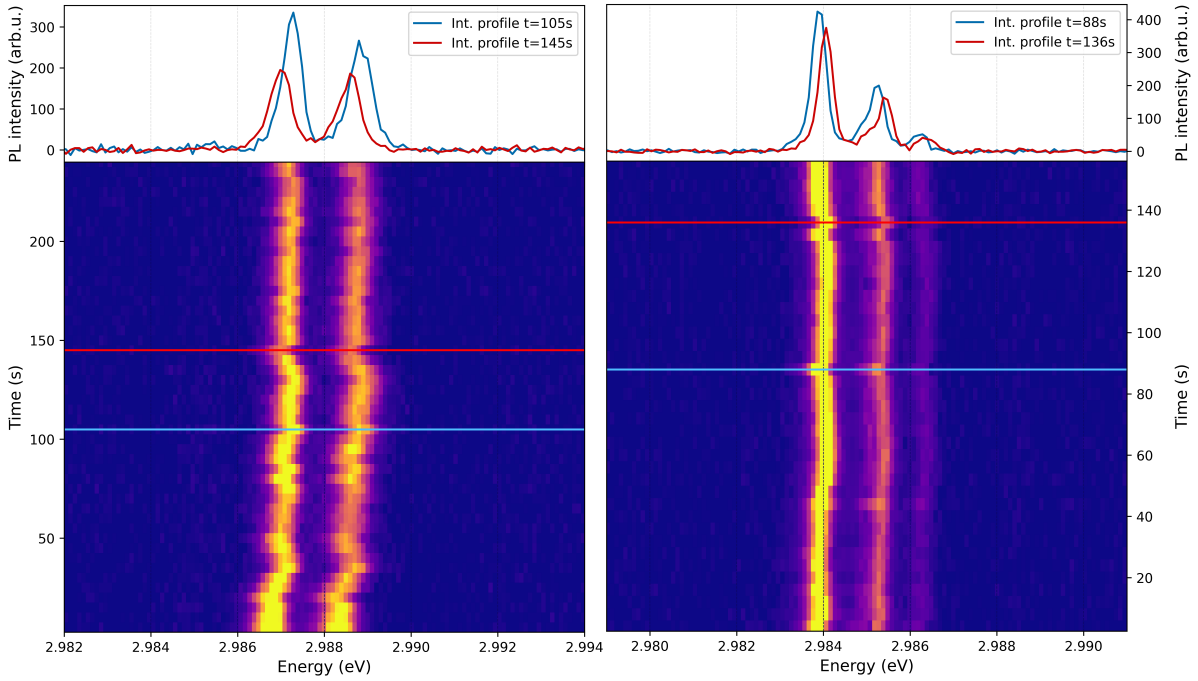

Figure 3.9: Spectro-temporal traces of $CsPbCl_3$ NCs EFS doublet (left side) and triplet (right side) captured at T = 7 K. Intensity profiles taken at two different moments are plotted on top of each trace. The concerted shifts of all the EFS lines are additional proofs of the individual object character of the collected PL.

between splitting amplitude and emission energy. More specifically, strong deviations from the theoretical curve are observed since the larger splittings are also measured for NCs presenting lower transition energies. From these arguments it appears necessary to invoke an additional parameter that might be responsible for this pronounced dispersion in Δ_{BB} while having a weak influence on the transition energy itself.

Considering a slight anisotropy in the NCs shape could be a straightforward solution to account for the variety of single objects emission responses, as well as the unexpected occurrence of triplets assuming NCs of tetragonal crystal lattice. This aspect is evidenced more exhaustively in the next section but, before that, the origin of the multiplicity in the EFS peaks needs to be discussed. From the theoretical developments of Sec. 1.3.4 the number of peaks in the EFS is governed by two aspects:

- The symmetry of the crystal phase: for NCs of perfect cubic shapes, doublets are expected in the tetragonal phase while triplets are characteristic of the lowest symmetry orthorhombic structure.

- The level of shape anisotropy: a modification of the NC shape (while remaining a cuboid) possibly leads – through the modification of the exchange interaction energy terms, Δ_{SR} and Δ_{LR} – to the lift of the degeneracy that subsists in the cubic and tetragonal phases of

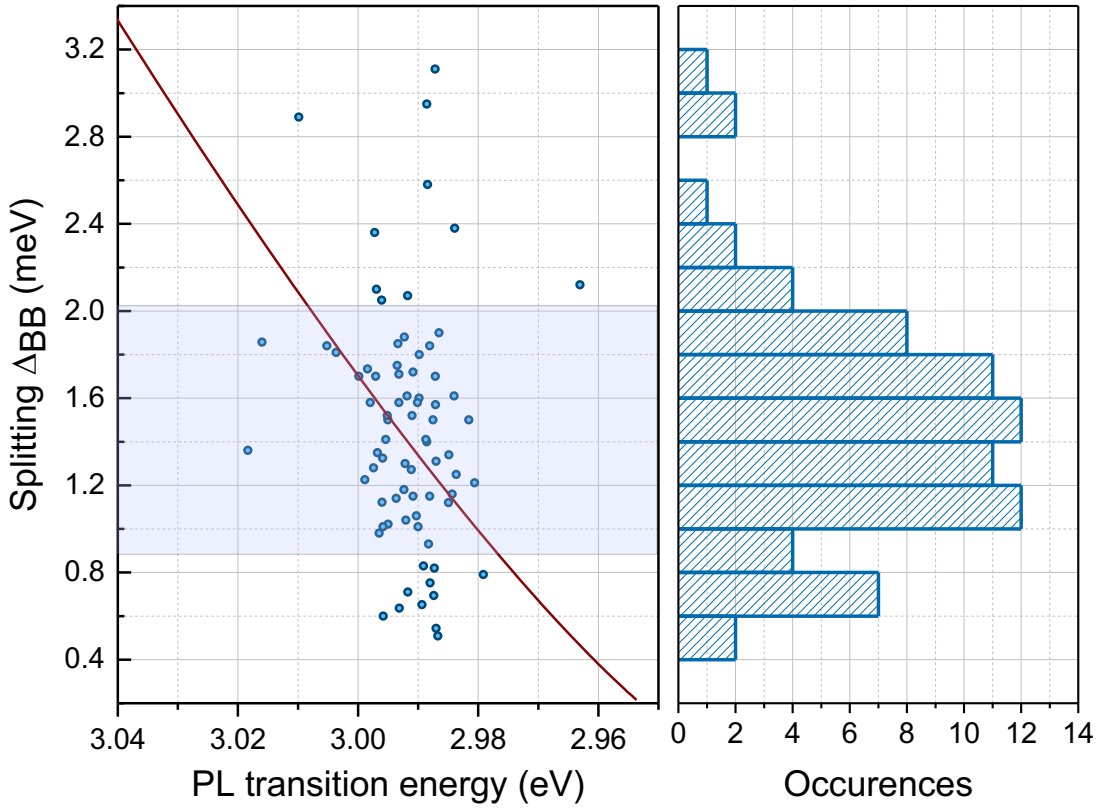

Figure 3.10: Left side: Observed EFS energy splittings Δ_{BB} of two peak spectra as a function of their PL transition energy (low energy peak position). The dark red curve represents a theoretical prediction obtained while varying the edge length L of perfect cubic shape NCs ($L = L_i$, $i = x, y, z$) in the intermediate quantum confinement regime. The blue shaded area indicates the standard deviation of the experimental splitting values. Right side: Histogram of the Δ_{BB} splittings.

perfectly cubic NCs.

The energy level diagram presented below in Fig. 3.11 was already displayed in Chap. 1 and summarizes how both factors tailor the EFS in LHP NCs.

In this work, the quasi-systematic observation of doublets and the occasional observation of triplets strongly support the hypothesis that the NCs have a lattice structure belonging to the tetragonal space group D_{4h}. Let us note that, at 77 K, the tetragonal symmetry was found to dominate the structure of $CsPbCl_3$ NCs in samples fabricated using a method similar to the one used in this work (method of L. Protesescu in [17]), as demonstrated by Liao and collaborators [41]. In general, phase transitions manifest themselves in the optical response of the NCs as a non-monotonous evolution of the excitonic transition, both in absorption and emission. No signature of that type could be evidenced throughout the optical measurements performed in this work between 7 K and 77 K (see Fig. 3.4 for absorption and Fig. 4.5b for emission). These

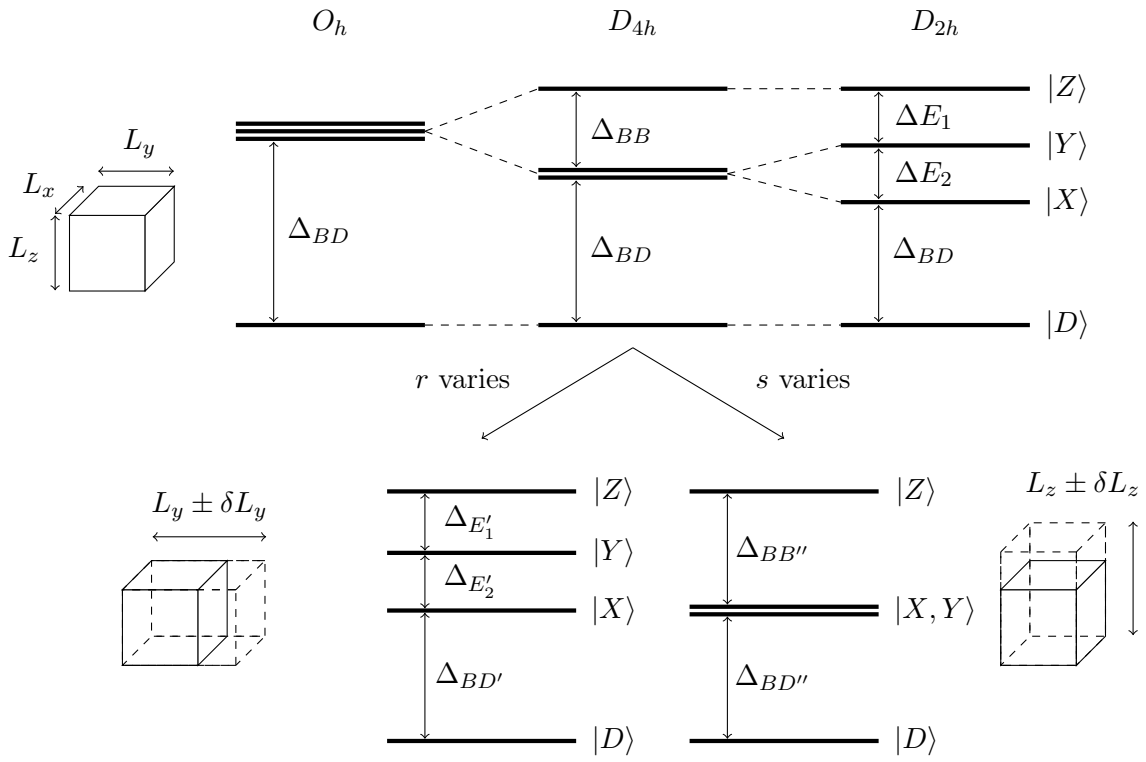

Figure 3.11: EFS energy level diagram in LHPs. The top part of the Figure illustrates how the fine structure levels split when the crystal phase varies from cubic (O_h) to orthorhombic (D_{2h}) while the shape of the NC is kept perfectly cubic. On the bottom, the effect of the NC shape anisotropy is taken into account on the tetragonal phase (D_{4h}) specifically by adjustment of the parameter $s = L_z/L_x$ or $r = L_y/L_x$. Note that the highest symmetry axis of the D_{4h} phase is assumed to be parallel to the Nanocrystal axis z.

results comfort the hypothesis of a major population of NCs being in the tetragonal phase in our low-temperature studies.

Therefore, in the hypothesis of a tetragonal structure, doublets essentially correspond to NCs that have been elongated or contracted along their crystallographic axis **c** (or that kept a cubic shape). One component of the doublet comes from the linearly polarized dipole, $|Z\rangle$, whereas the other should be associated to the 2-fold degenerate $|\pm 1\rangle$ state. Before going further in the analysis, let us briefly examine different aspects that may come as troublemakers in the working framework:

- The experimental configuration might significantly influence the micro-PL spectral patterns. Indeed, dipoles with axes perfectly aligned to the optical axis (microscope objective axis), contribute poorly to the collected PL. Consequently, one might argue that doublets should appear instead of triplets due to the strong artificial - detection dependent – attenuation of the dipole component parallel to the optical axis. However, there are two major objections to this argument: (i) A dipole oriented along the optical axis corresponds to a very particular

configuration that is realized when the NC has one of its face parallel to the substrate and cannot be envisaged as a general trend. Fig. B.3 (see Appendix B) and Fig. 3.12 depict the patterns that would be detected for NCs having different orientations with the optical axis. In the case of tetragonal NCs, doublets are predominantly observed whereas triplets would be quasi-exclusively observed for NCs of the orthorhombic phase. (ii) Whenever the highly specific orientations mentioned above were to occur, the microscope objective has a sufficiently broad angular acceptance ($\sim 34°$, corresponding to a numerical aperture of ~ 0.55) to detect emission from dipoles forming a small angle with the optical axis. Fig. B.3 and Fig. 3.12 are simulations of the expected polar diagrams for various orientations of the NC, considering the numerical aperture of the objective. These simulations were performed using the theoretical model of [183] detailed in Appendix B. For both tetragonal and orthorhombic cases, the ratio of maximum intensities between the dipole parallel and orthogonal to the optical axis is approximately 0.1, a value that compares well to the calculations made by Bohmler *et al.*, who found a ratio of about 0.2 in the worst-case scenario [184]. Therefore, a dipole parallel to the optical axis, if present, would always be detected.

- Thermalization effects additionally play a role: by strongly decreasing the highest energy state population, a triplet might be observed as a doublet. So far the issue of inter-bright states relaxation has not been addressed in perovskite NCs but the experiments show that the bright states cannot be considered as fully thermalized at low temperature. For example, doublets are detected with comparable amplitudes of their components at 7 K ($k_BT \approx 0.6$ meV) while the latter are separated by energies that span the 1.6 – 2 meV interval. More generally, the observation of bright states that are not quenched towards the low energy dark state also indicate a difficult thermalization process in the EFS. In perovskite cesium-bromide 2D systems (having large bright states – dark state separation) it was shown that the exciton temperature may be as high as 75 K even for a lattice temperature approaching 0 K [185]. Therefore, a thermalization process is probably at play in $CsPbCl_3$ NCs but cannot be an impeding process with regard to the discrimination between the emission patterns (actual doublets or triplets). Sec. 4.3.4 of the next chapter comes back to the issue of the thermalization dynamics (once a phenomenological model is set to explain the time resolved PL) and shows that at low temperature (T $\sim$ 10 K) the bright exciton sub-levels of the EFS is a 'hot system' *i.e* thermalizes on a timescale that is orders of magnitude larger than the effective lifetimes. Additionally, in Fig. 3.13, the evolution of a doublet with increasing temperature is displayed until 40 K ($k_BT \approx 3.5$ meV) so that if thermalization was at play, a third (triplet-belonging) component should have been detected both under the form of an emerging peak and an additional broadening of the spectrum at higher temperatures. The

measured spectra show that this is clearly not the case.

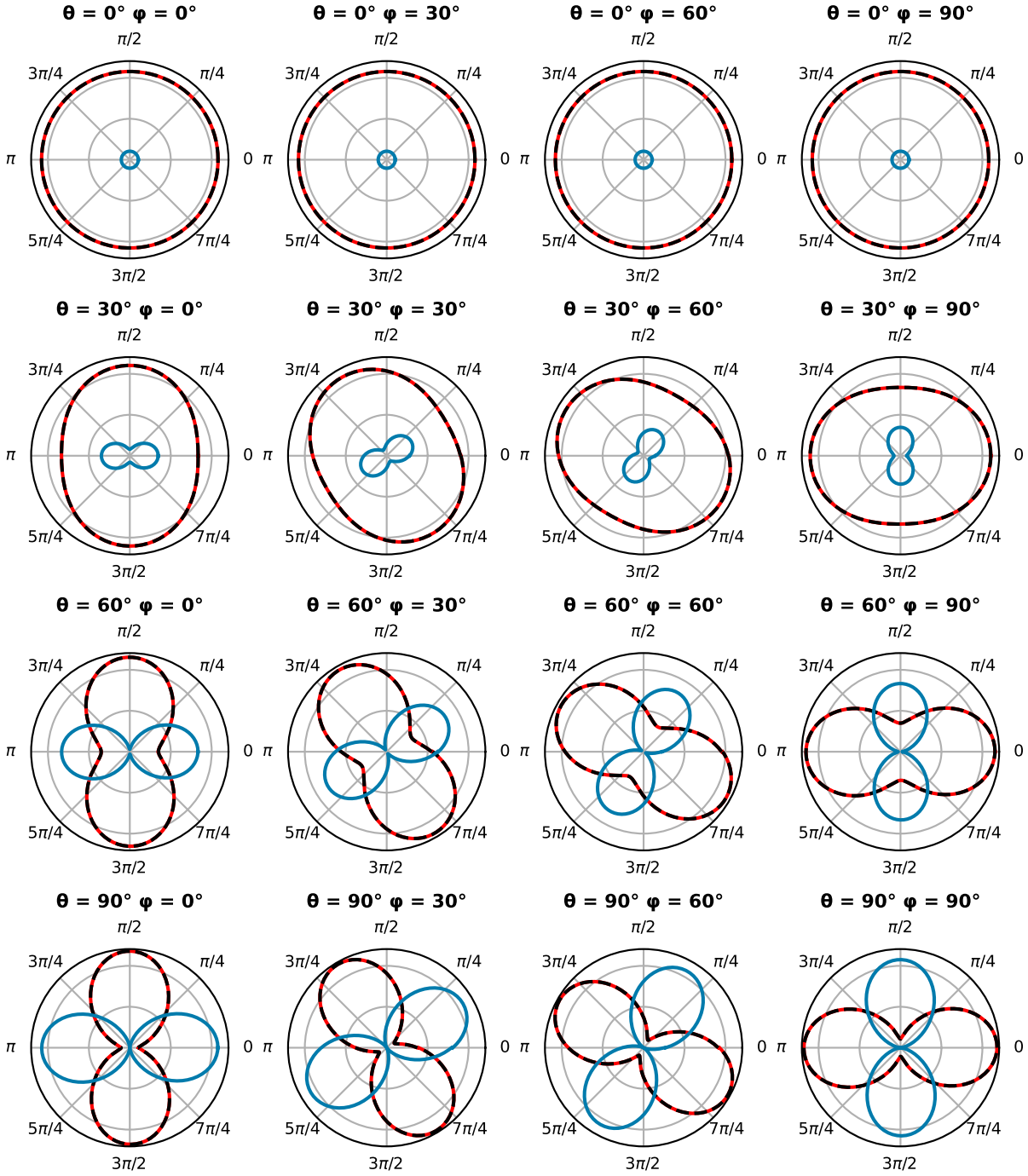

Figure 3.12: Simulated polar diagrams of three orthogonal emitting dipoles, corresponding to the emitting states of LHP NCs belonging to the tetragonal crystal phase. The angles Θ and φ give the orientation of the dipole $|Z\rangle$ (blue line), while the dipoles $|X\rangle$ and $|Y\rangle$ (red and black lines) are orthogonal to $|Z\rangle$ at all times.

At that point there remain two aspects that should be developed further: (i) the large dispersion of the doublet energy splittings presented on Fig. 3.10 and, (ii) the occurrence of triplets.

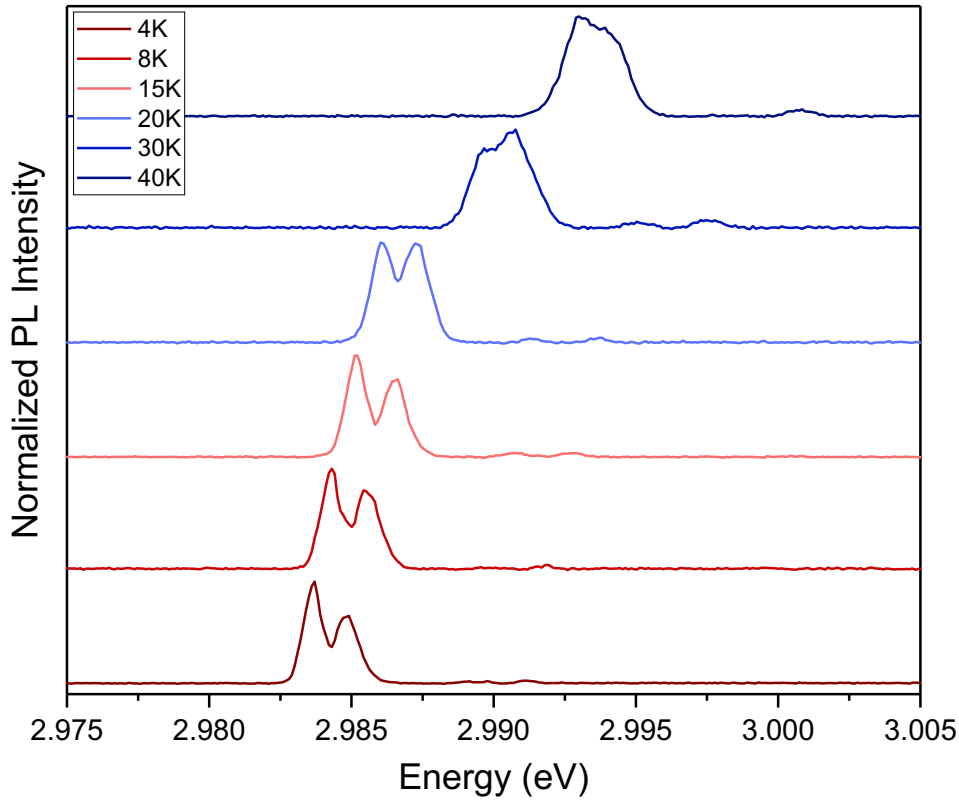

Figure 3.13: Exciton fine structure doublet followed in temperature. The transition energy blue shifts with increasing temperature, as expected with perovskites. The lower intensity peaks located at higher energy are most likely due to another object poorly excited by the laser (λ_{exc} = 395 nm).

This is done in the following paragraph where the role of the shape anisotropy is considered in a more exhaustive manner.

3.2.2 Effect of the shape anisotropy and dielectric discontinuity on the EFS

The prior discussion regarding the low-temperature crystal phase of $CsPbCl_3$ NCs and their spectroscopic signature discarded an essential parameter: the shape induced anisotropy. Indeed, given that Coulomb interactions depend on the overlap of the electron and hole wave functions, the EFS levels energies are strongly influenced by morphologies of reduced symmetry within confined nanostructures. Moreover, if the surrounding medium has a different dielectric constant, the screening of these Coulomb interactions will be affected, further modifying the EFS energy spectrum. In NCs these effects are well known and were already investigated by Efros, Bawendi and Norris as soon as 1996 [68].

In this section, spectroscopy results are compared with simulations conducted using an EFS model in $CsPbCl_3$ NCs that specifically takes into account the NCs' shape anisotropy. These numerical calculations were conducted in collaboration with the K. Boujdaria group from Carthage

University. They were based on the theoretical framework presented in Sec. 1.3.4 and were built on prior work on bromide or iodide LHP NCs by A.L. Efros and P. Tamarat and our group [180, 22, 186]. A complete derivation will not be provided here, but the reader can find more details in the work published by our group and collaborators [71, 186].

Variations in the anisotropy parameter s

Fig. 3.14 illustrates the energy of each EFS bright state $|X\rangle$, $|Y\rangle$ and $|Z\rangle$ defined by equation Eq. 1.42 within a tetragonal lattice $CsPbCl_3$ NC. These energy levels are plotted relative to the dark state energy set here at $E_D = 0$ eV. The NC size is either contracted or elongated (with volume $V = \langle L \rangle^3$ kept constant) by changing the value of the parameter s defined as $s = L_z/L_x$ and keeping the value of the parameter $r = L_y/L_x$ to unity. The situation with $r = s = 1$ therefore corresponds to a NC of perfect cubic shape.

Two dielectric environments are also considered on Fig. 3.14: A ligand-type surrounding medium characterized by a dielectric constant $\epsilon_2 = 2$ *i.e* $\eta = 0.53$ (with $\eta = (\epsilon_1 - \epsilon_2)/(\epsilon_1 + \epsilon_2)$ and ϵ_1 the dielectric constant inside the NCs) depicted by both solid lines, and an outside environment with $\epsilon_2 = 6.56$ *i.e* $\eta = 0$ that would typically be composed of other $CsPbCl_3$ NCs (dotted lines). It is worth noting that the latter scenario is unrealistic and just provides here a limiting case, as this would imply a continuity in the dielectric environment that is most likely not realized as single NCs are studied here.

Given that the model assumes the nanocrystal axis to be aligned with the tetragonal unit cell (which is the most commonly used and simple hypothesis), changing the value of s while keeping $r = 1$ translates into a deformation of the NC along the vector **c** of its tetragonal lattice while keeping a square like section in the plane defined by the lattice vectors **a** and **b** (orthogonal to **c**).

Regarding the exciton states $|X\rangle$ and $|Y\rangle$ this situation is rather similar to the case of a D_{4h} cubic NC without anisotropy: the symmetry of the structure is unchanged in the plane parallel to these dipoles and their degeneracy is maintained regardless of the s parameter value.
The simulated curves also demonstrate that a size reduction along the c axis leads to a continuous increase of the bright states splitting Δ_{BB} between the highest energy $|Z\rangle$ state and the $(|X\rangle, |Y\rangle)$ doublet. Indeed, the amplitude of Δ_{BB} is doubled from 1.42 to 2.79 meV when L_z experiences a 20% reduction (s decreasing from 1 to 0.82, respectively). A two peak spectrum possibly matching this situation is displayed on the top right of Fig. 3.14. Since the confinement gets stronger along the **c** direction, the electron and hole wavefunctions (WFs) overlap gets larger which leads to a sharp increase of the $|Z\rangle$ state energy while that of the $(|X\rangle, |Y\rangle)$ doublet remains more or less stable. This behaviour has been observed several times on anisotropic nanocubes and will result in giant bright-bright splittings similar to the ones observed on highly anisotropic nanoplatelets

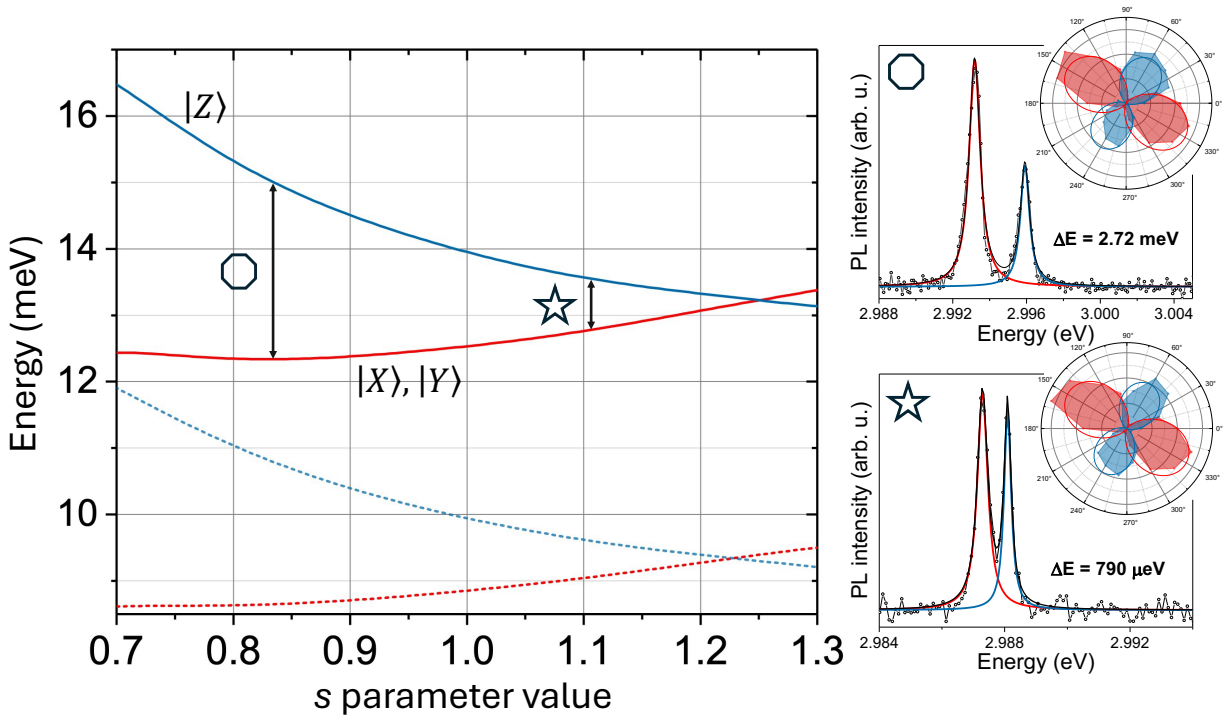

Figure 3.14: Simulated bright exciton energy levels with respect to the dark state energy and plotted against the value of the parameter s = Lz/Lx while keeping r = 1. The solid and dotted lines represent environments of respective $\epsilon_2 = 2$ and 6.56 dielectric constants. The black arrows and their associated symbols are two situations matching the two peaks spectra on the right side. Note that the role of an 'anisotropy' in the dielectric confinement (*i.e* a dielectric contrast that would change with the direction orthogonal to the NC faces) was not investigated here. Such considerations are left for further studies.

if the NC is flattened further [187].

On the contrary, a decrease in Δ_{BB} is predicted as the NC size is increased along the **c** axis ($s > 1$), an expected behaviour since the carriers WFs overlap declines when the confinement is reduced. The threshold above which state inversion occurs is expected around $s = s_0 = 1.25$. Again a spectrum acquired experimentally and possibly matching this situation is displayed on the bottom left of Fig. 3.14.

The reported dispersion of splittings Δ_{BB} displayed in Fig. 3.10 is thus well reproduced as s spans a wide interval (possibly with $s > s_0$). In particular, the average $\Delta_{BB} = 1.48$ meV is reached at the expected level of anisotropy *i.e* for a value of the s parameter around 1 and is compatible with the anisotropy standard deviation of $\sigma_{anis} = 1.2$ reported on Fig. 3.3.

Regarding the emission spectra and their associated polar diagrams, NCs deformed in such ways should statistically present an emission response matching closely with the polarisation simulations performed for cubic shaped NCs of D_{4h} crystal phase discussed in the previous section on Fig. 3.12: changing the NC orientation, an observer would see spectrally a majority of two peak spectra and a minority of one peak spectra (or with a second peak of much lower intensity).

Regarding the latest, the lack of observation of such emission response still does not find an answer here. An explanation could potentially be found in a preferential orientation of the NCs with respect to their substrate, although such behaviour did not find direct confirmation here.

Variations in the anisotropy parameter r

A second type of size modification was simulated on Fig. 3.15. This time the value of the parameter r was adjusted while keeping $s = 1$. This situation, illustrated on Fig. 3.15 corresponds to a distortion in the plane defined by the lattice vectors (**a**,**b**) orthogonal to the **c** axis, with a square-like section maintained in the (**a**,**c**) plane. Again, two different dielectric environments were tested: ligands (solid lines) or NCs (dotted lines) with $\epsilon_2 = 2$ and 6.56 respectively.

In sharp contrast with the first set of simulations, this type of morphological change lowers the NC symmetry further and leads to a complete lift of the bright exciton states degeneracies resulting in the emergence of three orthogonally polarized states $|X\rangle$, $|Y\rangle$ and $|Z\rangle$ as soon as r departs from 1 (with the exception of two crossing points where a degeneracy remains). This behaviour is very similar to the way that crystal phase symmetry reduction from tetragonal to orthorhombic impacts the EFS of cubic shaped crystals [39, 23].

On the right side of Fig. 3.15, three peak spectra associated to two situations on the simulation curves are provided. The first one correspond to $r = 0.91$ where the peak separation is assymetrical with ΔE_{XY} and ΔE_{YZ} on the order of the spectral linewidth and the second one corresponds to $r = 1.25$ with larger and symmetrical peak separations.

While these results clearly demonstrate that NCs of anisotropic shapes would lead to the observation of triplets in a majority of cases, it is worth noting that three peak spectra might also be associated with NCs in the orthorhombic phase with a larger EFS configuration space (the study of Han *et al.* on $CsPbI_3$ NCs provides a complete picture in that matter, incorporating the effect of anisotropy [188]). Finally, only systematic single-object correlative spectroscopy with both high-resolution electron microscopy imaging and optical micro-PL spectroscopy could allow distinguishing the different origins for the characteristic triplet-like response.

Additional comments on the EFS simulations

As final remarks on these numerical simulations, let us focus on a couple of points:

- Fluctuations in the dielectric environment may already lead to appreciable variations in the exciton fine structure splittings and contribute to their dispersion even for NCs of perfect cubic shapes. These fluctuations were also investigated here for reasonable variations of ϵ_2 from 3.0 ($\eta = 0.37$) to 1.0 ($\eta = 0.74$) while preserving a cubic shape, *i.e* r = s = 1. Doing so, a $\approx$ 200 μeV variation was observed in the ΔE_{BB} splitting value which is too

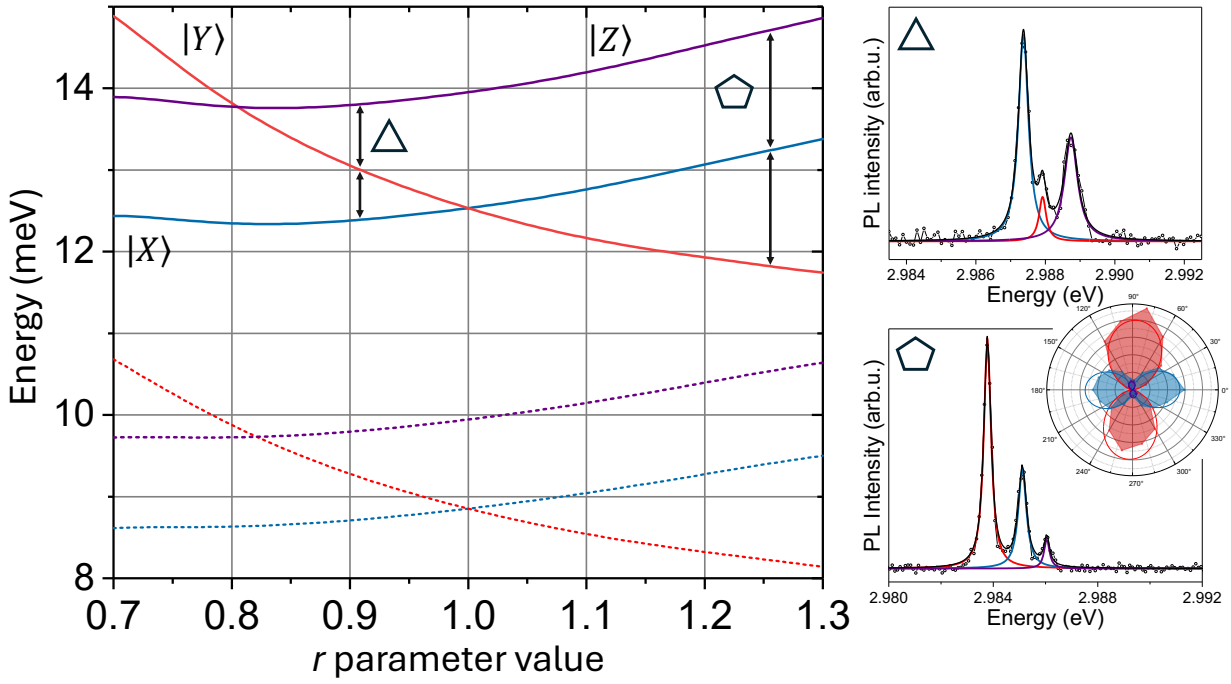

Figure 3.15: Simulated bright exciton energy levels with respect to the dark state energy and plotted against the value of the parameter $r = L_y/L_x$ while keeping $s = 1$. The solid and dotted lines represent environments of respective $\epsilon_2 = 2$ and 6.56 dielectric constants. The black arrows and their associated symbols are two situations matching the three peak spectra on the right side. Note that the role of an 'anisotropy' in the dielectric confinement (*i.e* a dielectric contrast that would change with the direction orthogonal to the NC faces) was not investigated here. Such considerations are left for further studies.

small to explain the experimental dispersion of Fig. 3.10. Moreover, assuming a tetragonal crystal lattice, the observation of triplets cannot be explained without introducing a specific asymmetry in the NC shape. Both arguments comfort the idea that anisotropy is a crucial parameter and plays an effective role in shaping the EFS.

- Despite the limited statistics, it seems that the occurrence ratio strongly favors the observation of two peaks spectra. This may find an explanation recalling that a large population of objects have no anisotropy or a rather small one. The results presented here point to a preferential anisotropic growth of the NCs alongside a specific crystallographic direction.

- Experimentally, bright states splittings below 0.5 meV (typically, $1.2 < s < 1.3$) were not observed whereas the simulated curves clearly predict their existence. Han and coauthors have demonstrated that a model of NCs with pseudocubic bounding facets, *i.e.* having their lattice vectors unaligned with the cuboid NC axis, changes the LR exchange interaction so that the $|X\rangle$ and $|Y\rangle$ EFS states couple to each other. This coupling translates into the

emergence of an avoided crossing on the fine structure energy spectra [188] that indeed leads to a limitation of the splitting. While noteworthy, the model requires the crystalline phase to be orthorhombic, which cannot be an initial postulate here. The lack of small bright states splittings cannot be explained in a straight forward manner but a possible explanation is that the actual NCs edge lengths distribution (on its sides) might not be strictly the same as the one characterized through the TEM images analysis. The chemical processes at stake during the dilution of the colloidal solutions (necessary to reach the spatial dispersion compatible with single-object experiments) are not perfectly known and the selective dissolution of certain NCs geometries can not be excluded.

3.2.3 Observation of other exciton species: trions and biexcitons

Chapter 1 reported that in semiconductor NCs, excitons can sometimes form charged species called trions, which result from the Coulomb interaction between an exciton or electron-hole (e-h) pair and another charge carrier present in the NC, either an electron or a hole (generated by an Auger recombination process). Furthermore, when multiple excitons are generated in the medium, biexcitons can also be formed. These systems typically require higher laser excitation powers to be generated, but are nevertheless regularly reported in micro-photoluminescence (micro-PL) studies on individual emitters. Although they are not the main focus of this work, biexcitons and trions represent interesting aspects of single object spectroscopic investigations of $CsPbCl_3$ and their characterization is essential either for classical or quantum light emission applications.

The micro-PL spectrum presented on Fig. 3.16 shows an exciton fine structure doublet from a single $CsPbCl_3$ NC acquired for a fairly long period of time, *i.e*, ∼10 s. Alongside this exciton, a single line shifted of ∼ 17 meV was captured on the low energy side. The polar diagram of this single line is also presented on Fig. 3.16 and demonstrate that this spectroscopic feature has no linear polarisation. As seen in Chap. 1, in charged excitons (also called trions) opposite sign electron-hole exchange interaction terms cancel each other. Therefore, trions do not exhibit fine structures and their emission is circularly polarized [76, 79]. For these reasons the single line of Fig. 3.16 is attributed to the trion X^*. The FWHM = 1.15 meV of this trion emission peak appears slightly larger than that of the EFS peaks and can be explained by a higher sensitivity of this charged species to its electrical environment resulting in an increased amplitude of spectral diffusion. The trion was already observed multiple times on $CsPbI_3$ and $CsPbBr_3$ NCs of similar sizes [182, 181, 24, 189] but never on the $CsPbCl_3$. Here, the measured energy shift appears very similar to the ones observed on other LHP materials.

Fig. 3.17 displays a PL map of another $CsPbCl_3$ nanocrystal EFS taken at different positions of the rotating half-wave plate. With no surprise the spectral signature of the EFS, noted X,

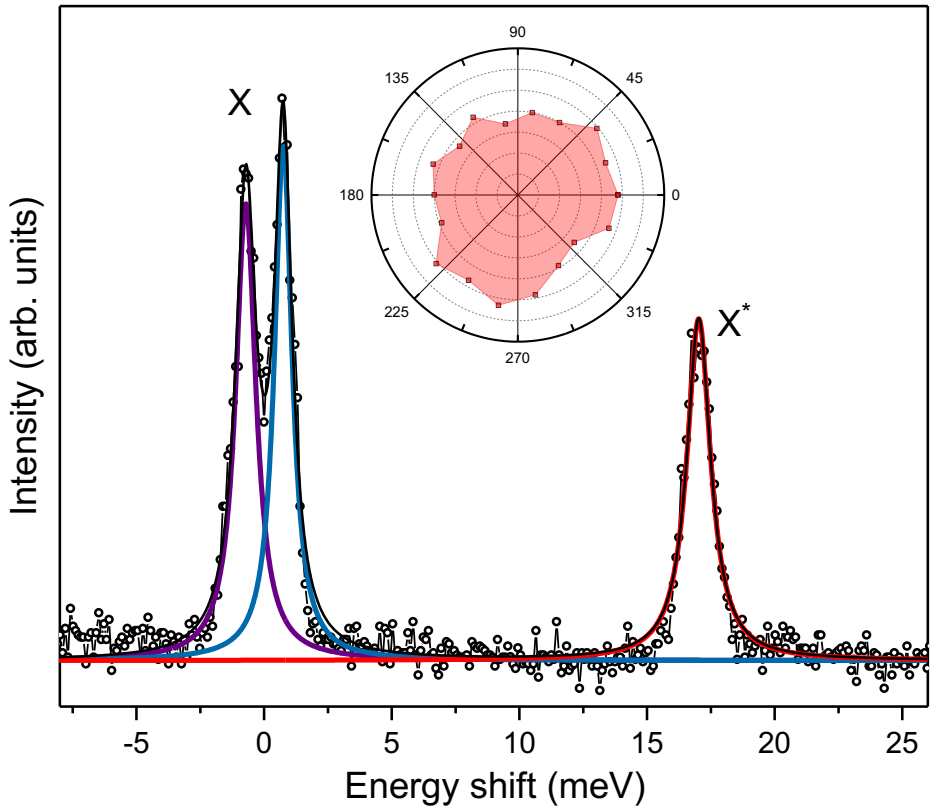

Figure 3.16: Two peaks EFS spectrum of a single $CsPbCl_3$ NC accompanied by its trion at 17 meV shift on the low energy side. The inset is a polar diagram of the trion line and shows no linear polarization. The absolute exciton transition energy here is $E_X = 2.986$ eV.

is retrieved on this map, alongside its crossed linear polarisation response, confirmed by the corresponding inset polar diagram. On the low energy side the trion emission, noted X^*, is found again at an energy shift of 17-18 meV from the EFS and does not show a linear polarization behavior. Note that, as observed by [182], since the trion is a charged exciton, it should not emit simultaneously with the neutral exciton. Here the integration time was set to 20 s for each angle position which is a way larger time scale than the $X \leftrightarrow X^*$ charging/decharging and therefore explains their "simultaneous" observation.

Further down the low energy side of the neutral exciton, a new spectral feature denoted XX, appears at $\sim$ 31 meV from the exciton transition. Looking at its corresponding polar diagram on the inset one can clearly see that its constituents have linear crossed polarisations that are anti-symmetric to the ones of the neutral exciton, X, *i.e*, its higher energy constituent has a maximum PL amplitude when the lower energy constituent of X has a maximum amplitude and *vice versa*. As seen in Chap. 1 (see Fig. 1.10) this behavior is characteristic of the emission response of a biexciton and has also been observed several times on other inorganic LHP NCs [181, 182, 24, 189].

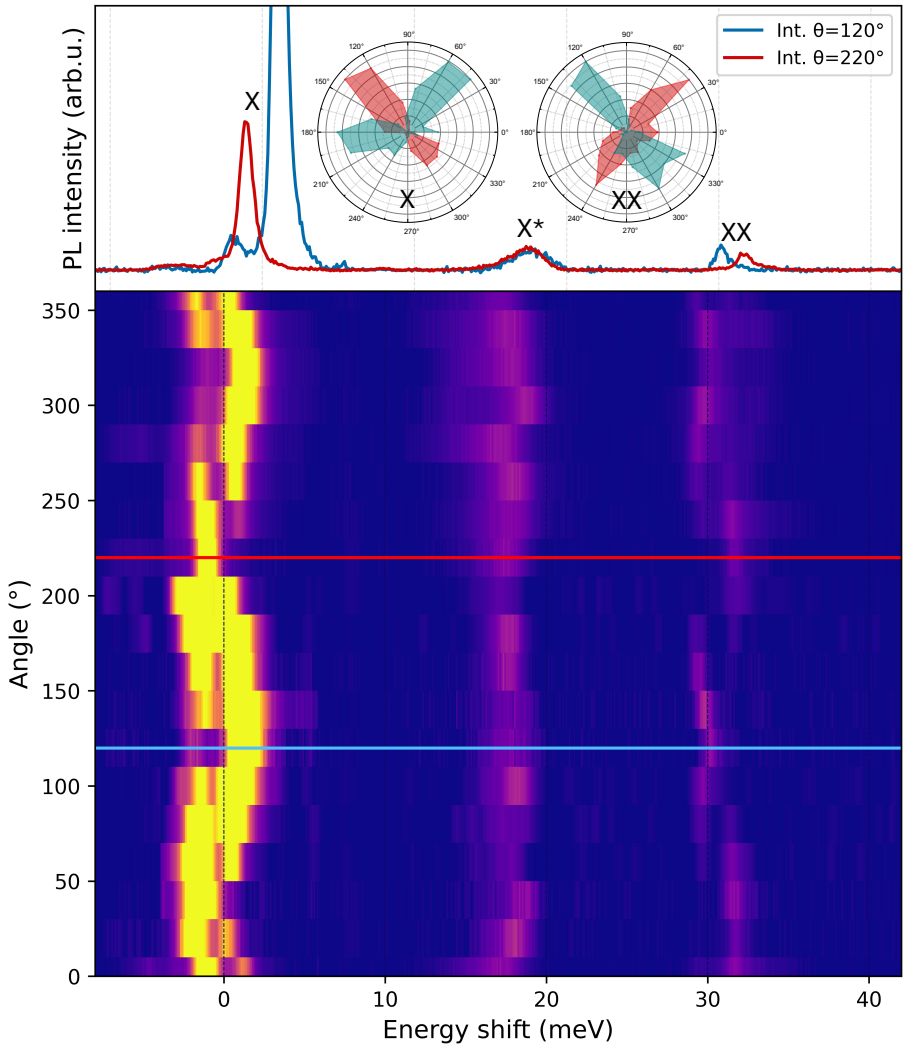

Figure 3.17: PL intensity map of a single $CsPbCl_3$ constructed from individual spectra captured at different positions of the rotating half wave plate. The top of the figure shows the intensity profiles for two different angles and the inserted polar diagrams are associated to the exciton X and the biexciton XX. The absolute exciton transition energy here is $E_X = 2.987$ eV.

Finally, it is worth mentioning that the intensity of these new exciton species were usually much lower (specially for the biexciton) than the ones of the neutral exciton and were therefore not observed as much. A small but relevant statistics of their energy positions is provided on Fig. 4.4 of Chap. 4 alongside the observed phonon replicas that will be discussed in greater details in the same chapter.

Conclusion

In this chapter a comprehensive study of cesium-lead-chloride perovskite NCs was presented thanks to the combination of TEM imaging, highly resolved microspectroscopy experiments and

numerical simulations. The emission patterns of single NCs were observed at multiple times allowing to build statistics that revealed a strong prevalence of two peak spectra although three peak emission responses were also observed occasionally. These findings were analyzed comprehensively considering a crystal lattice of tetragonal symmetry. Specifically, the large dispersion observed in the bright-bright splitting values, ΔE_{BB}, was explained successfully by an EFS theoretical model considering deviations in shape from the perfect cubic nanocrystal (NC) geometry. This explanation aligns with the level of shape anisotropy estimated from structural characterization via transmission electron microscopy (TEM). It was shown that even light deformation of the NCs edge lengths, whether along or orthogonal to the crystal main symmetry axis, can lead to a wide distribution of ΔE_{BB} values, potentially indicating a significant reorganization of the EFS in terms of state ordering. Depending on the nature of the deformation, the theory also predicts the emergence of three peaks emission patterns, a phenomenon clearly evidenced in the experiments.

CHAPTER

EXCITON-PHONON COUPLING IN $CsPbCl_3$ NANOCRYSTALS

4

In semiconductor nanocrystals, scattering of charge carriers and excitons by the underlying atomic lattice happens essentially through three mechanisms. First, the atomic displacements induced by acoustic and optical phonons affect the electronic band structure of the material and change the properties of the charge carriers. This perturbation is generally described by a deformation potential. Secondly, in structures lacking inversion symmetry, long wavelength acoustic phonons can induce a strain that will generate an electric field *via* the piezoelectric effect interacting with the carriers. Finally, the Coulomb coupling of the carriers with the electric field generated by the lattice optical phonons is called the Fröhlich interaction and creates a quasi particle called the polaron. Regarding inorganic lead halide perovskites (LHPs), Fröhlich interaction is the prevalent scattering mechanism of carriers, primarily due to their strong ionic nature and the soft character of their lattices [190]. In these materials the study of phonon interactions with charges is of prime importance as it can greatly modify the carriers transport and optical properties. For instance, these interactions reduce the mobility of carriers in hybrid perovskites by increasing their effective masses which is detrimental for solar cells applications [191, 192, 193]. Additionally, a slow cooling of hot carriers, induced by a phonon bottleneck effect, has been observed [194, 195, 196] and linked to an enhanced PL Stokes shift that changes the band edge optical spectra [197] and the linewidth of the emission which is detrimental for LED applications. Finally, some authors have demonstrated that interactions with phonons can ensure the thermal mixing of EFS bright and dark state populations, therefore modifying the dynamics and coherence properties of their

emission [198, 199].

The Chloride perovskite compound is special in this context because it possesses the highest energy optical phonon modes in all LHPs. Although some studies have already investigated $CsPbCl_3$ phonon modes in bulk and NCs, their impact on its PL properties have never been observed. In this Chapter, the exciton-phonon interactions in single $CsPbCl_3$ NCs are addressed and multiple optical phonon modes are highlighted. In addition, by precisely selecting single spectral lines - thanks to the polarization properties of the emission - the temperature evolution of the photoluminescence (PL) and its linewidth broadening are followed on individual $CsPbCl_3$ NCs. This work provides a better understanding of the processes at play in the context of exciton-phonon interactions in a high-energy emitting material with great potential for applications in optoelectronics. Additionally, it confirms general trends already observed in other halide perovskites emitting at lower energy [198, 22, 200, 120, 201, 202].

Finally, the reader may have noticed that the previous Chapter left aside a very important feature of the exciton fine structure (EFS) in the chloride compound: the dark state and its energy position relative to the bright ones. The last section of this Chapter is therefore dedicated to this issue and demonstrates that an indirect experimental observation of the dark state is made possible by investigating the emission dynamics of these NCs with temperature. Indeed, it will be demonstrated through the use of a phonon assisted thermal mixing model that the emission dynamics somehow reflects the coupling of the exciton to lattice optical phonons, rendering the measurement of the bright-dark EFS splitting possible in this material.

4.1 Phonon modes in $CsPbCl_3$ nanocrystals

In order to later study the various exciton-phonon interactions within $CsPbCl_3$ nanocrystals, the identification of the phonon modes in this material is a prerequisite. For this purpose, a brief review of the expected phonon modes is presented in this section, followed by the presentation of Raman spectroscopy measurements performed on $CsPbCl_3$ NCs.

4.1.1 Expected phonon modes in $CsPbCl_3$

The high temperature phase of $CsPbCl_3$ being the ideal cubic perovskite structure, its symmetry properties and normal vibration modes are well known and available in the literature [30]. Within the unit cell, 15 phonon modes classified into 3 acoustic and 12 optical modes are expected. Calistru *et al.* [170] have shown that, the IR spectrum of cubic phase $CsPbCl_3$ is expected to display 3 doubly degenerated TO modes at low energy and three non-degenerate LO modes at higher energies.

By lowering the space group symmetry, the degeneracy of each of the three *TO* modes is completely lifted and will consequently appear experimentally as distinct modes. With non-resonant Raman spectroscopy in the 0 to 400 cm^{-1} Raman shift domain, the 3 *LO* and 6 *TO* modes are measurable as it has been done with bulk $CsPbCl_3$ of orthorhombic crystal phase [170].

Regarding $CsPbCl_3$ NCs, Liao *et al.* have observed the complete lift of all the *TO* modes degeneracy by performing *in situ* both Raman spectroscopy and X-ray diffraction experiments on $CsPbCl_3$ NCs at temperatures spanning from 775 K down to 83 K [41]. In this work, the $CsPbCl_3$ NCs are synthesized using the same hot-injection method. As reported, Liao *et al.* kept observing a tetragonal crystal phase throughout the entire 83 K to $\sim$ 300 K temperatures range while measuring Raman resonances at similar energies as in [170, 203, 204]. They also clearly observed the three distinct *TO* mode doublets which are all revealed under $\sim$ 200 K until the low temperature limit of 83 K. Moreover, as already presented in Chap. 3 on Fig. 3.4, when the temperature was increased from 5 to 150 K, the variations of the absorption peaks (that correspond to different population sizes of $CsPbCl_3$ NCs) were monotonous. It is also the case for the blue-shifts of the single NC emission lines measured in the 5 to 90 K range and presented in the following on Fig. 4.5. Thus, combining these results with the work of Liao *et al.* the tetragonal crystal phase is likely to be maintained at low temperature.

4.1.2 Raman spectroscopy of $CsPbCl_3$ nanocrystals.

On Fig. 4.1 micro Raman spectra of $CsPbCl_3$ NCs are shown for 4 different temperatures between 110 K to 170 K. These spectra were acquired at the Gemac laboratory by I.Stenger using a continuous excitation at 514.5 nm (2.41 eV). On the lowest temperature spectrum, one can clearly see 3 sets of doublets between 15 and 150 cm^{-1} and a single peak located at higher energy around 200 cm^{-1}. This spectral doubling was verified several times prior to this work [170, 171, 41, 203] and is consistent with our previous analysis. The third doublet located at 115 cm^{-1} *i.e.* 14 meV is a superposition of both TO_3 and LO_1 modes. The single peak located at higher energy, around 200 cm^{-1} *i.e.* 25 meV is associated to a LO_2 phonon mode as already observed by both Calistru and Liao at the same energy [170, 41] and by Hirotsu at 220 cm^{-1} *i.e.* 28 meV [171]. It is worth noting that Calistru *et al.* identified the LO_3 mode at 375 cm^{-1} while the experiment of Fig. 4.1 was only performed up to 250 cm^{-1}.

The excellent agreement between the phonon energies observed in this work on NCs and those reported by Calistru and Hirotsu on bulk single crystals suggests that these phonon modes are not size-dependent,*i.e.*, not subject to quantum confinement. This finding was also supported by the experimental results of Kanemitsu, Amara and their co-authors [189, 24], as they did not

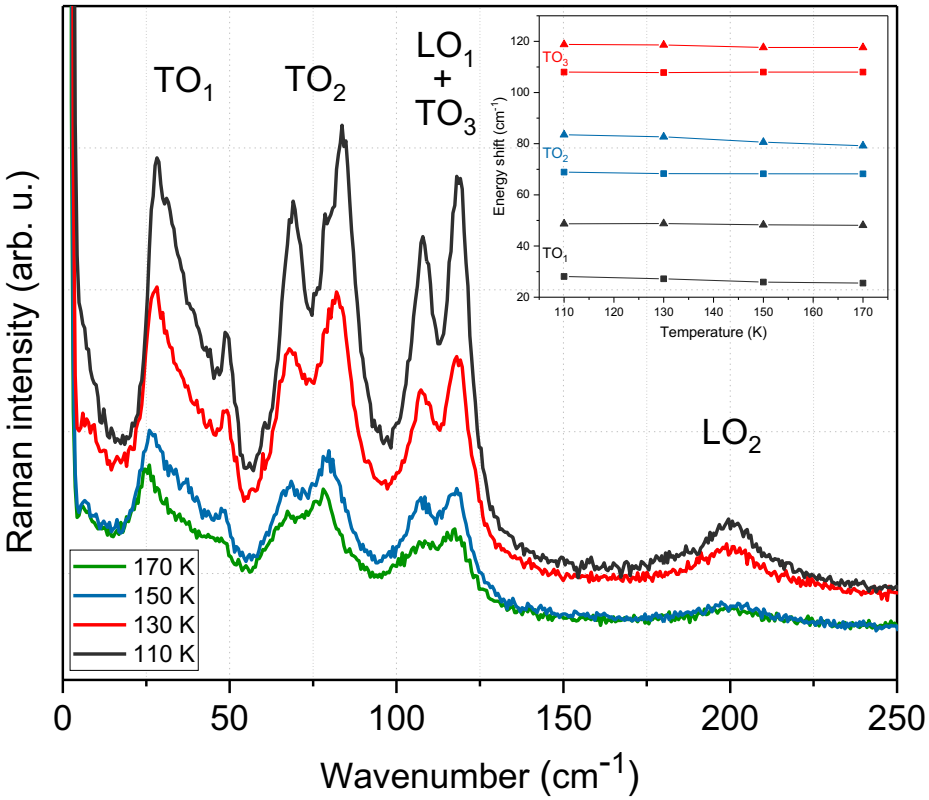

Figure 4.1: Raman spectra of $CsPbCl_3$ NCs taken at four different temperatures from 110 K to 170 K. Inset: Each TO doublet Raman shift is followed in temperature.

observe a size dependence of phonon energies in $CsPbBr_3$ NCs, which can be an indicator of the poor level of confinement usually encountered in LHP nanocubes.

On the right side of Fig. 4.1 the Raman shifts of the three TO doublets is followed in temperature as in [205]. It is evidenced that the energy of these TO modes is independent of the temperature in the explored domain, although a slight redshift of the higher frequency TO_2 mode doublet and that of the lower TO_1 mode is observed within the experimental accuracy. The monotonic behavior of the Raman shifts with temperature provides further evidence that there are no phase transitions in this temperature range.

4.2 Evidences of exciton-phonon interactions in $CsPbCl_3$ NCs

Optical phonons can interact with excitons and modify the emission properties of NCs. In single object spectroscopy they can appear as replicas or enlarge the spectral linewidth of the exciton leading to a loss of the emission purity and a reduction of the exciton coherence time [206, 207]. Having identified these phonons in $CsPbCl_3$ in the last section, their spectral signatures are investigated on single object spectroscopy experiments in the following.

4.2.1 Optical phonon replica on micro-PL spectra

Alongside the zero phonon exciton recombination lines, the emission from single nanocrystals is usually accompanied by a multitude of different spectral lines. Chap. 3 demonstrated that the variety of these spectral lines sometimes correspond to complex excitonic species such as biexcitons and trions. Phonons can also manifest themselves in micro-PL spectra under the form of Stokes shifted replicas and, less frequently (or at higher temperatures at least), as higher energy replicas *via* anti-Stokes processes. Although these spectral features are typically detrimental for applications - reducing the purity of the emission - they become valuable for characterizing the phonon spectrum of a material.

Fig. 4.2 displays the micro-PL spectrum of a single $CsPbCl_3$ NC on a large energy domain acquired at T = 5 K. One can see that peaks of weak intensity appear on the low energy side of the EFS lines. Since the energy of these peaks corresponds to the ones of the optical phonons highlighted in the last section both on bulk and NCs, they can rather confidently be associated to Stokes shifted phonon replicas. Thus, the peaks centered at 14 and 26 meV most likely correspond to the LO_1 and LO_2 phonons measured at 14 and 25 meV with Raman spectroscopy. This process is made possible because the spontaneous emission of phonons is independent of their occupation number and the temperature. In contrast, phonon absorption is proportional to their occupation number, making it highly dependent on the temperature. Therefore, at such low temperatures and given the relatively high energy of the first LO phonon, anti-Stokes replicas are highly unlikely to appear. Transverse optical phonons are also known to have considerably weaker coupling with carriers by Fröhlich interaction and should not appear or have an much lower intensity than the LO modes replicas [81]. Finally, no spectral features were observed at energy shifts of $\approx$ 35 meV from the EFS, hindering to confirm the existence of the LO_3 mode observed by Calistru in Raman spectroscopy [170].

As already stated in this manuscript, the PL quantum yield (PLQY) of $CsPbCl_3$ is particularly weak within the LHP family and, in order to reveal phonon replicas, the spectrum presented on Fig. 4.2 had to be acquired during 20 s which led to an enlargement of the peaks induced by spectral diffusion. Nevertheless the LO_2 peaks seem to reveal a fine structure, which is expected from phonon replica and has already been observed by Kanemitsu and other authors in $CsPbBr_3$ [189, 24]. On the contrary, the LO_1 peaks overlap too much to display well resolved fine structure replicas. The fits that were performed on the LO_2 peaks show an energy difference of $\sim$ 1.9 meV and is in good agreement with the measured splitting of the exciton fine structure peaks.

In Fig. 4.3, one can see a micro-PL map recorded by capturing different spectra for 10 s at each position of the rotating half-wave plate. The NC observed here is different from the one shown in Fig. 4.2 but exhibits similar spectral features. Optical phonon replicas are clearly observable and

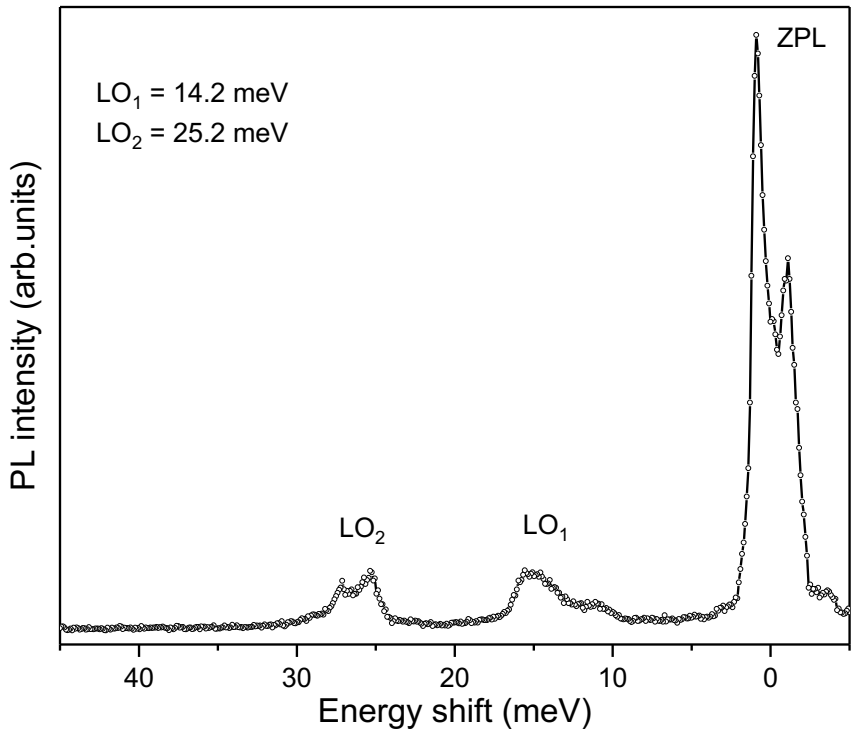

Figure 4.2: Micro-PL spectrum of $CsPbCl_3$ integrated for 20 s and showing an EFS doublet. The low energy side bands are labeled to their matching phonon energies. The absolute exciton transition is measured at E_X =2.976 eV (λ_{exc} = 395 nm).

located at E_{LO_1} = 13.9 meV and E_{LO_2} = 24.2 meV. Despite their very low intensity, especially for the LO_2 replica, their fine structures are clearly visible. The spectrum on top of Fig. 4.3 shows two intensity profiles on semi-log scale taken at two different angles. These profiles evidence that the components of the LO_1 replica fine structure have crossed linear polarisation in phase with their corresponding exciton fine structure peaks.

The histograms of the LO_1 and LO_2 phonon energy positions are displayed on Fig. 4.4 alongside the energy of the measured trions X^* and biexcitons XX to have a complete view of the spectral landscape usually encountered on the lower energy side of the EFS. For each population a gaussian distribution adjusts the data. It can first be noticed that there is a rather small population for each species (30, 24, 24 and 20, counts for respectively LO_1, X^*, LO_2 and XX) this is due to the extremely low intensity usually encountered with these spectral features. The populations of the trion and LO_1 replicas are clearly overlapping and although Fig. 4.3 shows an example of polarisation measurement on a LO_1 replica, such measurements were not possible to perform in most cases. Nevertheless two preferred classes are clearly identified on the histogram around 18 meV for the trion and 14 meV for the LO_1 replicas. The trion seems to have a more defined energy with a lower standard deviation of its population while the LO_1 fine structure (and the LO_2 for that matter) have a standard deviation of about 1.25 meV.

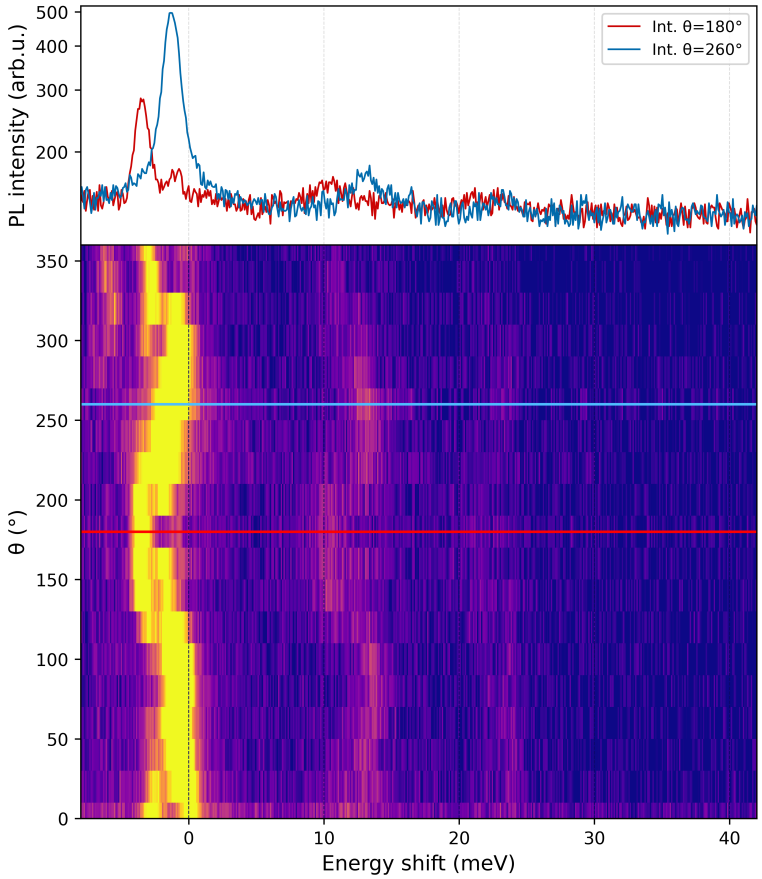

Figure 4.3: PL intensity map of a single $CsPbCl_3$ NC EFS on a 50 meV energy domain and as a function of the rotating halfwave plate angle θ. The top spectra are intensity profiles (semi-log scale) taken at $\theta = 180°$ and 260°. Two phonon replicas are clearly visible on the lower energy side. The LO_1 replica clearly shows the same polarization as the EFS peaks, while the intensity of the LO_2 seem to show the same behavior.

4.2.2 Spectral broadening in single $CsPbCl_3$ NCs

A significant challenge for quantum technology applications is the identification of exploitable two-level systems that are sufficiently isolated from their environment to maintain coherence for extended periods of time. In the case of semiconductor NCs when such systems are found, under the form of an exciton or an e-h pair, the coherence times are often damped by the interactions with the environment. These interactions are mainly due to the coupling of the exciton to the lattice phonons and to the spectral diffusion associated to the trapping and detrapping of carriers to lattice defects. Understanding and evaluating these interactions is of primary importance to have a better idea of the possibilities offered by a given material for advanced quantum applications. Single object spectroscopy offers a particular advantage in this regard, as it allows for the measurement of the spectral broadening of exciton emission lines, thereby enabling to directly probe the contributions from acoustic and optical phonons. This would not easily be feasible in

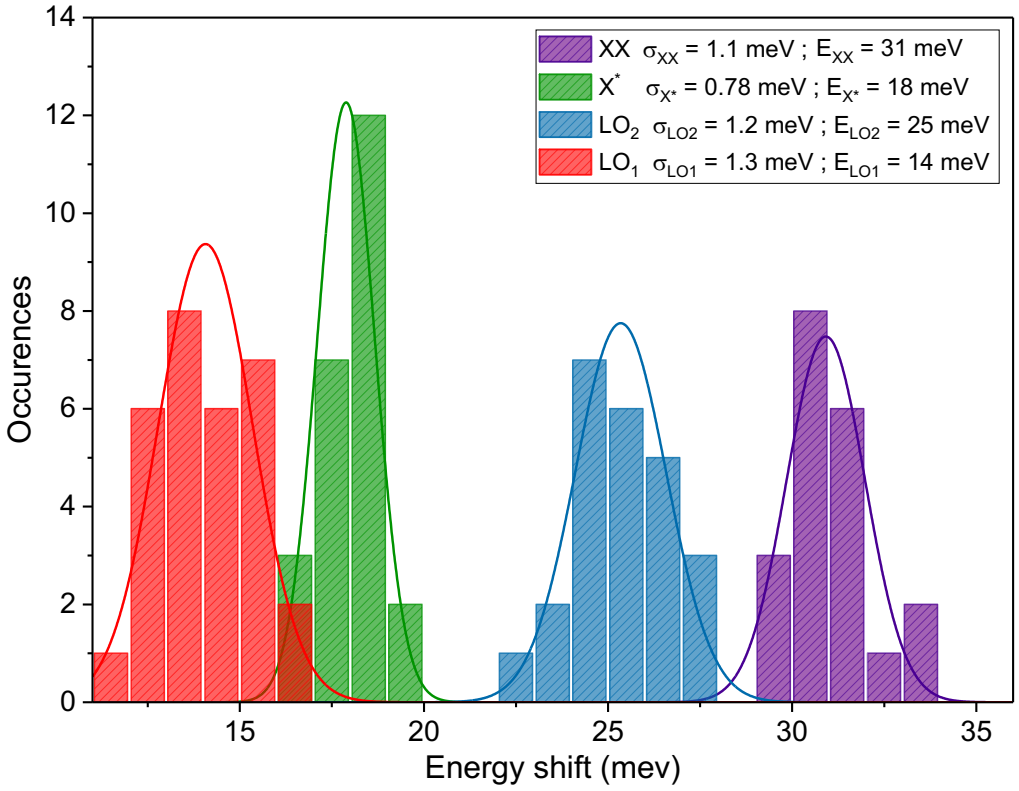

Figure 4.4: Histogram of the optical phonons LO_1 and LO_2 energies alongside the trion X_* and biexciton XX energies. The energy shift is measured from the lowest energy exciton fine structure line. Each population is adjusted with a Gaussian distribution of parameters provided in the labels.

ensembles of NCs due to the inhomogeneous broadening resulting from the dispersity of NC sizes.

To effectively address these exciton-phonon couplings in single $CsPbCl_3$ NCs, it is necessary to isolate a single spectral line from the exciton fine structure (EFS) doublets. This is because the close energy proximity of these lines would lead to their strong overlap at higher temperatures, making the measurements impossible. As demonstrated in Chap. 3, a simple polarizer can be placed in the optical path to carefully select the line of highest intensity, thanks to the cross-polarized property of the EFS doublet lines. Moreover, to ensure that the line of the same single NC is unambiguously followed across the different temperatures of the experiment, the temperature dependence of the peaks energies is monitored for each spectral line and the monotonous evolution of their slope is verified. This monotonous evolution also highlights the absence of a phase transition in the temperature range explored. This can be observed on Fig. 4.5b for four different doublets.

On Fig. 4.5b a blue-shift in energy with respect to the bulk is observed for each line when the temperature increases. The slopes measured here, $\langle\alpha\rangle \approx 0.3$ meV/K, are close to previous values found in $CsPbBr_3$ NCs [120], which indicates a similar influence of the temperature on the lattice

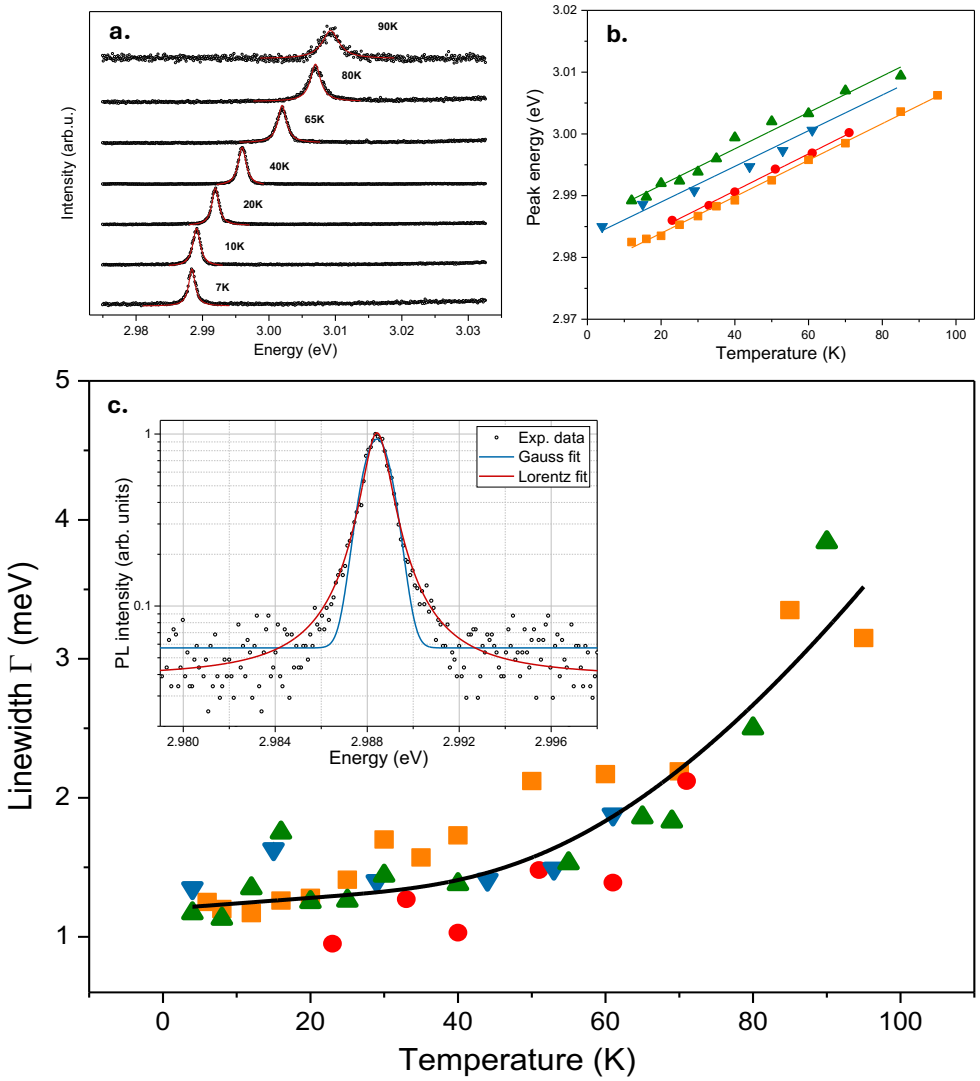

Figure 4.5: **a.** Stacked micro-PL spectra showing the spectral broadening and the blue shift of a single line for different temperatures. **b.** Spectral blue shift of the exciton transition when the temperature is raised for four different NCs. **c.** The linewidth of four selected lines are measured with temperature. The provided adjustment is performed while considering the four sets of data simultaneously using Eq. 4.1. The insert shows a comparison of Gaussian and Lorentzian adjustments to the data on a semi-log scale at 7K.

deformation and therefore on the energy band gap. Furthermore, this value of the parameter α is the same as what was found in the previous chapter while doing the experiment in absorption (see Fig. 3.4). Fig. 4.5c gathers the temperature dependence of the linewidth, $\Gamma(T)$, for the four selected doublet lines, obtained from the full width at half maximum (FWHM) of a Lorentzian fit, as illustrated on Fig. 4.5a.

The homogeneous spectral broadening of an exciton transition can be described as the sum of the broadening due to both acoustic and optical phonons. In LHPs and other semiconductors

the model given in Eq. 4.1 is generally used [198, 200, 82, 208]:

$$\Gamma(T) = \Gamma_0 + \sigma_{ac}T + \Gamma_{LO}n_{LO}(T) \tag{4.1}$$

The first term Γ_0 is temperature-independent and represents either the contribution due to the finite lifetime or the residual inhomogeneous linewidth at $T = 0$ K. When looking at single objects, this contribution is primarily attributed to spectral diffusion. The second term, encompassing the σ_{ac} coupling strength constant, represents the homogeneous broadening resulting from charge-acoustic phonon scattering due to the deformation potential effect. The third term, encompassing the Γ_{LO} constant, involves the LO phonons and their Fröhlich interaction with the carriers (and thus, the exciton) [82, 208, 209, 210]. In Eq. 4.1, the expression for $n_{LO}(T)$ is given by $n_{LO}(T) = 1/(e^{E_{LO}/k_bT} - 1)$ where k_b is the Boltzmann constant and E_{LO} is an average representative energy for the LO phonons [209, 210]. $n_{LO}(T)$ represents the Bose-Einstein occupation number for optical phonons and therefore strongly depends on the temperature. The expression given in Eq. 4.1 was used to fit the $\Gamma(T)$ data of all four selected spectral lines to improve our statistics and highlight an average behavior of the measured broadening.

In the linear 0-40 K temperature range the homogeneous broadening with temperature is essentially driven by the coupling to acoustic phonons. The coupling strength coefficient is measured at $\sigma_{ac} \approx 4$ μeV/K, which is in line with the values usually reported for inorganic LHP NCs (See Tab. 4.1). With no surprise, at temperatures higher than 40 K the scattering due to optical phonons starts to dominate as they follow the Bose-Einstein statistics, explaining the shape of the fitting curve in the 40-100 K temperature range. The best fit provides a value of ~ 25 meV for the Γ_{LO} coupling constant with an optical phonon energy of $E_{LO} = 21$ meV that matches the average value of the LO_1 (14 meV) and LO_2 (26 meV) phonons replicas observed on micro-PL spectra. Extrapolating to room temperature the fit used in Fig. 4.5, the obtained micro-PL linewidth for a $CsPbCl_3$ NC is of the order of 20 meV, comparable to that of equivalent Br-based material, $CsPbBr_3$ [120]. This value establishes a characteristic limit to the spectral width for short-wavelength light-emitting diodes using this material at ambient temperature.

The residual broadening contribution, Γ_0, is close to 1.2 meV, which is even higher than previous measurements made on $CsPbBr_3$ NCs (0.4 meV) [120] and gives a coherence time of the emission of $T_2 \approx 1$ ps at 5 K. Although the excitation power was kept at a low level, these experiments were performed in non-resonant excitation conditions favoring spectral diffusion during the micro-PL measurements due to the generation of a fluctuating charge distribution under photoexcitation. This extremely short coherence time in the chloride compound can be explained by a large concentration of defects observed on the surface of the NCs. These defects can trap or detrap charges thereby modifying the energy of the exciton by Stark effect [121]. For example,

with $CsPbI_3$ NCs and a non-resonnant excitation at 570 nm, Min Xiao and coauthors observed a 200 μeV linewidth [105] *via* conventional micro-PL spectrocopy at 4 K. Under resonnant excitation they later measured emission lines as thin as 11 μeV at 3 K associated to a pure exciton dephasing time T_2^* of 115 ps and limited essentially by the interaction with the acoustic phonons [211]. A better approach to suppress spectral diffusion happening on short time scales is to use interferometry techniques such as correlation Fourier spectroscopy. Using this method, Coolen *et al.* observed a linewidth of 6.5 μeV in CdSe NCs passivated with ZnS at 10 K [212, 213]. Later on, Bawendi and coauthors performed the same type of experiment on $CsPbBr_3$ NCs and measured a linewidth of $\approx$ 20 μeV leading to a coherence time $T_2 \approx T_2^* = 2\hbar/\Gamma =$ 66 ps [207] which, taking the radiative lifetime they measured at $T_1 = 270$ ps gives a ratio $T_2/2T_1 = 0.12$ a value two orders of magnitude higher than for core-shell II-VI NCs. Whether challenging, similar approaches (*i.e* resonant spectroscopies and Fourier correlation spectroscopy) would allow to gain insights into the mechanisms that contribute to the low temperature broadening and now appears as a logical continuation to this work. In particular, resonant PL excitation remains accessible to our group by exploiting the doublet configuration and its cross polarized nature.

Overall, in LHPs, the optical phonon energies revealed by the linewidth broadening of the exciton recombination line with temperature match the values reported with other spectroscopy techniques or numerical methods. Therefore single NC spectroscopy can be considered as a reliable and powerful tool to probe the role of different phonon modes. Tab. 4.1 summarizes the fit parameters values obtained by different groups that performed linewidth measurements with temperature while adjusting experimental data with Eq. 4.1. A wide variety of LHP materials under different forms of samples are listed. The optical phonon coupling constants Γ_{LO} and their associated average energies, measured here in $CsPbCl_3$, as well as those determined in hybrid or all inorganic perovskite materials are almost all of the same order of magnitude, which reflects the polar characteristics of the Pb-halide bonds and the overall ionic character of these materials.

4.3 Unveiling the EFS dark state in $CsPbCl_3$ nanocrystals

The discussion of the exciton fine structure in Chap. 3 focused essentially on the bright states and their energy positions. However, it was also mentioned that the exciton fine structure of LHPs and - $CsPbCl_3$ - also contains an optically non-active state called the 'dark-state'. Although it is weakly coupled to the electromagnetic field, this exciton state can interact with other particles (such as phonons) and have a profound impact on the emission properties of the NC. Therefore, in order to draw a complete picture of the EFS in this semiconductor material, and for its possible use in quantum emission based applications, the determination of the energy position of this state

Material	Sample type	σ_{ac} (μeV/K)	Γ_{LO} (meV)	E_{LO} (meV)	Ref.
$FAPbBr_3$	Single NCs	5 ± 5	52	15.2	[22]
	Polycryst. thin films	0*	61 ± 7	15.3 ± 1.4	[200]
$CsPbBr_3$	Single NCs	8 ± 3	42 ± 13	16	[120]
	Nanowire ensemble	0*	66	19	[202]
	NCs ensemble	8.9	≈ 100	≈ 18	[205]
	Single crystal	32	41.7	22.2	[201]
$MAPbBr_3$	Polycryst. thin films	0*	58 ± 2	$\approx$15	[200]
$FAPbI_3$	Polycryst. thin films	0*	40 ± 5	11.5 ± 1.2	[200]
	Single NCs	< 5	27	10.5 ± 0.8	[198]
$MAPbI_3$	Single crystal	0*	12 ± 2	4.2 ± 0.8	[214]
	Single crystals	93.5 ± 20.5	57 ± 22	16.1 ± 3.4	[215]
	Polycryst. thin films	0*	40 ± 2	≈ 11	[200]
$CsPbCl_3$	Single NCs	4 ± 1.5	25 ± 2	21	[179]

Table 4.1: Parameters obtained by other authors and our group while fitting the emission linewidth broadening in temperature with Eq. 4.1. Different organic and inorganic perovskite materials under several forms are reported. The asterisk after the 0 values in the third column indicates that the parameter has been set to zero for adjustments. In Ref. [200], measurements for MA compounds are done above 80 K. In Ref. [215], data are photocurrent measurements until 80 K.

as well as its impact upon the emission dynamics is necessary.

4.3.1 Magneto optical coupling

The most straightforward strategy to reveal the energy position of a dark state relies on evidencing its spectroscopic signature in magneto-optical experiments performed at the single NC scale [22, 181]. Indeed, *via* Zeeman effect, magnetic fields can induce a coupling between bright and dark state of the EFS. This technique has been commonly used with II-VI materials [216] and later on LHPs [22]. Let us first consider the exciton basis composed of the bright states $|X\rangle$, $|Y\rangle$, and $|Z\rangle$ given by Eq. 4.2 *i.e*:

$$|X\rangle = \frac{|+1\rangle - |-1\rangle}{\sqrt{2}}, \quad |Y\rangle = \frac{|+1\rangle + |-1\rangle}{\sqrt{2}} \quad \text{and} \quad |Z\rangle = |0_B\rangle\,. \tag{4.2}$$

While the dark state reads $|0_D\rangle$. When a magnetic field $\mathbf{B}$ is applied parallel to $|X\rangle$, (the exciton state corresponding to an emission dipole oriented in the X direction) the dark state $|0_D\rangle$ gets

coupled to $|X\rangle$ and their interaction can be described by the following Hamiltonian :

$$H_z = \frac{1}{2}\begin{pmatrix} -\Delta_{BD} & \delta g \mu_B B \\ \delta g \mu_B B & \Delta_{BD} \end{pmatrix} \tag{4.3}$$

Where δg, the coupling parameter, reads $\delta g = g_e - g_h$ and $g_{e(h)}$ is the electron (hole) Landé factor, μ_B, is the Bohr magneton and B the field amplitude. Similar expressions are obtained with a field, B, along the z axis. [61, 217]
The corresponding energies are given by:

$$E_{\pm} = \pm\frac{1}{2}\sqrt{(\Delta_{BD})^2 + (\delta g \mu_B B)^2} \tag{4.4}$$

And the eigenstates Ψ_- and Ψ_+ can be expressed as a function of the θ_B angle as:

$$\Psi_- = \begin{pmatrix} \cos\theta_B \\ \sin\theta_B \end{pmatrix} \quad , \quad \Psi_+ = \begin{pmatrix} -\sin\theta_B \\ \cos\theta_B \end{pmatrix} \quad \text{with: } \tan\theta_B = -\frac{\delta g \mu_B B}{2E_+ + \Delta_{BD}} \tag{4.5}$$

For $B = 0$, one consistently has $E_{\pm} = \pm\frac{\Delta_{BD}}{2}$, $\Psi_- = |0_D\rangle$ and $\Psi_+ = |X\rangle$.The ratio in the emission intensity of the coupled states reads [61]:

$$\frac{I_-}{I_+} = \tan^2\theta_B \approx \left(\frac{\delta g \mu_B B}{2\Delta_{BD}}\right)^2 \tag{4.6}$$

Here, the last approximation holds if the bright-dark energy splitting remains large in front of the characteristic magnetic energy, *i.e.* if $\Delta_{BD} \gg \delta g \mu_B B$.

Eq. 4.6 can then be used to predict the field amplitude required to obtain a measurable emission from the Ψ_- state in a regime where the $(\delta g \mu_B B)$ term remains small in front of Δ_{BD}. Following a recent study providing the Landé factors versus the gap energy in perovskite materials, one expects, for $CsPbCl_3$, $|\delta g| \leq 0.4$ [218]. With $\Delta_{BD} = 10$ meV one finds $B > 86$ T for $I_-/I_+ = 1$ % (whereas $B > 104$ T if $\Delta_{BD} = 12$ meV, assuming the same intensity ratio). A magnetic field of great amplitude is thus required to achieve a significant transfer of oscillator strength toward the dark state, indicating that a more accessible and immediate strategy should be employed to reach a reliable Δ_{BD} estimation. The following paragraph will demonstrate that time resolved PL is an indirect but powerful tool to reach that goal. For comparison, Tamarat *et al.* used magneto-optical spectroscopy to evidence the dark exciton emission in $FAPbBr_3$. With $\delta g \approx 2$ and $\Delta_{BD} = 2.6$ meV, the criteria = 1 % leads to $B = 3.5$ T. At the maximum field used in their study ($B = 7$ T), the ratio is equal to 7 %, in good agreement with the PL spectra provided. [22]

4.3.2 Thermal mixing models

Since magnetic field cannot reveal the EFS dark state in the chloride compound a less direct approach shall be considered. Thanks to the simulations presented in Sec. 3.2.2 the dark state is expected to lay below the bright states at an energy shift of $\sim$ 10 meV. The optical phonons unveiled in the last section have a similar energy, thus the possibility of a thermal mixing between the bright and dark states *via* the emission and/or absorption of optical phonons shall be considered. These phonon assisted thermal mixing models are based on the carrier-phonon interactions described in Chap. 1 and, specifically for LHPs, on a Fröhlich coupling mechanism involving optical phonons. The Hamiltonian describing this interaction does not include a spin part while any transfer between bright and dark states requires a spin flip between orthogonal exciton states which is forbidden. Fortunately, some authors have shown that the spin-orbit coupling - which plays a major role in LHP materials due to the presence of the heavy lead element - can mix orthogonal exciton states of different J and J_z [219]. In this section, two models commonly used to describe such behaviors will be introduced and applied afterwards to adjust the emission dynamics using time resolved PL spectroscopy as well as its evolution with temperature.

One Phonon model

The first model that is considered is sketched on Fig. 4.6. It involves the thermal mixing of the bright and dark state by absorption and emission of an optical phonon. Here, the band edge exciton fine structure is represented by only three levels: a bright state $|B\rangle$ that represents by itself the EFS bright state multiplet (*i.e.*, the splitting between the bright states is neglected) a zero exciton ground state written $|G\rangle$ and a dark state $|D\rangle$ that is assumed to be located underneath the bright one. Let us note that the position of the dark state, *i.e.*, whether located at higher or lower energy than the bright ones was recently the subject of an intense debate in the community. Indeed, an inversion symmetry breaking of the lattice, due to the instability of the organic FA^+,MA^+ or Cs^+ ion, was predicted by Becker and coauthors in 2018 for LHP NCs [21] and would have induced a Rashba effect resulting in the inversion of the exciton fine structure placing the dark state at higher energy. On the other hand, the absence of this effect would have left the EFS untouched with its dark state at lower energy. The debate was closed by Tamarat and coauthors [22] when they performed magneto-optical spectroscopy on $FAPbBr_3$ NCs and directly revealed the position of the dark state at $\approx$ 2.3 meV underneath the lowest energy bright one.

In the framework of the one-phonon model, both bright and dark states can decay towards $|G\rangle$ through radiative and non-radiative recombination with associated Γ_B and Γ_D decay rates, respectively and $\Gamma_B \gg \Gamma_D$. At zero temperature the bright-state population can also sponta-

neously decay towards the dark-state *via* the emission of a phonon, a process to which a rate γ_0 is associated and called "spin flip rate" since a carrier spin is reversed in the process from J=1 to J=0. At a temperature T, the occupation of a given phonon mode follows the Bose-Einstein statistics given by $n = 1/(\exp^{E_{LO_i}/k_bT} - 1)$ where E_{LO_i} is the energy of an optical phonon. The bright and dark states are thus thermalized by the absorption $|D\rangle \rightarrow |B\rangle$ or emission $|B\rangle \rightarrow |D\rangle$ of optical phonons with associated rates $\gamma_\uparrow$ and $\gamma_\downarrow$ respectively and energies matching the bright-dark splitting *i.e.* Δ_{BD}.

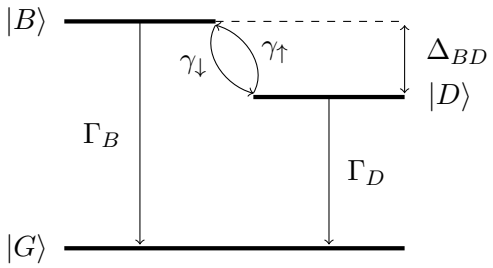

Figure 4.6: Energy levels diagram of the one phonon model. The bright and dark state thermalization is assured by the absorption ($\gamma_\uparrow$) or emission ($\gamma_\downarrow$) of an optical phonon with energy matching the bright-dark splitting Δ_{BD}.

In this model, the rates $\gamma_\uparrow$ and $\gamma_\downarrow$ take the following expressions:

$$\begin{cases} \gamma_\uparrow = \gamma_0 n \\ \gamma_\downarrow = \gamma_0 (n+1) \end{cases} \tag{4.7}$$

Considering all the processes that fill or empty the bright and dark states, their populations, ρ_B and ρ_D respectively, are given by a set of coupled differential equations that can be written under the form of a matrix equation $\dot{\boldsymbol{\rho}} = \mathcal{M}\boldsymbol{\rho}$:

$$\begin{pmatrix} \dot{\rho_B} \\ \dot{\rho_D} \end{pmatrix} = \begin{pmatrix} -\Gamma_B - \gamma_\downarrow & \gamma_\uparrow \\ \gamma_\downarrow & -\Gamma_D - \gamma_\uparrow \end{pmatrix} \begin{pmatrix} \rho_B \\ \rho_D \end{pmatrix} \tag{4.8}$$

The general solution of Eq. 4.8 is written as a sum of exponential decay functions such as:

$$\boldsymbol{\rho}(t) = A_1 \exp^{-\Gamma_L t} \mathbf{u_L} + A_2 \exp^{-\Gamma_S t} \mathbf{u_S} \tag{4.9}$$

Where $A_{1,2}$ are the amplitudes of each component and $\mathbf{u_{S,L}}$ the eigenvectors of matrix $\mathcal{M}$. Their detailed expressions are provided in Appendix C by Eq. C.6 and Eq. C.7 and depend on the parameters Γ_B, Γ_D, $\gamma_\downarrow$ and $\gamma_\uparrow$. The eigenvalues Γ_S and Γ_L of $\mathcal{M}$ are given by:

$$\Gamma_{S,L} = \frac{1}{2}\left[\Gamma_B + \Gamma_D + \gamma_\uparrow + \gamma_\downarrow \pm \sqrt{(\Gamma_B - \Gamma_D + \gamma_\downarrow - \gamma_\uparrow)^2 + 4\gamma_\uparrow\gamma_\downarrow}\right] \tag{4.10}$$

Finally, the total PL intensity is given by: $\sum_i \eta_i \Gamma_i \rho_i$ where η_i is the fluorescence quantum yield of state i. Considering here that $\eta_B = \eta_D = 1$ it gives:

$$I(t) = A_L \exp^{-\Gamma_L t} + A_S \exp^{-\Gamma_S t} \tag{4.11}$$

Where the expressions of $A_{S,L}$ are provided in Appendix C by Eq. C.11 and Eq. C.12.

Thus, in the model, the PL time decays are expected to have a characteristic bi-exponential profile with rate constants exhibiting the temperature behavior provided by Eq. 4.10. The analytical expressions of Γ_S and Γ_L are quite complex even for this rather basic model and contain, *a priori*, 4 unknown parameters ($\Gamma_B, \Gamma_D, \gamma_0$ and Δ_{BD}). Fortunately, using their asymptotic limits in temperature and the relations Eq. C.14 and Eq. C.15 provided in Appendix C (that express the combination of the rates with hyperbolic functions) one has access to the different parameters of the model:

- **Low temperature limit:** In this regime $k_B T \ll E_{LO} = \Delta_{BD}$. Using Eq. C.14 and Eq. C.15 this implies that coth and $\sinh^{-1}$ approach 1 and 0 respectively. Thus Γ_S and Γ_L are given in this limit by:

$$\Gamma_L = \Gamma_D \quad \text{and} \quad \Gamma_S = \Gamma_B + \gamma_0 \tag{4.12}$$

- **High temperature limit:** Here $k_B T \gg E_{LO} = \Delta_{BD}$ implies that both coth and $\sinh^{-1}$ functions approach $2k_b T/\Delta_{BD}$ leading to the expressions:

$$\Gamma_L = \frac{\Gamma_B + \Gamma_D}{2} \simeq \frac{\Gamma_B}{2} \quad \text{and} \quad \Gamma_S = \frac{2\gamma_0 k_b T}{\Delta_{BD}} \tag{4.13}$$

If it can be reached, the high temperature limit is extremely interesting since it provides a direct access to the radiative lifetime of the bright state Γ_B. Once this parameter is known, γ_0 can be obtained from the measurement of Γ_S at low temperature using the relation, $\gamma_0 = \Gamma_S - \Gamma_B$ and the relaxation scheme is fully characterized. The remaining challenge then is to link the absolute values of the extracted characteristic constants to the microscopic properties of the material. Furthermore, the energy gap, Δ_{BD}, is extracted from the adjustment of the $\Gamma_L(T)$ curve, which is usually the easiest to obtain experimentally (since the time constants involved are in the range 0.1 ns - 100 ns).

Two Phonon model

The second thermal mixing model considered in this work and illustrated on Fig. 4.7 was first presented in LHPs by Fu and coauthors [198] and inspired by the work of Tsitsishvili *et al.* [220]. Here the thermalization between the bright and dark state is realized with an upward and a downward mechanism both involving a two phonon process. The EFS is still represented by the degenerated bright multiplet $|B\rangle$, the lower energy dark state $|D\rangle$ and the zero exciton ground state as with the one phonon model. In this model, a higher energy state representing the exciton-phonon coupling and labelled $|E\rangle$ on the level diagram is also considered. This state plays the role of an intermediate between the absorption and emission of the LO_1 and LO_2 phonons.

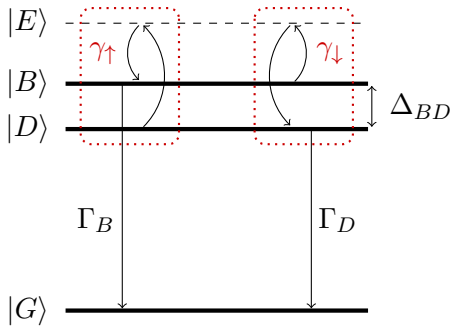

Figure 4.7: Energy levels diagram of the two phonons model introduced in the main text. The bright and dark state thermalisation is assured by a two phonon process: the $|D\rangle \rightarrow |B\rangle$ transition is done by absorbing a first phonon LO_2 towards an intermediate state followed by the emission of a LO_1 phonon towards the bright state. The $|B\rangle \rightarrow |D\rangle$ is the reversed process with phonon energies $E_{LO_2} > E_{LO_1}$.

Although the detailed expressions of the up and downward transition rates $\gamma_\uparrow$ and $\gamma_\downarrow$ are different from the one phonon model, the matrix rate equation $\dot{\boldsymbol{\rho}} = \mathcal{M}\boldsymbol{\rho}$ and the eigenvalues $\Gamma_{S,L}$ have the same general forms and are given by Eq. 4.8 and Eq. 4.10 respectively. As a consequence, PL decays having two components are also expected in the frame of this two phonon model.

The transition rates $\gamma_\uparrow$ and $\gamma_\downarrow$ now correspond to the absorption of a LO_2 (LO_1) phonon followed by the emission of a LO_1 (LO_2) phonon for $\gamma_\uparrow$ ($\gamma_\downarrow$). To be consistent with the first section of this Chapter the same notation for the optical phonons is kept recalling that $E_{LO_2} > E_{LO_1}$. The rates $\gamma_\uparrow$ and $\gamma_\downarrow$ thus take the following expressions:

$$\begin{cases} \gamma_\uparrow = \gamma_0 n_{LO_2}(n_{LO_1} + 1) \\ \gamma_\downarrow = \gamma_0 n_{LO_1}(n_{LO_2} + 1) \end{cases} \tag{4.14}$$

Where $n_{LO_i} = 1/(\exp^{E_{LOi}/k_bT} - 1)$ is the Bose-Einstein occupation number for phonon LO_i and γ_0 is a two phonon thermal mixing rate. Eq. C.17, C.18 provide useful expressions regarding the combination of these two rates with hyperbolic functions and are used in the following. Once again the low and high temperature limits give access to the parameters of the model:

- **Low temperature limit:** In this regime $k_BT \ll \Delta_{BD}$. This implies that coth and $\sinh^{-1}$ approach 1 and 0 respectively in Eq. C.17, C.18 which gives the following limits:

$$\Gamma_L = \Gamma_D \quad \text{and} \quad \Gamma_S = \Gamma_B \tag{4.15}$$

- **High temperature limit:** $k_BT \gg \Delta_{BD}$ implies that both coth and $\sinh^{-1}$ functions approach $2k_bT/\Delta_{BD}$ in Eq. C.17, C.18 leading to the expressions:

$$\Gamma_L = \frac{\Gamma_B + \Gamma_D}{2} \simeq \frac{\Gamma_B}{2} \quad \text{and} \quad \Gamma_S \simeq \frac{\Gamma_B}{2} + \frac{2\gamma_0(k_bT)^2}{E_{LO_1}E_{LO_2}} \tag{4.16}$$

4.3.3 Time resolved PL measurements

Having now described the relaxation models that will be used to reveal the bright-dark energy splitting, the time resolved photoluminescence (TRPL) measurements performed will be introduced and the emission dynamics of $CsPbCl_3$ NCs should be compared to these models.

Ideally, TRPL measurements are performed on single NCs to eliminate averaging effects [22] and directly access the emission rates of the different levels composing the EFS. Performing these experiments on single objects implies that they have a sufficient PL quantum yield and are stable under illumination for long periods of acquisition time (ideally more than $\sim$ 30 minutes). Such measurements have already been performed in the past on CdSe NCs by several groups and more recently on LHPs, notably on $FAPbI_3$ and $CsPbBr_3$ by the groups of Tamarat and Diederichs [198, 199]. Unfortunately, it became quickly evident in this work that such measurements would not be achievable on single $CsPbCl_3$ NCs due to their low PL quantum yield and stability under illumination. Measurements on NCs ensembles are therefore necessary and a good compromise is found by investigating samples from moderately diluted solutions while addressing the dynamics of lines with reduced inhomogeneous broadening. This approach combines a satisfactory signal-to-noise ratio with an acceptable level of averaging (over the NCs sizes) across the considered PL line width. Typically, bands centered around 3.025 eV were selected while making sure their widths remained below 40 meV. This guaranteed that only NCs with a $\Delta L \approx 2$ nm around the mean edge length $\langle L \rangle = 8$ nm in the cubic shape approximation contributed to the emission response collected. Consequently, in these experiments, populations of NCs with different average sizes could be selected so that a 'moderately' averaged picture should be obtained.

On Fig. 4.9 the PL decay dynamics of $CsPbCl_3$ NCs are presented for different temperatures spanning from 7 K to 110 K. These curves represent an averaged PL decay over $\sim$ 20-30 meV (Fig. 4.8). Analysing these decays, a mono exponential behavior with a rather constant characteristic time $\tau \approx 30$ ps is first noticed in the 7 - 40 K followed by the emergence of a second

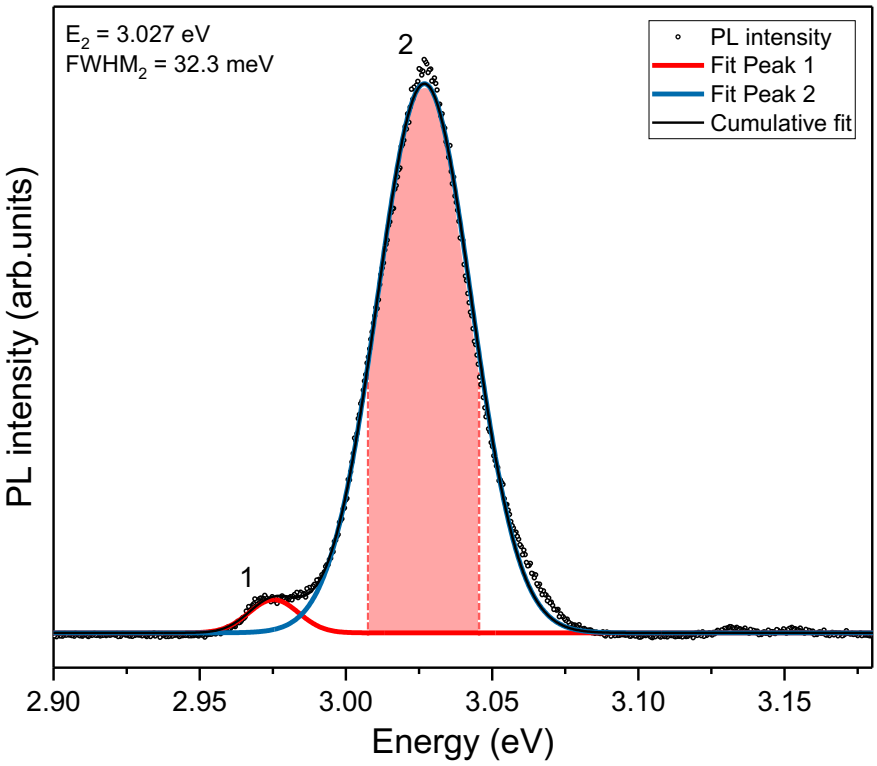

Figure 4.8: Typical PL emission profile used for emission dynamics experiments. The area colored in red represent the bandwidth of $\sim$ 30 meV typically selected during the measurements. Within this type of profile a rather homogeneous sub-population of the NCs is considered during the experiments (λ_{exc} = 395 nm).

exponential decay above 40 - 50 K typically. This bi-exponential behavior is observed distinctly in the 50 – 150 K interval and its rather sudden appearance represents the signature of a thermally activated process that can be described by the models presented in the last subsection. Therefore, in the following Γ_S and Γ_L will be used to denote the rates associated with the short and long components of such decays.

Adjustment to the one phonon model

From the bi-exponential intensity decays presented on Fig. 4.9 both short and long rates $\Gamma_S = 1/\tau_S$ and $\Gamma_L = 1/\tau_L$ are extracted and reported on Fig. 4.10 as black dot and triangle symbols representing the experimental data. Alongside these measurements and in the framework of the one phonon model, both theoretical rates are plotted using Eq. 4.12 for comparison and represented as blue and red solid lines. The phonon energy E_{LO_1} which, in this model, represents the Δ_{BD} energy splitting is taken at 14.2 meV to match with the energy of the first measured LO_1 optical phonon mode presented in Sec. 4.1. As stated before, in the one phonon thermal mixing model, the radiative rate of the bright state Γ_B can be obtained from the high temperature limit $\Gamma_L \approx \Gamma_B/2$.

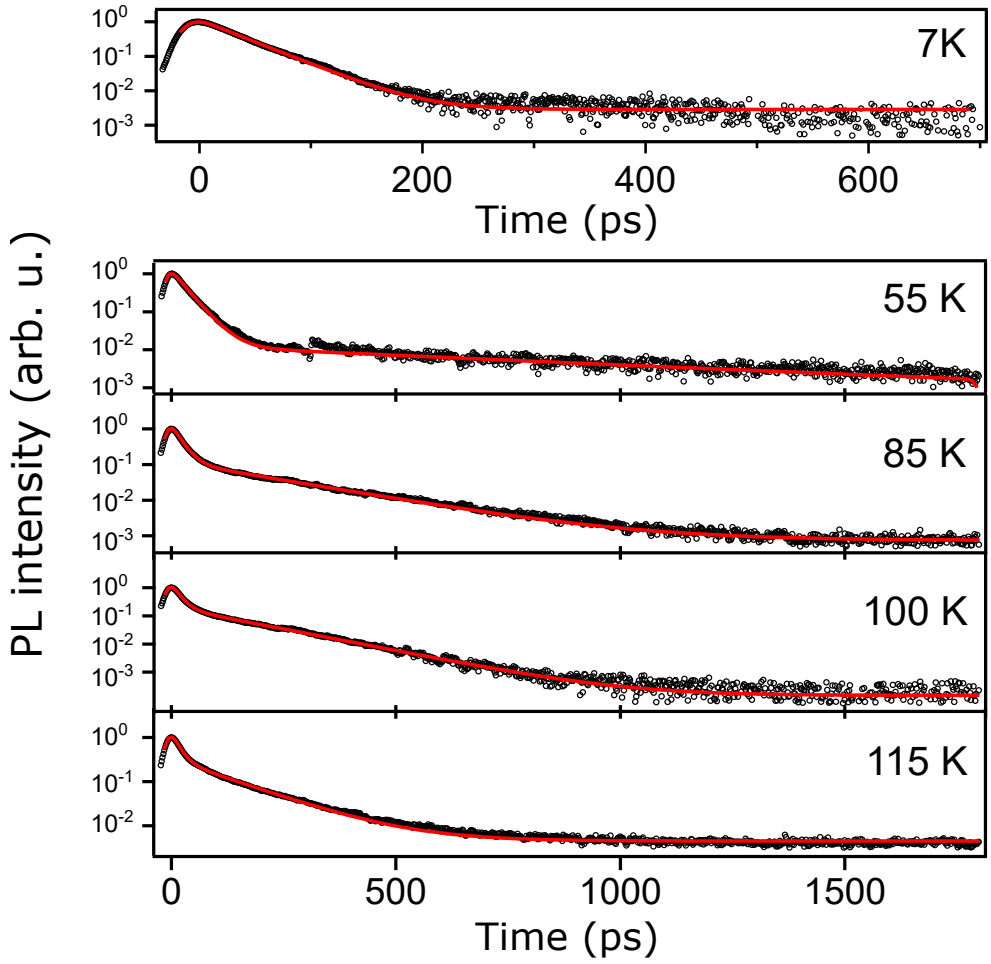

Figure 4.9: PL intensity decays, in semi-log scale, obtained by TRPL measurements with the streak camera for different temperatures. The experimental points (black dots) are adjusted with a biexponential decay function (red lines). Note that since the 7 K decay appears purely monoexponential it was captured on a smaller time domain. The decays were recorded in the automatic "background substraction mode" of the camera software, allowing to get rid of the photocathode response imperfection and identify the real background at negative delays. In this way reliable decay times values can be extracted.

Therefore, noticing that Γ_L measurements saturate around 10 to 15 ns^{-1}, a first approximation of Γ_B between 20 to 30 ns^{-1} can be found. Considering that at low temperature $\Gamma_S = \Gamma_B + \gamma_0$ the range where γ_0 should be located spans between 2 to 5 ns^{-1}, a rather large value that is characteristic of II-VI semiconductors based NCs [221]. Finally, the low temperature limit of Γ_L directly provides the value of Γ_D. While the temperature is increased progressively, the amplitude of Γ_L increases accordingly. This behavior relies on the Bose Einstein occupation number of the LO_1 phonon and therefore on its energy and the temperature. If the energy of the phonon is small enough (which is generally the case when this thermal mixing model is applied to II-VI NCs with acoustic phonons [222]) the process is activated at lower temperatures. On the other hand, and in the present situation, the high energy of the optical phonon taking part in the process (14.2

meV) does not allow any back transfer from the dark state before 35 K typically (corresponding, at this temperature, to a rate $\gamma_{\uparrow}$= 0.2 ns^{-1}). Combining this remark to the fact that, in the chloride compound the PLQY typically ranges from 5-10%, Γ_D cannot be probed directly, even by strongly increasing the experimental acquisition times. This lack of available measurement does not constitute a large problem because Γ_D is usually a few orders of magnitude weaker than the other parameters and has therefore a poor influence on the relaxation scheme except at very low temperatures. Indeed, by keeping all the other parameters constant, changing realistically its value from 10^{-3} ns^{-1} to 10^{-1} ns^{-1} does not change the general shape of Γ_S and affects Γ_L only in the 0-35 K temperature range, setting its low temperature limit. With these considerations in mind, Γ_D is fixed at 2×10^{-2} ns^{-1} in the following, to match the value measured by Fu *et al.* on $FAPbI_3$.

In Fig. 4.10, each plot was generated using fixed bright and dark state radiative rates of Γ_B =28 ns^{-1} and Γ_D =0.02 ns^{-1}, with different values of the spin flip rate γ_0 set to 2, 6 and 100 ns^{-1} for graphs a, b, and c, respectively. One can see that the experimental data points are poorly adjusted by these curves, regardless of the selected values of γ_0.

The last plot, located on the lower right, represents a concerted adjustment of both curves and was created by fixing E_{LO_1} and Γ_D while allowing Γ_B and γ_0 to take values within the ranges of 20 to 30 ns^{-1} and 2 to 6 ns^{-1} respectively. Although the concerted adjustments show a slight improvement, they still fail to match the high and low temperature limits of Γ_L and Γ_S measured experimentally. At this point, it must be recognized that this thermal mixing model is not adapted. In fact, with inorganic perovskites NCs it has failed to reproduce the experimental data multiple times [22] revealing that the model of a direct bright to dark state phonon assisted relaxation is not appropriate. A possible explanation could originate from the fact that the bright-dark energy splitting do not resonate with an optical (or, of course, acoustic for that matter) phonon having the proper energy (*i.e* the energy that perfectly matches the bright-dark splitting). However, some studies have shown that even when a phonon is found at the right energy, the fact that these quasi-particles usually do not carry angular momentum prohibits any one phonon spin relaxation mechanisms [181, 223].

Adjustment to the two phonon model

Although the bright-dark one phonon assisted spin relaxation model cannot explain the PL dynamics of $CsPbCl_3$ NCs, it was clearly evidenced in the last section that the bi-exponential nature of the PL is a thermally activated process. Therefore, to explain this dynamical behavior and the population transfers between bright and dark sub-levels this section proposes to adjust the Raman-like two phonons thermal mixing model to our experimental data. Despite the fact that

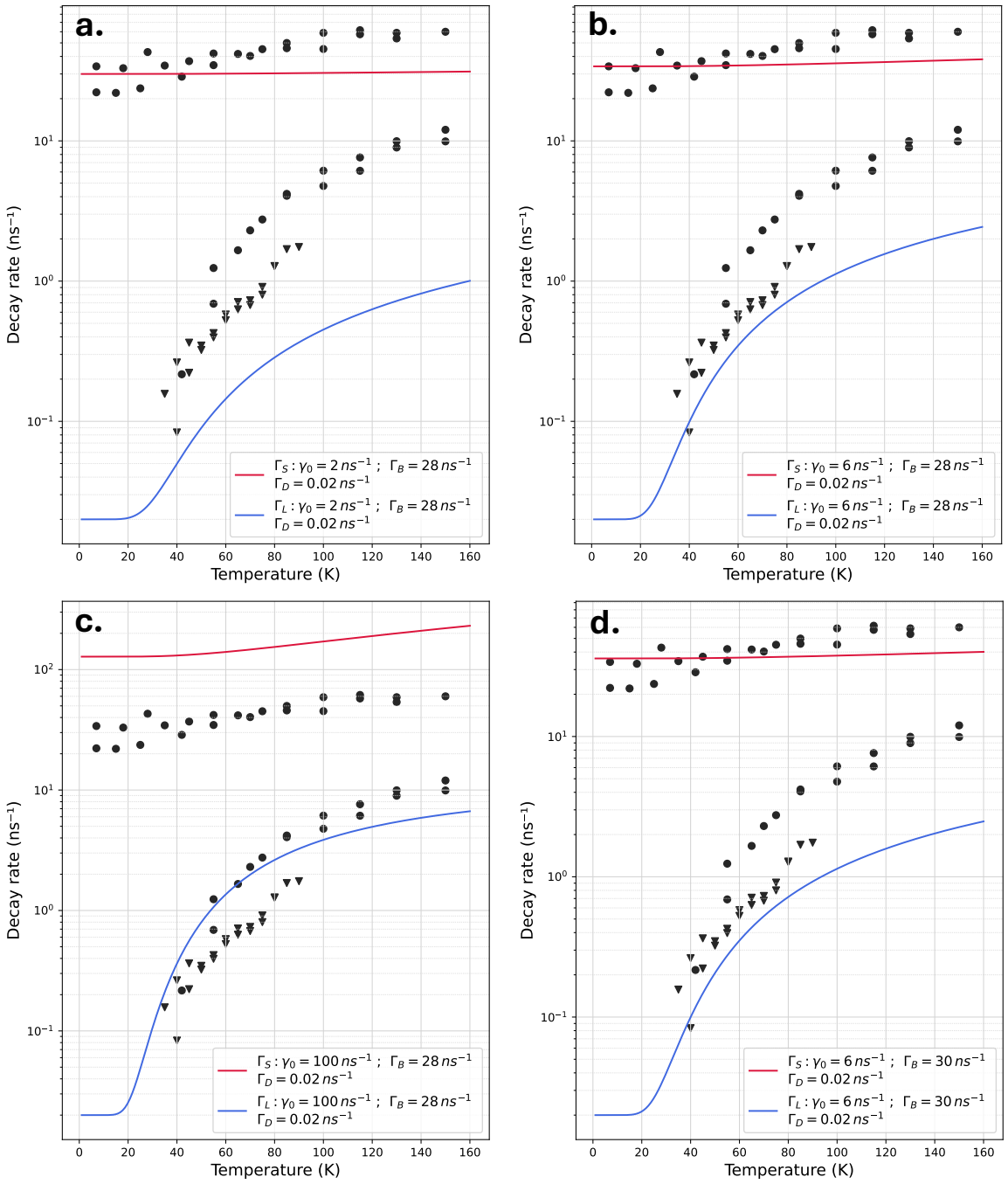

Figure 4.10: Evolution of the Γ_S and Γ_L rates with temperature. The black dots and triangles represent the data acquired by TRPL measurements with the Streak camera and the TCSPC respectively. For the TCSPC measurements the excitation wavelength is 405 nm and a repetition rate of 4 MHz is chosen. The red and blue lines represent the adjustments of Γ_S and Γ_L respectively to the one phonon model. Note that the plots **a, b** and **c** are attempts to adjust the experimental points 'manually' while **d** represents the best concerted adjustment to the measurements.

it does not bring strong microscopic insights into the coupling mechanism, this model has, so far, proved to efficiently reproduce exciton emission dynamics of LHP NCs [71, 198, 199].

The left side of Fig. 4.11 gives once again both Γ_S and Γ_L sets of data points acquired on several $CsPbCl_3$ NCs as a function of the temperature (black dots) alongside their adjustment with the two phonon model as red and blue solid lines. To adjust the experimental points, there is now five parameters to optimize: the intrinsic lifetimes of the bright and dark states (Γ_B and Γ_D, respectively), the longitudinal optical phonon energies, with an energy difference that matches the EFS bright-dark splitting, *i.e.*, $\Delta_{BD} = E_{LO_2} - E_{LO_1}$, and the two-phonon mixing rate, γ_0, that appears in the direct and back transfer rate expressions ($\gamma_\uparrow$ and $\gamma_\downarrow$, respectively) of Eq. 4.14. These transfer rates are themselves determined under the hypothesis that the phonon bath defines the thermal equilibrium [198].

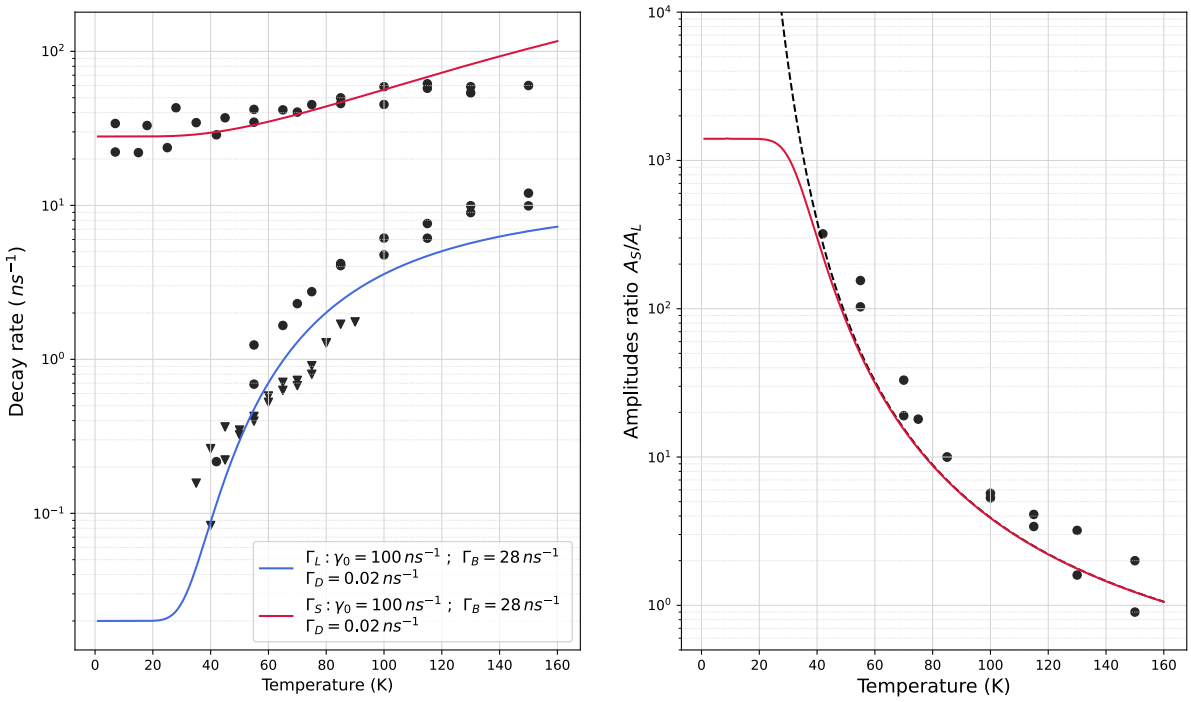

Figure 4.11: Left side: Evolution of the Γ_S and Γ_L rates with temperature. The black dots and triangles represent the data acquired by TRPL measurements with the Streak camera and the TCSPC respectively. The red and blue lines are the adjustments of Γ_S and Γ_L respectively to the two phonon model. Right side: Evolution of the measured (black dots) and calculated (red line) amplitude ratio A_S/A_L with the temperature. The dashed black line is the calculated ratio with $\Gamma_D = 10^{-9}$ ns^{-1} (quasi infinitely long-lived dark state).

In this model, at low temperature (*i.e*, $k_bT \ll \Delta E_{BD}$), Γ_B identifies with Γ_S so that it is unambiguously extracted from the data. In the following $\Gamma_B \approx 28$ ns^{-1} is used as the average of the Γ_S values measured at 7 K, in satisfactory agreement with the results from other studies in NC ensembles [224]. In the same vein as the one phonon model, the energy of the LO_1 phonon was set to the value acquired from the Raman spectroscopy measurements and the replicas observed on micro-PL experiments presented in Sec. 4.1 and 4.2, that is, E_{LO1}= 14.2 meV while the energy of the optical phonon E_{LO2} was left unconstrained to give some flexibility to the adjustment.

The low temperature limit of Γ_L should provide, as with the one phonon model, the value of Γ_D but it is still found inaccessible below 40 K. Since the values extracted from the adjustment procedure presented in the following are again found quasi-insensitive to Γ_D variations provided they are lower than $\approx 10^{-1}$ ns^{-1}, the upper value $\Gamma_D \approx 2.0\times10^{-2}$ ns^{-1} will be used again. From that point, the concerted fit of Γ_S and Γ_L leads to $\Delta_{BD} \approx 10.7 \pm 3.0$ meV and $\gamma_0 \approx 100 \pm 10$ ns^{-1} when including all the (Γ_S, Γ_L) pairs within the 7 – 120 K range so as to avoid the drop in Γ_S above 120 K that is not consistent with the model predictions (see the red fit in Fig. 4.11). The Δ_{BD} estimation is thus in good agreement with the theoretical results presented in Chap. 3 that predicted an energy separation of 13.2 meV between the dark state and the center of the bright doublet for cubic-shaped NCs of average edge length, $\langle L \rangle$, of 8 nm.

The graph presented on the right side of Fig. 4.11 displays the experimental variation of the amplitude ratio A_S/A_L (short and long component weight in the PL decay). The solid and dashed lines are calculations using the analytic expressions of $A_{S,L}$ provided in Appendix C. At low temperature it is found that A_S/A_L approaches Γ_B/Γ_D (for equally populated states at t = 0) which using the values discussed above gives $A_S/A_L \approx 1400$ as seen with the red curve. The calculated amplitude ratio also provides a good adjustment to the data which increases the confidence in the selected set of parameters. As a side note, one can see that by changing the value of Γ_D from 2×10^{-2} ns^{-1} to 10^{-9} ns^{-1} (quasi infinitely long-lived dark state) the amplitude ratio stays unaffected in the temperature range in which an access to Γ_L is actually possible. The adjustment in Fig. 4.11 is thus quasi-independent of the Γ_D value provided it is below the threshold value of $\Gamma_D = 2\times10^{-2}$ ns^{-1}

Using a bi-exponential decay function and the parameters Γ_S, Γ_L, A_S and A_L discussed in this section the PL decay is plotted on Fig. 4.12 for different temperatures. The experimental PL decays of Fig. 4.9 are well reproduced with this set of parameters and, interestingly, one can see that by considering the best experimental signal to noise ratio of $\sim$ 5000 obtained with the time correlated single photon counter equipment the bi-exponential character of these simulated decays only reveals itself around $\sim$ 35 K which is consistent with our measurements.

Finally, the global consistency of the approach is further supported by the following arguments:

- The proximity of E_{LO2} to the energy of the LO phonon identified by Calistru and coauthors at 24.8 meV [170] in bulk and by our group at 25 meV [179] in NCs (see Sec. 4.1.2) must be noted. The best adjustments displayed in Fig. 4.11 provide a value of 25 meV for E_{LO2}. Therefore, the "bright–dark coupling" is mediated by a two-phonon process operating close to resonance, likely explaining in part the relatively large value obtained for the two phonon mixing rate γ_0 [198, 220].

- It was verified that the overall PL intensity remained nearly constant within the studied in-

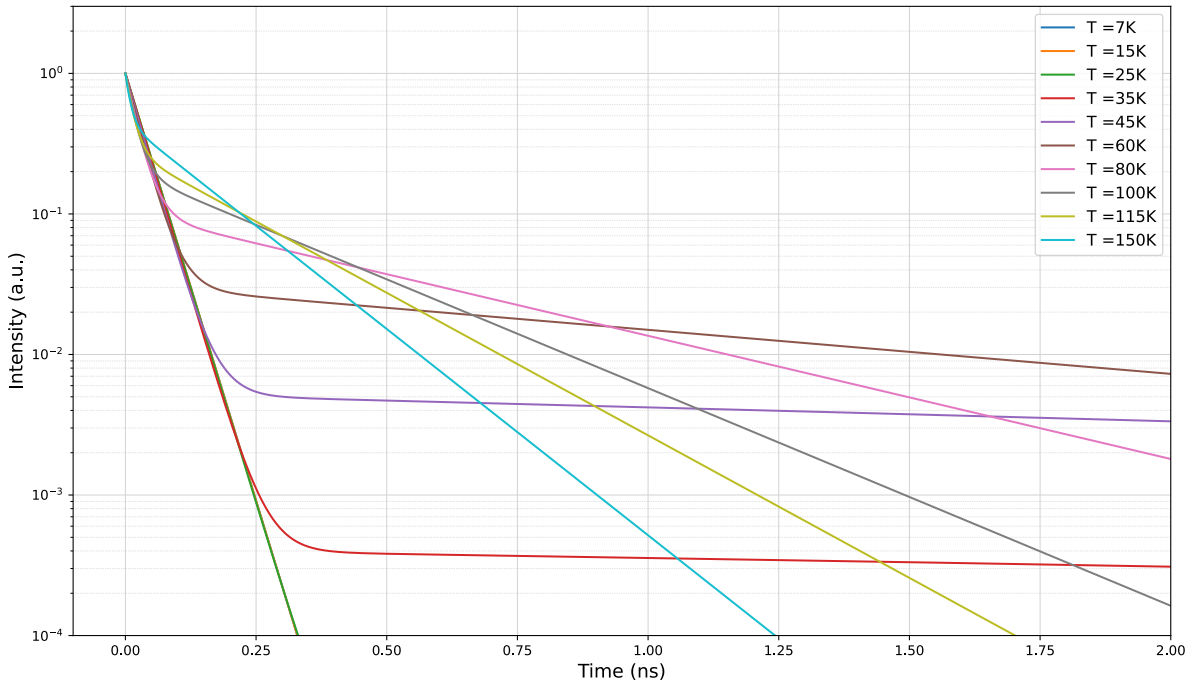

Figure 4.12: Simulated PL decays, in semi-log scale, obtained with the two phonon model for different temperatures. For these simulations the expression for the PL intensity given by Eq. 4.11 was used with Γ_S, Γ_L given by Eq. 4.10 and A_S, A_L given by Eq. C.11 and Eq. C.12 respectively. The parameters of Fig. 4.11 were also used *i.e:* $\Gamma_B = 28$ ns^{-1} ; $\Gamma_D = 2{\times}10^{-2}$ ns^{-1} ; $\gamma_0 = 10^2$ ns^{-1}.

terval, allowing the analysis to be performed while keeping the Γ_B and Γ_D rates independent of temperature, Γ_B and Γ_D incorporating both the radiative and nonradiative components of the relaxation.

4.3.4 Interpretation in terms of excited states thermalization

The two phonon relaxation model also helps to describe the thermalization of the bright excited states following their photogeneration. In the chloride compound, the involved phonons have a rather high energy compared to the phonons that were shown to play a role in other inorganic lead halide perovkite nanocrystals [22]. Efficient population of such phonon states will thus require a higher temperature, which questions the dynamics of the underlying thermalization process as the temperature varies.

In the model, the occupation numbers n_{LO_1} and n_{LO_2} remain small as long as T do not reaches T_{act} such that $k_b T_{act} \sim E_{LO_1}, E_{LO_2}$. In agreement, $\gamma_\uparrow$ and $\gamma_\downarrow$, that govern the bright-dark balance (see Eq. 4.14) should affect the bright and dark population relaxation dynamics only when n_{LO_1} and n_{LO_2} gain significant weight.

Fig. 4.13 shows how the dark and bright state population evolve in time - for different temperatures - in a fictious 3 levels system having no radiative / non radiative losses ($\Gamma_B = \Gamma_D = 0$) but

keeping the γ_0 value that led to the adjustment of the time resolved PL shown before (see Figure 4.12).

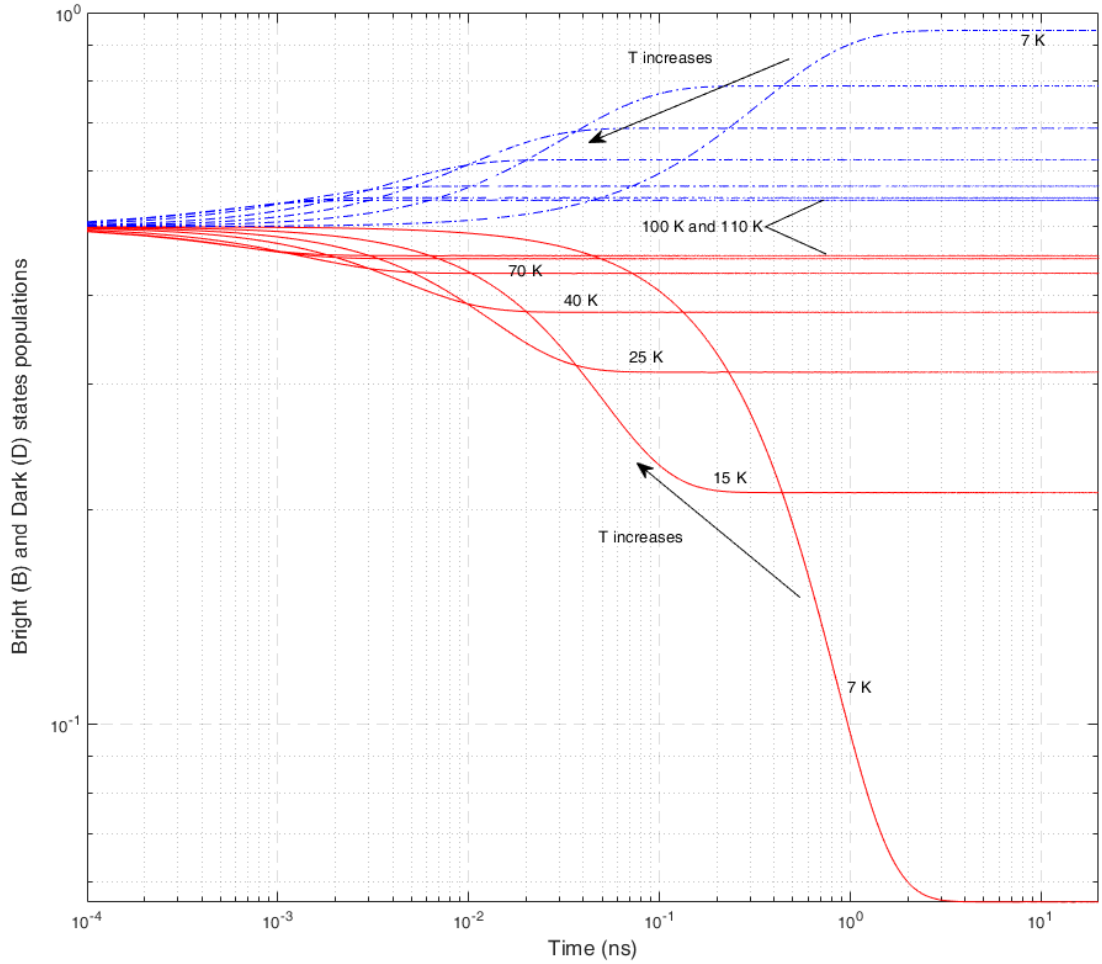

Figure 4.13: Evolution of the bright (red curves) and dark (blue curves) state populations over time for different temperatures. The bright and dark states are considered to be equally populated at t=0 due to the non-resonant nature of the excitation. The radiative channels are suppressed in order to estimate the time required to obtain stationnary populations in an equivalent 'radiatively uncoupled' system and reach an estimation of the underlying thermalization dynamics.

The thermalization of the bright-dark system is obtained as soon as the bright and dark populations become stationnary. The process is low at 7 K compared to the bright state effective relaxation time for it takes $\sim$ 3-4 ns ($\sim 100/\Gamma_B$, Γ_B previously determined) but it is seen to be already of the order of $\tau_0 = 1/\gamma_0$ at 40 K and only lasts a fraction of τ_0 ($\sim$ 3 ps) at 110 K. It is clear that, at $T = T_{lattice} = 7$ K, the bright state exciton cannot relax easily to the energetically lower dark state and thus should be considered as a 'hot' excitation.

Similar conditions have been reported recently in 2D perovskite materials [185]. In these systems the bright-dark energy separation does not match any of the differences that can be formed from the *LO* phonon energies. As a consequence, to scatter from the bright to the dark

state (using a high energy LO phonon), hot excitons need to be formed with considerable excess of energy ($\sim$ 15 meV typically) to compensate for the bright-dark energy splitting. Therefore, optically excited bright excitons first need to scatter up to higher momenta states by absorption of acoustic phonons, a process that is unlikely at cryogenic temperature (phonon bottleneck effect).

In the studied $CsPbCl_3$ NCs, the situation is different because the LO phonon modes allowing to relax the energy are present but still need to be populated, which leads to a slow Bright $\leftrightarrow$ Dark equilibrium dynamics (*i.e* slow thermalization) at low temperature. Below 10 K the thermalization process takes a time that is much longer - one order of magnitude typically - than the effective lifetime $1/\Gamma_B$, so that the bright states relax essentially through photon emission. In the fictional (not coupled to light) model, 50 % of the initial bright state population has not relaxed after a time equal to 10 times the lifetime of the actual bright states (see Fig. 4.13) when considering our set of parameters for γ_0, E_{LO_1} and E_{LO_2}. In other words, the thermalization time estimated on the basis of the fictional 3-levels system equals $1/\Gamma_B$ at $\sim$ 30 K. It is thus reasonable to think that around 10 K all the components of the bright EFS sublevels - in particular the higher energy component in triplets - should be clearly visible whatever their energy separations with the lower energy EFS states.

4.3.5 $CsPbCl_3$ NCs among the LHP family: some general considerations and trends

The work presented in this Chapter and the previous one highlights the complexity of EFS studies in lead halide perovskites and reveals a dependence on multiple factors, such as the absolute size of the NCs, their level of shape anisotropy and the nature of their dielectric environment. As stressed in a recent theoretical work [186], the amplitude of the EFS bright-dark splitting Δ_{BD} is especially sensitive to dielectric mismatch and essentially unaltered by the shape anisotropy whereas the bright-bright splitting Δ_{BB} shows schematically the opposite behavior. Drawing comparisons between existing LHP compounds and their EFS measured experimentally or calculated numerically should thus be made with great caution. In that regard, a good starting point for discussion consists of investigating a situation of reference with a reduced number of varying parameters allowing comparisons to be made between the different materials. Such situation is defined with the following characteristics:

- Crystal phase: the symmetry of the lattice is fixed to D_{4h} (tetragonal crystal phase).
- Cubic shapes: *i.e* shape anisotropy is not considered and the NCs are modelled as perfect cubes with edge lengths matching their average size.
- Absence of dielectric mismatch: the dielectric constant between the NC and its environment

is considered to be the same inside and outside and therefore $\eta = 0$.

- Weak confinement limit of excitons: only large NCs with edge lengths, L, such that $L \gg a_X$ are considered.

At this stage, the reader may recognize that this reference situation closely resembles a description of the bulk material making it difficult to distinguish between the two. The main difference lies in the chosen regime of confinement: while the bulk material is not subject to quantum confinement and necessitates the exchange interaction (EI) theory to account for k-dispersion [**pikus_exchange_nodate**, 55], the theoretical treatment of the intermediate and weak confinement limit follows the one presented in this work. Considering the situation described above and the model developed in this work for describing the exciton fine structure (EFS) through the combined effects of electron-hole exchange interaction and crystal field (see Chap. 1), both Δ_{BD} and Δ_{BB} splittings increase as the exciton Bohr radius (binding energy) decreases (increases). Fig. 4.14 illustrates these trends for different halide perovskites, with energy splittings calculated using Eq. 1.42 and data from Tab. 4.2.

The adjustments of the EFS splittings as a function of a_X assuming power laws provide an exponent $\kappa_{BD} = -2.67 \pm 0.09$ for Δ_{BD}, while a lower value is found for κ_{BB} with $\kappa_{BB} = -1.66 \pm 0.33$ (and with a larger dispersion in the experimental set). Both splittings are made of two contributions associated with the long range (LR) and short range (SR) parts of the e-h EI. In the expression of Δ_{BD} (see Eq. 1.42), the SR contribution is proportional to the short-range parameter, Δ_{SR}, shown to scale with a quasi-universal a_X^{-3} dependence regardless of the considered semiconducting material [54]. In contrast, the LR component of Δ_{BD} does not show this a_X^{-3} dependency. Moreover, the ratio of the SR term in the whole Δ_{BD} splitting varies from 23 % to 51 % when the halogen is changed from iodide to chloride in inorganic compounds (a similar evolution is observed for compounds containing organic cations). These two facts are responsible for the deviation of Δ_{BD} from the characteristic Δ_{SR} behavior ($\kappa_{BD} \neq$ -3). In Tab. 4.2 the same trend is noticed regarding the ratio of the SR contribution to the whole Δ_{BB}.

The $CsPbCl_3$ NCs exciton properties studied here are characteristic of the intermediate confinement regime. The experimental value for Δ_{BD} deduced from the PL dynamics presented in the last section is coherently found higher in these NCs with respect to the bulk ($\approx$ 30 % increase). For comparison, one order of magnitude enhancements have been observed in the iodide and bromide compounds in which a larger confinement range could be explored (see Fig. 4.14). Finally, for a given level of confinement (ratio $\langle L \rangle / 2a_X$) there is also a clear trend associated with the increase of Δ_{BD} in more tightly bound excitons. This is clearly seen when inspecting the cesium–lead series with Δ_{BD} passing from 2 meV in the iodide compound ($\langle L \rangle / 2a_X \approx 0.7$) to 3.5 meV in the bromide compound ($\langle L \rangle / 2a_X \approx 0.9$) to reach 10.7 meV in the chloride sys-

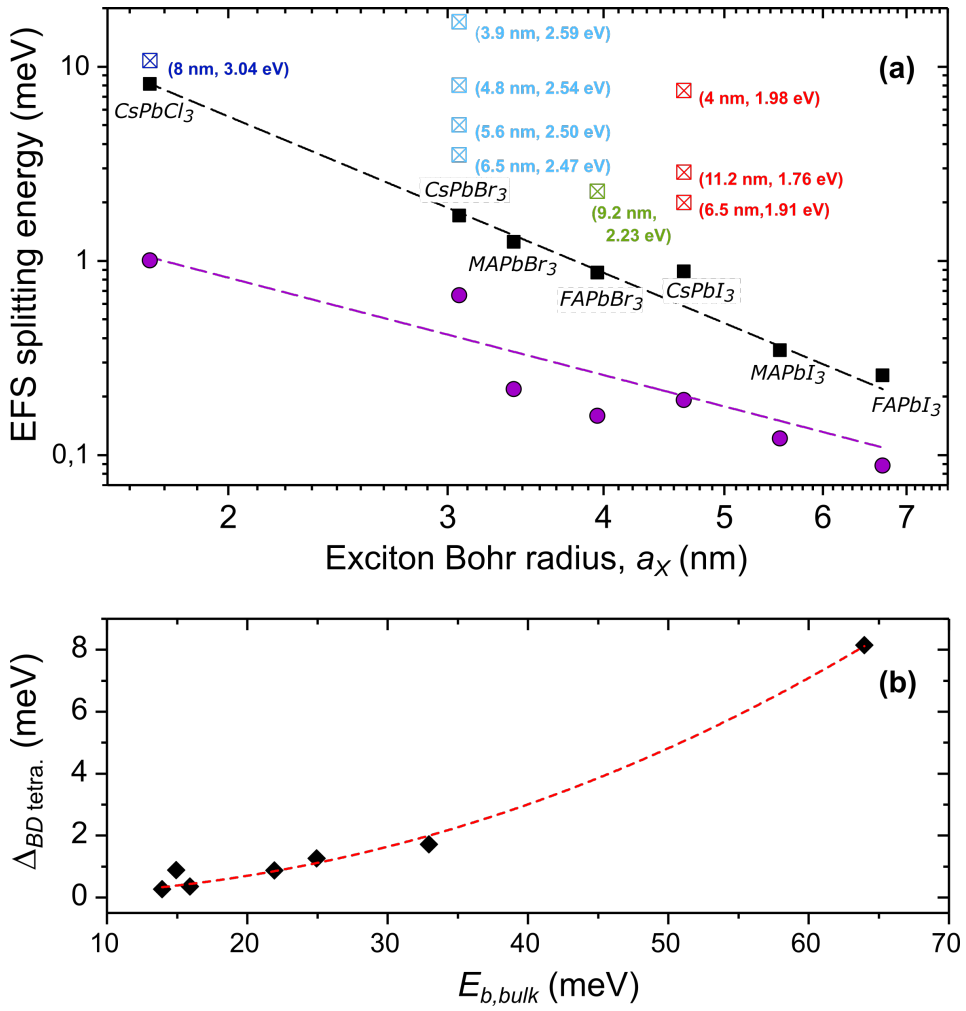

Figure 4.14: (a) Calculated bright-bright, Δ_{BB} (filled circles), and bright-dark, Δ_{BD} (filled squares), energy splittings as a function of the exciton Bohr radius, a_X, in hybrid and fully inorganic lead halide perovskite materials. All materials are treated in the same limit used as a reference: weak confinement of NCs (edge length, $L \gg a_X$), $\eta = 0$, and cubic shape. Adjustments using power laws (dashed lines) are also displayed: $\Delta_{BB} = c_{BB}(a_X/a_0)^{\kappa_{BB}}$ and $\Delta E_{BD} = c_{BD}(a_X/a_0)^{\kappa_{BD}}$ ($c_{BB} = 2.56 \pm 0.70$ meV, $\kappa_{BB} = -1.66 \pm 0.33$, $c_{BD} = 35.0 \pm 1.9$ meV, $\kappa_{BD} = -2.67 \pm 0.09$, and $a_0 = 1$ nm). The values are summarized in Tab. 4.2 as well as the physical parameters used for the calculations. For comparison, experimental ΔE_{BD} values for NCs are also reported (cross-tagged squares) as well as the associated NC edge length and exciton transition energy (text labels) for $CsPbI_3$, $FAPbBr_3$, $CsPbBr_3$, and $CsPbCl_3$ (this work). (b) Plot of the dark state-bright state splitting, ΔE_{BD}, as a function of the exciton binding energy (weak confinement limit, $\eta = 0$, isotropic shape): the dashed line is an adjustment proposal using a power law according to $\Delta_{BD} = c_1(E_{b,\text{bulk}}/E_b^0)^{c_2}$ with $c_1 = (1.2 \pm 0.6) \times 10^{-3}$ meV, $c_2 = 2.1 \pm 0.1$, and $E_b^0 = 1$ meV.

tem (though $\langle L \rangle / 2a_X \approx 2.3$ is comparatively - and adversely - much higher). The same trend is observed with regard to the evolution of Δ_{BB} even if its dependence on the shape anisotropy parameter is more pronounced and makes comparisons less straightforward, further confirming that the physics of the band edge exciton is mostly determined by the exchange interaction model

in those semiconducting materials.

Material (D_{4h})	E_g (eV)	ϵ_1	ϵ_X	a_X (nm)	$E_{b,bulk}$ (meV)	μ	θ (deg)	Δ_{SR} (meV)	$E_{P_{S,z}}$ (eV)	$E_{P_{S,\rho}}$ (eV)	Δ_{BD} (meV)	Δ_{BB} (meV)	Δ_{BD}^{SR} (%)	Δ_{BB}^{LR} (%)
$FAPbI_3$	1.501	11.4	6.4	6.7	14	0.090	39.76	0.076	18.25	19.04	0.26	0.09	26	29
$MAPbI_3$	1.653	10.9	6.6	5.5	16	0.104	40.06	0.134	15.36	16.45	0.35	0.12	34	40
$CsPbI_3$	1.738	10	4.3	4.6	15	0.114	39.56	0.229	17.03	19.81	0.88	0.19	23	39
$FAPbBr_3$	2.233	8.6	5.7	4.0	22	0.115	37.67	0.369	19.75	20.01	0.87	0.16	40	42
$MAPbBr_3$	2.292	7.5	5.6	3.4	25	0.117	38.14	0.586	16.45	17.97	1.25	0.22	43	58
$CsPbBr_3$	2.342	7.3	4.5	3.1	33	0.126	40.4	0.793	15.65	16.8	1.71	0.66	40	47
$CsPbCl_3$	3.056	6.6	4.1	1.7	64	0.202	37.65	4.422	15.24	17.21	8.15	1.01	51	79

Table 4.2: E_g is the energy gap [149]; ϵ_1 is the bulk dielectric constant; ϵ_X is the dielectric constant at the exciton resonance; a_X is the exciton Bohr radius; $E_{b,bulk}$ is the exciton binding energy [149]; μ is the exciton reduced mass [149]; θ is the Bloch function parameter (see [54, 175]); Δ_{SR} is the bulk short-range (SR) splitting parameter (calculated using $\Delta_{SR} = \frac{2C}{3\pi a_X^3}$, with $C = 107.6$ meV.nm^3 [54]); $E_{P_{S,\rho}}$ and $E_{P_{S,z}}$ are Kane energies [54, 175]; Δ_{BD} and Δ_{BB} are bright-dark and bright-bright EFS splittings, respectively, of excitons in the weak confinement limit in the absence of dielectric mismatch and for a cubic shape (*i.e.*, edge lengths, $L \gg a_X$), calculated with equation 1.39. Note that ϵ_1, ϵ_X, and $a_X = \frac{\epsilon_1 a_0}{\mu}$ ($a_0 = 0.529$ Å), $E_{P_{S,\rho}}$, $E_{P_{S,z}}$, and θ values are specific to the tetragonal crystal phase. Δ_{BD}^{SR} (Δ_{BB}^{LR}) is the contribution of the short-range (long-range) term to the Δ_{BD} (Δ_{BB} respectively) EFS splitting.

Conclusion

In this Chapter, the exciton-phonon interactions in $CsPbCl_3$ NCs were explored in great detail. The characterization of $CsPbCl_3$ NCs by micro-Raman experiments revealed optical phonon modes with energies closely matching previous results on bulk $CsPbCl_3$. Further confirmation of these optical phonon energies came from micro-PL spectroscopy measurements, which displayed Stokes-shifted phonon replicas indicative of exciton-phonon couplings. Individual peaks from single NCs' exciton fine structure (EFS) doublets were isolated, and their linewidths were analyzed as a function of increasing temperature. The linewidth broadenings were found to follow the model established by Segall and coauthors. This analysis provided the acoustic and optical constants of exciton-phonon couplings in $CsPbCl_3$, which aligned well with other measurements made on lead halide perovskites. Extrapolating the single NC linewidth measurements to room temperature suggested a linewidth of approximately 20 meV, comparable to that of similar Br-based materials. This value imposes a characteristic limit on the spectral width for short-wavelength light-emitting diodes using $CsPbCl_3$ at ambient temperature. However, further investigations are necessary to understand the residual broadening attributed to spectral diffusion caused by the electrostatic environment of the NCs.

Regarding the exciton fine structure, the general agreement between the theoretical model presented in Chapter 1 and 3 and the experimental output were confirmed through the determination of Δ_{BD} *via* complementary time-resolved experiments performed on NC ensembles with low size

dispersion. Although the thermal mixing model used in this work has an empirical character it has proved to furnish a powerful description of population transfers between bright and dark excitons in LHP NCs. The theoretical description, which attributes a major role to the dielectric confinement-enhanced electron-hole interaction (incorporating both the short and long-range terms), allows for advanced predictions regarding the EFS state organization and polarization for the chloride compound. Additionally, this work is supported by a general approach suitable for a refined description of any lead-chloride counterpart incorporating all physically relevant ingredients. The chloride compound is noted as emblematic of a system supporting the most tightly bound excitons in the lead-based perovskite family. The results obtained (largest amplitude of Δ_{BB} and Δ_{BD}) enhance the general understanding of the relationship between exciton binding and EFS structure in this class of semiconductors, perfectly conforming to the predictions of the electron-hole interaction model when examining the extensive range of available results in the field.

CHAPTER

$FAPbBr_3$ NANOCRYSTALS IN MESOPOROUS MATRICES

5

Throughout this manuscript, the outstanding optical properties of lead halide perovskite (LHP) nanocrystals (NCs) were praised on multiple occasions. However, films made from deposited perovskite NCs are highly sensitive to environmental factors and can degrade rapidly under exposure to moisture, oxygen, light or heat [17, 18]. This instability poses challenges for the long-term reliability of optoelectronic devices based on these materials. Regarding the fabrication of films of isolated NCs for fundamental studies or advanced quantum applications, the situation can be even worse. Upon dilution of the colloidal solutions of NCs, the interactions between the NCs and the ligands are reduced, which eventually leads to the desorption of ligands from the NC surface and to the aggregation of the NCs or the formation of bulk material thus loosing the benefits of quantum confinement.

To address these challenges, new fabrication strategies have been developed or adapted. One promising technique is encapsulation, where NCs are embedded within a protective matrix composed of materials such as polymers (PMMA or polystyrene), silica, or alumina, which shields the NCs from environmental degradation and enhances their stability. Among these encapsulation approaches, mesoporous silica matrices have emerged as a promising solution. Indeed, some research groups have demonstrated that NCs can be synthesized directly within their pores without the need of capping ligands, thereby protecting the NCs from the environment [225].

This final Chapter is dedicated to the study of these systems using another type of perovskite NC, the hybrid organic-inorganic $FAPbBr_3$. The first section characterizes this new sys-

tem through optical spectroscopy, focusing on low $FAPbBr_3$ NC content samples to determine if the NCs can be effectively isolated within the hosting matrix. Moreover, mesoporous matrices enable the trapping of various sizes and quantities of NCs within their pores. The absence of ligands and the close proximity of NCs within the pores open the door to collective behaviors, from amplified spontaneous emission to energy transfers, which are also briefly explored in this chapter. Although the work presented here is less accomplished than the previous chapters, it introduces an intriguing new system with high potential for application to various types of LHP NCs, offering new opportunities for the development of stable optoelectronic devices with adjustable NC densities.

5.1 Mesoporous matrices for isolated emitters

A mesoporous matrix is a type of material structure that contains a complex assemblage of voids of sizes in the nanometer to the tens of nanometer range that can be thought of as having a "sponge-like" structure at the nanoscale. These systems are usually made from metal oxide materials such as silica SiO_2 or titanium dioxide TiO_2. Depending on the fabrication process and the final use of these materials, the pores can be inter-connected or not. Mesoporous matrices have been employed to grow NCs directly into their pores using either gas or solution-phase impregnation methods and without the need of organic capping ligands [225, 226, 227, 228, 229]. This growth strategy presents the advantage of a fine control over the final size of the NCs, the size of the pores setting a limit to the NCs growth [225]. Additionally, the matrix can act as a protective barrier against threats of the environment such as water or other polar molecules, that have been shown to degrade the NCs chemical stability and their opto-electronic properties [96]. Further protection can also be realised by dip coating the impregnated matrices into PMMA to seal off the pores [230], which can be advantageous specially on the shallow surfaces of the material. Finally, the absence of ligands enhances the proximity of the NCs in the matrix which is desirable for the investigation of charge transfers, non linear effects or simply for the fundamental study of "bare NCs" [228, 225].

The II-VI semiconductors such as CdSe were the first kind of NCs to be implemented into mesoporous matrices [231, 232, 233] but the presence of trap states deep into their band gaps associated to the difficulty to grow an inorganic capping layer to passivate their surfaces inside the matrix pores made these semiconductors poor candidates for such uses. On the contrary, perovskite NCs have the advantage of a defect tolerant structure: although still present, the trap states are located inside or at close proximity to the conduction and valence band [234]. Thus, trap states in perovskite NCs generally not alter the optical properties and passivating inorganic layers are unnecessary. LHP NCs grown that way have demonstrated great PL properties, such

as a broad tunability of their emission, narrow linewidths and high PL-quantum yields that is photo-stable over long periods of time [230, 226].

The systems under focus in this chapter are mesoporous matrices made out of silica beads and filled with NCs. Fig. 5.1 shows an illustration of such system.

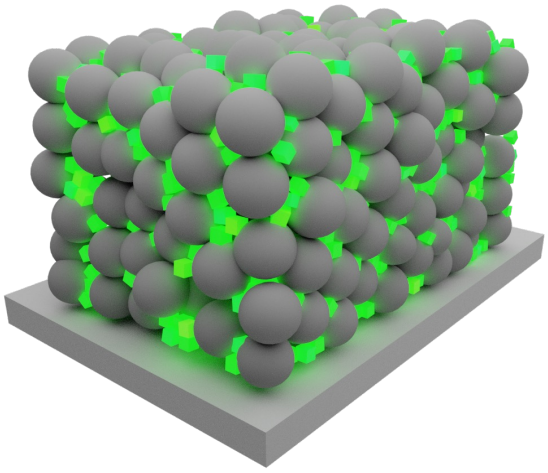

Figure 5.1: Illustration of the mesoporous matrix filled with $FAPbBr_3$ NCs studied in this chapter. The gray spheres of diameter $\sim$ 30 nm represent the silica beads while the NCs are depicted as the smaller green cubes of average edge legnth $L = 9$ nm.

In this structure, the spaces left in between the silica beads create a network of voids in which the perovskite NCs are grown. The fabrication procedure can be described into two main steps:

- First, the silica bead matrix is made. These 30 nm diameter beads are bought directly from a chemicals supplier under the form of a suspension solution in methanol and water. Their size is specifically chosen to be well below the wavelength of visible light to avoid light scattering effects and keep the film transparent. A glass substrate is then dip coated into this solution which triggers the coalescence of a layer of beads onto the surface. The process is repeated $\sim$ 7 times in order to obtain a $\sim$ 200 nm thickness layer, and the substrate is then thermally treated at 450°C to eliminate any solvent left.

- Once the mesoporous matrix is ready, a solution containing DMSO and the formamidinium bromide (FABr) and lead bromide ($PbBr_2$) precursors at the desired concentration in a 1:1 molar ratio is spin coated for 60s on the substrate to prevent the formation of a bulk perovskite overlayer. The precursors infiltrate the porous matrix and the sample is thermally treated at 100°C for an hour to fully eliminate the DMSO which triggers the cristalization of the precusors into NCs, directly inside the pores of the matrix.

The samples studied in this chapter were prepared by the team of Pr. Hernan Miguez at the Institute of Materials Science of Sevilla as part of a new collaboration with our research group.

In this work, several samples were investigated with different concentration of precursors. For clarity, these samples will be referred in the following as "X % sample" meaning that the sample was prepared with a solution containing a X % concentration of precursors by total weight.

5.1.1 Presentation of the system under study: Ensemble optical properties

Following the procedure of the previous chapters, let us first discuss the ensemble optical properties of this new system. Fig. 5.2 presents the absorption and PL spectra of a 30 % sample (panel **c.**) alongside the simulated exciton binding energy (panel **a.**) following the description of strong and weak confinement provided by Sercel *et al.* in [55].

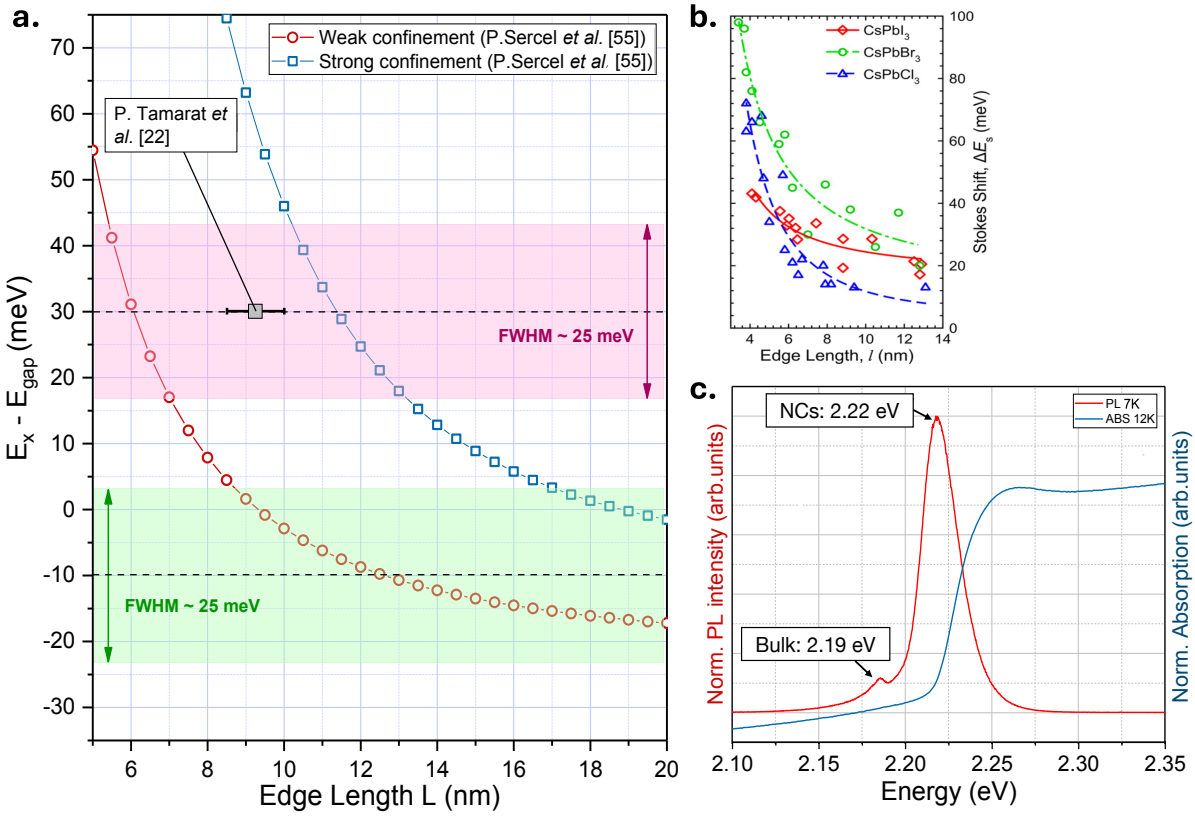

Figure 5.2: **a.** Simulated exciton shift $E_X - E_{gap}$ (E_{gap} = 2.23 eV being the bulk band gap) for strong (blue curve) weak (red curve) confinement regime in LHPs (adapted from P. Sercel *et al.* [55]). The green shaded area is centered around $E_X - E_{gap} = E_{max,PL} - E_{gap}$ (its width corresponding to the one measured on the PL spectrum of panel **c.**) and the red shaded area around $E_X - E_{gap} = E_{max,PL} - E_{gap} + \Delta_{SS}$ (with Δ_{SS} = 40 meV). The grey square, that falls in the center of the red area is the absorption transition energy measured by P. Tamarat *et al.* on FAPbBr$_3$ NCs of $\langle L \rangle$ = 9.2 nm [22]. **b.** Stokes shifts *vs* NC edge length, measured on the different all inorganic LHPs by Brennnan *et al.* [177]. **c.** Low temperature PL (red line) and absorption (blue line) spectra of a sample of FAPbBr$_3$ NCs embedded in the mesoporous silica matrix. The solution used to make this sample contained a 30 wt% concentration of precursors, resulting in a high density of NCs within the pores of the hosting matrix.

The absorption spectrum (blue solid line of panel **c.**) captured at 12 K reveals a poorly resolved single resonance around 2.27 eV. The PL spectrum presents on the other hand two well defined peaks at 2.19 and 2.22 eV. From the results of Ibrahim Dar *et al.* [235] obtained on bulk $FAPbBr_3$, the low energy peak observed on this spectrum is most likely due to the emission of bulk like NCs. Moreover, following the work of Tamarat and coauthors on films of deposited solutions of colloidal $FAPbBr_3$ NCs [22], the high-energy PL peak is attributed to the optical response of confined NCs of sizes laying around 9 nm. Given the low amplitude of the energy difference between the bulk and NCs PL peaks (34 meV) and the fact that the exciton Bohr radius was measured at $a_X = 4$ nm in this material (*i.e.* $L/a_X = 2.25$) a weak to intermediate quantum confinement regime should be considered here to describe the NCs (see panel **a.** of Fig. 5.2). The main PL resonance experiences a red shift estimated at $\sim$ 40 meV although this value might be slightly over estimated due to the poor definition of the absorption resonance. As a matter of comparison, Brennan *et al.* measured a Stokes shift of $\sim$ 30 - 35 meV on individual inorganic $CsPbBr_3$ NCs of 9 nm edge length (see panel **c.**).

5.1.2 Toward single object spectroscopy

The primary objectives of studying a system of NCs encapsulated in a mesoporous matrix was to determine whether this approach could effectively lead to an easy isolation of the NCs, ensure their long-term stability within the matrix, and eventually create a medium containing single photon emitters that could facilitate a deterministic integration within photonic components designed to collect the emission. To achieve this, samples were specifically designed from solutions containing a lower concentration of precursors (3%, 1%, and 0.5%). The procedure followed otherwise the description provided at the beginning of this section. Fig. 5.3 presents the typical PL spectra observed on the 3% sample.

The reduction of the precursors concentration appears to have had the desired effect. Indeed, the PL signals exhibit a multitude of dispersed peaks with a larger representation of NCs subject to low confinement, emitting at approximately 2.20 to 2.24 eV. At these energies, the PL signal likely originates from the sum of multiple single object responses. Several high intensity peaks, however, show linewidths that are already comparable to fine structure emission lines of individual objects, *i.e.* around the meV range. The sample is likely to have a lower concentration of "strongly" confined objects, which, associated with the lowering of the precursors concentration, allows for the observation of emitters that are almost isolated.

Since the lowering of the precursors concentration appears to have a positive impact, it was decided to carry out experiments on the 0.5 % sample. Unfortunately, on this sample, the distribution of the NCs was found to be extremely heterogeneous, with small areas responding with the

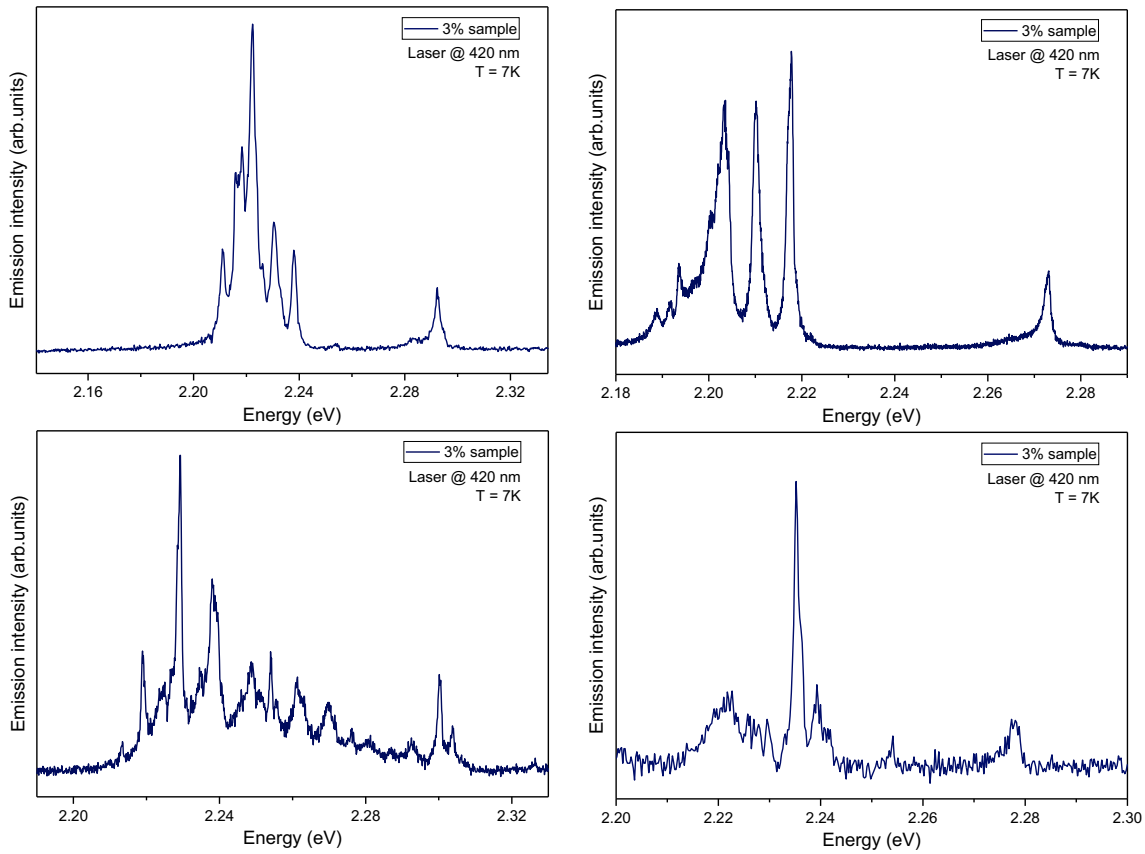

Figure 5.3: Typical emission spectra of encapsulated FAPbBr$_3$ NCs captured at T = 7 K across different regions of the 3% sample.

PL emission of large NC ensembles and the vast majority of the sample showing no emission at all. This effect is not yet understood but was observed repeatedly. It seems that there is a threshold in the precursors concentration below which the NC synthesis does not occur homogeneously.

Finally, the best compromise was found with the 1 % sample. Although most areas were still densely packed with NCs, a few regions were identified where the observation of single NCs was possible. Some spectra captured in such regions are presented in Fig. 5.4. The PL signal should now appear very familiar to the reader, as it is characteristic of the observation of single LHP NCs with EFS doublets and triplets of linewidths below the meV. The splittings between these fine structure peaks also match with previous work performed on isolated FAPbBr$_3$ NCs [22]. As a first impression and in a very qualitative manner, the emission appears to be more stable as compared to drop-casted films of NCs surrounded by ligands. Indeed even though the samples were brought from room to cryogenic temperatures and excited at moderate power for several days, the repeated observation of the EFS signature was still possible. This is likely due to a protective role played by the silica beads matrix against environmental threats such as moisture. Recently, Hernan Miguez *et al.* demonstrated that this stability of the emission could be further enhanced by dip-coating

the samples into a polymer solution such as PMMA [230]. Let us emphasize that the single NC responses are only observed at an energy significantly higher than the energy associated to the PL maximum (see Fig. 5.2), where the largest population is expected. As with films, the dilution mechanism also "operates" in the energy domain thanks to the dilution in energy in the wings of the distribution. Hence, the method does not seem to open better perspectives in separating the NCs composing the major population having the largest homogeneity.

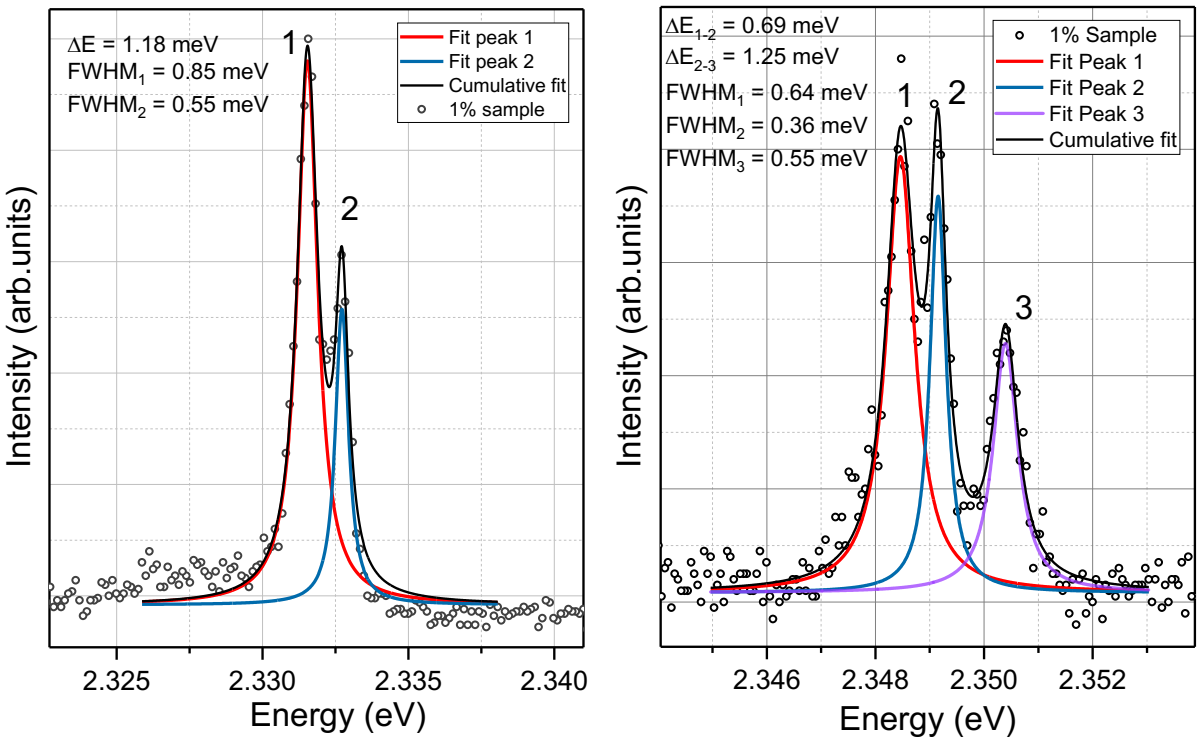

Figure 5.4: PL spectra of individual emitters acquired on the 1% sample at T = 7 K. The colored solid lines are Lorentzian fits. The linewidths and energy splitting values are reported in the figure panels.

In summary, these preliminary results indicate that using solutions of low precursor concentration to grow isolated LHP NCs within mesoporous matrices has mixed outcomes. While this approach successfully isolated a few single NCs and allowed for the observation of exciton fine structure responses, it did not prove to be more effective for this purpose than the films made from drop-casted solutions of colloidal NCs that were investigated in the previous chapters. However, the work presented here is of a very preliminary nature, and further research focused on developing a method to achieve greater homogeneity in single NC distribution within the hosting matrix could be highly beneficial. Additionally, studying the impact of the hosting matrix with or without the use of a polymer protective film, such as PMMA, on the long-term stability of single NCs would be valuable. Finally, the newly prepared NCs are generated uncapped and thus could provide an interesting platform to comparatively tackle issues related to Auger recombination

processes like photo assisted ionization or photon coincidence emission. These aspects, that fall within the advanced investigation of the material, remained behind the scope of the preliminary study carried out here.

5.1.3 Non linear effects in the emission

This manuscript was so far essentially focused on the emission properties of isolated emitters. However, most light-emitting applications of LHP NCs, such as LEDs and lasers, require high densities of NCs positioned in close proximity. As a result, interactions alongside collective emission behaviors between these NCs are anticipated. In this context, the silica bead matrices filled with densely packed NCs, as presented in this chapter, seem to be an appropriate medium for facilitating such processes.

The results presented in the forthcoming paragraphs remain sparse. They are mainly associated to an opportunity the group had (on a short lapse of time) of experiencing a newly developed set up that provides amplified light pulses, thus allowing to access to densities of excitation orders of magnitude larger and required to address non-linearities. Reporting on these effects is, however, interesting for the perspectives it straightforwardly opens in the field, validating the mesoporous matrix approach to undertake the study of collective processes with perovskite NCs.

The search for nonlinear effects requires a high NC density. Thus, the samples that were considered were made with the solutions containing a 30% concentration of precursors. In the experiments our excitation beam (SHG of an amplified Ti-Sapphire laser operating at 80 MHz, $\Delta t = 2$ ps; fluence ≤ 1 mJ/cm^2/pulse) was replaced by the output of an optical amplifier supplying much shorter pulses ($\Delta t \sim 50$ fs) with a lower repetition rate ($f = 1$ kHz). The microscopy configuration (described in Chap. 2) is also changed to a more "classical" scheme using an achromatic lens to focus light on the sample. In this new configuration, the available excitation fluence range now extended to ~ 200 mJ/cm^2/pulse.

Fig. 5.5 presents the emission spectra of encapsulated FAPbBr$_3$ NCs obtained in this high energy pulse excitation configuration at room temperature and for different values of the excitation fluence (adjusted thanks to a set of neutral density filters).

On these spectra, the room temperature emission response of the FAPbBr$_3$ NCs is retrieved at low excitation fluence, with a Gaussian line-shaped PL centered at 2.27 eV of ~ 120 meV linewidth. When the excitation fluence is increased, a narrow emission band appears on the low energy flank at ~ 2.25 eV from 5 mJ/cm^2 typically (see the inset spectra) with an amplitude that rapidly gains weight with the excitation fluence suggesting a non linear evolution. Fig. 5.6 shows the evolution of the amplitude of both spectral features as a function of the incident fluence on a log-log scale. One can see that the amplitude of the PL intensity of the main spectral band has a

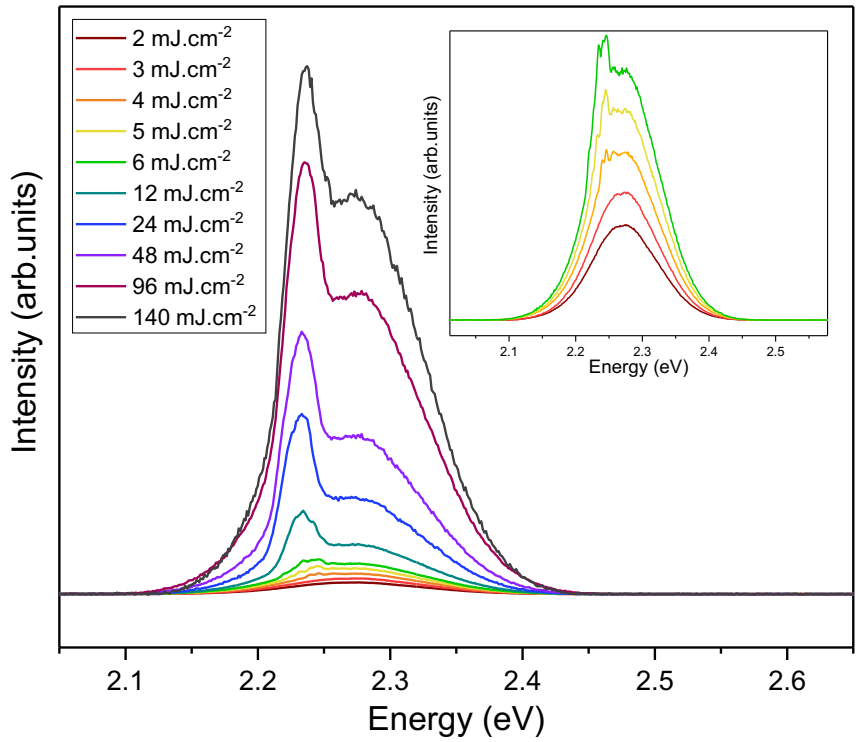

Figure 5.5: Room temperature PL spectra captured on the 30 % sample, at λ_{exc} = 420 nm, for different magnitudes of the excitation fluence (from 2 to 140 mJ/cm^2). The inset shows the lowest intensity spectra on a different scale. An f = 45 mm achromatic lens was used in the optical path.

slightly sub-linear behavior over the entire excitation fluence range (power low kx^n with $n = 0.9$ and $k = 5.3$). On the other hand, the low energy peak starts with a clear super-linear behavior up until 20 mJ/cm^2 typically and progressively reaches a plateau at high excitation fluence without ever exceeding the amplitude of the main PL band.

The behavior of the emerging spectral feature is typical of a phenomenon called amplified spontaneous emission (ASE). In a gain medium that has reached population inversion (by being optically pumped with a high power excitation) photons emitted by spontaneous emission can trigger stimulated emission while propagating through the medium. The initial spontaneous emission becomes amplified, explaining the name of the process. Even though ASE intensity can reach levels of laser emission, it has a very low temporal coherence. On the other hand, whereas luminescence is typically emitted in all spatial directions, ASE can be strongly directional and show a high level of spatial coherence. For laser applications, ASE is generally detrimental since it lowers the spectral purity of the emission. However, for the characterization of an optoelectronic material or optical gain media it can be useful since it is the signature of optical amplification taking place in a given medium, which is a prerequisite for the development of a laser.

In perovskite NCs, ASE has been investigated multiple times in dense films [236, 237, 238, 101, 239, 240]. Experimentally, the usual sign of ASE is the apparition of a narrow emission peak

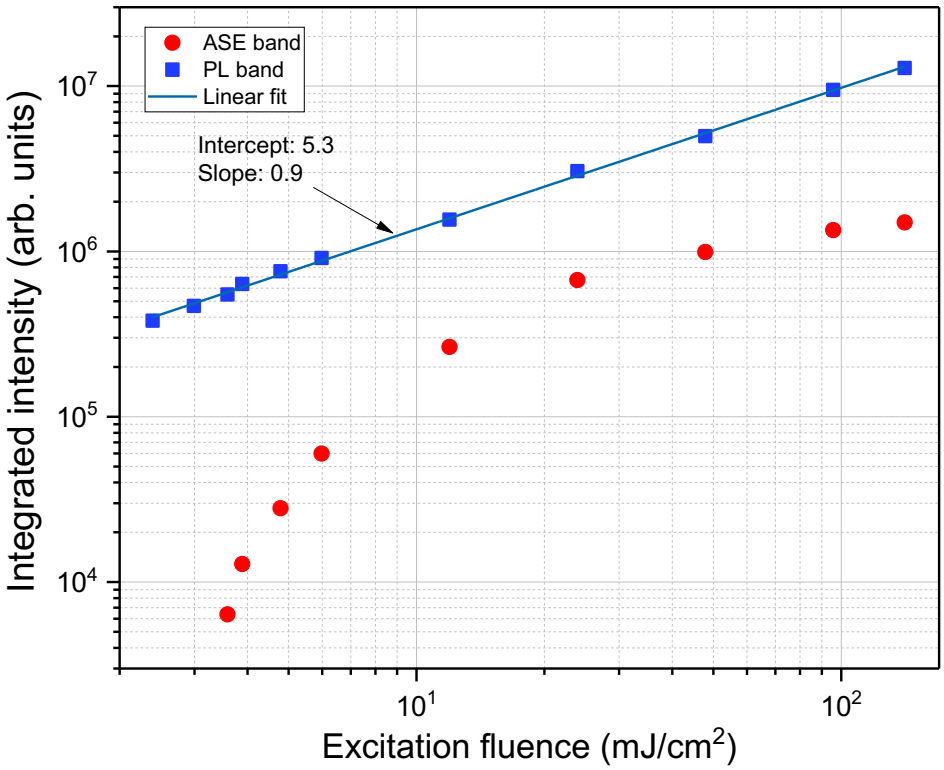

Figure 5.6: ASE intensity as a function of the excitation fluence. The filled blue squares represent the "classical PL" contribution in the two peak fits of the spectra presented on Fig. 5.5 while the filled red circles represent the ASE contribution. The blue line is the linear adjustment of the PL resorting to a power law of the type $I_{int} = k \times (P/P_0)^n$ where the reference P_0 is $P_0 = 1$ mJ/cm^2, with $n = 0.9$ and $k = 5.3$ (arb. u. -same type as I_{int}).

in a PL spectrum above a certain excitation fluence threshold followed by a super-linear intensity increase with the fluence. The observations of Fig. 5.5 and 5.6 thus strongly suggest that ASE is taking place in the system under study.

Comparing the rise in ASE intensity obtained in this work to experiments performed by other groups on perovskite NCs, the amplification seem to be much weaker here [236, 237, 101]. For example, working on films of drop casted FAPbBr$_3$ NCs, Liu and coauthors [237] also observed ASE at 2.25 eV but with a much larger total intensity increase and a threshold of 300 $\mu J/cm^2$, about 10 times lower than in the present system. In dense films of NCs, ASE and the optical gain that the process generates, are usually observed using a hemi-cylinder lens that creates an excitation stripe on the material. Spontaneous emission occurs along the stripe in all directions, which can then trigger stimulated emission exclusively along the stripe axis. The resulting emission is collected in a direction perpendicular to the excitation beam and along the stripe axis and depends super-linearly on the stripe length. Please let us note that such optimized experimental conditions were not the ones characterizing the first "test" presented here. As the optical gain

will ultimately depend on the number of emitting entities within it, ASE in this system cannot reach the levels observed in dense NC films, as reported in [237] and [236], which likely explains the plateau observed in Fig. 5.6.

Although the amplified stimulated effect uncovered in this section is relatively weak, the presented results show that optical amplification is possible in such environment. The results are preliminary and further studies on optimized samples (increased NC density and higher organization of the silica spheres and NC clusters) could show a stronger effect in the future. In particular, a packing of the silica spheres in a more ordered geometry could also boost the ASE in preferential directions by increasing the waveguide effect that was not studied in the available sample.

5.2 Energy transfers between $FAPbBr_3$ NCs : A FRET mediated approach

The last section uncovered a non linear effect in the emission of $FAPbBr_3$ NCs embedded in mesoporous silica matrices. Another phenomenon expected to play an important role in densely packed films (possibly interesting in NCs based devices), is the diffusion of excitons. Exciton diffusion in NCs is primarily attributed to two mechanisms: Photon recycling (*i.e.* re-absorption followed by re-emission) [241, 242, 243] and energy transfers, a non radiative type of interaction that can be described, in NCs, by FRET (Förster energy transfer) [244, 245] or DET (Dexter Energy transfer) [246, 247]. Although photon recycling has been shown to play an important role in exciton diffusion properties, some authors have recently demonstrated that their contribution are still weaker than the energy transfers in dense films of LHP NCs [243]. Since the system under study in this chapter is expected to have a smaller inter-particle distance than that of NC films (due to the absence of ligands) this section will primarily focus on energy transfers (ET). In particular, the use of a simple model shows how the time evolution of the PL band provides information on ET, allowing the extraction of a FRET rate for NCs in close contact.

5.2.1 Energy transfers in NCs

The two largest contributing mechanisms to energy transfers in NCs are the Förster Resonant Energy Transfer (FRET) and the Dexter Energy Transfer (DET). FRET is a process where the electronic excitation energy of an atom, molecule or nanocrystal called the donor is transferred to a similar atomic edifice in its vicinity and initially in its ground state, called the acceptor. This interaction can either happen between similar or different objects (*e.g* two NCs or molecules or a molecule and a NC) and is then called homo-FRET for the former or hetero-FRET for the later. This short-range interaction, sketched in Fig. 5.7 finds its origins in the inter-molecular

dipole-dipole coupling between the transition moments associated with the electronic transitions of the donor and the acceptor. Thus, the process is non radiative and a transition rate Γ_t is used to describe this energy transfer. Although FRET requires the acceptor and donor to be in close proximity (1-10 nm typically) no actual physical contact is needed between the two objects. DET on the other hand results from an electron exchange between the donor and the acceptor. Thus, the overlap of the donor and acceptor wavefunctions is required which gives it a maximum range that is too small for the system of NCs investigated here [248]. For this reason, only FRET will be considered in the following.

In a series of publications from the late 1940s Förster demonstrated that this type of energy transfer (*i.e* FRET) between two separated systems essentially occurs when three conditions are met [249, 250]: (i) the fluorescence and absorption transition energy of the donor and acceptor, respectively, are resonant *i.e.* their spectrum overlap on a certain energy range (ii) the Donor-Acceptor distance R_{DA} (or hopping distance) is short enough, (Förster demonstrated a R_{DA}^{-6} scaling law, see Eq. 5.1) (iii) the transition dipoles of the donor and the acceptor have the correct orientation with respect to each other. These conditions were summarized by Förster in the following set of equations:

$$\Gamma_t = \frac{1}{\tau_D}\left(\frac{R_0}{R_{DA}}\right)^6 \tag{5.1}$$

$$R_0^6 = \frac{9ln(10)\Phi_D\kappa^2}{128\pi^5\mathcal{N}n^4}J(\lambda) \qquad \text{with:} \quad J(\lambda) = \int_{-\infty}^{+\infty} F_D(\lambda)\epsilon_A(\lambda)\lambda^4\, d\lambda \tag{5.2}$$

The first equation gives the transfer rate Γ_t of the process and depends on the exciton lifetime $1/\tau_D = \Gamma_R + \Gamma_{NR}$ where Γ_R and Γ_{NR} are the radiative and non-radiative rates of the exciton transition. R_{DA} is the distance between the donor and the acceptor and R_0 is the distance at which the transfer has a 50% chance of happening. The second equation gives the detailed expression of the parameter R_0. Φ_D is the PL-quantum yield of the donor, $\mathcal{N}$ the Avogadro number, n the refractive index of the surrounding medium, κ^2 is the dipole-dipole orientation factor that is comprised between 0 and 4. A common assumption is to consider that transition dipoles moments in ensemble of chromophores are isotropically oriented yielding $\langle\kappa^2\rangle = 2/3$ although in systems with higher order, such as dense films of NCs or superlattices, a higher value could be obtained. Finally, $J(\lambda)$ is an overlap integral between the normalized fluorescence spectrum of the donor F_D and the absorption of the acceptor ϵ_A weighted by a function of the optical frequency (λ^4 term).

Resonant energy transfers have found a wide range of applications in biology and chemistry where molecular fluorophores can be used as sensors to detect the presence of chemicals or proteins,

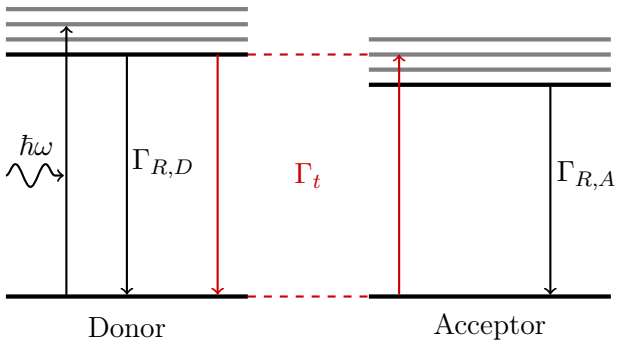

Figure 5.7: Principle of FRET: A carrier is excited in the donor system D and can either relax radiatively with rate $\Gamma_{R,D}$ or transfer its energy to a neighboring acceptor system A with associated rate Γ_t. The acceptor then either recombines radiatively $\Gamma_{R,A}$ or transfers the excitation further to a surrounding system of lower transition energy, therefore acting as a new donor.

evaluate their concentrations and study the kinetics of chemical or biological reactions. Following the first synthesis of colloidal NCs in the 1990s, FRET was predicted to play an important role in the inter-nanocrystal interactions of dense films. Indeed, contrary to molecular systems, NCs have much broader absorption spectra, allowing efficient off-resonance excitation. Their PL emission has a narrow lineshape, a large quantum yield and its energy is easily tuned by changing the NCs size. Finally, due to their high surface to volume ratio, they are interesting for the fixation of biological markers. All of these properties make them very good FRET donors for hetero-FRET (FRET between two different types of nano-structures).

Regarding optoelectronics, FRET can be desirable or detrimental depending on the application. For example, in photovoltaics, long diffusion lengths can facilitate the transport of excitons towards the charge separation interfaces of the device, which can improve the performances of a solar cell [251, 252, 253]. At present time, the highest values of FRET-mediated diffusion length and diffusivity (l = 200 nm, D = 0.1 cm^2/s) are, by the way, reported in higher ordered monolayers of "isoenergetic" NCs made of $CsPbBr_3$ [244]. In contrast, for light-emitting devices, a large diffusion of excitons is undesired, as it prevents a radiative recombination of the exciton from the NC where it was created, thus increasing the risk of non-radiative trapping in adjacent layers [254]. Either way, the understanding of exciton diffusion by FRET processes in new opto-electronic systems such as LHP NCs is of great importance.

Several groups have investigated energy transfers between II-VI semiconductor NCs [255, 256, 257, 245, 258] but much less studies have been published on perovskite NCs so far, even though their defect-tolerant properties are expected to limit the impact of trap states on the exciton diffusion properties. Among these studies De Weerd and coauthors [259] were the first to report FRET between $CsPbBr_3$ NCs. In 2D $CsPbBr_3$ NC films, Penzo *et al.* measured an exciton

diffusion length of about 200 nm [244], while Giovanni *et al.* [243] demonstrated that energy transfer *via* FRET is the dominant exciton transport process in the short range in MAPbBr$_3$ NC films and measured an exciton diffusion length of 1 μm, a value unexpectedly higher than what was measured in bulk. Their result shows that the ET between NCs counters the usual limitation of the exciton transport properties attributed to the surrounding ligands and the quantum confinement. Regarding FAPbBr$_3$ NCs nothing has yet been measured and more generally in systems of NCs freed from capping ligands. This will be the scope of the following paragraphs.

5.2.2 Experimental results

After this brief introduction of FRET, let us now analyze a few experimental results obtained on a sample of FAPbBr$_3$ NCs embedded in the silica matrix described in the last sections. The sample under study was made with a high concentration of precursors (∼30% sample), thus favoring interactions between the NCs. Fig. 5.8 shows the PL intensity emitted by this sample in the energy-time domain alongside the reconstructed PL spectrum (top graph) made by summing the intensity of PL over its temporal axis. It was captured at 7 K and the system was excited using the pulsed Ti:Saphire laser tuned at 397 nm (non resonant conditions) at a low excitation power of $\sim$ 1 μW. This energy-time map representation of the PL allows to quickly develop an idea of the dynamical mechanisms at play in the system. Indeed, here, the PL evolution in time has a striking asymmetry and is composed of a high energy tail of fast emission, followed at lower energy by a strong PL emission of a much longer decay time centered around 2.22 eV. This emission behavior is the sign of a residual distribution of NCs, likely with smaller sizes, which leads to an emission at higher energy than the rest.

From this raw PL map one can also build the time evolution of the PL intensity at specific energies that are displayed on the right side of Fig. 5.8 where the high energy side of the PL emission is decomposed over six evenly spaced decays. To improve the signal to noise ratio, the decays were constructed by summing up the intensity signal over energy slices of 2 meV thickness. There are two important things to notice here while the emission energy varies. First, the intensity decays are slowing down when the emission energy increases. Indeed at 2.26 eV the emission has a half-life time of about 55 ps with a multiexponential line shape while the emission at 2.22 eV shows a half-life of about 165 ps. Secondly, one can notice that the objects located at higher energy reach their emission maximum faster than the lower energy ones, with a time difference measured here around 30 ps between the 2.26 and 2.22 eV curves. It is worth noting that the intensity decays presented here have a more complicated behavior than the ones presented so far in this manuscript making their adjustment with mono or bi-exponential functions irrelevant (they are indeed the superposition of several exponential decays as seen thereafter), which is why

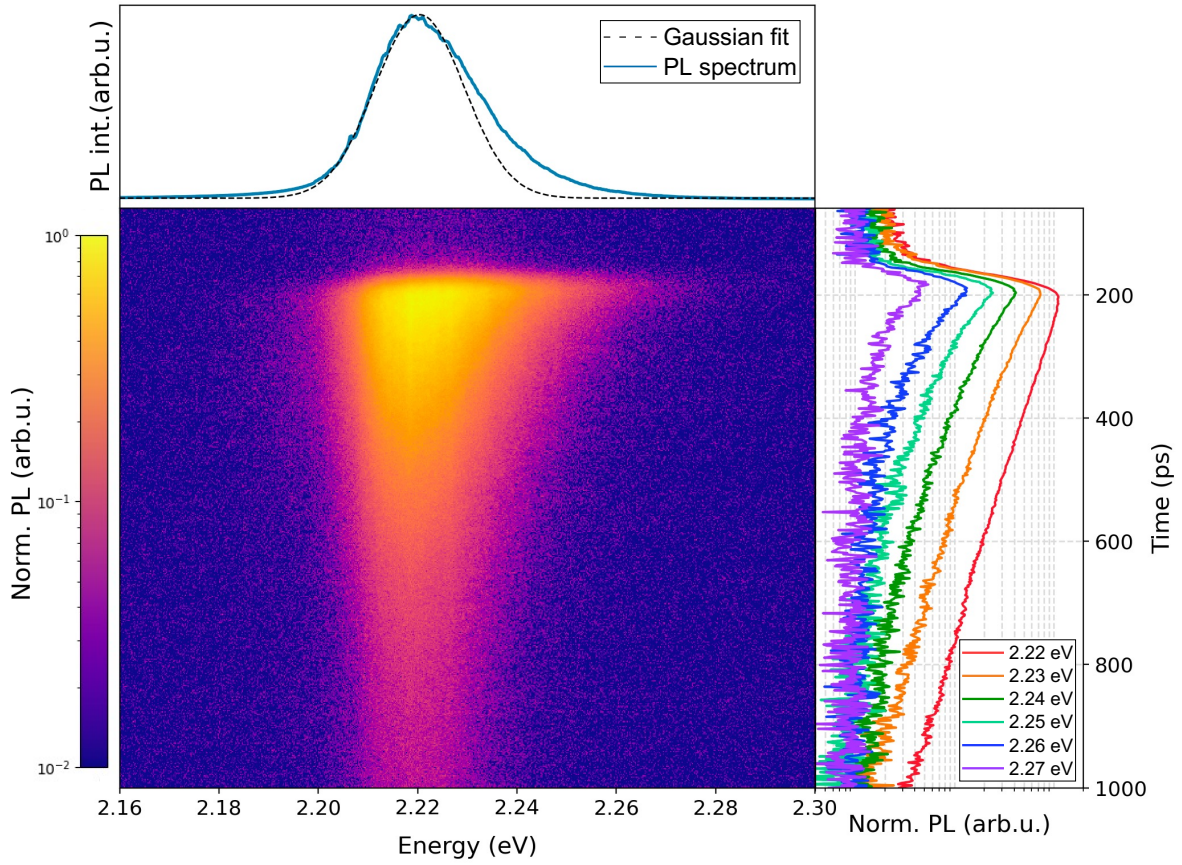

Figure 5.8: Energy-time domain PL intensity map measured on a sample of $FAPbBr_3$ NCs embedded in the mesoporous SiO_2 matrix and made with a 'high' concentration of precursors. The PL spectrum displayed on top (blue solid line) is a summation over the first $\sim$ 50 ps following the excitation. The dashed black line represents the best Gaussian adjustment to this spectrum. The six intensity decays presented on the right side (semi-log scale) result from the summation of the PL emission over 2 meV energy 'slices' centered around the energy provided in the legend for each curve.

a simple half-life was preferred here for their description.

The observations described above (also found in the emission of dense films) are generally the sign of an energy transfer taking place between the high energy NCs and the lower energy ones located in their vicinity [257, 243, 258]. Indeed, when higher energy objects are excited they can either recombine radiatively, non-radiatively or transfer their excitation to surrounding NCs provided that the later, *i.e.* the acceptors, have an exciton transition of lower energy (which translates into a larger size of the NC). Schematically, higher energy NCs will have a higher probability to transfer explaining their relatively shorter lifetime. In order to verify this hypothesis, numerical simulations constructed from a FRET model are performed in this work and adjusted to the experimental data *i.e* the spectro-temporal PL signal. For this purpose, the signal presented on Fig. 5.8, that was most frequently observed in the homogeneous regions of the sample (where very few variations are observed) will be considered as a typical response *i.e* a reference signal to

be reproduced in the simulations.

5.2.3 Theoretical model and numerical simulations

To model ETs in this system, the first hypothesis is that FRET is the only mechanism of exciton diffusion in this system, other mechanisms like DET or photon recycling are thereby discarded here. As seen in the first section of this chapter, the hosting matrix consists in a packing of silica spheres of $\sim$ 30 nm average diameter that has no particular order or symmetry, meaning that the pores between the silica spheres most likely follow a certain size distribution of which the measurement is beyond the scope of this work. Thus, to simplify the problem in the following, the clusters of NCs contained in the pores are modelled as 2D arrays of adjustable sizes. A model of pores filled with 3D arrays of NCs was also developed for this work. However, since it represents a simple generalization of the 2D model to higher dimension, it will not be described in this section, although the corresponding simulation results will be compared to the 2D model. Finally, it is worth noting that the matrix pores are assumed to be completely filled with NCs in the following.

The objective of the simulations is to determine if the emission dynamics of this system can be roughly reproduced with a simple FRET model that has proved to be effective for the modelization of energy transfers in other dense systems of II-VI NCs in the past [255, 260]. The approximations that were made above (100% filling of the pores and use of a 2D grid - that mainly determines the number of closest neighbors) will of course be discussed in the last part of this chapter that presents the simulation results. Fig. 5.9 presents an illustration of the 2D NC arrays. Only the nearest diagonal and non diagonal neighbor couplings are considered, thereby neglecting other long range processes.

The system under study consists of a network of pores that are separated by the silica beads. When the excitation laser is focused on the sample ($\sim$ 1 μm radius), several pores are excited at the same time. To reproduce this, the simulations are performed while including several clusters excited independently as illustrated on Fig. 5.9. In these simulations, intra-cluster energy transfers are allowed but not the inter-cluster ones. Following the work of Miyazaki and Kinoshita [255, 261] the exciton population dynamics of cell n can be described by the following set of first order differential equations:

$$\frac{d\rho_n}{dt} = \sum_{m \neq n} \Gamma_{t,nm}\rho_m - \left(\Gamma_{t,nn} + \Gamma_{R,n} + \Gamma_{N,n}\right)\rho_n \tag{5.3}$$

In this expression ρ is a vectorized version of the matrix of sites (the vectorization making the problem solvable numerically by Runge Kutta methods). This means that the n^{th} element of ρ is related to the matrix site (i, j) by the relation $n = (i-1)N+j$ where N is the total number of sites.

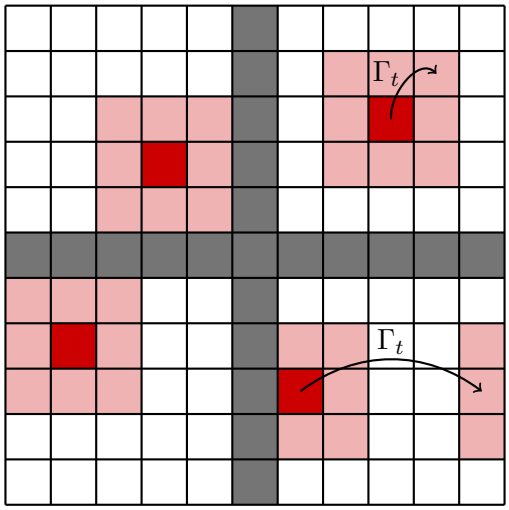

Figure 5.9: Illustration of the modelled NCs array. Initially, all the array sites are given an absorption energy (provided by the distribution function presented in Fig. 5.10) and excited with an off resonance and higher energy laser pump. The energy transfers are driven by FRET and an exciton on a specific site can only transfer (with an associated rate Γ_t) to a neighboring site if its emission spectrum overlaps with the absorption spectrum of the exciton on the neighboring site (see Eq. 5.4). On this illustration, only 4 excited sites and their associated neighbors are represented for clarity. The array shaded in gray represents barriers preventing transfers between two different clusters. The situation presented on the lower right array illustrates the periodic boundary conditions that are applied in this model.

In the following, the vector element n will be referred, loosely speaking, as "site n" even though it originally corresponds to site (i, j) in the matrix of sites. ρ_n is thus the occupation probability of site n, and $\Gamma_{R,n}$, $\Gamma_{N,n}$ denote respectively the radiative and non-radiative decay rates for the exciton on site n. The magnitude of these rates is extracted from the TRPL measurements.

The energy transfer is described through the $\Gamma_{t,kl}$ rates: $\Gamma_{t,nm}$ is the transfer rate from site m to n, (m and n being nearest neighbors on the original grid, *i.e* if n corresponds to site (i, j) then m is any site of the form $(i \pm 1, j)$; $(i, j \pm 1)$; $(i \pm 1, j \pm 1)$; $(i \mp 1, j \pm 1)$). Finally, $\Gamma_{t,nn}$ encompasses all the population transfers from site n to its nearest neighbours. The transfer rates $\Gamma_{t,nm}$ between coupled NCs on the array are given by the Förster expression following Fleming [262]:

$$\Gamma_{t,nm} = \frac{|C_{nm}|^2}{2\pi\hbar^2} \int_{-\infty}^{+\infty} F_m(\omega) A_n(\omega)\, d\omega \tag{5.4}$$

where the parameter C_{nm} represents a Coulomb dipole-dipole coupling constant between NC n and m and $A_n(\omega)$, $F_m(\omega)$ are the spectral line shapes of the acceptor (absorption) and the donor (fluorescence) respectively. In this model, both spectra are considered to have a Gaussian profile, *i.e.*:

$$A_n = \frac{\hbar}{\sqrt{2\pi}\sigma_h} \exp\left[-\frac{(\hbar\omega - \epsilon_n)^2}{2\sigma_h^2}\right] \tag{5.5}$$

$$F_m = \frac{\hbar}{\sqrt{2\pi}\sigma_h} \exp\left[-\frac{(\hbar\omega - \epsilon_m + \Delta_{SS})^2}{2\sigma_h^2}\right] \tag{5.6}$$

where σ_h is the homogeneous broadening extracted from linewidth measurements on single or quasi-single NCs presented on Fig. 5.4. In Eq. 5.6 Δ_{SS} represents the Stokes shift between the transition energy and its actual emission which was estimated from comparisons between absorption and luminescence in NC ensembles in the previous section. Finally, ϵ_m (respectively ϵ_n) is the exciton transition energy for the NC located on site m (n). As a first approach, the same coupling strength C_{nm} is assumed for adjacent NC pairs ; the total rate $\Gamma_{t,nm}$ will thus be uniquely determined by the level of overlap of the A and F lineshapes.

By changing the integration variable and using a proper normalization, the integral of Eq. 5.4 can be expressed as:

$$\Gamma_{t,nm} = \Gamma_{t,0} \int_{-\infty}^{+\infty} F_m^{'}(E) A_n^{'}(E)\, dE \tag{5.7}$$

where $\Gamma_{t,0}$ is now the transfer rate between two NCs that would have a perfect overlap between their "effective" $A^{'}$ and $F^{'}$ linewidth. Thus, for two NCs fulfilling this condition one has $\Gamma_{t,nm} = 1$ and $\epsilon_m = \epsilon_n + \Delta_{SS}$. In the following, $\Gamma_{t,0}$ will be one of the adjustable parameters in the simulation.

5.2.4 Simulation results and comparison to experimental work

In order to evaluate the efficiency of the model, the experimental results displayed in Fig. 5.8 are compared with the numerical simulations. In these simulations, each NC in the simulated array is assigned a specific transition energy for absorption. The line shape of the ensemble PL spectrum from Fig. 5.8 (considered only at early time, *i.e* in the first $\sim$ 50 ps) serves as the starting point and is used to model the Stokes shifted absorption spectrum of the optical transitions for the entire NC ensemble. To replicate the special line shape of the PL spectrum and its extension towards higher energies, a skew normal distribution is employed. This distribution is a generalized form of the normal (Gaussian) distribution that incorporates skewness, *i.e* asymmetry.

The top plot of Fig. 5.10 displays the original, at early time, ensemble PL (solid blue line), an attempt to adjust it with a classical Gaussian law (black dashed line) and its adjustment with the skew normal distribution (red dashed line). Following the results presented on Fig. 5.2 and the work of Brennan and coauthors [177], an adjustable Stokes shift of 30 to 45 meV towards the higher energies is then applied to the red dashed curve to simulate the distribution of absorption transition energies. The final curve is plotted on the bottom part of Fig. 5.10 for $\Delta_{SS} = 32$ meV. This distribution is used to generate an histogram of the transition energies of each NC over the simulated array composed of N objects ($n \times n$ grid). Note that this histogram was normalized such that the area under the histogram equals 1. The y-axis thus represents a probability density

rather than the number of occurrences for each energy class.

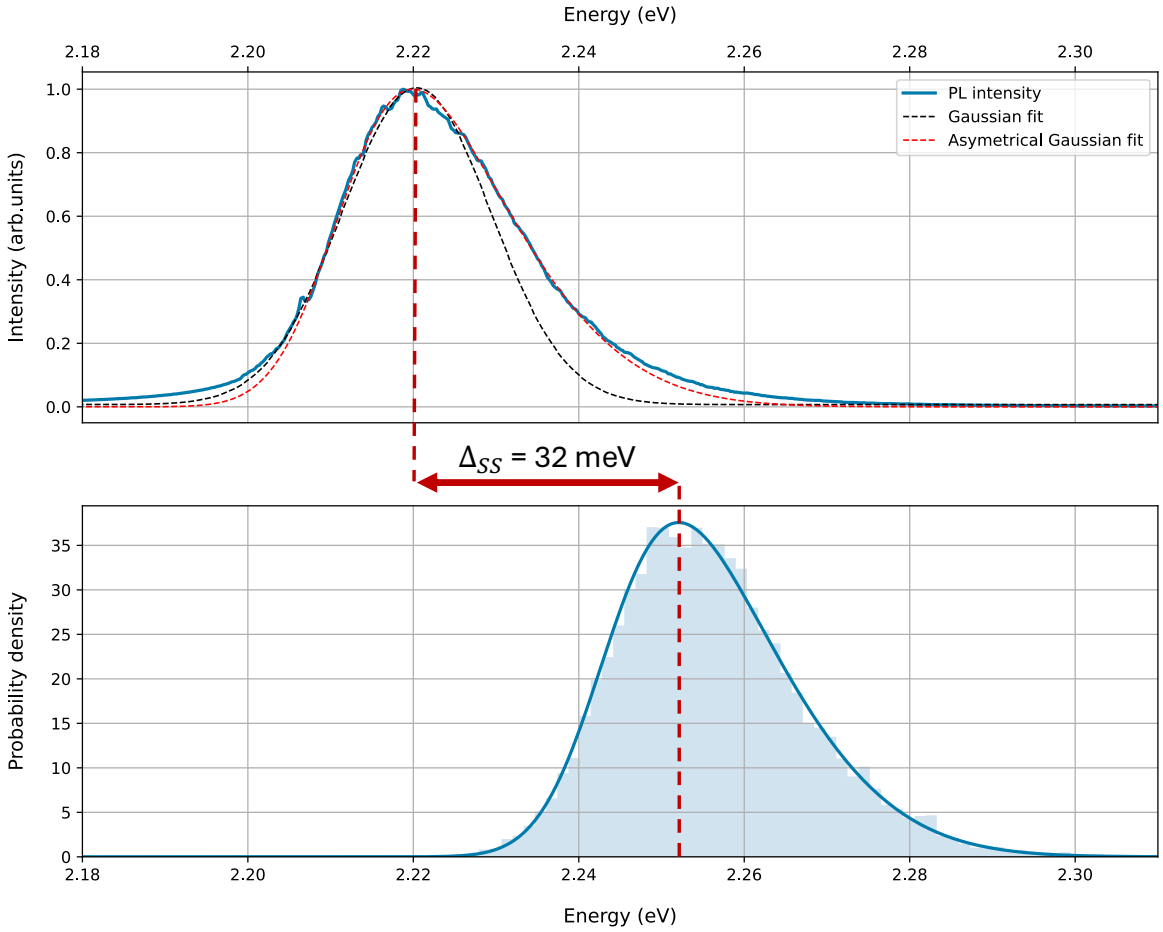

Figure 5.10: Top: The experimental PL spectrum of an ensemble of FAPbBr$_3$ NCs captured at T = 7 K (blue solid line). The best Gaussian (black dashed line) and asymmetrically stretched Gaussian (dashed red line) adjustments are also provided on the same graph. Bottom: The skew normal distribution (given by the red curve of the graph on the top) is translated of $\Delta_{SS} = 32$ meV, (Stokes-shift) and is used to generate an histogram of the absorption transition energies of the simulated NCs on the grid.

Now that the exciton energy distribution is set across the grid, the coupled differential equations defined by Eq. 5.3 can be solved. To do this, every transfer processes between an excited site n and its first neighbors m are computed and weighted by the overlap integral of Eq. 5.7. The fluorescence and absorption spectra of each individual site that intervene in this equation are defined by the Gaussian laws of Eq. 5.5 and 5.6 respectively. Again, the Stokes shift will be adjustable from 30 to 45 meV between simulations, since the value measured on Fig. 5.2 suffers from a rather large uncertainty. The energies ϵ_n and ϵ_m are given by the exciton energy distribution across the grid. The homogeneous broadening of each individual NC is fixed at $\sigma_h = 4$ meV to encompass all transitions of the exciton fine structure (keeping in mind that the actual broadening is hard to assess in environments of higher NCs density corresponding to the ones that are investigating

in TRPL). Finally, for a given simulation, the parameter C_{nm} of Eq. 5.4 or $\Gamma_{t,0}$ in Eq. 5.7, is held constant.

After integration, the time evolution of the exciton population for each site on the grid is obtained. Regrouping the simulated evolution of each site by energy classes of a ~ 2 meV width, the decays of the exciton population at specific energies (from which the PL intensity is proportional) are reconstructed and displayed on Fig. 5.11.

In Fig. 5.11 the simulated decays are plotted alongside their experimental counterpart and regrouped into the high (top graph) and low (bottom graph) side of the PL signal. For both sets of curves, the NC clusters were made of 5×5 elements with a number of clusters set at 600 in order to obtain a satisfying averaging. The adjustment of the parameters was performed as followed:

- Γ_R is defined from the long range behavior of the decays that correspond to the contribution of unperturbed NCs. It is besides quasi-independent of the emission energy (in agreement with the model) and according to this, $\Gamma_R = 4.8$ ns^{-1} is considered here. This value is found in good coherence with decays that may be directly measured in diluted phases of non-interacting NCs, as seen on Fig. 5.12.

- Two leading parameters remain to be adjusted: Δ_{SS} and $\Gamma_{t,0}$. No optimisation procedure is used as far as those parameters are concerned. It is found that Δ_{SS} pilots the manner the "fast" short-time decays evolve on the high energy side of the PL (the decays slowing down as the energy decreases). $\Delta_{SS} = 32 \pm 3$ meV provides good results (the fact that Δ_{SS} has no energy dependence is discussed below). Finally, $\Gamma_{t,0}$ is adjusted to obtain a good fit in the whole energy range and $\Gamma_{t,0} = 55 \pm 10$ ns^{-1} is found as an acceptable value.

In the graph located on the bottom of Fig. 5.11, the three highest energy decays are well reproduced within the first ~ 300 ps, initially showing a rapid multi-exponential decay followed by a mono-exponential behavior governed by the radiative rate, Γ_R. For longer time values, due to the small proportion of high-energy NCs, the experimental signal becomes too weak and is mixed with the background noise of the Streak camera. The two decays corresponding to NCs emitting at 2.23 and 2.22 eV are also reasonably well reproduced, although the simulation appears to slightly underestimate the amount of transfer at these energies, particularly for the 2.23 eV curve. Regarding the graph located on top of Fig. 5.11 (where the low energy side decays are presented), all four decays are well reproduced. The effect of energy transfer is weak in the emission dynamics but there is a clear signature that is mostly visible on the lowest energy curves under the form of a flattening of the decay at early times, to be associated to the feeding of the lower energy sites. The increase in the population of such NCs roughly operates with a dynamic similar to the one that depletes the NCs having higher energy transitions *i.e.* located at an energy distance equal to Δ_{SS}.

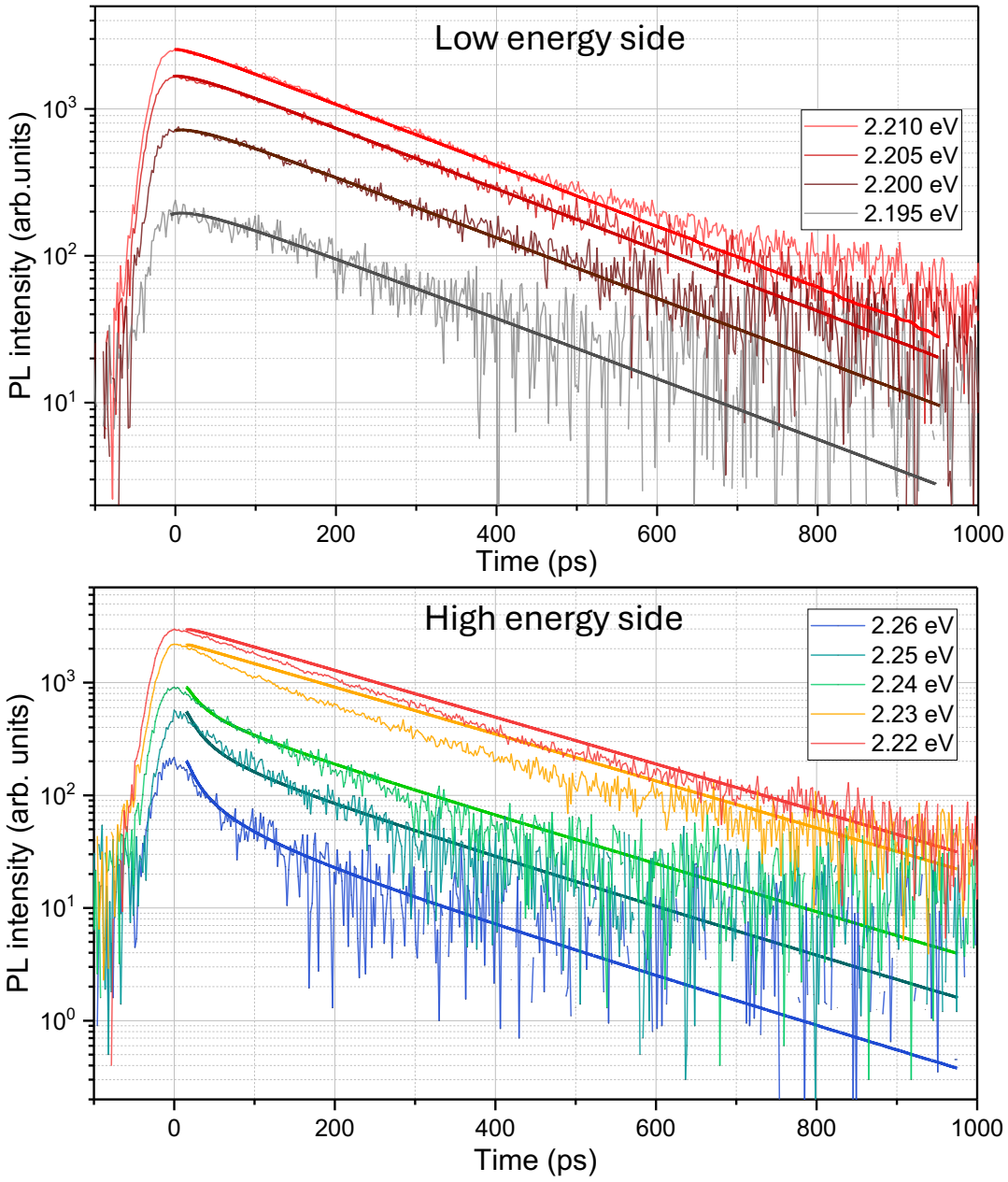

Figure 5.11: Comparison of the simulated decays with the 2D grid model to the experimental data acquired by TRPL in semi-log scale. The top graph regroups five decays taken on the low energy side of the emission spectrum at specific energy values provided in the legend. The decays on the bottom graph are also taken at different energy values on the high energy flank of the PL emission spectrum. To solve the set of differential equations, "solve ivp" from the module "integrate" of the Scipy library in Python was used with the standard Runge-Kutta method "RK45".

Overall, these simulations are successful as they already reproduce quite well the experimental observations with a rather simple model. At high energy, the fast initial decays are explained by the decline of the exciton population that transfers itself towards lower energy (or larger size) acceptors in its vicinity and on a shorter timescale than that of the radiative lifetime. On the

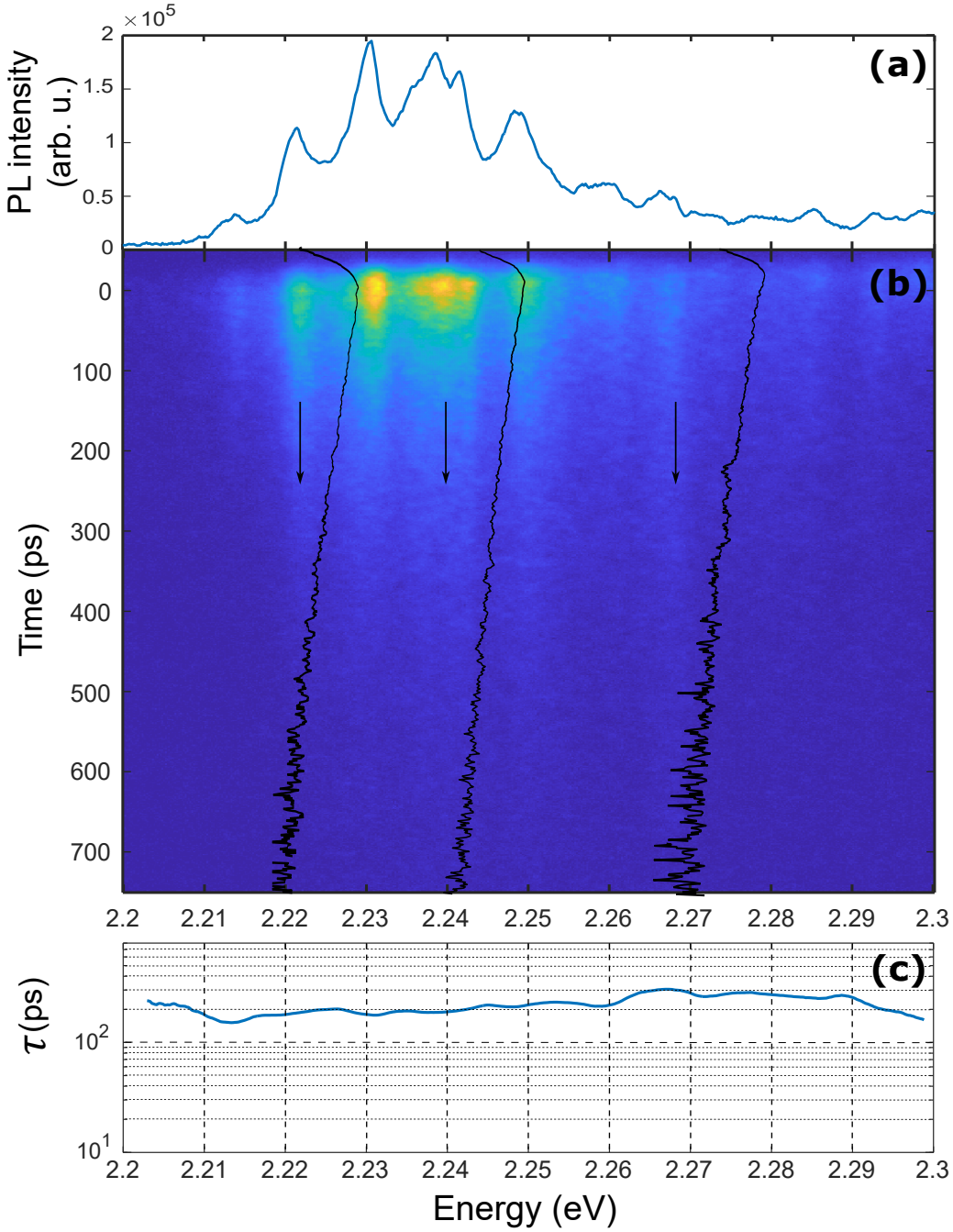

Figure 5.12: Typical emission dynamics pattern of non-interacting NCs (low concentration sample) measured across the spectral range corresponding to the inhomogeneous PL of higher concentration samples. **(a)** Time integrated PL spectrum **(b)** Time resolved PL (energy-time domain) **(c)** Decay constant extracted from the mono-exponential fit of the PL signal as a function of the emission energy. τ is found rather constant in the explored energy range ($\tau \approx 215 \pm 45$ ps). Illustrations of the decays are overlapped on panel **(b)**, the black arrows indicating the structures that have been considered for the plots.

low energy side, the decays are initially slowed down by the constant "feeding" of the exciton population by higher energy donors before retrieving a mono-exponential behavior after all the

exciton transfers have happened. Interestingly, the NCs emitting at energies located in the center of the PL spectrum keep a well defined mono-exponential behavior at all time. This phenomenon is explained by the much larger population of these objects as compared to the higher or lower energy ones and by the fact that these objects serve here as an intermediate between the two energy sides: the extra exciton population that they receive from donor objects of higher confinement is transferred directly to the acceptors which results in an exciton population that stays quasi-unaffected by this process over time.

Although the results presented above are satisfactory, the model still has notable weaknesses that need to be discussed. The first one is related to an intrinsic property of NCs to have their Stokes-shift dependent on their exciton transition energy (or size), in other words, $\Delta_{SS} = \Delta_{SS}(E)$. In the basic analysis performed in Sec. 5.1, a realistic size range was extracted ($\Delta L \sim 7$ nm at most around $\langle L \rangle \simeq 9$ nm). Using the reference curve measured by Brennan *et al.* on an analogous bromide LHP compound (see Fig. 5.2), would lead to a variation of ~ 30 % in the Δ_{SS} value over the whole L size range for the NCs involved in the emission process. This means that Δ_{SS} should decrease as the NC transition energy decreases, thus opening new possibilities of transfer towards NCs with the lower energy transitions. The effect is not taken into account here and very likely explains why decays located below the PL peak (around 2.22 eV typically, see Fig. 5.11) are not enough impacted by ET in the simulations. There is also a large uncertainty regarding what the microscopic organisation might actually be:

- When considering an FCC packing of the silica beads (most compact scaffold) the volume of the octahedral pores is estimated at $V \simeq 17^3$ nm^3 and could typically host ~ 8 NCs having an $\langle L \rangle \sim 8$ nm (considering a filling factor equal to 100%). For comparison, V raises to 26^3 nm^3 for a SC packing, allowing to host a number of NCs approximately three times larger. In the "ordered compact" situation, $\simeq 8$ NCs might be gathered at maximum making the choice of the 2D grid a reasonable one for 1 NC has in this situation 8 closest neighbors. More importantly, the Stokes-shift Δ_{SS} has a high value (~ 30 meV on average) that is of the same order of magnitude as the PL FWHM. This means that, on average, transfers of only one step can be achieved throughout the NCs population whatever the considered NC, and two steps energy cascades will very rarely occur. Under these conditions, a very poor influence of a cluster size extension is expected (this was indeed verified).

- The principal parameter here could be the average number of first neighbors that is significantly increased in the scenario of ET in 3D clusters. Let us note that (i) as far as the spatial diffusion process of excitons (associated to the ET) is not investigated, the actual "topology" of the NCs organisation is of no matter here. (ii) The 3D model with clusters

of 2^3 NCs (presented on Fig. 5.13) was shown to adjust the experimental PL in a slightly more satisfying manner but for quasi-unchanged values of the parameters ($\Gamma_{t,0} \sim 50$ ns^{-1} and $\Delta_{SS} = 32$ meV). In particular, the increase in the number of first neighbours seems to help adjusting the "mid-energy" decays. (iii) More generally, given the previous considerations, the actual organisation of the silica beads should have a limited effect as far as ET is concerned. This is a point that deserves further investigations, being able to connect well characterized matrix structures and PL patterns. Taking into account a distribution of pore sizes could be an easy extension of the present work and help to approach the real system (for it seems that the hosting matrix does not respect any particular order). However, let us emphasize again that the ET effects should essentially arise from the very local average environment of a given NC rather than the long range structure.

With the previous considerations in mind, let us formulate some short last comments before ending this chapter:

- The filling factor associated to the NC integration in the matrices is not a well defined quantity. The simulations were performed considering a complete occupancy of the available space (although this could also be easily modulated through numerical simulations).

- Given the NC average size, only first neighbors interactions have been considered as really contributing to the population changes. A second "shell" could also be considered by adding ETs associated to another C_{nm} (or $\Gamma_{t,0}$) coefficient (see Eq. 5.4 and 5.7) of strongly reduced value, so as to match the $1/r^6$ dependence that characterizes FRET processes. This is a point that would justify taking into account slightly expanded clusters. As an illustration, is was shown that three "active" shells around a Donor/Acceptor NC operate in ensembles of CdSe dots (in Langmuir-Blodgett films) having a diameter close to 4 nm [263].

- To the best of our knowledge, and despite the huge activity around perovskite based materials of reduced dimensionality, there is only one significant study that addresses the issue of ET by clearly exhibiting transfer rates. Proppe and collaborators indeed show that exciton funneling occurs within $\sim$ 100s of femtoseconds between narrow quantum wells towards wells made of a larger number of layers. They explain the transfers within the framework of FRET and determine transfer rates in the ps^{-1} range. This strong value is assigned to two facilitating factors: the good overlap between the optical responses (donor well emission *vs* acceptor absorption) but also an optimal orientation parameter for the dipoles in each structure [264]. Regarding our NCs, transfer rates $\Gamma_{t,0}$ in the tens of ns^{-1} range are retrieved (for perfect tuning between the absorption and emission). This is comparatively two order

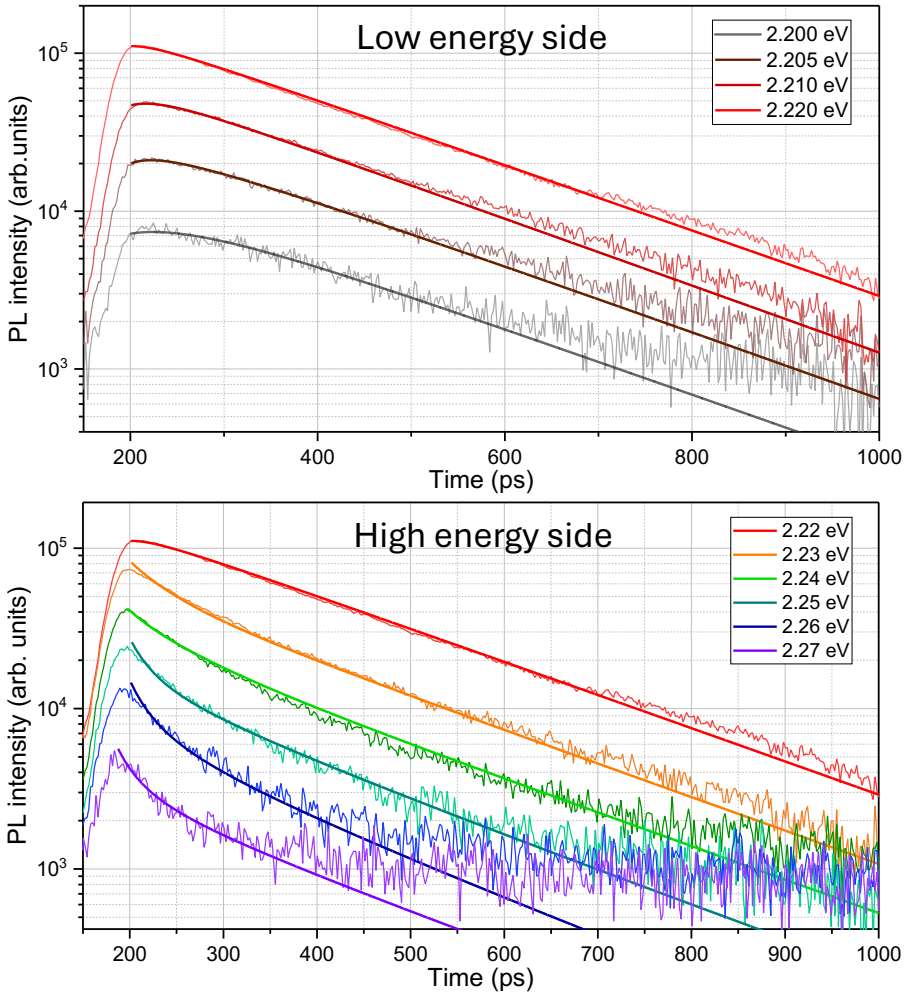

Figure 5.13: Comparison of the simulated decays obtained with the 3D and 2^3 NCs cluster model to the experimental data acquired by TRPL in semi-log scale. The top graph regroups four decays taken on the low energy side of the emission spectrum at specific energy values provided in the legend. The decays on the bottom graph are also taken at different energy values on the high energy flank of the PL emission spectrum. The simulation was performed with $\Gamma_{t,0} = 50$ ns^{-1} and $\Delta_{SS} = 32$ meV.

of magnitude lower but close to the values reported for II-VI based NCs in which resonance conditions - for ET - have been finely tuned [263, 265] or are quasi-naturally achieved [266].

Conclusion

This final chapter was centered on the investigation of $FAPbBr_3$ perovskite NCs encapsulated within a mesoporous silica bead matrix. The NCs were synthesized directly within the matrix pores, eliminating the need for capping ligands. This encapsulation method provides enhanced protection against external threats such as ambient moisture. An initial optical spectroscopy characterization was followed by low-temperature studies of samples with low NC densities. Single

emitter optical responses were occasionally detected although the aggregation of the NCs prevailed in most samples upon reducing their concentration. Further studies on a larger number of samples of different NC content are required to draw conclusions, but these results suggest that, so far and without efforts to control the inner pores reactivity, matrix encapsulation may not surpass the conventional drop-casted diluted colloidal solution method in terms of efficiency for observing the emission response of single objects. The following of the chapter contrasted with the rest of this manuscript in the sense that collective interactions between large numbers of NCs were investigated on high density samples. Using a PL spectroscopy set up comprising a high power femtosecond laser source, an effect of amplified spontaneous emission was uncovered in the system. Finally, in the last section, the study of this system through time resolved PL measurements suggested the existence of inter-NC energy transfer. The results were compared to numerical simulations based on a Förster resonant energy transfer model between nearest neighbors. 2D grids were favored as a starting point in the model but further analysis showed that the values of the main parameters should be poorly dependent on the actual geometry (results were quasi-unchanged when considering 3D clusters keeping the hypothesis of first neighbors coupling). This work provides a rough estimation of the transfer rate ($\Gamma_{t,0} = 50$ ns^{-1}) that would characterize "ideally" coupled NCs (*i.e* with perfect overlap of their absorption and emission line-widths in the Förster scheme). The value is in good agreement with previous findings in II-VI based NC assemblies and with that respect seems to indicate similar FRET properties shared between perovskite materials and more classical semiconductors.

CONCLUSION

This work offers a detailed exploration of the optical properties of lead halide perovskite nanocrystals (NCs), with a particular focus on their exciton fine structure, both at the single-object level and within NC assemblies. Two key materials were studied: the inorganic caesium lead chloride ($CsPbCl_3$) and the hybrid formamidinium lead bromide ($FAPbBr_3$) compound. Through a combination of advanced experimental techniques and theoretical modeling, significant insights have been gained into the excitonic properties in these materials.

The presentation of the experimental work began in Chapter 3 with a detailed study of $CsPbCl_3$ NCs employing TEM imaging, high-resolution micro-spectroscopy, and numerical simulations. At cryogenic temperature, the exciton fine structure emission of individual NCs revealed a majority of sub-meV linewidth two-peak spectral patterns, with the occasional occurence of three-peak spectral responses. These findings were successfully explained by considering a crystal lattice of tetragonal symmetry and deviations in NC shape from the ideal cubic geometry. Within the theoretical framework of the EFS described in Chapter 1, the observation of three peak spectra and the large dispersion in the bright-bright splitting values, Δ_{BB}, were both attributed to the NCs shape anisotropy and corroborated by the NCs size measurements performed on the TEM images. Additionally, although more challenging to detect due to weaker emission intensities, the observation of the spectral responses of the trion and biexciton was also reported in this chapter.

In parallel, an in-depth investigation of the exciton-phonon interactions in $CsPbCl_3$ NCs was presented in Chapter 4. The micro-Raman experiments revealed optical phonon modes that had already been reported in the bulk material. These observations were reinforced by micro-PL spectroscopy measurements that revealed Stokes shifted optical phonon replicas in the emission at energies matching the micro-Raman measurements and confirmed the exciton-phonon coupling scenario. The linewidth broadening of individual peaks from the single NCs' EFS doublets was analyzed as a function of temperature, allowing for the extraction of acoustic and optical coupling constants for the exciton-phonon interaction. Additionally, time-resolved PL experiments were conducted across varying temperatures on ensembles of NCs. By applying a thermal mixing model that involved the absorption and emission of optical phonons to describe the population

of bright and dark EFS states, the energy position of the dark state was determined. This dark state was found to lie below the bright exciton states, with an energy separation, Δ_{BD}, of approximately 10 meV. These results further confirmed the validity of the theoretical model presented in Chapter 1 and more specifically the role of dielectric confinement-enhanced electron-hole exchange interaction in the EFS state organization.

The final chapter focused on the investigation of $FAPbBr_3$ NCs synthesized directly within a mesoporous silica matrix. In samples with a low NC density, low-temperature optical spectroscopy occasionally detected single-emitter responses, although NC aggregation was predominant in most cases. Preliminary studies on samples of high NC density uncovered an effect of amplified spontaneous emission under high excitation fluence. Furthermore, the study of the emission dynamics by TRPL spectroscopy means suggested the existence of inter-NC energy transfers in these samples. These results were compared to numerical simulations based on a Förster resonant energy transfer model between nearest neighbors, and led to a rough estimation of the transfer rate that would characterize "ideally" coupled NCs, in agreement with previous studies on II-VI semiconductor based NCs.

Overall, this work presents the combination of experimental observations and theoretical modeling and offer a robust framework for understanding and possibly optimizing the performance of perovskite materials in optoelectronic applications. It also opens several perspectives for further research on both studied materials. Starting with $CsPbCl_3$, multiple groups have demonstrated that surface passivation or doping with Cd^{2+}, Zn^{2+}, or Nd^{3+} ions significantly improves the emission properties and colloidal stability of the NCs [267, 162, 268], *thus opening the possibility for prolonged studies of single objects with enhanced photostability.* Such developments would give the opportunity to place the NCs under magnetic or electric fields for extended periods of time. Regarding the EFS, two types of studies under magnetic fields would be particularly interesting. Under "low" intensity magnetic fields (*e.g.*, $\sim$ 5 T), it may be possible to split the degenerate EFS levels *via* the Zeeman effect. This was attempted during the thesis, given that our group has access to such fields; however, experimental challenges, primarily related to sample instability, prevented a deeper exploration. In contrast, at high intensity magnetic fields, (*i.e.*, as mentioned in Chapter 4, around 80 T), magneto-optical coupling between the bright and dark states [181] could enable the detection of dark-state emission, further confirming its energy position in the EFS. Such experiments require to be performed in a laboratory offering high fields facilities in demanding conditions with regard to the ability to control the NCs dilution and preservation. This adds to the general challenge. Finally, placing the NCs between conducting interdigitated electrodes could allow the application of a high-intensity electric field to a single NC, potentially shifting the EFS levels through the Stark effect. If successful, this approach could lead to a precise

control of the energy states within the fine structure, as it has been demonstrated by other groups in different systems [78].

An extension of this work could also consist in addressing NCs having a changed dimensionnality. In 2D colloidal MHP materials (*i.e.* nanoplatelets, NPLs), the ultra-high quantum confinement that can be achieved along the transverse dimension, is combined to the promotion of quantum dielectric effects. This association leads to a 'renewed' schematic organisation of the EFS sub-levels easily tunable by adjusting the NPL thickness (decoupling in energy between groups of dipoles depending on their orientation, large bright-dark splitting). The 2D geometry thus offers valuable insights and strategies for controlling the exciton relaxation/emission : adjustment of the emission anisotropy or engineering of the phonon bottleneck effect that was shown to govern the exciton thermalization and emission dynamics in bromide-based NPLs. All the issues have important implications for optimized optoelectronic devices using NPLs as components but they also own a fundamental character that deserves in depth investigations. $CsPbCl_3$ NPLs of high quality have already been synthesized in the laboratory (INSP). They thus could come as a prototypical system to be investigated (in a comparative approach regarding the results already existing in $CsPbBr_3$ NPLs and using the spectroscopic tools operated throughout this work), exploiting wisely our 'relatively good' knowledge of their NCs counterparts. The studies remain a real challenge for all the excitonic transitions are strongly shifted towards higher energy and positioned in the 340 nm – 400 nm range - in agreement with the increased level of confinement- that requires appropriate but attainable modifications of the setup.

Regarding now the $FAPbBr_3$ NCs embedded in the Silica matrix, the non linear effect reported in Chapter 5 at high excitation fluence would benefit from a deeper exploration. The excitation of the system using a semi-cylindrical lens associated to a collection of the emitted light in a direction orthogonal to the excited stripe axis, would place the system in the typical configuration for such studies. This approach would enable direct comparison with other perovskite NC systems like thin films (through the estimation of the gain and losses coefficients in particular) and help to determine if the observed effect deserves deeper investigation in this particular environment. Finally, regarding the use of the mesoporous matrix for the isolation of NCs, further developments are needed for the synthesis of samples containing a low density of NCs. Currently, NCs tend to aggregate at different points in the system. Achieving a uniform, low-concentration distribution would be highly beneficial for single-object studies, due to the apparent protective role of the mesoporous matrix regarding the chemical and photo-stability of the system.

APPENDIX

LONG RANGE EXCHANGE INTERACTION

A

As stated in Chap. 1 the long-range component of the electron-hole exchange interaction is given by the general expression [69]:

$$\mathcal{H}^{LR}_{\substack{c'v'\\cv}}\begin{pmatrix}\mathbf{r}'_e & \mathbf{r}'_h\\ \mathbf{r}_e & \mathbf{r}_h\end{pmatrix} = \sum_{i,j}\mathfrak{Q}^{ij}_{\substack{c'\mathcal{I}v\\ \mathcal{I}v'c}}\frac{\partial^2}{\partial r^i_e \partial r^j_h}\mathcal{W}(\mathbf{r}_e,\mathbf{r}'_h)\;\delta\left(\mathbf{r}_e-\mathbf{r}_h\right)\delta\left(\mathbf{r}'_e-\mathbf{r}'_h\right) \tag{A.1}$$

In this expression, $\mathcal{W}$ is obtained from $(-\mathcal{V}_{e-h})$ by replacing ϵ_1 by ϵ_X, the dielectric constant at the exciton resonance, in the denominator of Eq. 1.29. The Bloch states in the conduction band (the hole in the valence band) are denoted by the symbols c, c' (v , v'), while the coordinates of the electrons and holes are denoted by the symbols $(\mathbf{r}_e,\mathbf{r}'_e)$ and $(\mathbf{r}_h,\mathbf{r}'_h)$, respectively. The time-reversal operator, $\mathcal{I}$, alters the linear momentum $\mathbf{p}$ and the angular momentum by their opposite while leaving $\mathbf{r}$ unchanged. The $\mathfrak{Q}$ matrix implicates the products of the momentum operators [**pikus_exchange_nodate**, 70], their matrix elements are provided by:

$$\mathfrak{Q}^{ij}_{\substack{c'\mathcal{I}v\\ \mathcal{I}v'c}} = \frac{\hbar^2}{m_0^2}\frac{\langle c'|\,p_i\,|\mathcal{I}v'\rangle\,\langle\mathcal{I}v|\,p_j\,|c\rangle}{\left(E^0_c-E^0_v\right)\left(E^0_{c'}-E^0_{v'}\right)} \tag{A.2}$$

where m_0 is the free electron mass and p_i (p_j) is the i (j) component of the $\mathbf{p}$ momentum; E^0_ν ($\nu = c, c', v, v'$) is the ν^{th} band energy.

The expression of the LR Hamiltonian is obtained by calculating $\partial^2\mathcal{W}/\partial r^i_e\partial r^j_h$. To do that, the

Fourier transform is used to rewrite the $\mathcal{W}$ interaction as:

$$\left\{ \mathcal{W}(\mathbf{r}_e, \mathbf{r}'_h) = \frac{1}{(2\pi)^3} \frac{e^2}{\epsilon_0 \epsilon_X} \int \frac{d\mathbf{q}}{q^2} \sum_{m=-\infty}^{+\infty} \sum_{n=-\infty}^{+\infty} \sum_{p=-\infty}^{+\infty} \eta^{|m|+|n|+|p|} \exp iq_x(x_e - x'_{hm}) \exp iq_y(y_e - y'_{hn}) \right.$$
$$\left. \times \exp iq_z(z_e - z'_{hp}) \right. \tag{A.3}$$

One deduces

$$\left\{ \frac{\partial^2 \mathcal{W}}{\partial r_e^i \partial r_h^j}(\mathbf{r}_e, \mathbf{r}'_h) = -\frac{1}{(2\pi)^3} \frac{e^2}{\epsilon_0 \epsilon_X} \int d\mathbf{q} \frac{q_i q_j}{q^2} \sum_{m=-\infty}^{+\infty} \sum_{n=-\infty}^{+\infty} \sum_{p=-\infty}^{+\infty} (-1)^{\ell_j} \eta^{|m|+|n|+|p|} \exp iq_x(x_e - x'_{hm}) \right.$$
$$\left. \times \exp iq_y(y_e - y'_{hn}) \exp iq_z(z_e - z'_{hp}) \right. \tag{A.4}$$

with $\ell_j = m$, n or p, for $j = x$, y or z, respectively. Using the envelope function of the electron and the hole in the exciton state (Eq. 1.25), the matrix elements of $\mathcal{H}^{LR}$ can be written:

$$\left\{ -\frac{1}{(2\pi)^3} \frac{e^2}{\epsilon_0 \epsilon_X} \int \frac{d\mathbf{q}}{q^2} \sum_{i,j} \mathfrak{Q}^{ij}_{\substack{c'\mathcal{I}_v \\ \mathcal{I}_{v'} c}} q_i q_j \sum_{m=-\infty}^{+\infty} \sum_{n=-\infty}^{+\infty} \sum_{p=-\infty}^{+\infty} (-1)^{\ell_j} \eta^{|m|+|n|+|p|} \exp(-iq_x L_x) \exp(-iq_y L_y) \right.$$
$$\left. \exp(-iq_z L_z) \times \int d\mathbf{r} \Psi(\mathbf{r}, \mathbf{r}) \exp(\mathbf{iq}.\mathbf{r}) \int d\mathbf{r} \Psi(\mathbf{r}, \mathbf{r}) \exp(\mathbf{iq}.\xi_{m,n,p}) \right. \tag{A.5}$$

with

$$\xi_{m,n,p} = ((-1)^m x, (-1)^n y, (-1)^p z) \tag{A.6}$$

Based on the parity of the $\Psi(\mathbf{r}, \mathbf{r})$ envelope function, the two integrals in the expression (Eq. A.5) are equivalent and can be separated into three discrete summations. Summing apart on the integers m, n and p, one gets:

$$-\frac{1}{(2\pi)^3} \frac{e^2}{\epsilon_0 \epsilon_X} \int \frac{d\mathbf{q}}{q^2} \sum_{i,j} \mathfrak{Q}^{ij}_{\substack{c'\mathcal{I}_v \\ \mathcal{I}_{v'} c}} q_i q_j \prod_{\kappa=x,y,z} \mathfrak{D}_\kappa(q_\kappa, L_\kappa) \left| \int d\mathbf{r} \Psi(\mathbf{r}, \mathbf{r}) \exp(\mathbf{iq}.\mathbf{r}) \right|^2 \tag{A.7}$$

in which

$$\mathfrak{D}_\kappa(q_\kappa, L_\kappa) = \left\{ \begin{array}{ll} \mathfrak{D}_+(q_\kappa, L_\kappa) = \frac{(1-\eta^2)}{1+\eta^2+2\eta\cos(q_\kappa L_\kappa)} & \text{for } \kappa = j \\ \mathfrak{D}_-(q_\kappa, L_\kappa) = \frac{(1-\eta^2)}{1+\eta^2-2\eta\cos(q_\kappa L_\kappa)} & \text{for } \kappa \neq j \end{array} \right. \tag{A.8}$$

With the e-h pair basis $\{|+1\rangle, |-1\rangle, |0_B\rangle, |0_D\rangle\}$, one finds that the matrix $\underset{\mathcal{I}v'\ c}{\underset{c'\mathcal{I}v}{\mathfrak{Q}}}(\mathbf{q}) = \sum_{i,j} \underset{\mathcal{I}v'\ c}{\underset{c'\mathcal{I}v}{\mathfrak{Q}^{ij}}} q_i q_j$ has the following representation:

$$\frac{1}{E_g^2}\begin{bmatrix} \begin{pmatrix} \alpha^2 P_{S,x}^2 q_x^2 \\ +\beta^2 P_{S,y}^2 q_y^2 \end{pmatrix} & -\begin{pmatrix} \alpha P_{S,x} q_x \\ -i\beta P_{S,y} q_y \end{pmatrix}^2 & \sqrt{2}\gamma P_{S,z} q_z \begin{pmatrix} \alpha P_{S,x} q_x \\ -i\beta P_{S,y} q_y \end{pmatrix} & 0 \\ c.c. & \begin{pmatrix} \alpha^2 P_{S,x}^2 q_x^2 \\ +\beta^2 P_{S,y}^2 q_y^2 \end{pmatrix} & -\sqrt{2}\gamma P_{S,z} q_z \begin{pmatrix} \alpha P_{S,x} q_x \\ +i\beta P_{S,y} q_y \end{pmatrix} & 0 \\ c.c. & c.c. & 2\gamma^2 P_{S,z}^2 q_z^2 & 0 \\ 0 & 0 & 0 & 0 \end{bmatrix} \tag{A.9}$$

where *c.c.* refers to the conjugate complex. $(P_{S,x}, P_{S,y}, P_{S,z})$ are the Kane interband matrix elements under the D_{2h} point group symmetry [23]. In the limit of cubic crystal symmetry - O_h symmetry - the Kane parameters have the same values $P_{S,x} = P_{S,y} = P_{S,z} = P_s$ whereas in the tetragonal crystal phase - D_{4h} symmetry - $P_{S,x} = P_{S,y} = P_{S,\rho}$.

Taking into account the elements of the $\mathfrak{Q}$ matrix (see Eq. A.9) in the expression Eq. A.7, the LR exchange matrix takes the following form:

$$\mathcal{H}^{LR} = \begin{bmatrix} \Sigma_d & \Sigma_{od} & 0 & 0 \\ \Sigma_{od} & \Sigma_d & 0 & 0 \\ 0 & 0 & \Sigma_z & 0 \\ 0 & 0 & 0 & 0 \end{bmatrix} \tag{A.10}$$

In the expression Eq. A.10, Σ_d, Σ_{od} and Σ_z are given by:

$$\begin{cases} \Sigma_d = \left[\alpha^2 E_{P_{S,x}} I_x + \beta^2 E_{P_{S,y}} I_y\right] \Lambda\pi^9 \left(\frac{\pi a_X^3}{L_x^3}\right) \left(\frac{3|\mathcal{N}(a)|^2}{rs}\right) \\ \Sigma_{od} = \left[-\alpha^2 E_{P_{S,x}} I_x + \beta^2 E_{P_{S,y}} I_y\right] \Lambda\pi^9 \left(\frac{\pi a_X^3}{L_x^3}\right) \left(\frac{3|\mathcal{N}(a)|^2}{rs}\right) \\ \Sigma_z = 2\gamma^2 E_{P_{S,z}} I_z \Lambda\pi^9 \left(\frac{\pi a_X^3}{L_x^3}\right) \left(\frac{3|\mathcal{N}(a)|^2}{rs}\right) \end{cases} \tag{A.11}$$

In these expressions, the Kane parameters are substituted by the Kane energy, defined by, $E_{P_{S,j}} = \left(2m_0/\hbar^2\right) P_{S,j}^2$ $(j = x, y, z)$; Λ can be expressed in terms of basic parameters as follow:

$$\Lambda = \frac{1}{3E_g^2} \frac{\hbar^2}{2m_0} \frac{e^2}{\epsilon_0 \epsilon_X} \frac{1}{\pi a_X^3} \tag{A.12}$$

As noted above, the r and s parameters describe the shape elongation/contraction of the rectangular cuboid: $r = L_y/L_x$ and $s = L_z/L_x$. The exchange integrals, I_l $(l = x, y, z)$, can be

expressed in the following form:

$$\begin{cases} I_x = \int d\mathbf{u} \frac{r^2 s^2 u_x^2}{r^2 s^2 u_x^2 + s^2 u_y^2 + r^2 u_z^2} \frac{\sin^2 u_x}{u_x^2 (u_x^2 - \pi^2)^2} \frac{\sin^2 u_y}{u_y^2 \left(u_y^2 - \pi^2\right)^2} \frac{\sin^2 u_z}{u_z^2 (u_z^2 - \pi^2)^2} \underline{d}_+(u_x) \underline{d}_-(u_y) \underline{d}_-(u_z) \\ I_y = \int d\mathbf{u} \frac{s^2 u_y^2}{r^2 s^2 u_x^2 + s^2 u_y^2 + r^2 u_z^2} \frac{\sin^2 u_x}{u_x^2 (u_x^2 - \pi^2)^2} \frac{\sin^2 u_y}{u_y^2 \left(u_y^2 - \pi^2\right)^2} \frac{\sin^2 u_z}{u_z^2 (u_z^2 - \pi^2)^2} \underline{d}_-(u_x) \underline{d}_+(u_y) \underline{d}_-(u_z) \\ I_z = \int d\mathbf{u} \frac{r^2 u_z^2}{r^2 s^2 u_x^2 + s^2 u_y^2 + r^2 u_z^2} \frac{\sin^2 u_x}{u_x^2 (u_x^2 - \pi^2)^2} \frac{\sin^2 u_y}{u_y^2 \left(u_y^2 - \pi^2\right)^2} \frac{\sin^2 u_z}{u_z^2 (u_z^2 - \pi^2)^2} \underline{d}_-(u_x) \underline{d}_-(u_y) \underline{d}_+(u_z) \end{cases} \tag{A.13}$$

where $\underline{d}_\pm(u) = \left(1 - \eta^2\right) / \left(1 + \eta^2 \pm 2\eta \cos(2u)\right)$. The functions $\underline{d}_\pm$ reflect the correction caused by dielectric effects in the EI. Note that all the image charges, in the 3D space, are taken into account in the derivation of these integrals. The impact of the interaction between the NC and its microscopic environment, mainly the influence of the dielectric discontinuity on the NC surface, is controlled by $\underline{d}_\pm$; when there is no dielectric contrast, $\eta = 0$ and we have $\underline{d}_\pm(u) = 1$.

APPENDIX

MODELING EMISSION COLLECTION FROM ORTHOGONAL DIPOLES

B

The objective of this appendix is to derive the model used to simulated the collected intensity of the three orthogonal linear dipoles composing the EFS by an objective of a given numerical aperture. Here we directly use the work of Clotilde Lethiec and coauthors [183].

Fig. B.1 illustrates the situation of interest. A linear dipole in a medium of indice n is represented by the unitary vector $\vec{u_d}$. The direction of observation is represented by the vector $\vec{u_k}$. Thus, all the possible directions of observation (defined by the numerical aperture, NA, of the microscope objective) form a circular cone around the optical axis z, of angle θ_k:

In the far field limit, the electric field emitted by a dipole in a homogeneous medium is given by [183]:

$$E(r, \theta_k, \varphi_k) = \frac{D}{r}(\vec{u_k} \wedge \vec{u_d} \wedge \vec{u_k})e^{i(\mathbf{kr}-\omega t)} \tag{B.1}$$

Where $D = 1/4\pi c^2 \epsilon_0 \epsilon$ and ϵ_0, ϵ are the dielectric permittivity of the vacuum and the medium respectively. In Eq. B.1 the phase term $e^{i(\mathbf{kr}-\omega t)}$ will be discarded in the following since only the intensity emitted by the dipole is of interest here. In spherical coordinates $\vec{u_d}$ and $\vec{u_k}$ take the following expression:

$$\vec{u_i} = \begin{pmatrix} \sin\theta_i \cos\varphi_i \\ \sin\theta_i \sin\varphi_i \\ \cos\theta_i \end{pmatrix} \quad \text{with: } i = d, k \tag{B.2}$$

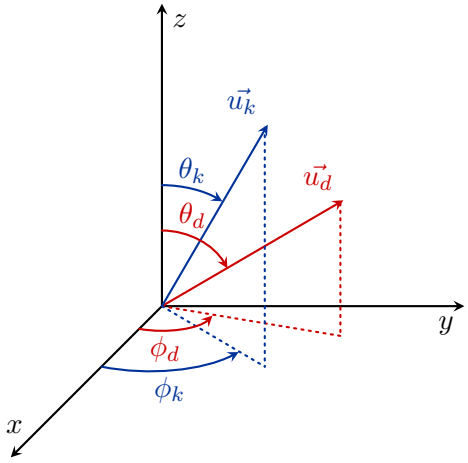

Figure B.1: Representation of the emitting dipole of axis defined by the vector $\vec{u_d}(\theta_d, \phi_d)$ and the observation direction defined by the vector $\vec{u_k}(\theta_k, \phi_k)$.

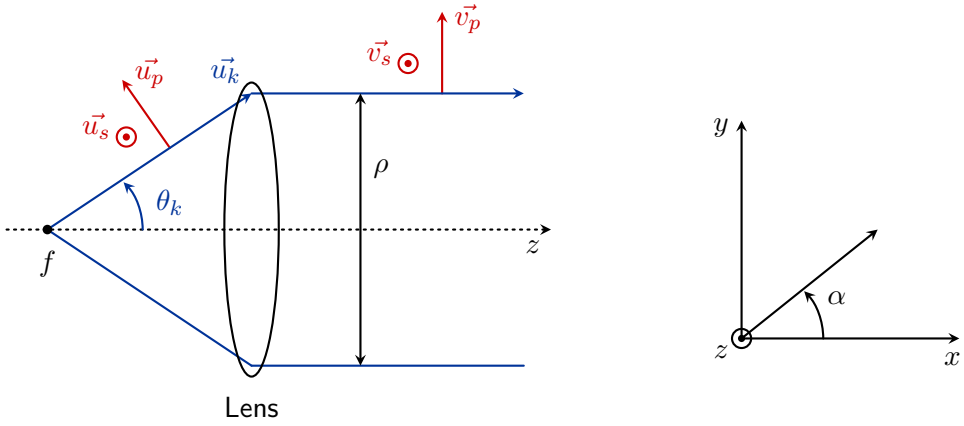

Figure B.2: Left: the spherical radiated wave is transformed into a plane wave after collection by the objective (represented here by a simple lens). Right: the rotating polarizer axis in the xy plane.

The electric field can be separated into two orthogonal components along unit vector $\vec{u_s}$ and $\vec{u_p}$ in the plane perpendicular to the direction of observation defined by vector $\vec{u_k}$ (see Fig. B.2 before the lens):

$$\vec{E}(\theta_k, \phi_k) = \frac{D}{r} \left[E_s(\theta_k, \phi_k)\vec{u_s} + E_p(\theta_k, \phi_k)\vec{u_p} \right] \tag{B.3}$$

Where the amplitudes of the electric field components, E_s and E_p, are given by:

$$\begin{cases} E_s(\theta_k, \phi_k) = \sin\theta_d \sin(\phi_k - \phi_d) \\ E_p(\theta_k, \phi_k) = -\cos\theta_d \sin\theta_k + \sin\theta_d \cos\theta_k \cos(\phi_d - \phi_k) \end{cases} \tag{B.4}$$

And the vectors $\vec{u_s}$, $\vec{u_p}$ by:

$$\vec{u_s} = \begin{pmatrix} \sin\phi_k \\ \cos\phi_k \\ 0 \end{pmatrix} \qquad \vec{u_p} = \begin{pmatrix} \cos\theta_k \cos\phi_k \\ \cos\theta_k \sin\phi_k \\ -sin\theta_k \end{pmatrix} \tag{B.5}$$

When the electric field arrives at the microscope objective (represented by the lens on Fig. B.2) it is still a spherical wave. Since the emitting dipole is located at the focal point f of the objective, the electric field is transformed into a plane wave (collimated beam) after the microscope objective (situation sketched on Fig. B.2). Thus, using the conservation of energy before and after the objective leads to the following expression for the electric field :

$$\left|\vec{E'}(\rho, \phi_k, z)\right|^2 = \left|\vec{E}(f, \phi_k, z)\right|^2 \tag{B.6}$$

Using Eq. B.3, $\vec{E'}(\rho, \phi_k, z)$ can be expressed in cylindrical coordinates as:

$$\vec{E'}(\rho, \phi_k, z) = \frac{D}{f}\left[E_s(\theta_k, \phi_k)\vec{v_s} + E_p(\theta_k, \phi_k)\vec{v_p}\right] \tag{B.7}$$

With the unit vectors $\vec{v_s} = \vec{u_s}$ and $\vec{v_p} = (\cos\phi_k, \sin\phi_k, 0)$ and f the focal length of the objective.

The electric field then passes through the polarizer system. If the polarizer axis makes an angle α with the x axis (parallel to the wave planes, see Fig. B.2) the normalized emitted power detected after the polarizer writes:

$$P(\alpha) = \int_{\rho=0}^{\rho_{max}} \int_{\phi=0}^{2\pi} \left|\vec{E'}(\rho, \phi_k, z) \cdot \vec{u_\alpha}\right|^2 \rho d\rho d\phi_k \tag{B.8}$$

In this work, and considering here exciton bright states that are non-degenerate (NC of orthorhombic crystal phase or tetragonal with an anisotropic shape), three linear and orthogonal emitting dipoles are considered (EFS states $|X\rangle$, $|Y\rangle$, $|Z\rangle$). Thus, if a first dipole has an orientation defined by (θ_d, ϕ_d), the second dipole will be defined by ($\theta_d + \pi/2$, ϕ_d) and the third by ($\pi/2$, $\phi_d + \pi/2$). With these considerations in mind, one can simulate the collected power for each dipole by the integration of Eq. B.8 and for each position of the polarizer angle α. The "initial" orientation of the dipoles can also be changed simply by adjusting the values of θ_d and ϕ_d (this translates into a change of the NC orientation). Fig. B.3 (see next page) presents the results obtained for the system described above.

Regarding now a system where two dipoles are degenerate (tetragonal crystal phase of MHPs) one has two circular polarization $|\Psi_+\rangle = [|X\rangle + i\,|Y\rangle]/\sqrt{2}$ and $|\Psi_-\rangle = [|X\rangle - i\,|Y\rangle]/\sqrt{2}$ (where

$|X\rangle$, $|Y\rangle$ are the degenerate dipoles) and a linear polarization $|Z\rangle$. The simulations can be simply adapted to these new expressions and the results were presented on Fig. 3.12 in the main text.

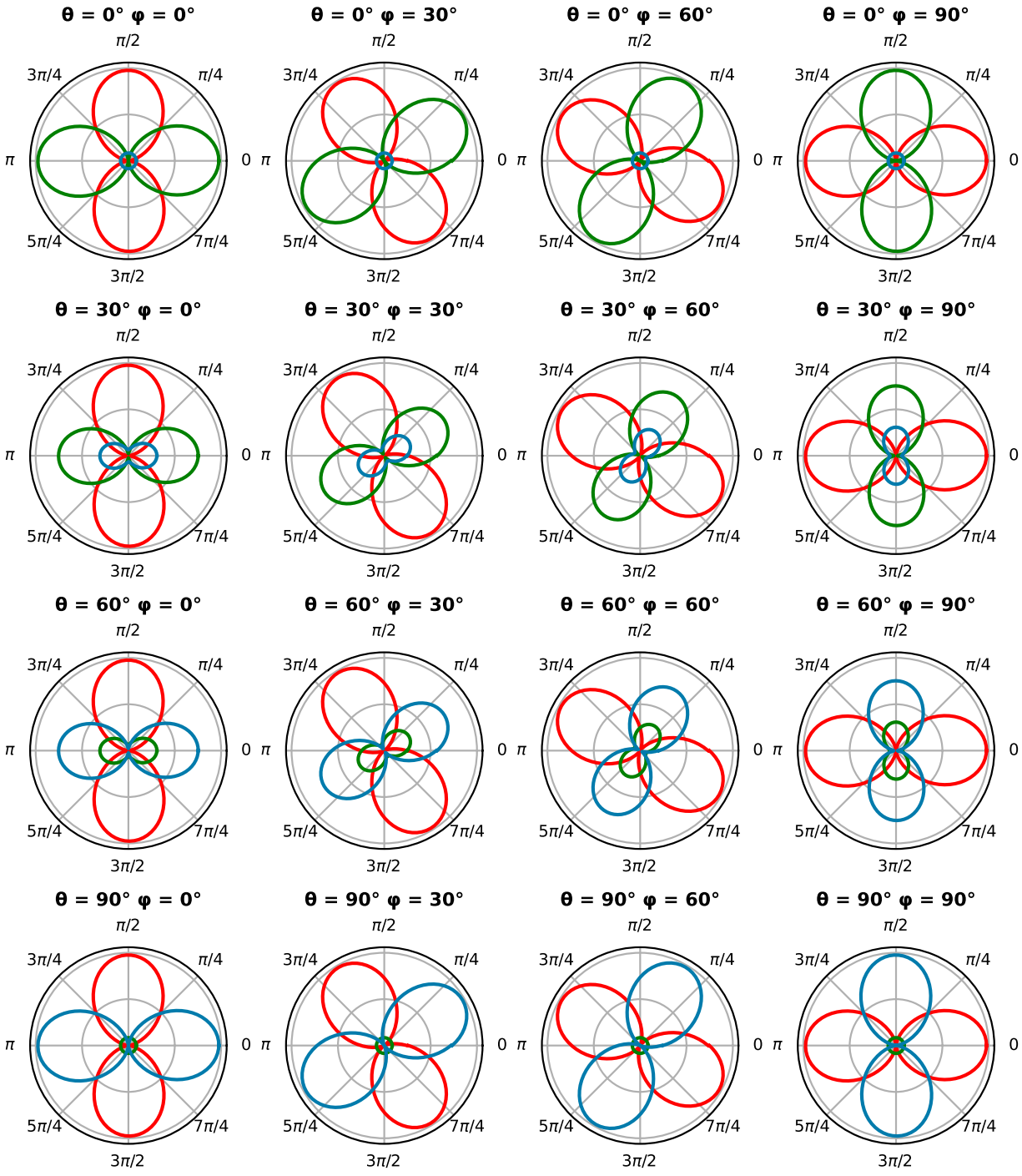

Figure B.3: Simulated polar diagrams of three orthogonal emitting dipoles, corresponding to the emitting states of LHP NCs of orthorhombic crystal phase. The angles Θ and φ give the orientation of the dipole $|Z\rangle$, while the dipoles $|X\rangle$ and $|Y\rangle$ are orthogonal to $|Z\rangle$ at all times. Note that here, the explored configurations keep a dipole (the red one) in the plane orthogonal to the optical axis z.

APPENDIX

THERMAL MIXING MODELS C

Both thermal mixing models presented in Chap. 4 and illustrated on Fig. C.1 can be described by the same general set of equations with specificities that will be detailed in the following.

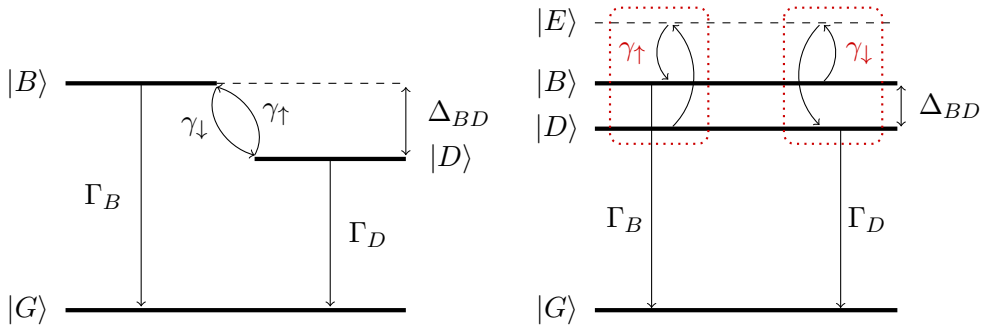

Figure C.1: Energy level diagrams of both thermal mixing models presented in this work. The bright and dark state population is assured by the absorption or emission of optical phonons with energy matching the bright-dark splitting.

For both models, considering all the processes that fill or empty the bright and dark states, their populations ρ_B and ρ_D are governed by the following set of differential equations:

$$\begin{cases} \dot{\rho_B} = -(\Gamma_B + \gamma_\downarrow)\rho_B + \gamma_\uparrow \rho_D \\ \dot{\rho_D} = -(\Gamma_D + \gamma_\uparrow)\rho_D + \gamma_\downarrow \rho_B \end{cases} \tag{C.1}$$

This system can also be written under the form of a matrix equation $\dot{\boldsymbol{\rho}} = \mathcal{M}\boldsymbol{\rho}$:

$$\begin{pmatrix} \dot{\rho_B} \\ \dot{\rho_D} \end{pmatrix} = \begin{pmatrix} a & b \\ c & d \end{pmatrix} \begin{pmatrix} \rho_B \\ \rho_D \end{pmatrix} \tag{C.2}$$

Where $a = -(\Gamma_B + \gamma_\downarrow)$, $b = \gamma_\uparrow$, $c = \gamma_\downarrow$ and $d = -(\Gamma_D + \gamma_\uparrow)$.

The general solution of Eq. C.2 is written as a sum of exponential decay functions such as:

$$\boldsymbol{\rho}(t) = A_1 \exp^{-\Gamma_L t} \mathbf{u_L} + A_2 \exp^{-\Gamma_S t} \mathbf{u_S} \tag{C.3}$$

Where $A_{1,2}$ are the amplitudes of each component and $\mathbf{u_{S,L}}$ are the eigenvectors of matrix $\mathcal{M}$. The eigenvalues $\Gamma_{S,L}$ are given by:

$$\Gamma_{S,L} = \frac{1}{2}\left[a + d + \pm\sqrt{(a+d)^2 + 4(ad - bc)}\right] \tag{C.4}$$

Thus the following vectors are eigenvectors of $\mathcal{M}$:

$$\boldsymbol{u_S} = \left(1, \frac{\Gamma_S - a}{b}\right) \qquad \boldsymbol{u_L} = \left(1, \frac{\Gamma_L - a}{b}\right) \tag{C.5}$$

At $t = 0$ considering that the bright state has a population ρ_0 the dark state has population $1 - \rho_0$ and thus $\boldsymbol{\rho}(t = 0) = A_S \mathbf{u_S} + A_L \mathbf{u_L} = (\rho_0\ ,\ 1 - \rho_0)$. Solving this equation gives the amplitude for A_1 and A_2:

$$A_1 = \frac{-b(1-\rho_0) + \rho_0(\Gamma_S - a)}{\Gamma_L - \Gamma_S} \tag{C.6}$$

$$A_2 = \frac{b(1-\rho_0) - \rho_0(\Gamma_L - a)}{\Gamma_L - \Gamma_S} \tag{C.7}$$

The total PL intensity can be written as:

$$I(t) = \Gamma_B \eta_B \rho_B(t) + \Gamma_D \eta_D \rho_D(t) \tag{C.8}$$

$$= \Gamma_B \eta_B \left[A_1 e^{-\Gamma_S t} + A_2 e^{-\Gamma_L t}\right] + \Gamma_B \eta_B \left[A_1 \left(\frac{\Gamma_S - a}{b}\right) e^{-\Gamma_S t} + A_2 \left(\frac{\Gamma_L - a}{b}\right) e^{-\Gamma_L t}\right] \tag{C.9}$$

Thus, solving for $t = 0$:

$$I(t=0) = A_1 \left[\Gamma_B \eta_B + \Gamma_D \eta_D \left(\frac{\Gamma_S - a}{b}\right)\right] + A_2 \left[\Gamma_B \eta_B + \Gamma_D \eta_D \left(\frac{\Gamma_L - a}{b}\right)\right] \tag{C.10}$$

The first term on the right side of Eq. C.10 gives the amplitude of the short decay A_S while the second term gives A_L, the long decay amplitude *i.e*:

$$A_S = A_1 \left[\Gamma_B \eta_B + \Gamma_D \eta_D \left(\frac{\Gamma_S - a}{b} \right) \right] \tag{C.11}$$

$$A_L = A_2 \left[\Gamma_B \eta_B + \Gamma_D \eta_D \left(\frac{\Gamma_L - a}{b} \right) \right] \tag{C.12}$$

with $a = -(\Gamma_B + \gamma_\downarrow)$ and $b = \gamma_\uparrow$ and A_1, A_2 given by Eq. C.6 and Eq. C.7.

Finally, the biexponential decay is given by:

$$I(t) = A_L \exp^{-\Gamma_L t} + A_S \exp^{-\Gamma_S t} \tag{C.13}$$

Depending on the thermal mixing model that is considered, the rates $\gamma_\uparrow$ and $\gamma_\downarrow$ take different expressions given in Eq. 4.7 for the one phonon model and Eq. 4.14 for the two phonon model. To simplify the calculation of the short and long decay rates Γ_S and Γ_L given by Eq. 4.10 in the main text, the following sets of equations, combining both $\gamma_\uparrow$ and $\gamma_\downarrow$ for each model can be used:

One phonon thermal mixing model:

$$\gamma_\uparrow + \gamma_\downarrow = \gamma_0(1 + 2n) = \gamma_0 \coth \left(\frac{E_{LO}}{2k_B T} \right) \tag{C.14}$$

$$\gamma_\uparrow \gamma_\downarrow = \gamma_0^2 n(1 + n) = \frac{1}{4} \gamma_0^2 \sinh^{-2} \left(\frac{E_{LO}}{2k_B T} \right) \tag{C.15}$$

Two phonon thermal mixing model:

$$\gamma_\uparrow + \gamma_\downarrow = \frac{\gamma_0}{2} \left[\coth \left(\frac{E_{LO_1}}{2k_B T} \right) \coth \left(\frac{E_{LO_2}}{2k_B T} \right) - 1 \right] \tag{C.16}$$

$$\gamma_\uparrow - \gamma_\downarrow = \frac{\gamma_0}{2} \left[\coth \left(\frac{E_{LO_1}}{2k_B T} \right) - \coth \left(\frac{E_{LO_2}}{2k_B T} \right) \right] \tag{C.17}$$

$$\gamma_\uparrow \gamma_\downarrow = \left[\frac{\gamma_0}{4} \sinh^{-1} \left(\frac{E_{LO_1}}{2k_B T} \right) \sinh^{-1} \left(\frac{E_{LO_2}}{2k_B T} \right) \right]^2 \tag{C.18}$$

Bibliography

[1] A. I. Ekimov, A. A. Onushchenko, and V. A. Tsekhomski. "Exciton Absorption by Copper Chloride Crystal in Glassy Matrix." In: *Fiz. Khim. Stekla* (1980) (Cited on page 13).

[2] A. I. Ekimov and A. A. Onushchenko. "Quantum Size Effect in Three Dimensional Microscopic Semiconductor Crystals." In: *JETP Lett.* (1981) (Cited on page 13).

[3] Al. L. Efros and A. L. Efros. "Interband absorption of light in a semiconductor sphere". In: *Soviet Physics Semiconductors Ussr* 16.7 (1982), pp. 772–775 (Cited on page 13).

[4] A. I. Ekimov, Al. L. Efros, and A. A. Onushchenko. "Quantum size effect in semiconductor microcrystals". In: *Solid State Communications* 56.11 (Dec. 1985), pp. 921–924. DOI: 10.1016/S0038-1098(85)80025-9 (Cited on page 13).

[5] R. Rossetti, S. Nakahara, and L. E. Brus. "Quantum size effects in the redox potentials, resonance Raman spectra, and electronic spectra of CdS crystallites in aqueous solution". In: *The Journal of Chemical Physics* 79.2 (July 1983), pp. 1086–1088. DOI: 10.1063/1.445834 (Cited on page 13).

[6] L. E. Brus. "Electron–electron and electron-hole interactions in small semiconductor crystallites: The size dependence of the lowest excited electronic state". In: *The Journal of Chemical Physics* 80.9 (May 1984), pp. 4403–4409. DOI: 10.1063/1.447218 (Cited on page 13).

[7] N. Chestnoy, R. Hull, and L. E. Brus. "Higher excited electronic states in clusters of ZnSe, CdSe, and ZnS: Spin-orbit, vibronic, and relaxation phenomena". In: *The Journal of Chemical Physics* 85.4 (Aug. 1986), pp. 2237–2242. DOI: 10.1063/1.451119 (Cited on page 13).

[8] C. B. Murray, D. J. Norris, and M. G. Bawendi. "Synthesis and characterization of nearly monodisperse CdE (E = sulfur, selenium, tellurium) semiconductor nanocrystallites". In: *Journal of the American Chemical Society* 115.19 (Sept. 1993). Publisher: American Chemical Society, pp. 8706–8715. DOI: 10.1021/ja00072a025 (Cited on page 13, 21, 55).

[9] Marcel Bruchez et al. “Semiconductor Nanocrystals as Fluorescent Biological Labels”. In: *Science* 281.5385 (Sept. 1998). Publisher: American Association for the Advancement of Science, pp. 2013–2016. DOI: 10.1126/science.281.5385.2013 (Cited on page 14).

[10] Benoit Dubertret et al. “In Vivo Imaging of Quantum Dots Encapsulated in Phospholipid Micelles”. In: *Science* 298.5599 (Nov. 2002). Publisher: American Association for the Advancement of Science, pp. 1759–1762. DOI: 10.1126/science.1077194 (Cited on page 14).

[11] A. J Nozik. “Quantum dot solar cells”. In: *Physica E: Low-dimensional Systems and Nanostructures* 14.1 (Apr. 2002), pp. 115–120. DOI: 10.1016/S1386-9477(02)00374-0 (Cited on page 14).

[12] Emmanuel Lhuillier et al. “Infrared Photodetection Based on Colloidal Quantum-Dot Films with High Mobility and Optical Absorption up to THz”. In: *Nano Letters* 16.2 (Feb. 2016). Publisher: American Chemical Society, pp. 1282–1286. DOI: 10.1021/acs.nanolett.5b04616 (Cited on page 14).

[13] Yu-Ho Won et al. “Highly efficient and stable InP/ZnSe/ZnS quantum dot light-emitting diodes”. en. In: *Nature* 575.7784 (Nov. 2019). Publisher: Nature Publishing Group, pp. 634–638. DOI: 10.1038/s41586-019-1771-5 (Cited on page 14).

[14] Talha Erdem and Hilmi Volkan Demir. “Colloidal nanocrystals for quality lighting and displays: milestones and recent developments”. en. In: *Nanophotonics* 5.1 (June 2016). Publisher: De Gruyter, pp. 74–95. DOI: 10.1515/nanoph-2016-0009 (Cited on page 14).

[15] V. I. Klimov et al. “Optical Gain and Stimulated Emission in Nanocrystal Quantum Dots”. In: *Science* 290.5490 (Oct. 2000). Publisher: American Association for the Advancement of Science, pp. 314–317. DOI: 10.1126/science.290.5490.314 (Cited on page 14).

[16] B. Lounis et al. “Photon antibunching in single CdSe/ZnS quantum dot fluorescence”. In: *Chemical Physics Letters* 329.5 (Oct. 2000), pp. 399–404. DOI: 10.1016/S0009-2614(00)01042-3 (Cited on page 14).

[17] Loredana Protesescu et al. “Nanocrystals of Cesium Lead Halide Perovskites ($CsPbX_3$, X = Cl, Br, and I): Novel Optoelectronic Materials Showing Bright Emission with Wide Color Gamut”. In: *Nano Letters* 15.6 (June 2015). Publisher: American Chemical Society, pp. 3692–3696. DOI: 10.1021/nl5048779 (Cited on page 14, 18, 21, 22, 47, 49, 56, 57, 73, 86, 131).

[18] Quinten A. Akkerman et al. "Genesis, challenges and opportunities for colloidal lead halide perovskite nanocrystals". en. In: *Nature Materials* 17.5 (May 2018). Publisher: Nature Publishing Group, pp. 394–405. DOI: 10.1038/s41563-018-0018-4 (Cited on page 14, 22, 47, 131).

[19] Congyang Zhang et al. "Narrow-Band Violet-Light-Emitting Diodes Based on Stable Cesium Lead Chloride Perovskite Nanocrystals". In: *ACS Energy Letters* 6.10 (Oct. 2021). Publisher: American Chemical Society, pp. 3545–3554. DOI: 10.1021/acsenergylett.1c01380 (Cited on page 14, 74).

[20] Jun Cui et al. "Facile, low-cost, and large-scale synthesis of $CsPbBr_3$ nanorods at room-temperature with 86 % photoluminescence quantum yield". In: *Materials Research Bulletin* 124 (Apr. 2020), p. 110731. DOI: 10.1016/j.materresbull.2019.110731 (Cited on page 14).

[21] Michael A. Becker et al. "Bright triplet excitons in caesium lead halide perovskites". en. In: *Nature* 553.7687 (Jan. 2018), pp. 189–193. DOI: 10.1038/nature25147 (Cited on page 14, 82, 112).

[22] Philippe Tamarat et al. "The ground exciton state of formamidinium lead bromide perovskite nanocrystals is a singlet dark state". en. In: *Nature Materials* 18.7 (July 2019), pp. 717–724. DOI: 10.1038/s41563-019-0364-x (Cited on page 14, 49, 82, 91, 100, 110, 111, 112, 116, 119, 123, 134, 135, 136).

[23] R. Ben Aich et al. "Bright-Exciton Splittings in Inorganic Cesium Lead Halide Perovskite Nanocrystals". en. In: *Physical Review Applied* 11.3 (Mar. 2019), p. 034042. DOI: 10.1103/PhysRevApplied.11.034042 (Cited on page 14, 37, 82, 93, 163).

[24] Mohamed-Raouf Amara et al. "Spectral Fingerprint of Quantum Confinement in Single $CsPbBr_3$ Nanocrystals". In: *Nano Letters* 23.8 (Apr. 2023). Publisher: American Chemical Society, pp. 3607–3613. DOI: 10.1021/acs.nanolett.3c00793 (Cited on page 14, 95, 96, 101, 103).

[25] H. L. Wells. "Über die Cäsium- und Kalium-Bleihalogenide". en. In: *Zeitschrift für anorganische Chemie* 3.1 (Jan. 1893), pp. 195–210. DOI: 10.1002/zaac.18930030124 (Cited on page 17).

[26] Chr Kn Møller. "Crystal Structure and Photoconductivity of Cæsium Plumbohalides". en. In: *Nature* 182.4647 (Nov. 1958). Publisher: Nature Publishing Group, pp. 1436–1436. DOI: 10.1038/1821436a0 (Cited on page 18, 75).

[27] Dieter Weber. "$CH_3NH_3PbX_3$, a Pb(II)-System with Cubic Perovskite Structure". en. In: *Zeitschrift für Naturforschung B* 33.12 (Dec. 1978). Publisher: De Gruyter, pp. 1443–1445. DOI: 10.1515/znb-1978-1214 (Cited on page 18).

[28] Akihiro Kojima et al. "Organometal Halide Perovskites as Visible-Light Sensitizers for Photovoltaic Cells". In: *Journal of the American Chemical Society* 131.17 (May 2009). Publisher: American Chemical Society, pp. 6050–6051. DOI: 10.1021/ja809598r (Cited on page 18).

[29] Sidra Khatoon et al. "Perovskite solar cell's efficiency, stability and scalability: A review". In: *Materials Science for Energy Technologies* 6 (Jan. 2023), pp. 437–459. DOI: 10.1016/j.mset.2023.04.007 (Cited on page 18).

[30] Richard J. D. Tilley. *Perovskites: Structure-Property Relationships*. en. Section: 1 _eprint: https://onlinelibrary.wiley.com/doi/pdf/10.1002/9781118935651.ch1. John Wiley & Sons, Ltd, 2016. DOI: 10.1002/9781118935651.ch1 (Cited on page 18, 19, 100).

[31] C. Li et al. "Formability of ABX_3 (X = F, Cl, Br, I) halide perovskites". en. In: *Acta Crystallographica Section B: Structural Science* 64.6 (Dec. 2008). Publisher: International Union of Crystallography, pp. 702–707. DOI: 10.1107/S0108768108032734 (Cited on page 18, 19).

[32] Sebastian F. Hoefler, Gregor Trimmel, and Thomas Rath. "Progress on lead-free metal halide perovskites for photovoltaic applications: a review". en. In: *Monatshefte für Chemie - Chemical Monthly* 148.5 (May 2017), pp. 795–826. DOI: 10.1007/s00706-017-1933-9 (Cited on page 18).

[33] V. M. Goldschmidt. "Die Gesetze der Krystallochemie". de. In: *Naturwissenschaften* 14.21 (May 1926), pp. 477–485. DOI: 10.1007/BF01507527 (Cited on page 19).

[34] Hiroki Tanaka, Takeo Oku, and Naoki Ueoka. "Structural stabilities of organic–inorganic perovskite crystals". en. In: *Japanese Journal of Applied Physics* 57.8S3 (Aug. 2018), 08RE12. DOI: 10.7567/JJAP.57.08RE12 (Cited on page 19).

[35] W. Travis et al. "On the application of the tolerance factor to inorganic and hybrid halide perovskites: a revised system". en. In: *Chemical Science* 7.7 (June 2016). Publisher: The Royal Society of Chemistry, pp. 4548–4556. DOI: 10.1039/C5SC04845A (Cited on page 19).

[36] Mengmeng Ma et al. "In situ imaging of the atomic phase transition dynamics in metal halide perovskites". en. In: *Nature Communications* 14.1 (Nov. 2023). Publisher: Nature Publishing Group, p. 7142. DOI: 10.1038/s41467-023-42999-5 (Cited on page 19, 20).

[37] Hisham A. Maddah, Vikas Berry, and Sanjay K. Behura. "Cuboctahedral stability in Titanium halide perovskites *via* machine learning". In: *Computational Materials Science* 173 (Feb. 2020), p. 109415. DOI: 10.1016/j.commatsci.2019.109415 (Cited on page 19).

[38] Aida Alaei et al. "Polymorphism in metal halide perovskites". en. In: *Materials Advances* 2.1 (Jan. 2021). Publisher: RSC, pp. 47–63. DOI: 10.1039/D0MA00643B (Cited on page 20).

[39] Ming Fu et al. "Neutral and Charged Exciton Fine Structure in Single Lead Halide Perovskite Nanocrystals Revealed by Magneto-optical Spectroscopy". In: *Nano Letters* 17.5 (May 2017). Publisher: American Chemical Society, pp. 2895–2901. DOI: 10.1021/acs.nanolett.7b00064 (Cited on page 20, 31, 82, 84, 93).

[40] Julien Ramade et al. "Fine structure of excitons and electron–hole exchange energy in polymorphic $CsPbBr_3$ single nanocrystals". en. In: *Nanoscale* 10.14 (Apr. 2018). Publisher: The Royal Society of Chemistry, pp. 6393–6401. DOI: 10.1039/C7NR09334A (Cited on page 20, 31, 82, 84).

[41] Mengling Liao, Beibei Shan, and Ming Li. "In Situ Raman Spectroscopic Studies of Thermal Stability of All-Inorganic Cesium Lead Halide ($CsPbX_3$, X = Cl, Br, I) Perovskite Nanocrystals". In: *The Journal of Physical Chemistry Letters* 10.6 (Mar. 2019). Publisher: American Chemical Society, pp. 1217–1225. DOI: 10.1021/acs.jpclett.9b00344 (Cited on page 20, 81, 86, 101).

[42] Claudine Katan, Nicolas Mercier, and Jacky Even. "Quantum and Dielectric Confinement Effects in Lower-Dimensional Hybrid Perovskite Semiconductors". In: *Chemical Reviews* 119.5 (Mar. 2019). Publisher: American Chemical Society, pp. 3140–3192. DOI: 10.1021/acs.chemrev.8b00417 (Cited on page 20).

[43] Ruo Xi Yang et al. "Spontaneous Octahedral Tilting in the Cubic Inorganic Cesium Halide Perovskites $CsSnX_3$ and $CsPbX_3$ (X = F, Cl, Br, I)". In: *The Journal of Physical Chemistry Letters* 8.19 (Oct. 2017). Publisher: American Chemical Society, pp. 4720–4726. DOI: 10.1021/acs.jpclett.7b02423 (Cited on page 20).

[44] T. Lanigan-Atkins et al. "Two-dimensional overdamped fluctuations of the soft perovskite lattice in $CsPbBr_3$". en. In: *Nature Materials* 20.7 (July 2021). Publisher: Nature Publishing Group, pp. 977–983. DOI: 10.1038/s41563-021-00947-y (Cited on page 20).

[45] Krishna Seshan. *Handbook of Thin Film Deposition*. Third Edition. William Andrew Publishing, 2012. DOI: 10.1016/B978-1-4377-7873-1.00023-1 (Cited on page 21).

[46] Christof P. Dietrich et al. “GaAs integrated quantum photonics: Towards compact and multi-functional quantum photonic integrated circuits”. In: *Laser & Photonics Reviews* 10.6 (2016). _eprint: https://onlinelibrary.wiley.com/doi/pdf/10.1002/lpor.201500321, pp. 870–894. DOI: 10.1002/lpor.201500321 (Cited on page 21).

[47] Stefan Hepp et al. “Semiconductor Quantum Dots for Integrated Quantum Photonics”. en. In: *Advanced Quantum Technologies* 2.9 (2019), p. 1900020. DOI: 10.1002/qute.201900020 (Cited on page 21).

[48] Sean Keuleyan, Emmanuel Lhuillier, and Philippe Guyot-Sionnest. “Synthesis of Colloidal HgTe Quantum Dots for Narrow Mid-IR Emission and Detection”. In: *Journal of the American Chemical Society* 133.41 (Oct. 2011). Publisher: American Chemical Society, pp. 16422–16424. DOI: 10.1021/ja2079509 (Cited on page 21).

[49] Corentin Dabard et al. “Double-crowned 2D semiconductor nanoplatelets with bicolor power-tunable emission”. en. In: *Nature Communications* 13.1 (Aug. 2022). Publisher: Nature Publishing Group, p. 5094. DOI: 10.1038/s41467-022-32713-2 (Cited on page 21).

[50] Peter Y. Yu and Manuel Cardona. *Fundamentals of Semiconductors: Physics and Materials Properties*. en. Graduate Texts in Physics. Berlin, Heidelberg: Springer, 2010. DOI: 10.1007/978-3-642-00710-1 (Cited on page 23, 24).

[51] R. Neffati, I. Saïdi, and K. Boujdaria. “Full-zone k.p model for the electronic structure of unstrained $GaAs_{1-x}P_x$ and strained $Al_xIn_{1-x}As$ alloys”. In: *Journal of Applied Physics* 112.5 (Sept. 2012), p. 053716. DOI: 10.1063/1.4751353 (Cited on page 24).

[52] Jacky Even et al. “Importance of Spin–Orbit Coupling in Hybrid Organic/Inorganic Perovskites for Photovoltaic Applications”. In: *The Journal of Physical Chemistry Letters* 4.17 (Sept. 2013). Publisher: American Chemical Society, pp. 2999–3005. DOI: 10.1021/jz401532q (Cited on page 25).

[53] Violette Steinmetz et al. “Anisotropic shape of $CsPbBr_3$ colloidal nanocrystals: from 1D to 2D confinement effects”. en. In: *Nanoscale* 12.36 (2020), pp. 18978–18986. DOI: 10.1039/D0NR03901B (Cited on page 25, 26, 82).

[54] R. Ben Aich et al. “Multiband k·p Model for Tetragonal Crystals: Application to Hybrid Halide Perovskite Nanocrystals”. In: *The Journal of Physical Chemistry Letters* 11.3 (Feb. 2020). Publisher: American Chemical Society, pp. 808–817. DOI: 10.1021/acs.jpclett.9b02179 (Cited on page 26, 36, 126, 128).

[55] Peter C. Sercel et al. "Exciton Fine Structure in Perovskite Nanocrystals". In: *Nano Letters* 19.6 (June 2019). Publisher: American Chemical Society, pp. 4068–4077. DOI: 10.1021/acs.nanolett.9b01467 (Cited on page 26, 36, 37, 79, 126, 134).

[56] J. Frenkel. "On the Transformation of light into Heat in Solids. I". In: *Physical Review* 37.1 (Jan. 1931). Publisher: American Physical Society, pp. 17–44. DOI: 10.1103/PhysRev.37.17 (Cited on page 28).

[57] J. Frenkel. "On the Transformation of Light into Heat in Solids. II". In: *Physical Review* 37.10 (Jan. 1932). Publisher: American Physical Society, pp. 1276–1294. DOI: 10.1103/PhysRev.37.1276 (Cited on page 28).

[58] Monique Combescot and Shiue-Yuan Shiau. *Excitons and Cooper Pairs: Two Composite Bosons in Many-Body Physics*. Oxford Graduate Texts. Oxford, New York: Oxford University Press, Dec. 2015 (Cited on page 28).

[59] Gregory H. Wannier. "The Structure of Electronic Excitation Levels in Insulating Crystals". In: *Physical Review* 52.3 (Aug. 1937). Publisher: American Physical Society, pp. 191–197. DOI: 10.1103/PhysRev.52.191 (Cited on page 28).

[60] Kenichiro Tanaka et al. "Electronic and Excitonic Structures of Inorganic–Organic Perovskite-Type Quantum-Well Crystal $(C_4H_9NH_3)_2PbBr_4$". en. In: *Japanese Journal of Applied Physics* 44.8R (Aug. 2005). Publisher: IOP Publishing, p. 5923. DOI: 10.1143/JJAP.44.5923 (Cited on page 31).

[61] Z. G. Yu. "Effective-mass model and magneto-optical properties in hybrid perovskites". en. In: *Scientific Reports* 6.1 (June 2016). Publisher: Nature Publishing Group, p. 28576. DOI: 10.1038/srep28576 (Cited on page 31, 111).

[62] Michel Schott. "A note on image potentials at dielectric interfaces and their possible relevance in organic electronics". In: *Synthetic Metals* 184 (Nov. 2013), pp. 48–51. DOI: 10.1016/j.synthmet.2013.09.025 (Cited on page 33).

[63] Masami Kumagai and Toshihide Takagahara. "Excitonic and nonlinear-optical properties of dielectric quantum-well structures". en. In: *Physical Review B* 40.18 (Dec. 1989), pp. 12359–12381. DOI: 10.1103/PhysRevB.40.12359 (Cited on page 33, 34).

[64] G. E. Pikus and G. L. Bir. "Exchange interaction in excitons in semiconductors". In: *Soviet Physics JETP* (1971) (Cited on page 36, 37).

[65] G. Bir, G. E. Pikus. *Symmetry and strain-induced effects in semiconductors*. Nauka, Moscow, 1972 (Cited on page 36).

[66] M.M.Denisov, V.P.Makarov. "Longitudinal and Transverse Excitons in Semiconductors - Denisov; Wiley, New-York". In: (1973) (Cited on page 36).

[67] U. Rössler and H.-R. Trebin. "Exchange and polaron corrections for excitons in the degenerate band case". In: *Physical Review B* 23.4 (Feb. 1981). Publisher: American Physical Society, pp. 1961–1970. DOI: 10.1103/PhysRevB.23.1961 (Cited on page 36).

[68] Al. L. Efros et al. "Band-edge exciton in quantum dots of semiconductors with a degenerate valence band: Dark and bright exciton states". en. In: *Physical Review B* 54.7 (Aug. 1996), pp. 4843–4856. DOI: 10.1103/PhysRevB.54.4843 (Cited on page 36, 41, 90).

[69] H. Tong and M. W. Wu. "Theory of excitons in cubic III-V semiconductor GaAs, InAs and GaN quantum dots: Fine structure and spin relaxation". en. In: *Physical Review B* 83.23 (June 2011), p. 235323. DOI: 10.1103/PhysRevB.83.235323 (Cited on page 37, 161).

[70] S. V. Goupalov and E. L. Ivchenko. "Electron—hole long-range exchange interaction in semiconductor quantum dots". In: *Journal of Crystal Growth* 184-185 (Feb. 1998), pp. 393–397. DOI: 10.1016/S0022-0248(98)80083-3 (Cited on page 38, 161).

[71] Victor Guilloux et al. "Exciton Fine Structure of $CsPbCl_3$ Nanocrystals: An Interplay of Electron–Hole Exchange Interaction, Crystal Structure, Shape Anisotropy, and Dielectric Mismatch". In: *ACS Nano* 17.13 (July 2023). Publisher: American Chemical Society, pp. 12266–12277. DOI: 10.1021/acsnano.3c00772 (Cited on page 38, 49, 91, 120).

[72] Guy Fishman. *Semi-conducteurs : les bases de la théorie k.p.* 2010th ed. Les Éditions de l'École polytechnique (Cited on page 41, 42).

[73] A.J. Shields et al. "Quenching of excitonic optical transitions by excess electrons in GaAs quantum wells". In: *Physical Review B* 51.24 (June 1995). Publisher: American Physical Society, pp. 18049–18052. DOI: 10.1103/PhysRevB.51.18049 (Cited on page 42).

[74] K. Kheng et al. "Observation of negatively charged excitons X- in semiconductor quantum wells". In: *Physical Review Letters* 71.11 (Sept. 1993). Publisher: American Physical Society, pp. 1752–1755. DOI: 10.1103/PhysRevLett.71.1752 (Cited on page 42).

[75] Yoshihiko Kanemitsu. "Trion dynamics in lead halide perovskite nanocrystals". en. In: *The Journal of Chemical Physics* 151.17 (Nov. 2019), p. 170902. DOI: 10.1063/1.5125628 (Cited on page 42, 43).

[76] Alexander Högele et al. "Voltage-Controlled Optics of a Quantum Dot". en. In: *Physical Review Letters* 93.21 (Nov. 2004), p. 217401. DOI: 10.1103/PhysRevLett.93.217401 (Cited on page 42, 44, 95).

[77] M. Müller et al. "On-demand generation of indistinguishable polarization-entangled photon pairs". en. In: *Nature Photonics* 8.3 (Mar. 2014). Publisher: Nature Publishing Group, pp. 224–228. DOI: 10.1038/nphoton.2013.377 (Cited on page 43).

[78] Chen Chen et al. "Wavelength-tunable high-fidelity entangled photon sources enabled by dual Stark effects". en. In: *Nature Communications* 15.1 (July 2024). Publisher: Nature Publishing Group, p. 5792. DOI: 10.1038/s41467-024-50062-0 (Cited on page 43, 159).

[79] R. Seguin et al. "Size-Dependent Fine-Structure Splitting in Self-Organized InAs / GaAs Quantum Dots". en. In: *Physical Review Letters* 95.25 (Dec. 2005), p. 257402. DOI: 10.1103/PhysRevLett.95.257402 (Cited on page 44, 95).

[80] Mackillo Kira and Stephan W. Koch. *Semiconductor Quantum Optics*. Cambridge: Cambridge University Press, 2011. DOI: 10.1017/CBO9781139016926 (Cited on page 46).

[81] Jasprit Singh. *Electronic and Optoelectronic Properties of Semiconductor Structures*. Cambridge: Cambridge University Press, 2003. DOI: 10.1017/CBO9780511805745 (Cited on page 46, 103).

[82] S. Rudin, T. L. Reinecke, and B. Segall. "Temperature-dependent exciton linewidths in semiconductors". en. In: *Physical Review B* 42.17 (Dec. 1990), pp. 11218–11231. DOI: 10.1103/PhysRevB.42.11218 (Cited on page 46, 108).

[83] Zhibin Fang et al. "Dual Passivation of Perovskite Defects for Light-Emitting Diodes with External Quantum Efficiency Exceeding 20%". en. In: *Advanced Functional Materials* 30.12 (2020). _eprint: https://onlinelibrary.wiley.com/doi/pdf/10.1002/adfm.201909754, p. 1909754. DOI: 10.1002/adfm.201909754 (Cited on page 47).

[84] Takayuki Chiba et al. "Anion-exchange red perovskite quantum dots with ammonium iodine salts for highly efficient light-emitting devices". In: *Nature Photonics* (2018). DOI: 10.1038/s41566-018-0260-y (Cited on page 47).

[85] Yu Cao et al. "Perovskite light-emitting diodes based on spontaneously formed submicrometre scale structures". In: *Nature* (2018). DOI: 10.1038/s41586-018-0576-2 (Cited on page 47).

[86] Joo Sung Kim et al. "Ultra-bright, efficient and stable perovskite light-emitting diodes". en. In: *Nature* 611.7937 (Nov. 2022). Publisher: Nature Publishing Group, pp. 688–694. DOI: 10.1038/s41586-022-05304-w (Cited on page 47, 48).

[87] Young-Hoon Kim et al. "Comprehensive defect suppression in perovskite nanocrystals for high-efficiency light-emitting diodes". en. In: *Nature Photonics* 15.2 (Feb. 2021). Publisher: Nature Publishing Group, pp. 148–155. DOI: 10.1038/s41566-020-00732-4 (Cited on page 47).

[88] Haifeng Zhao et al. “High-Brightness Perovskite Light-Emitting Diodes Based on $FAPbBr_3$ Nanocrystals with Rationally Designed Aromatic Ligands”. In: *ACS Energy Letters* 6.7 (July 2021). Publisher: American Chemical Society. DOI: 10.1021/acsenergylett.1c00812 (Cited on page 47).

[89] Xiaoyu Yang et al. “Focus on perovskite emitters in blue light-emitting diodes | Light: Science & Applications”. In: (2023). DOI: 10.1038/s41377-023-01206-2 (Cited on page 47, 73).

[90] Max Karlsson et al. “Mixed halide perovskites for spectrally stable and high-efficiency blue light-emitting diodes”. en. In: *Nature Communications* 12.1 (Jan. 2021). Publisher: Nature Publishing Group, p. 361. DOI: 10.1038/s41467-020-20582-6 (Cited on page 47).

[91] Hongwei Wang et al. “Efficient Quasi-2D Perovskite Based Blue Light-Emitting Diodes with Carbon Dots Modified Hole Transport Layer”. In: *Nano Letters* 24.28 (July 2024). Publisher: American Chemical Society, pp. 8702–8708. DOI: 10.1021/acs.nanolett.4c02110 (Cited on page 47).

[92] Bernhard J. Bohn et al. “Boosting Tunable Blue Luminescence of Halide Perovskite NPLs through Postsynthetic Surface Trap Repair”. en. In: *Nano Letters* 18.8 (Aug. 2018). DOI: 10.1021/acs.nanolett.8b02190 (Cited on page 48).

[93] Guoqing Cheng et al. “Efficient All-Inorganic Perovskite Light-Emitting Diodes with Improved Operation Stability”. In: *ACS Applied Materials & Interfaces* 12.15 (Apr. 2020). Publisher: American Chemical Society, pp. 18084–18090. DOI: 10.1021/acsami.9b23170 (Cited on page 48).

[94] Maksym V. Kovalenko, Loredana Protesescu, and Maryna I. Bodnarchuk. “Properties and potential optoelectronic applications of lead halide perovskite nanocrystals”. In: *Science* (2017). DOI: 10.1126/science.aam7093 (Cited on page 48).

[95] Shaoni Kar et al. “Recent advancements and perspectives on light management and high performance in perovskite light-emitting diodes”. In: *Nanophotonics* (2021). DOI: 10.1515/nanoph-2021-0033 (Cited on page 48).

[96] Shangjun Cheng and Haizheng Zhong. “What Happens When Halide Perovskites Meet with Water?” In: *The Journal of Physical Chemistry Letters* 13.10 (Mar. 2022). Publisher: American Chemical Society, pp. 2281–2290. DOI: 10.1021/acs.jpclett.2c00166 (Cited on page 48, 132).

[97] Jeffrey A. Christians, Pierre A. Miranda Herrera, and Prashant V. Kamat. "Transformation of the Excited State and Photovoltaic Efficiency of $CH_3NH_3PbI_3$ Perovskite upon Controlled Exposure to Humidified Air". In: *Journal of the American Chemical Society* 137.4 (Feb. 2015). Publisher: American Chemical Society, pp. 1530–1538. DOI: 10.1021/ja511132a (Cited on page 48).

[98] Jae Sung Yun et al. "Humidity-Induced Degradation via Grain Boundaries of $FAPbI_3$ Planar Perovskite Solar Cells". en. In: *Advanced Functional Materials* 28.11 (2018). _eprint: https://onlinelibrary.wiley.com/doi/pdf/10.1002/adfm.201705363, p. 1705363. DOI: 10.1002/adfm.201705363 (Cited on page 48).

[99] Tao Zhu, Yongrui Yang, and Xiong Gong. "Recent Advancements and Challenges for Low-Toxicity Perovskite Materials". In: *ACS Applied Materials & Interfaces* 12.24 (June 2020). Publisher: American Chemical Society, pp. 26776–26811. DOI: 10.1021/acsami.0c02575 (Cited on page 48).

[100] Tom C. Jellicoe et al. "Synthesis and Optical Properties of Lead-Free Cesium Tin Halide Perovskite Nanocrystals". In: *Journal of the American Chemical Society* 138.9 (Mar. 2016). Publisher: American Chemical Society, pp. 2941–2944. DOI: 10.1021/jacs.5b13470 (Cited on page 48).

[101] Maria Luisa De Giorgi et al. "Amplified Spontaneous Emission Threshold Reduction and Operational Stability Improvement in $CsPbBr_3$ Nanocrystals Films by Hydrophobic Functionalization of the Substrate". en. In: *Scientific Reports* 9.1 (Nov. 2019). Publisher: Nature Publishing Group, p. 17964. DOI: 10.1038/s41598-019-54412-7 (Cited on page 48, 139, 140).

[102] Li Na Quan et al. "Perovskites for Next-Generation Optical Sources". In: *Chemical Reviews* 119.12 (June 2019). Publisher: American Chemical Society, pp. 7444–7477. DOI: 10.1021/acs.chemrev.9b00107 (Cited on page 49).

[103] Andrew P.Schlaus, Michael S. Spencer, and X-Y. Zhu. "Light–Matter Interaction and Lasing in Lead Halide Perovskites". In: *Accounts of Chemical Research* (2019). DOI: 10.1021/acs.accounts.9b00382 (Cited on page 49).

[104] Guichuan Xing et al. "Low-temperature solution-processed wavelength-tunable perovskites for lasing". en. In: *Nature Materials* 13.5 (May 2014). Publisher: Nature Publishing Group, pp. 476–480. DOI: 10.1038/nmat3911 (Cited on page 49).

[105] Fengrui Hu et al. "Slow Auger Recombination of Charged Excitons in Nonblinking Perovskite Nanocrystals without Spectral Diffusion". In: *Nano Letters* 16.10 (Oct. 2016). Pub-

lisher: American Chemical Society, pp. 6425–6430. DOI: 10.1021/acs.nanolett.6b02874 (Cited on page 49, 109).

[106] Haiming Zhu et al. "Lead halide perovskite nanowire lasers with low lasing thresholds and high quality factors". en. In: *Nature Materials* 14.6 (June 2015). Publisher: Nature Publishing Group, pp. 636–642. DOI: 10.1038/nmat4271 (Cited on page 49, 50).

[107] Samuel W. Eaton et al. "Lasing in robust cesium lead halide perovskite nanowires". In: *Proceedings of the National Academy of Sciences* 113.8 (Feb. 2016). Publisher: Proceedings of the National Academy of Sciences, pp. 1993–1998. DOI: 10.1073/pnas.1600789113 (Cited on page 49).

[108] Siqi Li et al. "Water-resistant perovskite nanodots enable robust two-photon lasing in aqueous environment". en. In: *Nature Communications* 11.1 (Mar. 2020). Publisher: Nature Publishing Group, p. 1192. DOI: 10.1038/s41467-020-15016-2 (Cited on page 49).

[109] Can Huang et al. "Ultrafast control of vortex microlasers". In: *Science* 367.6481 (Feb. 2020). Publisher: American Association for the Advancement of Science, pp. 1018–1021. DOI: 10.1126/science.aba4597 (Cited on page 49).

[110] P. Brenner et al. "Comment on "Room-Temperature Continuous-Wave Operation of Organo metal Halide Perovskite Lasers"". In: *ACS Nano* 13.11 (Nov. 2019). Publisher: American Chemical Society, pp. 12257–12258. DOI: 10.1021/acsnano.9b00133 (Cited on page 49).

[111] Chuanjiang Qin et al. "Stable room-temperature continuous-wave lasing in quasi-2D perovskite films". en. In: *Nature* 585.7823 (Sept. 2020). Publisher: Nature Publishing Group, pp. 53–57. DOI: 10.1038/s41586-020-2621-1 (Cited on page 49).

[112] Tobias Haeger, Ralf Heiderhoff, and Thomas Riedl. "Thermal properties of metal-halide perovskites". en. In: *Journal of Materials Chemistry C* 8.41 (2020). Publisher: Royal Society of Chemistry, pp. 14289–14311. DOI: 10.1039/D0TC03754K (Cited on page 49).

[113] Chao Shen et al. "Thermal conductivity of suspended single crystal $CH_3NH_3PbI_3$ platelets at room temperature". en. In: *Nanoscale* 9.24 (June 2017). Publisher: The Royal Society of Chemistry, pp. 8281–8287. DOI: 10.1039/C7NR01894K (Cited on page 49).

[114] Yufei Jia et al. "Factors that Limit Continuous-Wave Lasing in Hybrid Perovskite Semiconductors". en. In: *Advanced Optical Materials* 8.2 (2020), p. 1901514. DOI: 10.1002/adom.201901514 (Cited on page 49).

[115] Wei Gao and Siu Fung Yu. "Reality or fantasy—Perovskite semiconductor laser diodes". en. In: *EcoMat* 3.1 (2021), e12077. DOI: 10.1002/eom2.12077 (Cited on page 49).

[116] Qing Zhang et al. “Halide Perovskite Semiconductor Lasers: Materials, Cavity Design, and Low Threshold”. In: *Nano Letters* 21.5 (Mar. 2021). Publisher: American Chemical Society, pp. 1903–1914. DOI: 10.1021/acs.nanolett.0c03593 (Cited on page 49).

[117] Meiying Leng et al. “Optically Pumped Polaritons in Perovskite Light-Emitting Diodes | ACS Photonics”. In: (2023). DOI: 10.1021/acsphotonics.2c01999 (Cited on page 49).

[118] Rui Su et al. “Room Temperature Polariton Lasing in All Inorganic Perovskite Nanoplatelets”. In: *Nano Letters* 17.6 (June 2017). Publisher: American Chemical Society, pp. 3982–3988. DOI: 10.1021/acs.nanolett.7b01956 (Cited on page 49).

[119] Brahim Lounis and Michel Orrit. “Single-photon sources”. en. In: *Reports on Progress in Physics* 68.5 (Apr. 2005), p. 1129. DOI: 10.1088/0034-4885/68/5/R04 (Cited on page 49).

[120] Julien Ramade et al. “Exciton-phonon coupling in a $CsPbBr_3$ single nanocrystal”. en. In: *Applied Physics Letters* 112.7 (Feb. 2018), p. 072104. DOI: 10.1063/1.5018413 (Cited on page 50, 78, 100, 106, 108, 110).

[121] S. A. Empedocles and M. G. Bawendi. “Quantum-Confined Stark Effect in Single CdSe Nanocrystallite Quantum Dots”. en. In: *Science* 278.5346 (Dec. 1997), pp. 2114–2117. DOI: 10.1126/science.278.5346.2114 (Cited on page 50, 108).

[122] R. Stockill et al. “Quantum dot spin coherence governed by a strained nuclear environment”. en. In: *Nature Communications* 7.1 (Sept. 2016). Publisher: Nature Publishing Group, p. 12745. DOI: 10.1038/ncomms12745 (Cited on page 50).

[123] Marianna D’Amato et al. “Color-Tunable Mixed-Cation Perovskite Single Photon Emitters”. In: *ACS Photonics* (2023). DOI: 10.1021/acsphotonics.2c01437 (Cited on page 51, 52).

[124] Federica Ricci et al. “Investigations of Coherence in Perovskite Quantum Dots with Classical and Quantum Light”. In: *The Journal of Physical Chemistry* (2023). DOI: 10.1021/acs.jpcc.2c08455 (Cited on page 51).

[125] Fengrui Hu et al. “Superior Optical Properties of Perovskite Nanocrystals as Single Photon Emitters”. In: *ACS Nano* 9.12 (Dec. 2015). Publisher: American Chemical Society, pp. 12410–12416. DOI: 10.1021/acsnano.5b05769 (Cited on page 52).

[126] Chenglian Zhu et al. “Room-Temperature, Highly Pure Single-Photon Sources from All-Inorganic Lead Halide Perovskite Quantum Dots”. In: *Nano Letters* (2022). DOI: 10.1021/acs.nanolett.2c00756 (Cited on page 52).

[127] Marianna D'Amato et al. "Highly Photostable Zn-Treated Halide Perovskite Nanocrystals for Efficient Single Photon Generation". In: *Nano Letters* (2023). DOI: 10.1021/acs.nanolett.3c02739 (Cited on page 52).

[128] Chenglian Zhu et al. "Single-photon superradiance in individual caesium lead halide quantum dots". en. In: *Nature* 626.7999 (Feb. 2024). Publisher: Nature Publishing Group, pp. 535–541. DOI: 10.1038/s41586-023-07001-8 (Cited on page 52).

[129] Stefania Castelletto, Filippo De Angelis, and Alberto Boretti. "Prospects and challenges of quantum emitters in perovskites nanocrystals". In: *ScienceDirect* (2022). DOI: 10.1016/j.apmt.2022.101401 (Cited on page 52).

[130] Adrien Dousse et al. "Ultrabright source of entangled photon pairs". en. In: *Nature* 466.7303 (July 2010). Publisher: Nature Publishing Group, pp. 217–220. DOI: 10.1038/nature09148 (Cited on page 52).

[131] M. Arcari et al. "Near-Unity Coupling Efficiency of a Quantum Emitter to a Photonic Crystal Waveguide". In: *Physical Review Letters* 113.9 (Aug. 2014). Publisher: American Physical Society, p. 093603. DOI: 10.1103/PhysRevLett.113.093603 (Cited on page 52).

[132] Seongmoon Jun et al. "Ultrafast and Bright Quantum Emitters from the Cavity-Coupled Single Perovskite Nanocrystals". In: *ACS Nano* (2024). DOI: 10.1021/acsnano.3c06760 (Cited on page 52).

[133] Victor K. LaMer and Robert H. Dinegar. "Theory, Production and Mechanism of Formation of Monodispersed Hydrosols". In: *Journal of the American Chemical Society* 72.11 (Nov. 1950). Publisher: American Chemical Society, pp. 4847–4854. DOI: 10.1021/ja01167a001 (Cited on page 56).

[134] Nadesh Fiuza-Maneiro et al. "Ligand Chemistry of Inorganic Lead Halide Perovskite NCs". In: *ACS Energy Letters* 8.2 (Feb. 2023). Publisher: American Chemical Society, pp. 1152–1191. DOI: 10.1021/acsenergylett.2c02363 (Cited on page 57).

[135] Clara Otero-Martínez et al. "Dimensionality Control of Inorganic and Hybrid Perovskite Nanocrystals by Reaction Temperature: From No-Confinement to 3D and 1D Quantum Confinement". en. In: *Angewandte Chemie International Edition* 60.51 (Dec. 2021). DOI: 10.1002/anie.202109308 (Cited on page 57, 58).

[136] Jizhong Song et al. "Quantum Dot Light-Emitting Diodes Based on Inorganic Perovskite Cesium Lead Halides ($CsPbX_3$)". In: *Advanced Materials* 27.44 (2015), pp. 7162–7167. DOI: 10.1002/adma.201502567 (Cited on page 57).

[137] Quinten A. Akkerman et al. "Solution Synthesis Approach to Colloidal Cesium Lead Halide Perovskite Nanoplatelets with Monolayer-Level Thickness Control". In: *Journal of the American Chemical Society* 138.3 (Jan. 2016). Publisher: American Chemical Society, pp. 1010–1016. DOI: 10.1021/jacs.5b12124 (Cited on page 58).

[138] Yehonadav Bekenstein et al. "Highly Luminescent Colloidal Nanoplates of Perovskite Cesium Lead Halide and Their Oriented Assemblies". In: *Journal of the American Chemical Society* 137.51 (Dec. 2015). Publisher: American Chemical Society, pp. 16008–16011. DOI: 10.1021/jacs.5b11199 (Cited on page 58).

[139] Guilherme Almeida et al. "Role of Acid–Base Equilibria in the Size, Shape, and Phase Control of Cesium Lead Bromide Nanocrystals". In: *ACS Nano* 12.2 (Feb. 2018). Publisher: American Chemical Society, pp. 1704–1711. DOI: 10.1021/acsnano.7b08357 (Cited on page 58).

[140] Aizhao Pan et al. "Insight into the Ligand-Mediated Synthesis of Colloidal $CsPbBr_3$ Perovskite Nanocrystals: The Role of Organic Acid, Base, and Cesium Precursors". In: *ACS Nano* 10.8 (Aug. 2016). Publisher: American Chemical Society, pp. 7943–7954. DOI: 10.1021/acsnano.6b03863 (Cited on page 58).

[141] Javad Shamsi et al. "Colloidal Synthesis of Quantum Confined Single Crystal $CsPbBr_3$ Nanosheets with Lateral Size Control up to the Micrometer Range". In: *Journal of the American Chemical Society* 138.23 (June 2016). Publisher: American Chemical Society, pp. 7240–7243. DOI: 10.1021/jacs.6b03166 (Cited on page 58).

[142] Jizhong Song et al. "Monolayer and Few-Layer All-Inorganic Perovskites as a New Family of Two-Dimensional Semiconductors for Printable Optoelectronic Devices". In: *Advanced Materials* 28.24 (2016), pp. 4861–4869. DOI: 10.1002/adma.201600225 (Cited on page 58).

[143] Mark C. Weidman, Aaron J. Goodman, and William A. Tisdale. "Colloidal Halide Perovskite Nanoplatelets: An Exciting New Class of Semiconductor Nanomaterials". In: *Chemistry of Materials* 29.12 (June 2017). Publisher: American Chemical Society, pp. 5019–5030. DOI: 10.1021/acs.chemmater.7b01384 (Cited on page 59).

[144] Vikash Kumar Ravi et al. "Origin of the Substitution Mechanism for the Binding of Organic Ligands on the Surface of $CsPbBr_3$ Perovskite Nanocubes". In: *The Journal of Physical Chemistry Letters* 8.20 (Oct. 2017). Publisher: American Chemical Society, pp. 4988–4994. DOI: 10.1021/acs.jpclett.7b02192 (Cited on page 59).

[145] Dandan Zhang et al. “Solution Phase Synthesis of Cesium Lead Halide Perovskite NWs”. In: *Journal of the American Chemical Society* 137.29 (July 2015). Publisher: American Chemical Society, pp. 9230–9233. DOI: 10.1021/jacs.5b05404 (Cited on page 59).

[146] Clive R. Bealing et al. “Predicting Nanocrystal Shape through Consideration of Surface-Ligand Interactions”. In: *ACS Nano* 6.3 (Mar. 2012). Publisher: American Chemical Society, pp. 2118–2127. DOI: 10.1021/nn3000466 (Cited on page 59).

[147] Hamamatsu Photonics. *Guide To Streak Cameras* (Cited on page 69).

[148] W. Becker. “The bh TCSPC handbook. 10th edition (2023). Available on www.becker-hickl.com”. In: () (Cited on page 70).

[149] Michal Baranowski et al. “Exciton binding energy and effective mass of $CsPbCl_3$: a magneto-optical study”. EN. In: *Photonics Research* 8.10 (Oct. 2020). Publisher: Optica Publishing Group, A50–A55. DOI: 10.1364/PRJ.401872 (Cited on page 73, 80, 128).

[150] T. Hayashi et al. “Exciton dynamics related with phase transitions in $CsPbCl_3$ single crystals”. In: *Journal of Luminescence*. International Conference on Dynamical Processes in Excited States of Solids 94-95 (Dec. 2001), pp. 255–259. DOI: 10.1016/S0022-2313(01)00289-7 (Cited on page 73).

[151] D. Fröhlich et al. “Cesium-trihalogen-plumbates a new class of ionic semiconductors”. In: *Journal of Luminescence* 18-19 (Jan. 1979), pp. 385–388. DOI: 10.1016/0022-2313(79)90146-7 (Cited on page 73).

[152] K. Heidrich, H. Künzel, and J. Treusch. “Optical properties and electronic structure of $CsPbCl_3$ and $CsPbBr_3$”. In: *Solid State Communications* 25.11 (Mar. 1978), pp. 887–889. DOI: 10.1016/0038-1098(78)90294-6 (Cited on page 73).

[153] Chun Che Lin et al. “Luminescent manganese-doped $CsPbCl_3$ perovskite quantum dots”. en. In: *Scientific Reports* 7.1 (Apr. 2017). Publisher: Nature Publishing Group, p. 45906. DOI: 10.1038/srep45906 (Cited on page 73).

[154] Kunyuan Xu, Jara F. Vliem, and Andries Meijerink. “Long-Lived Dark Exciton Emission in Mn-Doped $CsPbCl_3$ Perovskite Nanocrystals”. In: *The Journal of Physical Chemistry C* 123.1 (Jan. 2019). Publisher: American Chemical Society, pp. 979–984. DOI: 10.1021/acs.jpcc.8b12035 (Cited on page 73).

[155] Francesco Meinardi et al. “Doped Halide Perovskite Nanocrystals for Reabsorption-Free Luminescent Solar Concentrators”. In: *ACS Energy Letters* 2.10 (Oct. 2017). Publisher: American Chemical Society, pp. 2368–2377. DOI: 10.1021/acsenergylett.7b00701 (Cited on page 73).

[156] Rui Sun et al. "Samarium-Doped Metal Halide Perovskite Nanocrystals for Single Component Electroluminescent White Light Emitting Diodes". In: *ACS Energy Letters* 5.7 (July 2020). Publisher: American Chemical Society, pp. 2131–2139. DOI: 10.1021/acsenergylett.0c00931 (Cited on page 73).

[157] Xiangtong Zhang et al. "Yb^{3+} and Yb^{3+}/Er^{3+} doping for near-infrared emission and improved stability of $CsPbCl_3$ nanocrystals". en. In: *Journal of Materials Chemistry C* 6.37 (Sept. 2018). Publisher: The Royal Society of Chemistry, pp. 10101–10105. DOI: 10.1039/C8TC03957G (Cited on page 73).

[158] Runchen Lai and Kaifeng Wu. "Picosecond electron trapping limits the emissivity of $CsPbCl_3$ perovskite nanocrystals". In: *The Journal of Chemical Physics* 151.19 (Nov. 2019), p. 194701. DOI: 10.1063/1.5127887 (Cited on page 73).

[159] James M. Ball and Annamaria Petrozza. "Defects in perovskite-halides and their effects in solar cells". en. In: *Nature Energy* 1.11 (Oct. 2016). Publisher: Nature Publishing Group, pp. 1–13. DOI: 10.1038/nenergy.2016.149 (Cited on page 73).

[160] Ruben Ahumada-Lazo et al. "Emission Properties and Ultrafast Carrier Dynamics of $CsPbCl_3$ Perovskite Nanocrystals". In: *The Journal of Physical Chemistry C* 123.4 (Jan. 2019). Publisher: American Chemical Society, pp. 2651–2657. DOI: 10.1021/acs.jpcc.8b11906 (Cited on page 73).

[161] Somnath Das, Modasser Hossain, and Anunay Samanta. "Stable and Intense Violet Emitting $CsPbCl_3$ Nanocrystals for Light Emitting Diodes: Directly Obtained by L Type Surface Passivation". In: *ACS Applied Nano Materials* 6.6 (Mar. 2023). Publisher: American Chemical Society, pp. 4812–4820. DOI: 10.1021/acsanm.3c00371 (Cited on page 74).

[162] Navendu Mondal, Apurba De, and Anunay Samanta. "Achieving Near-Unity Photoluminescence Efficiency for Blue-Violet-Emitting Perovskite Nanocrystals". In: *ACS Energy Letters* 4.1 (Jan. 2019). Publisher: American Chemical Society, pp. 32–39. DOI: 10.1021/acsenergylett.8b01909 (Cited on page 74, 158).

[163] Yunqin Zhang et al. "Engineering the Bandgap and Surface Structure of $CsPbCl_3$ Nanocrystals to Achieve Efficient Ultraviolet Luminescence". en. In: *Angewandte Chemie International Edition* 60.17 (2021), pp. 9693–9698. DOI: 10.1002/anie.202017370 (Cited on page 74).

[164] Ghada H. Ahmed et al. "Giant Photoluminescence Enhancement in $CsPbCl_3$ Perovskite Nanocrystals by Simultaneous Dual-Surface Passivation". In: *ACS Energy Letters* 3.10 (2018). Publisher: American Chemical Society. DOI: 10.1021/acsenergylett.8b01441 (Cited on page 74).

[165] Jingru Zhang et al. "High-performance transparent ultraviolet photodetectors based on inorganic perovskite $CsPbCl_3$ nanocrystals". en. In: *RSC Advances* 7.58 (2017). Publisher: Royal Society of Chemistry, pp. 36722–36727. DOI: 10.1039/C7RA06597C (Cited on page 74).

[166] Andrea Erroi et al. "Ultrafast Nanocomposite Scintillators Based on Cd-Enhanced $CsPbCl_3$ Nanocrystals in Polymer Matrix". In: *ACS Energy Letters* 9.5 (May 2024). Publisher: American Chemical Society, pp. 2333–2342. DOI: 10.1021/acsenergylett.4c00778 (Cited on page 74).

[167] Stefano Pierini et al. "Highly Photostable Perovskite Nanocubes: Toward Integrated Single Photon Sources Based on Tapered Nanofibers". en. In: *ACS Photonics* 7.8 (Aug. 2020), pp. 2265–2272. DOI: 10.1021/acsphotonics.0c00820 (Cited on page 74).

[168] G. Murtaza and Iftikhar Ahmad. "First principle study of the structural and optoelectronic properties of cubic perovskites $CsPbM_3$ (M=Cl, Br, I)". In: *Physica B: Condensed Matter* 406.17 (Sept. 2011), pp. 3222–3229. DOI: 10.1016/j.physb.2011.05.028 (Cited on page 75).

[169] L. Q. Jiang et al. "Prediction of lattice constant in cubic perovskites". In: *Journal of Physics and Chemistry of Solids* 67.7 (July 2006), pp. 1531–1536. DOI: 10.1016/j.jpcs.2006.02.004 (Cited on page 75).

[170] Dana M. Calistru et al. "Identification of the symmetry of phonon modes in $CsPbCl_3$ in phase IV by Raman and resonance-Raman scattering". en. In: *Journal of Applied Physics* 82.11 (Dec. 1997), pp. 5391–5395. DOI: 10.1063/1.366307 (Cited on page 75, 81, 100, 101, 103, 122).

[171] Shunsuke Hirotsu. "Experimental Studies of Structural Phase Transitions in $CsPbCl_3$". In: *Journal of the Physical Society of Japan* 31.2 (Aug. 1971). Publisher: The Physical Society of Japan, pp. 552–560. DOI: 10.1143/JPSJ.31.552 (Cited on page 75, 101).

[172] Zhiya Dang et al. "In Situ Transmission Electron Microscopy Study of Electron Beam-Induced Transformations in Colloidal Cesium Lead Halide Perovskite Nanocrystals". In: *ACS Nano* 11.2 (Feb. 2017). Publisher: American Chemical Society, pp. 2124–2132. DOI: 10.1021/acsnano.6b08324 (Cited on page 76).

[173] Ling-yi Huang and Walter R. L. Lambrecht. "Electronic band structure, phonons, and exciton binding energies of halide perovskites $CsSnCl_3$, $CsSnBr_3$, and $CsSnI_3$". In: *Physical Review B* 88.16 (Oct. 2013). Publisher: American Physical Society, p. 165203. DOI: 10.1103/PhysRevB.88.165203 (Cited on page 77).

[174] Y. P. Varshni. "Temperature dependence of the energy gap in semiconductors". In: *Physica* 34.1 (Jan. 1967), pp. 149–154. DOI: 10.1016/0031-8914(67)90062-6 (Cited on page 77).

[175] Amal Ghribi et al. "Dielectric Confinement and Exciton Fine Structure in Lead Halide Perovskite Nanoplatelets". en. In: *Nanomaterials* 11.11 (Nov. 2021). Number: 11 Publisher: Multidisciplinary Digital Publishing Institute, p. 3054. DOI: 10.3390/nano11113054 (Cited on page 79, 128).

[176] Nivedita Pandey, Abhishek Kumar, and Subhananda Chakrabarti. "Investigation of the structural, electronic, and optical properties of Mn-doped $CsPbCl_3$: theory and experiment". en. In: *RSC Advances* 9.51 (Sept. 2019). Publisher: The Royal Society of Chemistry, pp. 29556–29565. DOI: 10.1039/C9RA05685H (Cited on page 79).

[177] Michael C. Brennan et al. "Universal Size-Dependent Stokes Shifts in Lead Halide Perovskite Nanocrystals". In: *The Journal of Physical Chemistry Letters* 11.13 (July 2020). Publisher: American Chemical Society, pp. 4937–4944. DOI: 10.1021/acs.jpclett.0c01407 (Cited on page 81, 134, 148).

[178] Michael C. Brennan et al. "Origin of the Size-Dependent Stokes Shift in $CsPbBr_3$ Perovskite Nanocrystals". In: *Journal of the American Chemical Society* 139.35 (Sept. 2017). Publisher: American Chemical Society, pp. 12201–12208. DOI: 10.1021/jacs.7b05683 (Cited on page 81).

[179] Victor Guilloux et al. "Phonon modes and exciton-phonon interactions in $CsPbCl_3$ single nanocrystals". In: *Physica E: Low-dimensional Systems and Nanostructures* 151 (July 2023), p. 115713. DOI: 10.1016/j.physe.2023.115713 (Cited on page 81, 110, 122).

[180] Peter C. Sercel et al. "Quasicubic model for metal halide perovskite nanocrystals". In: *The Journal of Chemical Physics* 151.23 (Dec. 2019), p. 234106. DOI: 10.1063/1.5127528 (Cited on page 82, 91).

[181] Philippe Tamarat et al. "The dark exciton ground state promotes photon-pair emission in individual perovskite nanocrystals". en. In: *Nature Communications* 11.1 (Nov. 2020). Publisher: Nature Publishing Group, p. 6001. DOI: 10.1038/s41467-020-19740-7 (Cited on page 82, 95, 96, 110, 119, 158).

[182] Chunyang Yin et al. "Bright Exciton Fine Structure Splittings in Single Perovskite NCs". en. In: *Physical Review Letters* 119.2 (July 2017). DOI: 10.1103/PhysRevLett.119.026401 (Cited on page 84, 95, 96).

[183] Clotilde Lethiec et al. “Measurement of Three-Dimensional Dipole Orientation of a Single Fluorescent Nanoemitter by Emission Polarization Analysis”. In: *Physical Review X* 4.2 (May 2014). Publisher: American Physical Society, p. 021037. DOI: 10.1103/PhysRevX.4.021037 (Cited on page 88, 165).

[184] Miriam Böhmler et al. “Enhancing and redirecting carbon nanotube photoluminescence by an optical antenna”. en. In: *Optics Express* 18.16 (Aug. 2010), p. 16443. DOI: 10.1364/OE.18.016443 (Cited on page 88).

[185] Joshua J. P. Thompson et al. “Phonon-Bottleneck Enhanced Exciton Emission in 2D Perovskites”. en. In: *Advanced Energy Materials* 14.20 (2024), p. 2304343. DOI: 10.1002/aenm.202304343 (Cited on page 88, 124).

[186] A. Ghribi et al. “Dielectric effects, crystal field, and shape anisotropy tuning of the exciton fine structure of halide perovskite nanocrystals”. In: *Physical Review Materials* 6.10 (Oct. 2022). Publisher: American Physical Society, p. 106001. DOI: 10.1103/PhysRevMaterials.6.106001 (Cited on page 91, 125).

[187] Moritz Gramlich et al. “Dark and Bright Excitons in Halide Perovskite Nanoplatelets”. en. In: *Advanced Science* 9.5 (2022), p. 2103013. DOI: 10.1002/advs.202103013 (Cited on page 92).

[188] Yaoyao Han et al. “Lattice distortion inducing exciton splitting and coherent quantum beating in $CsPbI_3$ perovskite quantum dots”. en. In: *Nature Materials* 21.11 (Nov. 2022). Publisher: Nature Publishing Group, pp. 1282–1289. DOI: 10.1038/s41563-022-01349-4 (Cited on page 93, 95).

[189] Kenichi Cho et al. “Exciton–Phonon and Trion–Phonon Couplings Revealed by Photoluminescence Spectroscopy of Single $CsPbBr_3$ Perovskite Nanocrystals”. In: *Nano Letters* 22.18 (Sept. 2022). Publisher: American Chemical Society, pp. 7674–7681. DOI: 10.1021/acs.nanolett.2c02970 (Cited on page 95, 96, 101, 103).

[190] Kiyoshi Miyata et al. “Large polarons in lead halide perovskites”. In: *Science Advances* 3.8 (Aug. 2017). Publisher: American Association for the Advancement of Science, e1701217. DOI: 10.1126/sciadv.1701217 (Cited on page 99).

[191] Jarvist Moore Frost. “Calculating polaron mobility in halide perovskites”. In: *Physical Review B* 96.19 (Nov. 2017). Publisher: American Physical Society, p. 195202. DOI: 10.1103/PhysRevB.96.195202 (Cited on page 99).

[192] Samuel Poncé, Martin Schlipf, and Feliciano Giustino. “Origin of Low Carrier Mobilities in Halide Perovskites”. In: *ACS Energy Letters* 4.2 (Feb. 2019). Publisher: American Chemical Society, pp. 456–463. DOI: 10.1021/acsenergylett.8b02346 (Cited on page 99).

[193] Michael Sendner et al. "Optical phonons in methylammonium lead halide perovskites and implications for charge transport". en. In: *Materials Horizons* 3.6 (Oct. 2016). Publisher: The Royal Society of Chemistry, pp. 613–620. DOI: 10.1039/C6MH00275G (Cited on page 99).

[194] Mingjie Li et al. "Slow Hot-Carrier Cooling in Halide Perovskites: Prospects for Hot-Carrier Solar Cells". en. In: *Advanced Materials* 31.47 (Nov. 2019). Publisher: John Wiley & Sons, Ltd, p. 1802486. DOI: 10.1002/adma.201802486 (Cited on page 99).

[195] Fumiya Sekiguchi. "Enhancing the Hot-Phonon Bottleneck Effect in a Metal Halide Perovskite by Terahertz Phonon Excitation". In: *Physical Review Letters* 126.7 (2021). DOI: 10.1103/PhysRevLett.126.077401 (Cited on page 99).

[196] Ye Yangi et al. "Observation of a hot-phonon bottleneck in lead-iodide perovskites". en. In: *Nature Photonics* 10.1 (Jan. 2016). Publisher: Nature Publishing Group, pp. 53–59. DOI: 10.1038/nphoton.2015.213 (Cited on page 99).

[197] Takumi Yamada, Tomoko Aharen, and Yoshihiko Kanemitsu. "Up-converted photoluminescence from $(CH_3NH_3)PbI_3$ perovskite semiconductors: Implications for laser cooling". In: *Physical Review Materials* 3.2 (Feb. 2019). Publisher: American Physical Society, p. 024601. DOI: 10.1103/PhysRevMaterials.3.024601 (Cited on page 99).

[198] Ming Fu et al. "Unraveling exciton–phonon coupling in individual $FAPbI_3$ nanocrystals emitting near-infrared single photons". en. In: *Nature Communications* 9.1 (Aug. 2018). Publisher: Nature Publishing Group, p. 3318. DOI: 10.1038/s41467-018-05876-0 (Cited on page 100, 108, 110, 115, 116, 120, 121, 122).

[199] Mohamed-Raouf Amara et al. "Impact of Bright-Dark Exciton Thermal Population Mixing on the Brightness of $CsPbBr_3$ Nanocrystals". In: *Nano Letters* 24.14 (Apr. 2024). Publisher: American Chemical Society, pp. 4265–4271. DOI: 10.1021/acs.nanolett.4c00605 (Cited on page 100, 116, 120).

[200] Adam D. Wright et al. "Electron–phonon coupling in hybrid lead halide perovskites". en. In: *Nature Communications* 7.1 (May 2016), p. 11755. DOI: 10.1038/ncomms11755 (Cited on page 100, 108, 110).

[201] Xianzhong Zhou and Ziyang Zhang. "Electron–phonon coupling in $CsPbBr_3$". en. In: *AIP Advances* 10.12 (Dec. 2020), p. 125015. DOI: 10.1063/5.0017149 (Cited on page 100, 110).

[202] Zhuang Zhao et al. "Simultaneous Triplet Exciton–Phonon and Exciton–Photon Photoluminescence in the Individual Weak Confinement $CsPbBr_3$ Micro/Nanowires". In: *The Journal of Physical Chemistry C* 123.41 (Oct. 2019). Publisher: American Chemical Society, pp. 25349–25358. DOI: 10.1021/acs.jpcc.9b06643 (Cited on page 100, 110).

[203] C. Carabatos-Nédelec, M. Oussaïd, and K. Nitsch. "Raman scattering investigation of cesium plumbochloride, $CsPbCl_3$, phase transitions". en. In: *Journal of Raman Spectroscopy* 34.5 (May 2003). Publisher: John Wiley & Sons, Ltd, pp. 388–393. DOI: 10.1002/jrs.1005 (Cited on page 101).

[204] S. Hirotsu. "Far-infrared reflectivity spectra of $CsPbCl_3$". In: *Physics Letters A* 41.1 (Aug. 1972), pp. 55–56. DOI: 10.1016/0375-9601(72)90631-7 (Cited on page 101).

[205] Aparna Shinde, Richa Gahlaut, and Shailaja Mahamuni. "Low-Temperature Photoluminescence Studies of $CsPbBr_3$ Quantum Dots". In: *The Journal of Physical Chemistry C* 121.27 (July 2017). Publisher: American Chemical Society, pp. 14872–14878. DOI: 10.1021/acs.jpcc.7b02982 (Cited on page 102, 110).

[206] Francesco Masia et al. "Spin-Flip Limited Exciton Dephasing in CdSe/ZnS Colloidal Quantum Dots". In: *Physical Review Letters* 108.8 (Feb. 2012). Publisher: American Physical Society, p. 087401. DOI: 10.1103/PhysRevLett.108.087401 (Cited on page 102).

[207] Hendrik Utzat et al. "Coherent single-photon emission from colloidal lead halide perovskite quantum dots". en. In: *Science* 363.6431 (Mar. 2019), pp. 1068–1072. DOI: 10.1126/science.aau7392 (Cited on page 102, 109).

[208] Tadashi Itoh and Masayuki Furumiya. "Size-dependent homogeneous broadening of confined excitons in CuCl microcrystals". In: *Journal of Luminescence* 48-49 (Jan. 1991), pp. 704–708. DOI: 10.1016/0022-2313(91)90223-I (Cited on page 108).

[209] Peter Y. Yu and Manuel Cardona. *Fundamentals of Semiconductors*. Graduate Texts in Physics. Berlin, Heidelberg: Springer, 2005. DOI: 10.1007/b137661 (Cited on page 108).

[210] X. B. Zhang et al. "Influence of electron-phonon interaction on the optical properties of III nitride semiconductors". en. In: *Journal of Physics: Condensed Matter* 13.32 (July 2001), p. 7053. DOI: 10.1088/0953-8984/13/32/312 (Cited on page 108).

[211] Yan Lv et al. "Exciton-acoustic phonon coupling revealed by resonant excitation of single perovskite nanocrystals". en. In: *Nature Communications* 12.1 (Apr. 2021). Publisher: Nature Publishing Group, p. 2192. DOI: 10.1038/s41467-021-22486-5 (Cited on page 109).

[212] L. Coolen, X. Brokmann, and J.-P. Hermier. "Modeling coherence measurements on a spectrally diffusing single-photon emitter". en. In: *Physical Review A* 76.3 (Sept. 2007), p. 033824. DOI: 10.1103/PhysRevA.76.033824 (Cited on page 109).

[213] L. Coolen et al. "Emission Characterization of a Single CdSe-ZnS Nanocrystal with High Temporal and Spectral Resolution by Photon-Correlation Fourier Spectroscopy". In: *Physical Review Letters* 100.2 (Jan. 2008). Publisher: American Physical Society, p. 027403. DOI: 10.1103/PhysRevLett.100.027403 (Cited on page 109).

[214] Hiba Diab et al. "Narrow Linewidth Excitonic Emission in Organic–Inorganic Lead Iodide Perovskite Single Crystals". In: *The Journal of Physical Chemistry Letters* 7.24 (Dec. 2016). Publisher: American Chemical Society, pp. 5093–5100. DOI: 10.1021/acs.jpclett.6b02261 (Cited on page 110).

[215] Le Quang Phuong et al. "Free Excitons and Exciton–Phonon Coupling in $CH_3NH_3PbI_3$ Single Crystals Revealed by Photocurrent and Photoluminescence Measurements at Low Temperatures". In: *The Journal of Physical Chemistry Letters* 7.23 (Dec. 2016). Publisher: American Chemical Society, pp. 4905–4910. DOI: 10.1021/acs.jpclett.6b02432 (Cited on page 110).

[216] L. Biadala et al. "Band-Edge Exciton Fine Structure of Single CdSe-ZnS Nanocrystals in External Magnetic Fields". In: *Physical Review Letters* 105.15 (Oct. 2010). Publisher: American Physical Society, p. 157402. DOI: 10.1103/PhysRevLett.105.157402 (Cited on page 110).

[217] Patrick Odenthal et al. "Spin-polarized exciton quantum beating in hybrid organic inorganic perovskites". en. In: *Nature Physics* 13.9 (Sept. 2017). Publisher: Nature Publishing Group, pp. 894–899. DOI: 10.1038/nphys4145 (Cited on page 111).

[218] Natalia E. Kopteva et al. "Weak Dispersion of Exciton Landé Factor with Band Gap Energy in Lead Halide Perovskites: Approximate Compensation of the Electron and Hole Dependences". en. In: *Small* 20.16 (2024), p. 2300935. DOI: 10.1002/smll.202300935 (Cited on page 111).

[219] E. Tsitsishvili, H. Kalt, and R. v. Baltz. "Exciton-spin relaxation in weakly confining quantum dots due to spin–orbit interaction". en. In: *physica status solidi (b)* 243.10 (2006). _eprint: https://onlinelibrary.wiley.com/doi/pdf/10.1002/pssb.200668005, pp. 2274–2277. DOI: 10.1002/pssb.200668005 (Cited on page 112).

[220] E. Tsitsishvili, R. v. Baltz, and H. Kalt. "Temperature dependence of polarization relaxation in semiconductor quantum dots". In: *Physical Review B* 66.16 (Oct. 2002). Publisher:

American Physical Society, p. 161405. DOI: 10.1103/PhysRevB.66.161405 (Cited on page 115, 122).

[221] Olivier Labeau, Philippe Tamarat, and Brahim Lounis. "Temperature Dependence of the Luminescence Lifetime of Single CdSe/ZnS Quantum Dots". In: *Physical Review Letters* 90.25 (June 2003). Publisher: American Physical Society, p. 257404. DOI: 10.1103/PhysRevLett.90.257404 (Cited on page 118).

[222] L. Biadala et al. "Direct Observation of the Two Lowest Exciton Zero-Phonon Lines in Single CdSe/ZnS Nanocrystals". In: *Physical Review Letters* 103.3 (July 2009). Publisher: American Physical Society, p. 037404. DOI: 10.1103/PhysRevLett.103.037404 (Cited on page 118).

[223] Hai Wei, Guang-Can Guo, and Lixin He. "Slow exciton spin relaxation in single self-assembled $In_{1-x}Ga_xAs/GaAs$ quantum dots". In: *Phys. Rev. B* 89.24 (June 2014), p. 5305. DOI: https://doi-org.inp.bib.cnrs.fr/10.1103/PhysRevB.89.245305 (Cited on page 119).

[224] Benjamin T. Diroll, Hua Zhou, and Richard D. Schaller. "Low-Temperature Absorption, Photoluminescence, and Lifetime of $CsPbX_3$ (X = Cl, Br, I) Nanocrystals". en. In: *Advanced Functional Materials* 28.30 (2018), p. 1800945. DOI: 10.1002/adfm.201800945 (Cited on page 121).

[225] Andrea Rubino et al. "Mesoporous Matrices as Hosts for Metal Halide Perovskite Nanocrystals". en. In: *Advanced Optical Materials* 8.9 (May 2020), p. 1901868. DOI: 10.1002/adom.201901868 (Cited on page 131, 132).

[226] Victor Malgras et al. "Stable Blue Luminescent $CsPbBr_3$ Perovskite Nanocrystals Confined in Mesoporous Thin Films". en. In: *Angewandte Chemie International Edition* 57.29 (2018). _eprint: https://onlinelibrary.wiley.com/doi/pdf/10.1002/anie.201802335, pp. 8881–8885. DOI: 10.1002/anie.201802335 (Cited on page 132, 133).

[227] Stepan Demchyshyn et al. "Confining metal-halide perovskites in nanoporous thin films". In: *Science Advances* 3.8 (Aug. 2017). Publisher: American Association for the Advancement of Science, e1700738. DOI: 10.1126/sciadv.1700738 (Cited on page 132).

[228] David O. Tiede et al. "Effect of Connectivity on the Carrier Transport and Recombination Dynamics of Perovskite Quantum-Dot Networks". In: *ACS Nano* 18.3 (Jan. 2024). Publisher: American Chemical Society, pp. 2325–2334. DOI: 10.1021/acsnano.3c10239 (Cited on page 132).

[229] Victor Malgras et al. "Observation of Quantum Confinement in Monodisperse Methylammonium Lead Halide Perovskite Nanocrystals Embedded in Mesoporous Silica". In: *Journal of the American Chemical Society* 138.42 (Oct. 2016). Publisher: American Chemical Society, pp. 13874–13881. DOI: 10.1021/jacs.6b05608 (Cited on page 132).

[230] Carlos Romero-Pérez et al. "Ultrapure Green High Photoluminescence Quantum Yield from $FAPbBr_3$ Nanocrystals Embedded in Transparent Porous Films". In: *Chemistry of Materials* 35.14 (July 2023). Publisher: American Chemical Society, pp. 5541–5549. DOI: 10.1021/acs.chemmater.3c00934 (Cited on page 132, 133, 137).

[231] Michael Wark, Hartwig Wellmann, and Jiri Rathousky. "Homogeneously distributed CdS and CdSe nanoparticles in thin films of mesoporous silica". In: *Thin Solid Films* 458.1 (June 2004), pp. 20–25. DOI: 10.1016/j.tsf.2003.11.189 (Cited on page 132).

[232] Ping Wang et al. "Synthesis of CdSe nanoparticles into the pores of mesoporous silica microspheres". In: *Acta Materialia* 56.5 (Mar. 2008), pp. 1144–1150. DOI: 10.1016/j.actamat.2007.11.006 (Cited on page 132).

[233] T. E. Hodgson et al. "Mesoporous matrices for quantum computation with improved response through redundance". In: *Journal of Applied Physics* 101.11 (June 2007), p. 114319. DOI: 10.1063/1.2745438 (Cited on page 132).

[234] Dmitry N. Dirin et al. "Harnessing Defect-Tolerance at the Nanoscale: Highly Luminescent Lead Halide Perovskite Nanocrystals in Mesoporous Silica Matrixes". In: *Nano Letters* 16.9 (Sept. 2016). Publisher: American Chemical Society, pp. 5866–5874. DOI: 10.1021/acs.nanolett.6b02688 (Cited on page 132).

[235] M. Ibrahim Dar et al. "Origin of unusual bandgap shift and dual emission in organic-inorganic lead halide perovskites". In: *Science Advances* 2.10 (Oct. 2016). Publisher: American Association for the Advancement of Science, e1601156. DOI: 10.1126/sciadv.1601156 (Cited on page 135).

[236] Sergii Yakunin et al. "Low-threshold amplified spontaneous emission and lasing from colloidal nanocrystals of caesium lead halide perovskites". en. In: *Nature Communications* 6.1 (Aug. 2015). Publisher: Nature Publishing Group, p. 8056. DOI: 10.1038/ncomms9056 (Cited on page 139, 140, 141).

[237] Zhengzheng Liu et al. "Two-Photon Pumped Amplified Spontaneous Emission and Lasing from Formamidinium Lead Bromine Nanocrystals". In: *ACS Photonics* 6.12 (Dec. 2019). Publisher: American Chemical Society, pp. 3150–3158. DOI: 10.1021/acsphotonics.9b01226 (Cited on page 139, 140, 141).

[238] Yue Wang et al. "All-Inorganic Colloidal Perovskite Quantum Dots: A New Class of Lasing Materials with Favorable Characteristics". In: *Advanced Materials* 27.44 (2015). _eprint: https://onlinelibrary.wiley.com/doi/pdf/10.1002/adma.201503573, pp. 7101–7108. DOI: 10.1002/adma.201503573 (Cited on page 139).

[239] Antonio Balena et al. "Temperature Dependence of the Amplified Spontaneous Emission from $CsPbBr_3$ Nanocrystal Thin Films". In: *The Journal of Physical Chemistry C* 122.10 (Mar. 2018). Publisher: American Chemical Society, pp. 5813–5819. DOI: 10.1021/acs.jpcc.8b01419 (Cited on page 139).

[240] Stefania Milanese et al. "Rationalizing the Amplified Spontaneous Emission Mechanism in $CsPbBr_3$ Perovskite Nanocrystals Films by means of Optical Gain Measurements". en. In: *Advanced Optical Materials* n/a.n/a (), p. 2401078. DOI: 10.1002/adom.202401078 (Cited on page 139).

[241] Zhixing Gan et al. "External stokes shift of perovskite nanocrystals enlarged by photon recycling". In: *Applied Physics Letters* 114.1 (Jan. 2019), p. 011906. DOI: 10.1063/1.5081805 (Cited on page 141).

[242] Changsoon Cho et al. "The role of photon recycling in perovskite light-emitting diodes". en. In: *Nature Communications* 11.1 (Jan. 2020). Publisher: Nature Publishing Group, p. 611. DOI: 10.1038/s41467-020-14401-1 (Cited on page 141).

[243] David Giovanni et al. "Origins of the long-range exciton diffusion in perovskite nanocrystal films: photon recycling vs exciton hopping". en. In: *Light: Science & Applications* 10.1 (Jan. 2021). Publisher: Nature Publishing Group, p. 2. DOI: 10.1038/s41377-020-00443-z (Cited on page 141, 144, 145).

[244] Erika Penzo et al. "Long-Range Exciton Diffusion in Two-Dimensional Assemblies of Cesium Lead Bromide Perovskite Nanocrystals". In: *ACS Nano* 14.6 (June 2020). Publisher: American Chemical Society, pp. 6999–7007. DOI: 10.1021/acsnano.0c01536 (Cited on page 141, 143, 144).

[245] Zakarya Ouzit et al. "FRET-Mediated Collective Blinking of Self-Assembled Stacks of CdSe Semiconducting Nanoplatelets". In: *ACS Photonics* 10.2 (Feb. 2023). Publisher: American Chemical Society, pp. 421–429. DOI: 10.1021/acsphotonics.2c01441 (Cited on page 141, 143).

[246] Chen Wang et al. "A Surface Engineering Approach for Promoting Dexter Energy Transfer from Lead Halide Perovskite Nanocrystals". In: *The Journal of Physical Chemistry C* 127.2 (Jan. 2023). Publisher: American Chemical Society, pp. 1135–1144. DOI: 10.1021/acs.jpcc.2c07664 (Cited on page 141).

[247] Chaochao Qin et al. "Ultrafast energy transfer from perovskite quantum dots to chromophore". In: *Results in Physics* 51 (Aug. 2023), p. 106664. DOI: 10.1016/j.rinp.2023.106664 (Cited on page 141).

[248] Joseph R. Lakowicz, ed. *Principles of Fluorescence Spectroscopy*. en. Boston, MA: Springer US, 2006. DOI: 10.1007/978-0-387-46312-4 (Cited on page 142).

[249] Theodor Förster. "Energy migration and fluorescence". en. In: *Journal of Biomedical Optics* 17.1 (2012), p. 011002. DOI: 10.1117/1.JBO.17.1.011002 (Cited on page 142).

[250] Th. Förster. "Zwischenmolekulare Energiewanderung und Fluoreszenz". de. In: *Annalen der Physik* 437.1-2 (1948), pp. 55–75. DOI: 10.1002/andp.19484370105 (Cited on page 142).

[251] Michael Graetzel et al. "Materials interface engineering for solution-processed photovoltaics". en. In: *Nature* 488.7411 (Aug. 2012). Publisher: Nature Publishing Group, pp. 304–312. DOI: 10.1038/nature11476 (Cited on page 143).

[252] Cherie R. Kagan et al. "Building devices from colloidal quantum dots". en. In: *Science* 353.6302 (Aug. 2016), aac5523. DOI: 10.1126/science.aac5523 (Cited on page 143).

[253] Leepsa Mishra et al. "Förster Resonance Energy Transfer Assisted Enhancement in Optoelectronic Properties of Metal Halide Perovskite Nanocrystals". In: *The Journal of Physical Chemistry Letters* 13.19 (May 2022). Publisher: American Chemical Society, pp. 4357–4364. DOI: 10.1021/acs.jpclett.2c00764 (Cited on page 143).

[254] Polina O. Anikeeva et al. "Quantum Dot Light-Emitting Devices with Electroluminescence Tunable over the Entire Visible Spectrum". In: *Nano Letters* 9.7 (July 2009). Publisher: American Chemical Society, pp. 2532–2536. DOI: 10.1021/nl9002969 (Cited on page 143).

[255] Jun Miyazaki and Shuichi Kinoshita. "Site-selective spectroscopic study on the dynamics of exciton hopping in an array of inhomogeneously broadened quantum dots". en. In: *Physical Review B* 86.3 (July 2012), p. 035303. DOI: 10.1103/PhysRevB.86.035303 (Cited on page 143, 146).

[256] C. R. Kagan et al. "Electronic Energy Transfer in CdSe Quantum Dot Solids". In: *Physical Review Letters* 76.9 (Feb. 1996). Publisher: American Physical Society, pp. 1517–1520. DOI: 10.1103/PhysRevLett.76.1517 (Cited on page 143).

[257] S. A. Crooker et al. "Spectrally Resolved Dynamics of Energy Transfer in Quantum-Dot Assemblies: Towards Engineered Energy Flows in Artificial Materials". In: *Physical Review Letters* 89.18 (Oct. 2002). Publisher: American Physical Society, p. 186802. DOI: 10.1103/PhysRevLett.89.186802 (Cited on page 143, 145).

[258] C. R. Kagan, C. B. Murray, and M. G. Bawendi. "Long-range resonance transfer of electronic excitations in close-packed CdSe quantum-dot solids". en. In: *Physical Review B* 54.12 (Sept. 1996), pp. 8633–8643. DOI: 10.1103/PhysRevB.54.8633 (Cited on page 143, 145).

[259] Chris de Weerd et al. "Energy Transfer between Inorganic Perovskite Nanocrystals". In: *The Journal of Physical Chemistry C* 120.24 (June 2016). Publisher: American Chemical Society, pp. 13310–13315. DOI: 10.1021/acs.jpcc.6b04768 (Cited on page 143).

[260] Rongfeng Yuan et al. "A composite electrodynamic mechanism to reconcile spatiotemporally resolved exciton transport in quantum dot superlattices". In: *Science Advances* 9.42 (Oct. 2023). Publisher: American Association for the Advancement of Science, eadh2410. DOI: 10.1126/sciadv.adh2410 (Cited on page 146).

[261] Jun Miyazaki and Shuichi Kinoshita. "Temperature-Dependent Exciton Hopping in an Array of Inhomogeneously Broadened Quantum Dots". en. In: *Journal of the Physical Society of Japan* 81.7 (July 2012), p. 074708. DOI: 10.1143/JPSJ.81.074708 (Cited on page 146).

[262] Mino Yang and Graham R Fleming. "Influence of phonons on exciton transfer dynamics: comparison of the Redfield, Förster, and modified Redfield equations". en. In: *Chemical Physics* (2002) (Cited on page 147).

[263] Marc Achermann et al. "Picosecond Energy Transfer in Quantum Dot Langmuir-Blodgett Nanoassemblies". In: *The Journal of Physical Chemistry B* 107.50 (Dec. 2003). Publisher: American Chemical Society, pp. 13782–13787. DOI: 10.1021/jp036497r (Cited on page 154, 155).

[264] Andrew H. Proppe et al. "Spectrally Resolved Ultrafast Exciton Transfer in Mixed Perovskite Quantum Wells". In: *The Journal of Physical Chemistry Letters* 10.3 (Feb. 2019). Publisher: American Chemical Society, pp. 419–426. DOI: 10.1021/acs.jpclett.9b00018 (Cited on page 154).

[265] T. Franzl et al. "Fast energy transfer in layer-by-layer assembled CdTe nanocrystal bilayers". In: *Applied Physics Letters* 84.15 (Apr. 2004), pp. 2904–2906. DOI: 10.1063/1.1702136 (Cited on page 155).

[266] Clare E. Rowland et al. "Picosecond energy transfer and multiexciton transfer outpaces Auger recombination in binary CdSe nanoplatelet solids". en. In: *Nature Materials* 14.5 (May 2015). Publisher: Nature Publishing Group, pp. 484–489. DOI: 10.1038/nmat4231 (Cited on page 155).

[267] Jiamin Xiong et al. “Enhanced photoluminescence efficiencies of $CsPbCl_{3-x}Br_x$ nanocrystals by incorporating neodymium ions”. In: *Journal of Luminescence* 243 (Mar. 2022), p. 118658. DOI: 10.1016/j.jlumin.2021.118658 (Cited on page 158).

[268] Ghada H. Ahmed et al. “Giant Photoluminescence Enhancement in $CsPbCl_3$ Perovskite Nanocrystals by Simultaneous Dual-Surface Passivation | ACS Energy Letters”. In: (2018). DOI: 10.1021/acsenergylett.8b01441 (Cited on page 158).